POLYTECHNIQUE MONTRÉAL
affiliée à l'Université de Montréal

Small-scale experiments for the development and characterization of novel hypergolic hybrid rocket fuel systems

OLIVIER JOBIN
Département de génie mécanique

Thèse présentée en vue de l'obtention du diplôme de *Philosophiæ Doctor*
Génie mécanique

Décembre 2023

POLYTECHNIQUE MONTRÉAL
affiliée à l'Université de Montréal

Cette thèse intitulée :

Small-scale experiments for the development and characterization of novel hypergolic hybrid rocket fuel systems

présentée par **Olivier JOBIN**
en vue de l'obtention du diplôme de *Philosophiæ Doctor*
a été dûment acceptée par le jury d'examen constitué de :

Frédérick GOSSELIN, président
Étienne ROBERT, membre et directeur de recherche
Jerin JOHN, membre externe
Steven F. SON, membre externe

DEDICATION

To my family and friends
Thank you so much for everything...

À ma famille et mes ami.e.s,
un grand merci pour tout...

"Roads go ever ever on,
Over rock and under tree,
By caves where never sun has shone,
By streams that never find the sea"

- Bilbo Baggins
in *The Hobbit* by J.R.R. Tolkien

ACKNOWLEDGEMENTS

First of all, I would like to thank my thesis director Professor Étienne Robert for his support over the past few years. He introduced me to scientific research during my undergraduate studies, and since then, guided me in conducting experiments and testing my ideas. I could not have been better guided on this fascinating scientific journey. I do not think that every professor would have liked to see their student in a full hazmat suit, handling strong acids, rocket fuels, and burning stuff in his lab. I am fortunate and very grateful to have been given a wide latitude to explore and test in his lab. Thank you for your trust in me.

This project would not have been possible without the countless and invaluable help of Benoît Dumas. He helped me, during two summer internships and during his master's degree, to conduct experiments, develop ideas, find the 1.5 mm hex key, and successfully (and sometimes not so successfully...) try to obtain the results that are presented here.

Although I have been fascinated by rockets since my youth, I was introduced to real rocket science by my good friend Bachar Elzein. Thank you for the trust you placed in me during our time working together. I hope we will work together again on future projects!

I would like to thank Mathieu Chartray-Pronovost and William Kaprolat for their help in conducting the hypergolic slab burner experiments. This work would also not have been possible without you. It takes a special kind of person to test rocket fuels - someone you can trust. You are that kind of person, thank you very much!

I would like to thank my lab mates for bringing the *philosophical* aspect of my Ph.D. (in no particular order: Dominic, Marianne, Martin, Elie, Mathieu C.-P., Arona, Mathieu G., William, Benoît, Alexis, Gabriel D. (x2), Guillaume, Alain, Antonella, Marc-André, Olivier, Xavier, Pablo, Jean, Cristian, Tanja, Joanna, Israe, Kobra, Vincent,). I enjoyed our lunches and (extended) coffee breaks discussing weird theories, fun stuff, and sometimes... science. There was never a boring day with you around! A special thanks to the interns who worked on my project, Benoît, Israe, Alexis, and Joanna.

Thanks to Philippe Massé, Philippe Versailles, and Professor Jérôme Vétêl for their help in the lab. Thanks also to Professor Bruno Savard for your input on my project. Another special thanks go to Tanja, Cristian, and Pablo for the kind lab introduction at the very beginning of my project. You helped me figure out so much and were a much-needed guiding light working in the lab. I am also very grateful to the research team at McGill, Hatem, Cristina, Joe, and Prof. Friščić. Thanks to my friends outside of Polytechnique for their

support! I also acknowledge the financial support of the Natural Sciences and Engineering Research Council of Canada and the Canadian Space Agency.

It goes without saying that my project would not have been completed without the never-ending support of my family. Je suis tellement chanceux d'avoir eu votre support continu tout au long de mon projet. À mon frère Louis, ma maman Sophie et mon papa Pierre, je vous remercie et vous aime énormément! Un merci aussi à Odette, Jean-Maurice, Catherine, Guy, croquette et mini-croquette.

Finally, my biggest thanks go to Hélène. Thank you for your endless support, your love and your friendship. You inspire me to always give my best in everything I do. I am so grateful to have you in my life and I am looking forward to our future projects together. Je t'aime et merci pour tout!

ABSTRACT

Hypergolic materials can rapidly ignite upon contact with an oxidizer. This property makes them attractive for propulsion systems such as rocket engines to reduce the complexity and increase the reliability of ignition systems. Hypergolic propellants eliminate the need for complex and heavy ignition modules that must be implemented in rockets, increasing operational, development and testing costs. Hypergolicity in hybrid rocket propulsion is often realized through additives in the solid fuel. These spontaneously ignite when in contact with an appropriate oxidizer. Research on hypergolic ignition in hybrid engines is not as mature as its counterpart for liquid engines, with the underlying physical and chemical phenomena still poorly understood. Therefore, laboratory-scale experiments are needed to gain knowledge on the dynamics associated with hypergolic fuel additives. The results of these experiments are intended to aid in the selection of materials for the propulsion system, as well as to provide valuable information for the simulation and prediction of the hypergolic behavior of these fuels.

First, a detailed literature review is presented. It covers the general combustion theory of hybrid rocket engines and identifies commonly used fuels. Additives are also introduced as they provide the ability to finely tune combustion behavior and fuel properties such as ignition delay, burn rate, performance, and mechanical properties. A review of the most common hypergolic additives is then presented. It covers the experiments usually conducted to study their hypergolic character. Finally, the literature review also presents existing laboratory-scale combustion visualization research facilities used to study the combustion behavior of hybrid fuel, with a discussion of challenges and knowledge gaps. For example, hypergolicity in hybrid engines has already shown promising results in some space applications such as satellite maneuvering, spacecraft orbit control, and further simplifies the ignition sequence of rocket engines. However, the ignition tests typically performed do not represent the real-world operating conditions of a typical engine. They are often conducted at ambient pressure, with air surrounding the fuel and oxidizer, and by dropping a single, rather large, oxidizer droplet into a small amount of fuel.

Given the challenges associated with hypergolic ignitions in hybrid rocket propulsion, the general objective of this thesis is to support the development of hypergolic hybrid rocket engines by conducting small-scale experiments and providing experimental results. First, a slab burner was designed to visualize the combustion rate and combustion instabilities of hybrid rocket fuels. Paraffin fuel with alpha-olefin (Vybar) additive is evaluated. Alpha-olefins

have previously been identified as good candidates to increase the mechanical properties and viscosity of paraffin without affecting its performance. However, their effect on regression rate was not previously known. The results show that the addition of 20 wt.% alpha-olefin to a paraffin fuel reduces its regression rate by approximately 20 %. These measurements are made using an automated image analysis tool developed for this project. This tool automatically analyzes images captured by a high-speed camera and tracks the edge of the burning fuel. The regression rate is then determined.

The second section of the thesis presents the results of the evaluation of novel hypergolic materials called hypergolic metal-organic frameworks. An experimental test campaign is conducted to evaluate the suitability of these additives to react when mixed with paraffin wax. The results show very fast ignition, with most of the tested configurations igniting in less than 10 ms with white fuming nitric acid as oxidizer. Theoretical performance calculations are carried out and show that the penalty on the specific impulse for utilizing these additives for their hypergolic properties is only 2% compared to neat paraffin.

Then, paraffin/ammonia borane fuels are tested when exposed to a spray of liquid oxidizer, as opposed to traditional droplet ignition tests. This configuration is chosen because it is closer to the conditions found in real hybrid engines. Hypergolic ignition reveals a relationship between the velocity of the droplet in the spray hitting the fuel pellet and the ignition delay. In addition, the ignition delays measured are greater than those measured in droplet ignition tests.

Finally, the slab burner developed for this project is adapted to the use of liquid oxidizers. This allows the study of hypergolic ignition of paraffin/ammonia borane fuels in conditions representative of a hybrid rocket engine. The study examines hypergolic phenomena in two configurations: one using nitric acid as the oxidizer, and the other where gaseous oxygen is the oxidizer, but nitric acid is used to ignite the fuel through its hypergolic effect on the additives. Both operating modes achieved successful ignition and reignition, albeit with a longer ignition delay compared to droplet ignition experiments. Experiments using gaseous oxygen as the primary oxidizer show significantly faster ignition (approximately 300 ms) than those relying solely on nitric acid (ranging from 2000 to 3000 ms).

This work is expected to have two major impacts. First, it is anticipated to influence the methodologies used for small-scale experimental studies within the hypergolic hybrid rocket community, particularly in the study of ignition, whether through spray tests or slab burners. Second, it is expected to provide significant insight, particularly in the use of metal-organic frameworks as hypergolic additives and in revealing the effect of oxidizer spray conditions on ignition.

RÉSUMÉ

Les matériaux hypergoliques ont la capacité de s'enflammer rapidement au contact d'un oxydant. Cette propriété les rend intéressants pour les systèmes de propulsion tels que les moteurs de fusée, afin de réduire la complexité et d'augmenter la fiabilité des systèmes d'allumage. Les propergols hypergoliques éliminent le besoin de modules d'allumage complexes et lourds qui doivent être mis en œuvre dans les fusées, ce qui augmente les coûts opérationnels, de développement et d'essai. La création de propergols hypergoliques pour la propulsion de fusées hybrides est souvent réalisée en ajoutant des additifs au combustible solide. Ces additifs s'enflamment spontanément au contact d'un oxydant liquide. La recherche sur l'allumage hypergolique dans les moteurs hybrides n'est pas aussi avancée que son équivalent pour les moteurs liquides, et les phénomènes ainsi que la chimie sous-jacents sont mal compris. C'est pourquoi des expériences à l'échelle du laboratoire sont souvent menées pour obtenir des informations et des connaissances sur les additifs hypergoliques. Les résultats de ces expériences sont destinés à faciliter la sélection des matériaux pour le système de propulsion et à fournir des informations précieuses pour la simulation et la prédiction du comportement hypergolique de ces carburants.

Tout d'abord, une analyse détaillée de la littérature est présentée. Elle couvre la théorie générale de la combustion des fusées hybrides et identifie les carburants couramment utilisés. Les additifs sont également présentés, car ils permettent de modifier précisément le comportement de la combustion et les propriétés du carburant, telles que la vitesse de combustion, les performances et les propriétés mécaniques. Une revue des additifs hypergoliques les plus couramment testés est ensuite présentée. Elle couvre les expériences habituellement menées pour étudier leur capacité hypergolique. La revue de la littérature présente également les installations de recherche sur la visualisation de la combustion à l'échelle du laboratoire utilisées pour étudier le comportement de combustion des carburants hybrides d'une manière unique en utilisant des techniques d'imagerie à grande vitesse. Enfin, les défis et les lacunes en matière de connaissances sont abordés. Par exemple, l'hypergolicité dans les moteurs hybrides a déjà montré des résultats prometteurs dans certaines applications spatiales telles que la manœuvre des satellites, le contrôle de l'orbite des engins spatiaux, et simplifie davantage la séquence d'allumage des moteurs hybrides. Cependant, les essais d'allumage généralement effectués ne représentent pas les conditions réelles de fonctionnement d'un moteur typique. Ils sont généralement réalisés à la pression ambiante, avec de l'air entourant le carburant et l'oxydant, et en laissant tomber une seule gouttelette d'oxydant, plutôt grosse, dans une petite quantité de carburant.

Étant donné les défis associés aux allumages hypergoliques dans la propulsion des fusées hybrides, l'objectif général de cette thèse est de soutenir le développement des moteurs-fusées hybrides hypergoliques en menant des expériences à petite échelle et en fournissant des résultats expérimentaux.

Tout d'abord, un brûleur (slab burner) a été conçu pour visualiser la vitesse de combustion et les instabilités de combustion des carburants hybrides pour fusées. Les carburants paraffiniques avec des additifs alpha-oléfiniques (Vybar) sont évalués. Les alpha-oléfines ont été précédemment identifiées comme de bons candidats pour augmenter les propriétés mécaniques et la viscosité de la paraffine sans affecter ses performances. Cependant, leur effet sur le taux de régression n'était pas connu jusqu'à présent. Les résultats montrent que l'ajout de 20% en poids d'alpha-oléfines à un carburant à base de paraffine réduit son taux de régression d'environ 20%. Ces mesures sont effectuées à l'aide d'un outil d'analyse d'images automatisé développé pour ce projet. Cet outil analyse automatiquement les images capturées par une caméra à grande vitesse et suit le bord du combustible en combustion. Le taux de régression est ensuite déterminé.

La deuxième partie de la thèse présente les résultats de l'évaluation de nouveaux matériaux hypergoliques appelés cadres métallo-organiques hypergoliques. Une campagne de tests expérimentaux est menée pour évaluer l'aptitude de ces additifs à réagir lorsqu'ils sont mélangés à de la cire de paraffine. Les résultats montrent un allumage très rapide, la plupart des configurations testées s'allumant en moins de 10 ms avec de l'acide nitrique fumant blanc comme oxydant. Des calculs théoriques de performance sont effectués et montrent que le coût de performance de l'utilisation de ces additifs pour leurs propriétés hypergoliques n'est que de 2% par rapport à la paraffine pure.

Ensuite, les carburants paraffine/borazane sont testés lorsqu'ils sont exposés à une pulvérisation d'oxydant liquide, par opposition aux tests traditionnels d'allumage de gouttelettes. Cette configuration a été choisie parce qu'elle est plus proche des conditions rencontrées dans les moteurs hybrides réels. L'allumage hypergolique révèle une relation entre la vitesse de la gouttelette dans le spray impactant la pastille de combustible et le délai d'allumage. De plus, les délais d'allumage mesurés sont plus importants que ceux mesurés lors des essais d'allumage en gouttelettes.

Enfin, le brûleur (slab burner) conçu précédemment est adapté à l'utilisation d'oxydants liquides. Cela permet d'étudier l'allumage hypergolique des carburants paraffine/borazane dans une configuration de moteur. L'étude examine les phénomènes hypergoliques dans deux configurations : l'une utilisant l'acide nitrique comme oxydant, et l'autre où l'oxygène gazeux est l'oxydant principal mais où l'acide nitrique enflamme le moteur de manière hypergolique.

Les deux modes de fonctionnement permettent actuellement un allumage et un rallumage réussis, bien que le délai d'allumage soit plus long que pour les expériences d'allumage de gouttelettes. Les expériences utilisant l'oxygène gazeux comme oxydant primaire montrent un allumage significativement plus rapide (environ 300 ms) que celles reposant uniquement sur l'acide nitrique (entre 2000 et 3000 ms).

Ces travaux devraient avoir deux conséquences majeures. Premièrement, il devrait influencer les méthodologies utilisées pour de telles études au sein de la communauté hypergolique, en particulier dans l'étude de l'allumage hypergolique, que ce soit par le biais d'essais d'allumage par pulvérisation ou de brûleurs à braises hypergoliques. Deuxièmement, il devrait fournir des informations importantes, en particulier sur l'utilisation des MOF comme additifs hypergoliques et en révélant l'effet des conditions de pulvérisation de l'oxydant sur l'allumage hypergolique.

TABLE OF CONTENTS

LIST OF TABLES

LIST OF FIGURES

LIST OF SYMBOLS AND ACRONYMS

Symbols

A	Area [m^2]
$a*$	Second color coordinate in CIELAB space [-]
$b*$	Third color coordinate in CIELAB space [-]
c	Effective exhaust velocity [m/s]
$C*$	Characteristic velocity [m/s]
C_d	Discharge coefficient [-]
D_{50}	Median diameter [µm]
f	Primary hybrid oscillation frequency [Hz]
F	Thrust [N]
g	Earth's gravitational constant [m/s^2]
G_{ox}	Oxidizer mass flux [kg/m^2s]
h	thickness of melt layer [m]
H	Enthalpy [J]
L	Length [m]
$L*$	First color coordinate in CIELAB space [-]
I	Signal intensity [-]
I_{sp}	Specific impulse [s]
$I_{turbulence}$	Turbulence intensity [-]
$\dot{m}$	Mass flow rate [kg/s]
M_W	Molecular weight [g/mol]
P	Pressure [Pa]
$\dot{r}$	Regression rate [mm/s]
R^2	Coefficient of determination
t	Time [s]
T	Temperature [K]
T	Turbulence intensity [-]
u	Velocity [m/s]
U	Velocity [m/s]
$\bar{U}$	Mean velocity [m/s]
U'	Velocity fluctuation [m/s]
U_{RMS}	Root mean square of velocity [m/s]

V	Velocity [m/s]
w	Total velocity [m/s]
Y	Mass fraction [-]
γ	Specific heat ratio [-]
ΔE	Color difference [-]
Δh_f^0	Standard enthalpy of formation [kJ/mol]
Δm	Mass difference [g]
μ	Dynamic viscosity [Pa ·s]
ρ	Density [kg/m^3]
ρI_{sp}	Density specific impulse [s·kg/m^3]
σ	Surface tension [N/m]
σ	Standard deviation [-]
σ^2	Variance [-]

Acronyms

AB	Ammonia borane
BOS	Background-oriented Schlieren
CEA	Chemical Equilibrium with Applications
DAQ	Data acquisition
DLR	German Aerospace Center (Deutsches Zentrum für Luft- und Raumfahrt)
EDBB	Ethylenediamine-bisborane
EVA	Ethylene vinyl-acetate
FFT	Fast Fourier transform
fps	Frames per second
GOx	Gaseous oxygen
HDPE	High density polyethylene
HMOF	Hypergolic metal-organic framework
HTP	High-test peroxide (H_2O_2)
HTPB	Hydroxyl-terminated polybutadiene
ID	Ignition delay
IF	Impact factor
IRFNA	Inhibited red fuming nitric acid
K-H	Kelvin-Helmotlz instabilities
LAH	Lithium aluminum hydride

LDPE	Low density polyethylene
LOX	Liquid oxygen
MAV	Mars Ascent Vehicle
MMH	Monomethyl-hydrazine
MOF	Metal-organic framework
MON	Mixed oxides of nitrogen
NTO	Nitrogen tetroxide
O/F	Oxidizer-to-fuel ratio
ONERA	Office National d'Etudes et de Recherches Aérospatiales
P&ID	Piping and instrumentation diagram
PBTSA	Potassium bis(trimethylsilyl)amide
PDA	Phase doppler anemometry
PIV	Particle image velocimetry
PMMA	Poly(methyl methacrylate)
Re	Reynolds number
RFNA	Red fuming nitric acid
RGB	Red, green, blue
RMS	Root mean square
RP-1	Rocket-grade kerosene
SPLab	Space Propulsion Laboratory
SSTO	Single stage to orbit
STD	Standard deviation
TEA-TEB	Triethylaluminum-triethylborane
TMEDBB	Tetramethylethylenediamine-bisborane
TTL	Transistor-Transistor-Logic
UDMH	Unsymmetrical dimethylhydrazine
UTC	United Technology Center
We	Weber number
WFNA	White fuming nitric acid
ZIF	Zeolitic imidazolate frameworks

LIST OF APPENDICES

CHAPTER 1 INTRODUCTION

1.1 Rocket propulsion - a brief background

Access to space and the development of suborbital flights are critical for several scientific and industrial fields such as telecommunications, space exploration, space tourism, understanding climate change, geological studies, national security, and many more. Although space propulsion has been studied for several decades, launching a payload into space is still an extremely complex task. For more than 80 years, chemical propulsion has been the only choice for launching payloads beyond Earth's atmosphere, with no alternatives planned for the foreseeable future.

Superpower political entities such as Russia, the United-States, the European Union and China have developed large-scale space programs allowing them to conduct a wide range of space missions. Their ability to launch rockets into space is based on the enormous resources available for these missions. Countries such as Canada, where the space industry is comparatively underdeveloped, do not have the expertise nor the resources to develop an equivalent space launch program. However, smaller launch vehicles could help smaller countries get their own payloads into space.

Similarly to aircrafts, rockets come in different sizes, depending on the payload that needs to be carried into orbit and they can be adapted to transport only small satellites. In addition, the development, production and launch costs of smaller rockets are generally much lower than those of larger spacecraft. Compared to larger rockets, the reduced number of mechanical parts in small rockets requires fewer resources for certification, design and manufacturing. As a result, smaller rockets also enable faster launch response time in the event of an emergency. For example, if a catastrophic situation occurs on Earth (flooding, volcanic eruption, wildfire, etc.), requiring a dedicated satellite for observation, such small rockets would be adequate to launch it quickly.

A typical rocket configuration can be as follows: an engine providing thrust to the rocket, a body containing the fuel and the oxidizer needed for combustion and a fairing that contains a payload. A rocket may also contain several engine-body sections called stages. As the vehicle ascends and consumes its fuel, the stages separate and other engines are ignited.

Rockets are powered by different types of engines; they can be classified according to the physical state of the oxidizer and the fuel used. Solid-fuel rockets use a premixed combination of fuel and oxidizer in a solid phase. Once ignited, this type of engine cannot be stopped as

there is no "flow" of reactant to control. The lack of plumbing, injectors and other mechanical parts makes them simple to operate. However, this simplicity for in-flight operation comes at a significant cost in pre-flight handling and safety hazards. Common solid rockets can generate thrust comparable to liquid engines, but with simpler mechanical parts, as shown in Figure 1.1. They are therefore well suited for applications such as liftoff rocket boosters or military operations.

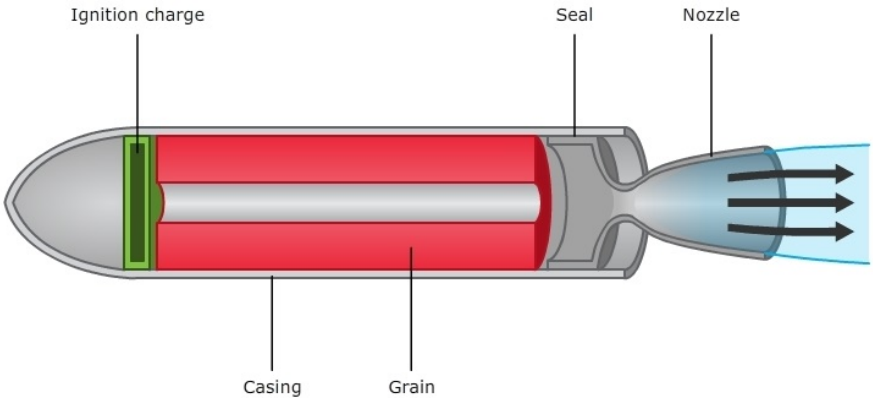

Figure 1.1 Schematic representation of a solid rocket motor [1]. With permissions (© The University of Waikato Te Whare Wānanga o Waikato | www.sciencelearn.org.nz)

Liquid engines are powered by oxidizer and fuel in their liquid state. This type of engine is known to be efficient and is the first choice nowadays. Saturn V, the Space Shuttle, Falcon Heavy, Atlas V and many other rockets are powered by liquid engines. In this configuration, two tanks contain the propellants. The liquids are pressurized through turbopumps into the combustion chamber where the violent exothermic reaction occurs. A schematic representation is presented in Figure 1.2, where the main components are pictured. Typical fuels include cryogenic hydrogen (H_2), liquid methane (CH_4), rocket-grade kerosene (RP-1). Oxidizers include liquid oxygen (O_2, also abbreviated LOX) or rocket-grade hydrogen peroxide (H_2O_2, also abbreviated HTP for high-test peroxide). The high efficiency achievable with liquid engines require complex piping systems (not shown in Figure 1.2), mainly because it is necessary to power the pumps with the same reactants that the rocket uses. This increases the cost of manufacturing operations and launches.

The hybrid engine approach is a combination of the solid and liquid engines. A liquid or gaseous oxidizer is injected into a combustion chamber containing a solid fuel. Before entering the combustion chamber, the oxidizer passes through an injector. An ignition system is required to initiate the combustion process. Generally, ignition is achieved by heating a portion of the fuel grain (i.e., the fuel geometry) to vaporize a small amount of fuel. The fuel vapor mixes with the injected oxidizer; the heat provided by the ignition system then initiates

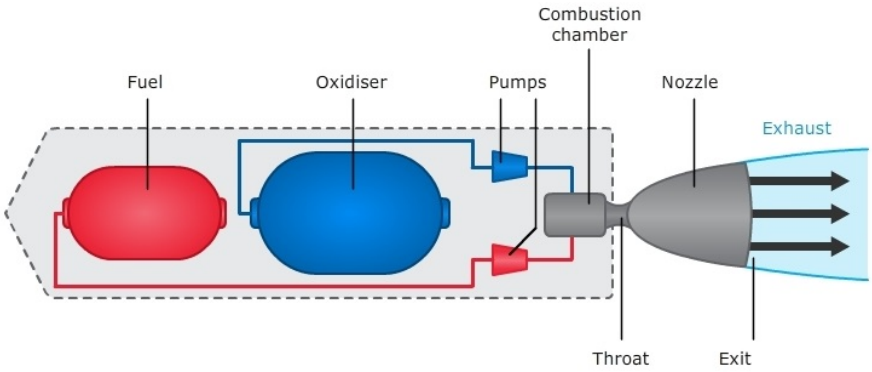

Figure 1.2 Schematic representation of a liquid rocket engine [1]. With permissions (© The University of Waikato Te Whare Wānanga o Waikato | www.sciencelearn.org.nz)

combustion. Once ignited, combustion continues as long as enough oxidizer is injected into the combustion chamber or as long as there is fuel remaining. The combustion products are then accelerated by passing through a nozzle to produce thrust.

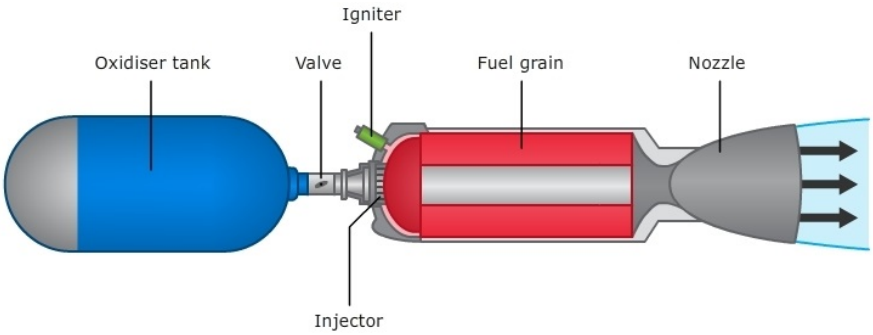

Figure 1.3 Schematic representation of a hybrid rocket engine [1]. With permissions (© The University of Waikato Te Whare Wānanga o Waikato | www.sciencelearn.org.nz)

Hybrid rockets have several advantages over liquid and solid rockets. First, unlike solid rockets, the rate of the combustion reaction can be controlled. Combustion can be stopped, restarted, and throttled as required. The ability to stop and throttle the combustion process results in a safer engine and allows the creation of different thrust profiles depending of the mission. Another interesting aspect is that the oxidizer and fuel are completely separated until they mix in the combustion chamber. This increases the safety of storage and handling operations prior to launch. Finally, since the control system can be as simple as a single valve, it is cheaper to manufacture and mechanically simpler than liquid rockets that use complex pumps and piping assemblies. However, current hybrid engines have performance levels that do not allow them to compete with liquid-fueled engines.

Among other ways to further simplify the operation of hybrid engines, the use of hypergolic fuels is being actively researched. An ignition system is not required when the combination of fuel and oxidizer is hypergolic, meaning it has the ability to spontaneously ignite when the two reactants come into contact. It is used as a reliable ignition source that replaces heavy and complex devices such as torch igniters, electric arcs or pyrotechnic devices. This technology is already used as an igniter in some liquid rocket engines, where a mixture of triethylaluminum-triethylborane ($C_{12}H_{30}Al_2$, $(CH_3CH_2)_3B$, known as *TEA-TEB*), ignites with LOX. As discussed in detail in Chapter 2, one way to impart hypergolic behavior to hybrid engines is through the use of additives to the fuel that ignite with the oxidizer. This technology is still relatively new and lacks the maturity needed to be used in the few hybrid engines in operation. Only a handful of research groups are focused on better understanding the underlying mechanisms of hypergolic ignition in hybrid rocket engines. Experiments are mainly conducted with small amounts of propellant in a configuration far removed form the engine itself, and very few scientific articles report hypergolic ignition under more realistic conditions. This aspect of hybrid rocket combustion is the focus of this thesis.

1.2 General objectives & expected impact

The work presented here focuses on experimental investigations of hybrid rocket engine propellant systems, with an emphasis on hypergolic ignition. The objective of this thesis is to enable the development of hypergolic hybrid rocket engines by providing experimentally based results from small-scale tests. The need to provide lower cost and easier access to space necessitates the development of alternatives to the high performance rockets currently in use. The hybrid engine configuration is one such technology that could potentially fill a gap in this market. However, a deep, scientific understanding of the combustion phenomena behind these engines is required to propel these ideas to orbit. The work presented in this thesis does not attempt to address challenges associated with hybrid engines from every angle. However, it aims to provide useful information on how hypergolic ignition systems can be used in hybrid rocket engines to further simplify their operation, improve safety, and lower cost.

To achieve this objective, a series of experiments are performed. First, a unique and novel laboratory-scale test rig is developed. It provides the capability to observe the liquefying process of fuels subjected to an oxidizing grazing flow that mimics the fluid dynamic conditions in a hybrid engine. A promising additive, that provides control over the fuel viscosity, is tested and the combustion rate is measured, among other parameters such as performance or combustion instabilities. As will be highlighted in the subsequent chapter, controlling the

combustion rate through increased viscosity is highly desirable in such engines, as it allows for more flexibility in the design phase.

Then, a new class of hypergolic additives, namely hypergolic metal-organic frameworks (HMOFs), is investigated in a multidisciplinary scientific assessment. The HMOFs are evaluated through theoretical performance computations and experimental ignition tests. The use of novel hypergolic additives is expected to bring, again, more flexibility in ignition system design by providing alternatives to other investigated additives.

Third, as a first step towards transitioning from small-scale ignition experiments to more representative experiments, the ignition behavior of hypergolic fuels is assessed under oxidizer sprays. This test configuration is intended to better represent engine conditions, as opposed to conventional ignition tests where only a single droplet of oxidizer is deposited on the fuel. The impact of this experiment is expected to expand the knowledge of the hypergolic ignition of hybrid fuels.

Finally, the laboratory-scale test rig used in the first experiment is revisited to implement the oxidizer spray systems previously characterized. In this configuration, the ignition sequence and mechanism of hypergolic hybrid engines are examined under more realistic engine conditions. Two operating modes are considered and proposed. This experiment is expected to be a stepping stone to larger hypergolic hybrid engine experiments, with a focus on understanding the various mechanisms at play.

1.3 Organization of the thesis

The first chapter of this thesis, which concludes here, provides a brief overview of rocket propulsion. The different types of rocket propulsion engines are introduced, followed by the general objective of the project and its expected impact. Chapter 2 reviews the different propellants used for hybrid rocket combustion. It also provides a summary of the experiments used to characterize them. The literature review continues with a description of additives used to enhance the performance or induce hypergolicity of hybrid fuels. Several laboratory-scale experiments are discussed and compared, to provide information on current research for hybrid rocket applications. Chapter 3 details the research objectives and presents the organization of the subsequent chapters. Chapter 4 provides information on the methodology employed to conduct the experiments described in this document. Chapters 5, 6, 7, 8 contain the findings of this project in the form of four peer-reviewed journal articles. Chapter 9 gives a general discussion of the results presented in the articles. Finally, in Chapter 10, conclusions are drawn followed by the limitations of the project and recommendations for future research.

CHAPTER 2 LITERATURE REVIEW

The present literature review is divided in three major sections. The first section covers the general theory of the combustion process in a hybrid rocket engine and its limitations. The common fuels and fuel additives are described. The second part reviews the current state of the art for hypergolic rocket fuels. It introduces the common additives that impart hypergolic properties to the fuel, followed by laboratory-scale experiments used to measure an important metric, the ignition delay (ID). The third part provides an overview of existing research test facilities and the different results that they have produced. Finally, it also describes optical diagnostic techniques commonly used in combustion research.

2.1 Hybrid rocket combustion

Hybrid rocket engines are a combination of liquid and solid propellant engines. The similarity between solid rocket engines and hybrid rocket engines is that the fuel is in its solid phase in a combustion chamber within a geometric arrangement called a *grain*. In the hybrid configuration however, the oxidizer is separated from the fuel and is stored in a tank before entering the combustion chamber, much like with liquid engines. A control system is placed between the oxidizer and the fuel to regulate the injection rate of the oxidizer entering the combustion chamber. The products of combustion are then accelerated through a nozzle that produces the thrust to propel the rocket [2]. Figure 2.1 shows a simplified schematic representation of the principal components of a hybrid engine.

The dynamic of combustion inside a hybrid rocket engine was first studied by Marxman et al. in the 1960s [3–5] and later extended by Karabeyoglu in 1998 [6]. They developed a combustion model of an oxidizer flow over a fuel surface. As the oxidizer enters the combustion chamber, a turbulent boundary layer forms at the top of the fuel surface. An igniter initially heats a small portion of the fuel, initiating the reaction process. A diffusion flame settles in this boundary layer and the heat generated by the combustion is transferred to the fuel surface through convective and radiative heat transfer. As a result, the fuel evaporates and enters the reaction zone above it, sustaining the combustion process. The rate of the fuel consumption is characterized by its *regression rate* (mm/s) and is mathematically denoted by $\dot{r}$. A schematic representation of the combustion dynamic of a hybrid fuel is shown in Figure 2.2.

The main drawback of hybrid engines is their low power, as a results of the combustion rate

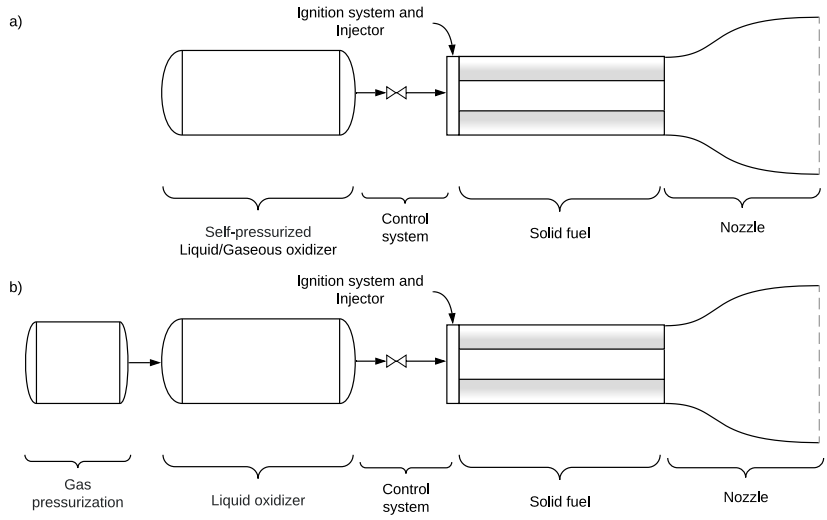

Figure 2.1 Simplified schematic representation of the main components of a hybrid rocket engine. Configuration a) uses a self-pressurized oxidizer, configuration b) uses an external pressurized gas to supply the oxidizer.

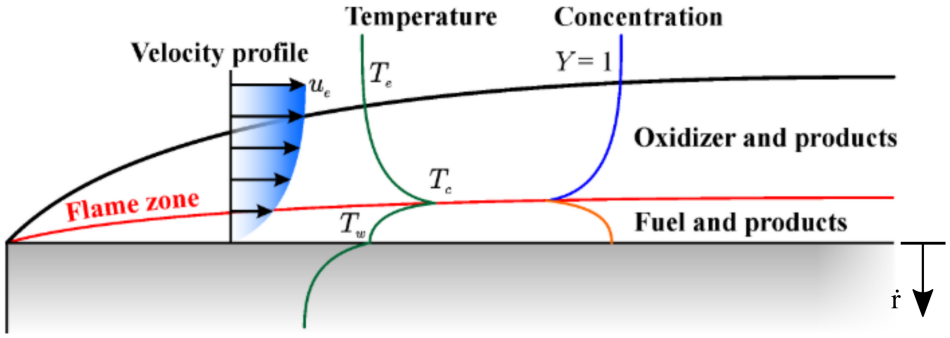

Figure 2.2 Schematic representation of the dynamics of combustion on top of the fuel surface of non-liquefying fuels adapted from [7]. With permissions (Creative Commons Attribution Non Commercial 3.0 Unported license, CC BY-NC).

being constrained by the limited contact surface between reactants [8, 9]. This leads to poor performance and low thrust densities, i.e., low thrust produced per amount of fuel used in the engine. This limitation can be partially addressed by complex fuel geometries such as multiport grains to increase the exposed surface area of the fuel. A significant breakthrough in hybrid propulsion is the discovery of liquefying fuels as a way to improve the regression rate. Karabeyoglu demonstrated that fuels that form a liquid layer over their surface prior to vaporization have a higher regression rate compared to classical vaporizing fuels [6]. This discovery paved the way for the design of hybrid engines with higher thrust. Karabeyoglu

studied solid hydrocarbon fuels under cryogenic conditions, such as solid pentane (C_5H_{12}), and later tested solid fuels at room conditions, such as paraffin wax. Upon melting, the fuel forms an unstable liquid layer that is blown away by the grazing flow of oxidizer and combustion products in the chamber. The shear stress applied to the liquid layer breaks the melt layer and creates small droplets of fuel that enter the reaction zone. This phenomenon is called entrainment. This mechanism is shown in Figure 2.3, where Kelvin-Helmoltz (K-H) instabilities form at the surface of the liquid fuel phase. The waves, also named roll waves, grow until they reach a size where elongated filaments of liquid fuel are formed. The ligaments break into droplets that are entrained in the flow due to a Plateau-Rayleigh instability [10–12]. Taking this effect into account, Karabeyoglu et al. [8] redefined the typical regression rate formula as:

$$\dot{r} = \dot{r}_v + \dot{r}_{ent} \tag{2.1}$$

where $\dot{r}$ is the total regression rate, $\dot{r}_v$ is the regression rate from fuel evaporation and $\dot{r}_{ent}$ is the entrainment regression rate. The latter is only applicable to liquefying fuels. Additionally, a mass flow corresponding to the entrainment effect is defined [9]:

$$\dot{m}_{ent} = \rho_l \cdot \dot{r}_{ent} \tag{2.2}$$

where ρ_l is the density of the liquid fuel layer. The entrainment effect mass flow rate is mainly affected by four variables and mechanical properties of the fuel: the dynamic pressure on the fuel P_d, the thickness of the melt layer h, the surface tension of the melted fuel σ and the viscosity of the melt layer μ. Overall, the mass flow is proportional to these parameters through the following relationship:

$$\dot{m}_{ent} \propto \frac{P_d^a h^b}{\mu^c \sigma^d} \tag{2.3}$$

where a, b, c and d are coefficients to be determined for each fuel formulation.

Experimentally, the regression rate is measured and reported as a time and spatially averaged law written as:

$$\dot{r}_{fuel} = a \cdot G_{ox}^n \tag{2.4}$$

where G_{ox} is the mass flux of oxidizer and the variables a and n depend on the propellant used. They are obtained experimentally by measuring the regression rate at different oxidizer mass flux and plotting the result as the power law of eq. 2.4.

Finally, when it comes to evaluate the performance of a rocket engine, different parameters are defined. Typically, the specific impulse (I_{sp}, measured in s) is used to compare one engine

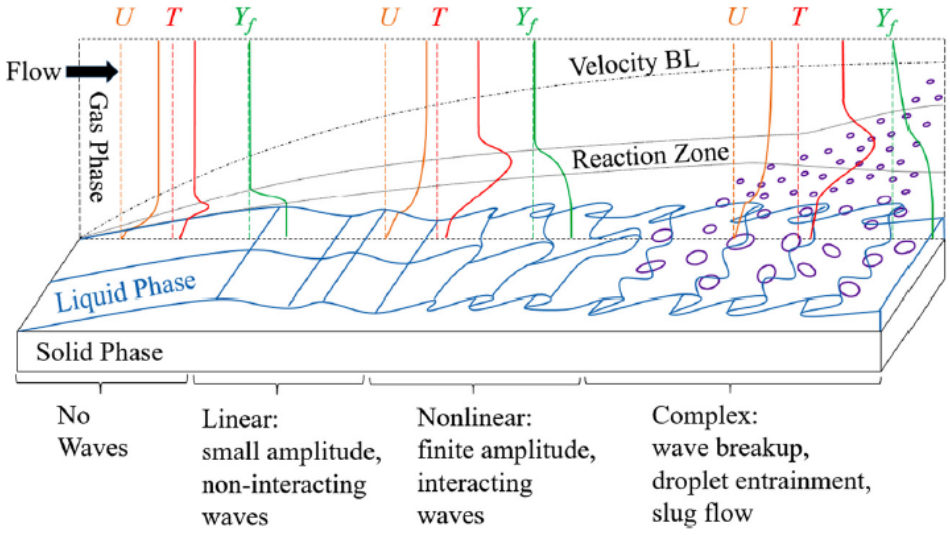

Figure 2.3 Close-up representation of the melted fuel layer instabilities leading to breakup in small droplets [13]. U is the velocity, T is the temperature and Y_f is the fuel fraction. With permissions.

to another, as expressed by the following equations:

$$I_{sp} = \frac{F}{g\dot{m}} \tag{2.5}$$

$$I_{sp} = \frac{c}{g} = \frac{1}{g}\sqrt{\frac{2\gamma R_u T_c}{(\gamma - 1)\, M_W}\left(1 - \frac{P_e}{P_c}\right)^{\frac{\gamma-1}{\gamma}}} \tag{2.6}$$

where F is the thrust produced by the engine, g is the Earth's gravitational constant, $\dot{m}$ is the mass flow of propellants and c is the effective exhaust velocity of the combustion products [2]. The effective exhaust velocity is a function of the combustion temperature T_c, the mean molecular weight of the combustion gas M_W, the ratio of the exit pressure to the combustion pressure $\frac{P_e}{P_c}$, and the specific heat ratio γ. The specific impulse of hybrid rocket engines typically ranges from 270 s to 300 s at sea level, compared to 270 s to more than 400 s for liquid rocket engines and 190 s to 270 s for solid rocket engines [2].

2.1.1 Fuels

As seen in previous sections, liquefying fuels can improve the performance of hybrid rocket engines due to the entrainment effect. Originally, solid hydrocarbons maintained at cryogenic conditions were used as the solid fuel. Obviously, the use of such fuels increases the complexity of the rocket and its engines, thus multiplying the costs of a launch. However, liquefying

fuels storable at room conditions do exist. Karabeyoglu et al. [8, 14, 15], George et al. [16], and Zilliac et al. [17] have investigated various types of hybrid rocket fuels, including paraffin waxes, hydroxyl-terminated polybutadiene (HTPB), polyethylene waxes, and high-density polyethylene polymer (HDPE). HTPB is widely used in solid rocket fuels and has been investigated as a hybrid propellant. A major advantage of using HTPB is its manufacture. Two parts are mixed together and cured at room temperature, a simple process that allows for complex grain geometries. Sorbitol, a non-toxic sugar alcohol, has also been studied for its liquefying properties and its high density and strength [18, 19].

By conducting small and large scale tests with various alkane-based fuels, Karabeyoglu et al. [14, 15] found that paraffin waxes have a regression rate 3 to 4 times higher than non-liquefying HTPB or HDPE-based fuels. The regression rate of paraffin waxes is similar to that of solid pentane, without the need for cryogenic fuel handling, as they are in a solid phase at room temperature and pressure. This solution allows to reduce the complexity and thus the operating costs of hybrid rockets. Key values of common hybrid fuels are presented in the Table 2.1.

Table 2.1 Properties of common fuels for hybrid rocket [8, 15, 18, 20]

Fuel	Molecular Formula	Heat of Formation [kJ/mol]	Regression Rate Factor Relative to Paraffin Wax [-]
Cryogenic Pentane	C_5H_{12}	-146.8	1.10
HDPE	$(C_2H_4)_n$	-221.8	0.20
HTPB	$(C_{7.337}H_{10.982}O_{0.058})_n$	12.4	0.20
Paraffin Wax (FR 5560)	$C_{32}H_{66}$	-933.0	1.00
PMMA	$(C_5H_8O_2)_n$	-430.5	0.60
Sorbitol	$C_6H_{14}O_6$	-1353.7	> PMMA

2.1.2 Limitations

The main reason why hybrid rockets are not used by major manufacturers is their lower power density compared to liquid rocket engines, mainly due to the slow regression rate of hybrid fuels. To produce a sufficient flow rate of combustion products to propel the rocket, multi-port grains and complex port geometries (e.g., a star instead of a central hole) are used to increase the wetted surface area of the fuel, as shown in Figure 2.4. The use of paraffin wax and liquefying fuels partially addresses these low regression rates.

However, complex grain port geometry, multi-port and paraffin-based fuels lead to problems related to incomplete combustion. Portions of the fuel grain can break off and be expelled

through the nozzle without being burned, resulting in a loss of performance.

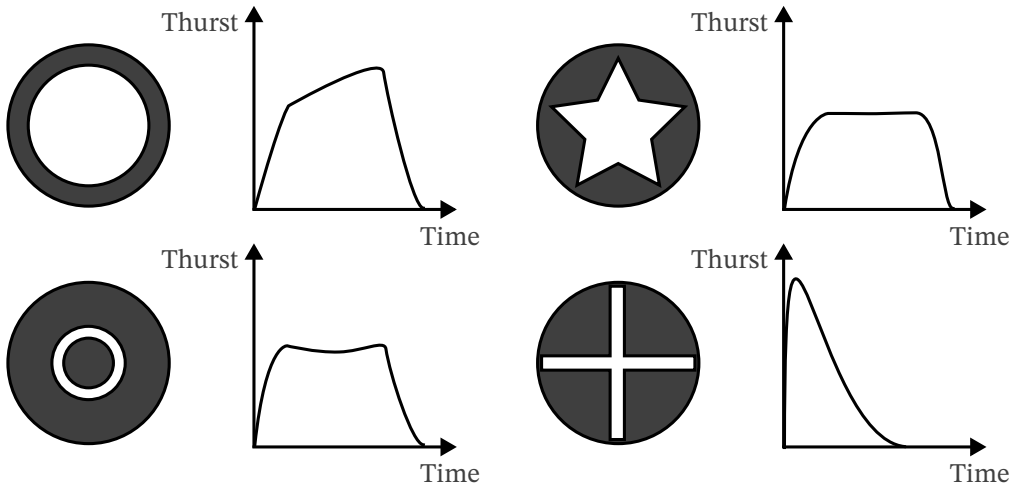

Figure 2.4 Examples of grain geometry and their effect on thrust.

Finally, due to the coupling between the regression rate and the oxidizer mass flow, the "optimal" oxidizer-to-fuel mass ratio (O/F), meaning the O/F that maximizes the specific impulse, is only obtained for a limited duration. As the fuel burns, the grain port increases the area of the fuel grain exposed to the oxidizer, thus changing the O/F and reducing the regression rate. Contrary to liquid rocket engines, where the optimal O/F is maintained throughout the combustion, O/F in hybrid engines will always shift if the oxidizer mass flux is maintained constant. Evans et al. [21] claimed that secondary injection systems or grain designs could eliminate the shift in mixture ratio. Thus, fuels that have a broad optimal O/F peak are therefore desirable to maintain high performance throughout the entire burn duration.

2.1.3 Fuel additives

In some cases, it is useful to be able to adjust the regression rate of a fuel. For example, if the fuel burns too fast, the size of the combustion chamber may be too large for long duration burns. The use of fuel additives that increase the viscosity of the melt layer, thereby decreasing the regression rate, is an interesting option. In addition, Elzein et al. [22] reported that increasing the melt layer viscosity reduces the ignition delay of hypergolic additives.

A major drawback of paraffin-based fuels is weak mechanical properties that result in poor structural integrity of the fuel grain. In addition, as liquid paraffin solidifies, volume shrinkage causes void bubbles to form within the grain. The poor mechanical properties and voids can lead to catastrophic engine failure. For example, if parts of the fuel break off and block

the nozzle, a pressure increase occurs. Engine performance is also compromised when large amounts of unburned fuel are expelled.

To address these issues, additives can be incorporated into the fuel matrix to improve its mechanical properties and viscosity. By changing the viscosity, the rate of regression can be controlled. Low density polyethylene (LDPE) has been extensively studied as an additive to pure paraffin wax [23, 24]. LDPE itself is not considered a liquefying fuel, so its regression rate is not affected by the entrainment effect and is lower than that of pure paraffin. By modifying the viscosity of the melt layer, LDPE reduces the regression rate of combined LDPE/paraffin fuels, thereby potentially reducing the thrust of the engine. However, a key benefit is that the addition of up to 10 wt.% of LDPE in the paraffin matrix increased the tensile and compressive strength of the fuel by 42.4% and 42.2%, respectively, compared to pure paraffin. Finally, the theoretical performance of an LDPE/paraffin fuel was found to be slightly increased [23, 24].

Another extensively studied additive is ethylene vinyl-acetate copolymer (EVA) [25–28]. EVA is known to be soluble in paraffin wax and has superior mechanical properties. By adding EVA to paraffin wax, the tensile strength increases by 75% at a concentration of 20 wt.%. EVA also increases the viscosity of the melting fuel by approximately 500%, which means that a reduction in the regression rate is expected. By performing combustion experiments at a fixed pressure and oxidizer mass flux, the regression rate decreased by approximately 35%.

Bilge et al. [29] identified a class of additives, known as tackifier resins, capable of increasing the mechanical properties without affecting the fuel viscosity. An increase in mechanical strength of up to 70% have been measured at concentrations as low as 20 wt.%. Although tackifiers seem very promising for solving mechanical problems with paraffin waxes, more work needs to be done with these types of additives regarding regression rate.

2.2 Hypergolic rocket fuels

Hypergolicity is the property of a propellant combination to ignite spontaneously upon contact between the fuel and the oxidizer. The use of hypergolic propellants in rockets greatly reduces the complexity of various tasks and systems. The ignition system is not required and the firing sequence is much simpler. Because ignition can be almost instantaneous, hypergolic propulsion systems are well suited for precise control maneuvers (e.g., altitude control for satellites or the upper stages of rockets) [30]. It can also be argued that hypergolic ignition systems are safer due to the inherent reliability of ignition.

Hypergolicity has been achieved primarily with liquid rocket propellants. Common hypergolic liquid propellants include hydrazine (N_2H_4) and hydrazine derivatives such as monomethylhydrazine (MMH) and unsymmetrical dimethylhydrazine (UDMH). They are typically used with oxidizers such as nitrogen tetroxide (NTO), mixed oxides of nitrogen (MON), white fuming nitric acid (WFNA), red fuming nitric acid (RFNA) or hydrogen peroxide (H_2O_2) [31,32]. Some of these combinations have been used on Roscosmos' rockets, the Apollo command module and the Space Shuttle orbital maneuvering system [2]. Hypergolic ignition also allows spacecraft to be conveniently restarted in flight, a task for which a reduced number of parts is highly desirable to increase reliability.

Despite the considerable advantages of hypergolic fuels, there are significant drawbacks. Most hypergolic fuels or oxidizers currently in use can be extremely toxic or carcinogenic. These effects require unavoidable safety measures that increase the cost and complexity of handling these chemical compounds. In addition, hypergolic ignition of liquid engines can lead to a "hard start", a detonation within the engine. To minimize the risk of hard starts and prevent rocket failure, a low ignition delay, typically less than 50 ms, is required. The low ignition delay limits the amount of fuel and oxidizer that fills the combustor prior to ignition, preventing too much fuel from igniting at the same time.

Hypergolic hybrid engines have been tested, but to a limited extent compared to their liquid counterparts. Typically, in hybrid applications, the fuel itself is not hypergolic with the oxidizer, but additives are included in the fuel matrix to enable hypergolicity. Hard starts in hybrid engines are less of a concern compared to liquid engines. Because the fuel is solid and in a predetermined geometry, flooding of the engine cannot occur in the event of a long ignition delay. It is not possible for more fuel to react in the chamber than is exposed on the surface of the grain, making hypergolic hybrid engines inherently safer than hypergolic liquid engines.

2.2.1 Hypergolic additives

Hypergolicity in hybrid rocket propulsion is typically achieved by incorporating additives into a fuel binder such as HTPB or paraffin wax. A complete list of hypergolic additives is presented in Table 2.2 whereas the main ones are described in this section.

Amine boranes

Pfeil et al. conducted extensive research on the addition of amine boranes ($C_aH_bB_cN_d$) as hypergolic additives with inhibited red fuming nitric acid (IRFNA) as oxidizer [30,33]. Upon

contact between the reactants, hydrogen contained in the amine boranes is released (by an exothermic dehydrogenation reaction) and ignites. The heat from this ignition then liquefies the fuel surface and the combustion is self-sustained as long as oxydants are added. They found that amine boranes are not only well suited for hypergolic ignitions, but can also be used as an energetic additive that increases the specific impulse of engines, as shown in Fig. 2.5. Amine boranes containing a higher wt.% of boron presented a wider range of suitable O/F ratios. Ammonia borane (AB, BH_3NH_3) was then identified as the more promising amine borane additive.

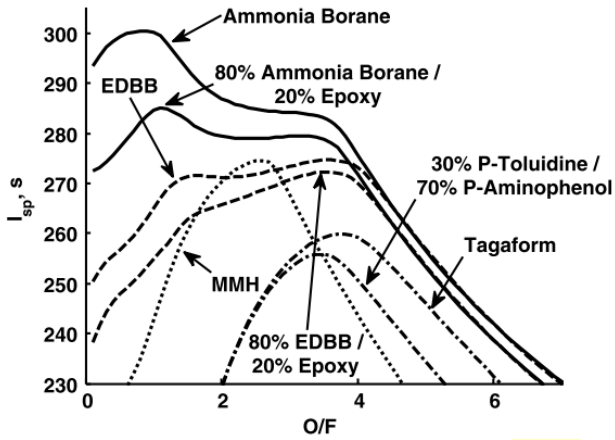

Figure 2.5 Specific impulse as a function of the oxidizer-to-fuel ratio of different fuels using IRFNA as the oxidizers [33]. With permissions.

Ammonia borane provides the highest I_{sp} compared to other hypergolic fuels. This increase is principally due to the high hydrogen content of AB (19.5 wt.%) [34]. It is also characterized by a dual peak of performance, the first at an O/F ratio of 1.0 and the second at approximately 3.7. A high O/F ratio allows for less fuel to sustain peak performance combustion, thus reducing the size of the combustion chamber. However, the density of the reactants must be taken into account when analyzing the effect of the O/F ratio, as it is calculated by mass. For example, in the case where AB is used as the fuel and IRFNA as the oxidizer, since the density of IRFNA (1.55 g/ml) is higher than the density of AB (0.78 g/ml), the second peak of performance (at 3.7) will be preferred in order to reduce the volume of the reactants. Figure 2.5 also reveals that the performance of AB incorporated in a fuel matrix containing 20 wt.% epoxy is lower than pure AB. However, epoxy being a liquefying fuel, the entrainment effect increases the regression rate of the grain and therefore the engine thrust.

Hypergolic metal-organic frameworks

In addition to the amine boranes, another class of material can provide hypergolicity and an energetic boost to hybrid propulsion: metal-organic frameworks (MOF). MOFs are porous materials primarily used for gas adsorption and catalysis [35–38]. They are composed of metal ions and organic linkers that combine to form porous crystals. Hypergolicity has been achieved with WFNA as the oxidizer [39], releasing the energy stored inside the MOF, thus acting as a hypergolic energetic additive. Paraffin-based engines using these additives have yet to be tested. Following the publication of our article presented in Chapter 6, other copper-based MOFs have been synthesized and tested in the form of powders [40, 41], but are yet to be implemented in a fuel binder.

H_2O_2 catalysis as "hypergolic" ignition

A "green" oxidizer, H_2O_2, has recently gaining a lot of attention for ignitions systems. The majority of additives hypergolic with WFNA are also exhibiting this behavior using hydrogen peroxide. Hydrogen peroxide decomposes with products being steam and oxygen [42, 43]:

$$H_2O_2(l) \rightarrow H_2O(g) + \frac{1}{2}O_2(g) + \Delta H \tag{2.7}$$

where ΔH is 98.1 kJ/mol. These products are non-toxic, which is not the case for nitrogen oxides (NO_X) normally produced by the combustion of WFNA. Hydrogen peroxide is already used as a monopropellant in rocket propulsion when it is decomposed through a catalyst [44–46]. Hydrogen peroxide at high concentration (85% to 98%) is also known as high-test peroxide (HTP). The utilization of HTP in rocket applications is focused on reaction control systems (RCS) and as an oxidizer. Amri et al. [44] and Santi et al. [46] respectively developed a 1N and 10N monopropellant thruster using HTP for orbital adjustment and in-space maneuvers.

An innovative way of using hydrogen peroxide in hybrid motors is by decomposing it through a catalyst bed and letting the hot steam and oxygen enter the combustion chamber containing a liquefying fuel. Different catalysts can be used: for example, manganese and aluminum oxides (MnOx/AlOx) [45, 47], platinum [48] and silver [42]. The catalyst can be in the form of screens, meshes and honeycombs or a stacked bed of pellets [49]. The exhaust temperature of the resulting steam and oxygen can reach up to 1000K [46]. Bozic et al. [50] developed a catalyst bed that provides up to 1 kg/s of oxidizer to a combustion chamber containing HTPB and metallic additives. The heat resulting from the exothermic decomposition of HTP through the catalyst acts as the ignition source in the combustion chamber. Therefore, an

injection system that uses hydrogen peroxide coupled with a catalyst acts like a hypergolic engine: it can be restarted without the need for an externally ignition system.

H_2O_2 promoted hypergolic ignition

H_2O_2 is also hypergolic at room temperature with ammonia borane [51], metal hydrides such as lithium aluminum hydride (LAH, $LiAlH_4$) and sodium borohydride ($NaBH_4$) [31] and other catalysts ($CuCl_2$, $FeCl_2$ and $FeCl_3$) [52]. These fuel-oxidizer pairs do not require catalysts and thus, have the advantage of reducing the mass of the rocket.

Researchers from Kwon's research group at the Korea Advanced Institute of Science and Technology [53–56] had the clever idea of combining hypergolic additives, here AB, with a H_2O_2 catalyst to increase the hypergolic performance. They used activated carbon as a support for metal catalysts based on Platinum, Manganese, Ruthenium or Palladium. They mixed the activated carbon-catalyst with AB and a fuel (HDPE, paraffin wax and HTPB).

Effect of hypergolic additives on the regression rate

Hypergolic additives also affect the regression rate of hybrid fuels, and few experiments have studied this effect. Weismiller et al. [57] demonstrated that the addition of AB at 10wt.% in paraffin wax increased the regression rate of the fuel. Karabeyoglu et al. and Karakas et al. [20, 58] studied the addition of LAH and AB to paraffin wax. However, these experiments were not conducted using hypergolic-triggering liquid oxidizer, but rather gaseous oxygen (GOx). The first group of researchers demonstrated that LAH and AB could theoretically improve the specific impulse of the engines and the second group performed experimental verification of their claims. They postulated that the increase in regression rate does not justify the addition of these costly additives, but the increase in specific impulse must be taken into account when designing a hybrid engine. They also suggested that LAH could replace pure aluminum as an energetic additive.

2.2.2 Ignition delay measurement

The length of time between the moment the fuel and the oxidizer are put in contact and ignition is a parameter of critical importance to ensure hypergolic propellants for safe and reliable engine operation. A convenient way to measure this ignition delay is the pellet ignition experiment (or droplet ignition experiment) [19, 22, 30, 32, 33, 51, 59–63]. These experiments involve a small sample of fuel lying under a syringe containing the oxidizer. The syringe is manipulated so that a single droplet of oxidizer falls onto the fuel pellet. The exact vol-

ume, or mass of the droplet, is usually known. High-speed imaging is used to determine the time between the droplet impact and the onset of combustion. Because the dynamics of the droplet impact and the distribution of hypergolic additives in the fuel sample can be variable, multiple experiments are often performed.

This simple method is used to compare hybrid fuel additives using only the hypergolic additive itself or using the additive embedded in a fuel matrix such as epoxy, HTPB or paraffin wax. Pfeil et al. [30, 33], Baier et al. [61], Clements et al. [62, 64], Bhosale et al. [51], Elzein et al. [22] and Dumas et al. [19] performed hypergolic droplet tests using both pure amine-borane additives and a mixture of amine boranes and common hybrid fuels. Titi et al. [39] used this technique to record ignition delays of MOFs. A summary of the additives tested and of their ID is presented respectively in Table 2.2 and Table 2.3. Measured ignition delays range from sub-milliseconds up to more than one hundred milliseconds, with AB demonstrating the lowest ignition delay when used with WFNA. MOFs-based additives, along with sodium borohydride, also exhibit ignition delays lower than 5 ms at standard pressure and temperature.

Clements et al. [64] investigated different parameters inherent to this method affecting the ignition delay. For instance, they measured high disparities in results when the surface of the pellet was sanded, broadening the distribution of the ignition delay measurement. Their experiments revealed that the height of the syringe, correlated with the impact velocity, also affects the ignition delay. Finally, they suggested that epoxy as a fuel binder helped reduce the splashing of WFNA following impact, thus maintaining more oxidizer in contact with the fuel and reducing the ignition delay. Nath et al. [65, 66] also studied parameters such as the droplet diameters, additive loading, impact velocity and HTP concentration. They reported that increasing the velocity of the droplet, the concentration and the oxidizer droplet diameter decreased the ignition delay when using $NaBH_4$/HDPE fuel with HTP. Both studies report similar effects of the droplet velocity on the ID highlighting the need to further evaluate this parameter.

Fuel binders also have a significant effect on the ignition delay of hypergolic fuels. For example, Dumas et al. [19] shows that increasing the sorbitol content in a sorbitol/paraffin fuel binder, using AB as the hypergolic additive and WFNA as the oxidizer, reduced the ignition delay following a linear and monotonic trend from 60.3 ms with pure paraffin to 8.2 ms with pure sorbitol. It is hypothesized that the wettability of sorbitol with WFNA and its higher bulk density are the main parameters explaining this behavior.

Stober et al. [32, 60, 63] studied the effect of external pressure on the ignition delay of LAH particles embedded in paraffin wax by performing droplet ignition experiments in a custom-

designed test bench. They used analytical reagent-grade nitric acid (69.3 wt.%) as the oxidizer. As the pressure inside their combustion chamber increased, the ignition delay decreased from 31.3 ms at atmospheric pressure (0.10 MPa) to 6.9 ms at 2.1 MPa. However, the effect of pressure quickly reached a plateau around 0.3 MPa with no observable effect as the pressure was further increased, leading the authors to believe that there are two regimes: a pressure-limited regime and a geometry-limited regime. The first regime is based on the pressure dependence of gas-phase reaction [67], which leads to a higher intermolecular collision rate (reaction rate) as the pressure is increased. The latter regime is correlated with the time required for the oxidizer to wet the surface of the pellet. The longest of these two times appears to set a limit for the ignition delay measured with droplet ignition experiments at elevated pressures. A similar behavior was observed using sodium borohydride in a solid LDPE matrix with 90% H_2O_2 as the oxidizer.

In addition to nitric acid and HTP, mixed oxides of nitrogen (MON-X, a mixture of N_2O_4 and NO where X is the concentration of NO), is also a strong oxidizer that promotes the hypergolic behavior of several materials. For example, Benhidjeb-Carayon et al. [68–70] from Purdue University and Cortopassi et al. [71] from Pennsylvania State University studied the hypergolic behavior of MON-3 and MON-25 with additives such as sodium amide ($NaNH_2$) and potassium bis(trimethylsilyl)amide (PBTSA).

The hypergolic additives were tested with WFNA or less concentrated nitric acid (AR-nitric acid), HTP or MON as the oxidizer. The most promising amine boranes (AB and EDBB) and sodium borohydride were tested in a fuel binder. AB was tested with epoxy, a silicone elastomer (Sylgard-184), paraffin and sorbitol binders, while EDBB was tested in both epoxy and paraffin fuel binders with cut or sanded surfaces. Researchers studying the activated carbon-catalyst also used fuel binders to test the ID of their additives. They reported that adding as little as 1% carbon catalyst to the fuel composition reduced the ID by about 50%, with sub-millisecond ignition (0.9 ms for 10 wt.% AB, 1 wt.% Pd-C (Palladium-activated carbon catalyst) and 89 wt.% paraffin wax) being reported. Hypergolic MOFs exhibit fast ignition with WFNA and HTP and their addition into fuel binders needs to be further studied to assess their suitability as potential additives. PBTSA and sodium amide were tested with MON as the oxidizer, again showing ignition delays well below the 10.0 ms target.

The use of droplet ignition tests is critical in the preliminary screening of suitable additives. They allow a rapid comparison of the various additive/oxidizer pairs. However, as some studies that have focused on the influence of droplet parameters on ignition delay have shown, even in this simple configuration, multiple factors influence the ignition delay. This makes comparisons difficult when evaluating suitable additives. The need for a standardized

Table 2.2 Hypergolic hybrid additives used with WFNA and/or HTP.

Hypergolic Additive	Molecular Formula
Ammonia Borane (AB)	BH_3NH_3
Cd(**AIm**)$_2$	$Cd(C_5H_3N_2)_2$
Cd(**VIm**)$_2$	$Cd(C_5H_5N_2)_2$
Cis-2,6-dimethylpiperidine-borane	$C_7H_{18}BN$
Co(**AIm**)$_2$	$Co(C_5H_3N_2)_2$
Co(**VIm**)$_2$	$Co(C_5H_5N_2)_2$
Cu(**AIm**)$_4Cl_2$	$C_{24}H_{32}N_8Cl_2Cu$
Cu(**AIm**)$_4(NO_3)_2$	$C_{24}H_{32}N_{10}O_6Cu$
Cu(**EIm**)$_4(NO_3)_2(H_2O)_2$	$C_{20}H_{36}N_{10}O_8Cu$
Cu-PMIM-1	$C_{14}H_{16}Br_4Cu_4N_4$
Cu-PMIM-2	$C_{14}H_{18}Br_6Cu_4N_4$
Cu-PVIM-1	$C_{16}H_{16}Br_4Cu_2N_4$
Cu-PVIM-2	$C_8H_9Br_2CuN_2$
Cyclohexylamine-borane	$C_6H_{16}BN$
Ethylenediamine-bisborane (EDBB)	$C_2H_14B_2N_2$
Lithium Aluminum Hydride	$LiAlH_4$
N,N-dimethylpiperazine-bisborane	$C_6H_{20}B_2N_2$
N-methylpiperazine-bisborane	$C_5H_{18}B_2N_2$
Piperazine-bisborane	$C_4H_{16}B_2N_2$
Piperidine-borane	$C_5H_{14}B_2N_2$
Potassium bis(trimethylsilyl)amide (PBTSA)	$KSI_2C_6NH_{18}$
Sodium Amide	$NaNH_2$
Sodium Borohydride	$NaBH_4$
Tetramethylethylenediamine-bisborane (TMEDBB)	$C_6H_{22}B_2N_2$
Zn(**AIm**)$_2$	$Zn(C_5H_3N_2)_2$
Zn(**VIm**)$_2$	$Zn(C_5H_5N_2)_2$
1-propanamine-borane	$C_3H_{12}BN$

procedure, or at least the reporting of complete experimental details, is critical and warranted. In addition, droplet ignition tests do not reflect the complex flow dynamics, temperature and pressure encounters under engine conditions. It is clear that more work should be done on the ignition, re-ignition, and experimental performance of hypergolic hybrid engines.

Table 2.3 Summary of previous hypergolic hybrid fuel experiments.

Fuel	Oxidizer	Ignition Delay [ms]	Comments	Ref.
Ammonia borane	95% H_2O_2	8.1	-	[51]
Ammonia borane	NTO	80.1	-	[61]
Ammonia borane	WFNA	9.6	-	[33]
Ammonia borane	WFNA	6.4	Average of various synthesis method	[61]
80% Ammonia borane/20% Sylgard-184	WFNA	31.9	-	[61]
30% Ammonia borane/70% Epoxy	WFNA	6.4	Surface cut	[62]
30% Ammonia borane/70% Epoxy	WFNA	0.9	Surface sanded	[62]
25% Ammonia borane/74% Paraffin/1% Pd-C	95% H_2O_2	1.2	Palladium/activated-carbon catalyst	[53]
20% Ammonia borane/74% PE/1%C	95% H_2O_2	18.0	Activated carbon catalyst support	[55]
20% Ammonia borane/74% PE/1% Mn-C	95% H_2O_2	17.0	Manganese/activated-carbon catalyst	[55]
20% Ammonia borane/74% PE/1% Pd-C	95% H_2O_2	9.8	Palladium/activated-carbon catalyst	[55]
20% Ammonia borane/74% PE/1% Pt-C	95% H_2O_2	11.6	Platinum/activated-carbon catalyst	[55]

20% Ammonia borane/74% PE/1% Ru-C	95% H_2O_2	11.6	Ruthenium/activated-carbon catalyst	[55]
20% Ammonia borane/80% Paraffin	WFNA	31.7	-	[19]
20% Ammonia borane/80% Sorbitol	WFNA	9.7	-	[19]
Cd(**AIm**)$_2$	WFNA	5.0	Metal-organic framework	[39]
Cd(**VIm**)$_2$	WFNA	35.0	Metal-organic framework	[39]
Cis-2,6-dimethylpiperidine-borane	WFNA	16.2	-	[33]
Co(**AIm**)$_2$	WFNA	2.0	Metal-organic framework	[39]
Co(**VIm**)$_2$	WFNA	11.0	Metal-organic framework	[39]
Cu(**AIm**)$_4Cl_2$	90% H_2O_2	127.0	Metal-organic framework	[40]
Cu(**AIm**)$_4(NO_3)_2$	90% H_2O_2	3.0	Metal-organic framework	[40]
Cu(**EIm**)$_4(NO_3)_2(H_2O)_2$	90% H_2O_2	15.0	Metal-organic framework	[40]
Cu-PMIM-1	90% H_2O_2	12.0	Metal-organic framework	[41]
Cu-PMIM-2	90% H_2O_2	52.0	Metal-organic framework	[41]
Cu-PVIM-1	90% H_2O_2	14.0	Metal-organic framework	[41]
Cu-PVIM-2	90% H_2O_2	69.0	Metal-organic framework	[41]
Cyclohexylamine-borane	WFNA	78.7	-	[33]
30% EDBB/70% Epoxy	WFNA	88.0	Surface sanded	[33]
30% EDBB/70% paraffin	WFNA	100.7	Surface cut	[33]
30% EDBB/70% paraffin	WFNA	111.1	Surface sanded	[33]

Lithium aluminum hydride	AR-nitric acid	31.3	Also performed at higher pressure	[32]
N,N-dimethylpiperazine-bisborane	WFNA	3.6	-	[33]
N-methylpiperazine-bisborane	WFNA	7.3	-	[33]
Piperazine-bisborane	WFNA	12.5	-	[33]
Piperidine-borane	WFNA	142.6	-	[33]
PBTSA	MON-25	1.1	Test in an N_2 atmosphere	[69]
PBTSA	N_2O_4	7.3	-	[69]
Tetramethylethylenediamine-bisborane	WFNA	26.2	-	[33]
Sodium amide	MON-25	4.8	Test in an N_2 atmosphere	[69]
Sodium amide	N_2O_4	96.6	-	[69]
Sodium borohydride	90% H_2O_2	4.0	-	[52]
Sodium borohydride/HDPE	90% H_2O_2	≈5.0 - 15.0	Parametric study	[65, 66]
25%Sodium borohydride/75% LDPE	90% H_2O_2	9.5	Also performed at higher pressure	[52]
50%Sodium borohydride/50% LDPE	90% H_2O_2	7.2	Also performed at higher pressure	[52]
Zn(**AIm**)$_2$	WFNA	2.0	Metal-organic framework	[39]
Zn(**VIm**)$_2$	WFNA	29.0	Metal-organic framework	[39]
1-propanamine-borane	WFNA	45.7	-	[33]

2.2.3 Hypergolic ignition in hybrid engine configuration

Tests of hypergolic ignition in an engine configuration were recently performed by Benhidjeb-Carayon et al. [68, 70, 72, 73] for the Mars Ascent Vehicle (MAV) under development at NASA [74–76]. The MAV is a single stage to orbit (SSTO) space vehicle designed for Mars sample return experiments. This rocket would launch from the surface of Mars and reach orbit around the planet. NASA was considering a hypergolic hybrid engine for the MAV, using MON as the oxidizer and boron-based hypergolic additives in a proprietary liquefying fuel binder. For this purpose, Benhidjeb-Carayon et al. demonstrated ignition and re-ignition at atmospheric and reduced pressure using a cylindrical combustion chamber. MON-25 was used as the oxidizer and sodium amide or PBTSA was used as the hypergolic additive. The first grain of the engine was mainly made up of hypergolic additives, with a composition of 90 wt.% hypergolic additives and 10 wt.% fuel binder. The injection system was a full-cone spray injector. They measured ignition delays of approximately 200ms with $NaBH_4$, which is significantly higher than most droplet ignition results.

Jeong et al. [54] used their palladium/activated carbon catalyst/AB hypergolic combinations as an ignitor grain inside a 50 and a 120 N thrust engine. The first section of their engine used a mixture of 25 wt.% AB, 1 wt.% Pd-C and 74 wt.% of paraffin wax. The two fuels were polyethylene or PMMA. The hypergolic igniter successfully initiated the engine combustion after approximately half a second of the igniter onset, but the ignition delay of the igniter is not reported.

Similar to the article presented in Chapter 7, Nath et al. [77] performed a variant of the droplet ignition experiment using a spray as the oxidizer dispenser. They used 25 wt.% sodium borohydride ($NaBH_4$) embedded in an HDPE fuel binder in the form of a large rectangular fuel pellet. The oxidizer sprayed was HTP. They conducted a single test, in which the first observable flame kernel appeared 15 ms after the initial contact. Multiple ignition kernels that lasted only few milliseconds were detected, but no sustained flame was not observed.

Although useful for evaluating the performance of a propulsion system, testing in an engine configuration limits the diagnostics that can be implemented to thoroughly evaluate hypergolic ignition. It may be difficult to explain why ignition occurred or failed in certain situations. Therefore, dedicated experiments that mimic as close as possible an engine configuration, are needed.

2.3 Existing laboratory-scale combustion visualization research facilities

Observations of the dynamics of combustion occurring inside a hybrid rocket engine have already been made using specialized research facilities typically called slab burners. They consist of three sections, as seen in Figure 2.6: an injector/flow straightener, a combustion chamber with windows to allow visualization of the combustion, and a nozzle to adjust the combustion pressure. This section of the literature review focuses on recent insights on hybrid rocket propulsion obtained from these test facilities. A summary of each research setup identified is presented in Table 2.4.

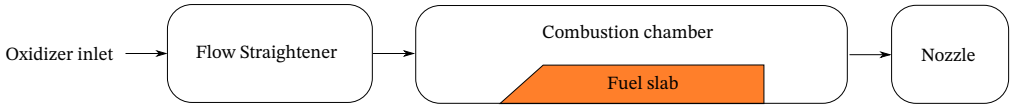

Figure 2.6 Schematic representation of the main components of a slab burner.

2.3.1 Test facilities

The first slab burner documented in the literature was put into operation in 1963 by Marxman et al. [78, 79] of the United Technology Center (UTC). They used PMMA as the fuel with GOx as the oxidizer to validate Marxman's theory for the regression rate of non-liquefying hybrid fuels. The setup used a laboratory-scale wind tunnel to provide a uniform flow inside the combustion chamber. The wind tunnel straightened the flow by breaking the turbulence vortices using a convergent-divergent section coupled with a honeycomb channel. Optical accesses on the side of the burner allowed visualization of the combustion dynamics and measurement of the regression rate using high-speed cameras. Schlieren imaging techniques were used to study the boundary layer combustion phenomena.

In the 1990s, Strand et al. [80, 81] at the Jet Propulsion Laboratory investigated the effect of particulate additives such as aluminum and coal on the regression rate of HTPB under a GOx flow. Their experimental setup operated at pressures up to 1.4 MPa. Two circular windows, one at the leading edge and the other one at the trailing edge of the fuel slab, allowed the visualization of the combustion phenomena. The main result they obtained is the confirmation that some additives can be used to increase the regression rate. In addition, they confirmed that the regression rate for HTPB is independent of the combustion pressure, and is controlled by the oxidizer mass flux entering the combustion chamber (G_{ox}).

Experiments at elevated pressures were pursued at Pennsylvania State University [21, 82–84] in the late 1990s and early 2000s. Chiaverini and colleagues studied hybrid fuels burning at

pressures up to 5.5 MPa and GOx mass fluxes ranging from 112.5 to 457.0 kg/m^{2}s. Instead of using windows to measure the instantaneous regression rate, they implemented instantaneous X-ray radiography and ultrasonic pulse-echo sensors. In addition,, thermocouples were embedded in the fuels to record the combustion temperature. The main results obtained by this team are related to the measurement of the regression rate of HTPB doped with ultrafine activated aluminum and carbon black, as well as the demonstration of X-ray radiography to assess combustion in hybrid rocket engines during operation.

NASA Ames Research Center also performed visualizations of hybrid engines under elevated pressures in 2003. However, due to a sealing problem the test facility exploded and the investigation was stopped [85].

The identification of liquefying fuels as a way to achieve high regression rates for hybrid rocket applications led to the creation of several testing facilities. Researchers from the Office National d'Etudes et de Recherches Aérospatiales (ONERA), in France [10, 86], developed from 2009 to 2012 a visualization experiment to investigate the melt layer of paraffin wax under a stream of hot gases. In their investigations, hydrogen and oxygen were mixed and ignited in a combustion chamber to produce hot gases, before being injected into the main hybrid combustion chamber. The setup was equipped with two lateral windows and a top window. The regression rate was measured optically with high-speed cameras and with ultrasonic pulse-echo probes. Their main results were related to the measurement of the thickness of the melt layer and the regression rate of the fuels. In parallel, they developed a predictive model for the regression rate, which they validated in their experiment. The ONERA experimental facility could be operated at a maximum pressure of 3.0 MPa.

Tokai University [25, 26, 87] and Korea Aerospace University [23, 24] each designed a similar test bench. They were operated at atmospheric pressure and used to investigate the addition of EVA (Tokai University) and LDPE (Korea Aerospace University) on the regression rate of paraffin wax. They used their slab burner to measure the decrease of the regression rate at different wt.% of EVA and LDPE added to a paraffin wax, as reported in Section 2.1.3.

Wada et al. from Akita University [88] designed a vertical double-slabbed burner, where two slabs of fuel faced each other in a vertical position. PMMA, paraffin and low melting point thermoplastics were used with GOx as the oxidizer. By placing an infrared filter in front of a high-speed camera, they were able to reduce the intensity of the flame and enhance the overall quality of the images. Then they were able to observe fuel particles being expelled without completely burning. Finally, by carrying tests at atmospheric pressure and higher pressure, they concluded that the number and size of the fuel droplets entrained are independent of the chamber pressure.

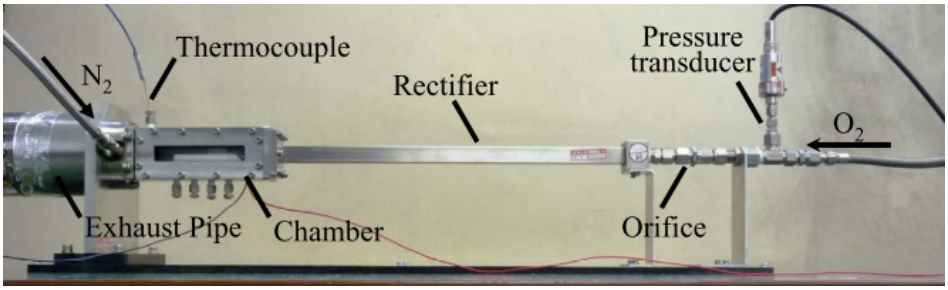

Figure 2.7 Research setup at Tokai University [26]. With permissions.

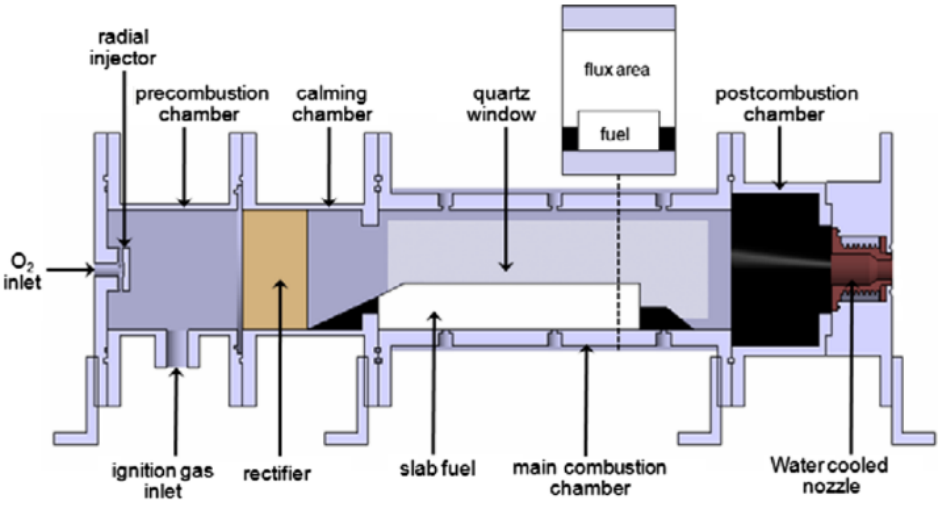

Figure 2.8 Research setup at Korea Aerospace University [24]. With permissions.

A joint experiment by the German Aerospace Center (DLR) and the Space Propulsion Laboratory (SPLab) of Politecnico di Milano in Italy is still in operation and dedicated to the study of on paraffin combustion using GOx [11, 89–98]. Several data acquisition techniques are used in this setup. Particle Image Velocimetry (PIV) was used to characterize the flow field entering the combustion chamber. High-speed color imaging and Schlieren techniques are also used. CH* chemiluminescence is used to precisely visualize the regions where the combustion takes place. In addition, the combustion chamber is designed to allow probing to measure reacting gaseous species. The experimental rig can also operate at high pressure (the exact pressure is not known). To date, the main results observed with this experiment are related to the regression rate of fuels and the instabilities appearing in the melt layer. SPLab has also designed their own double slab burner for the study of paraffin wax and gelled wax doped with nanoparticles of aluminum and metal hydrides (MgH_2 and $LiAlH_4$) [99].

A team at Stanford University has also developed a slab burner [7, 85, 100–104]. Fuels inves-

Figure 2.9 Research setup at the German Aerospace Center (DLR) [11]. With permissions (Creative Commons Creative Commons Attribution 4.0 International License | Link).

tigated are paraffin, PMMA, HDPE as well as HTPB. GOx is used as the oxidizer and the combustion pressure can be up to 1.5 MPa. Schlieren imaging and OH* chemiluminescence are used, with the main results related to the confirmation of the entrainment mechanism proposed by Karabeyoglu et al. [9, 105] and comprehensive studies of flame instabilities located on top of the surface of the fuel.

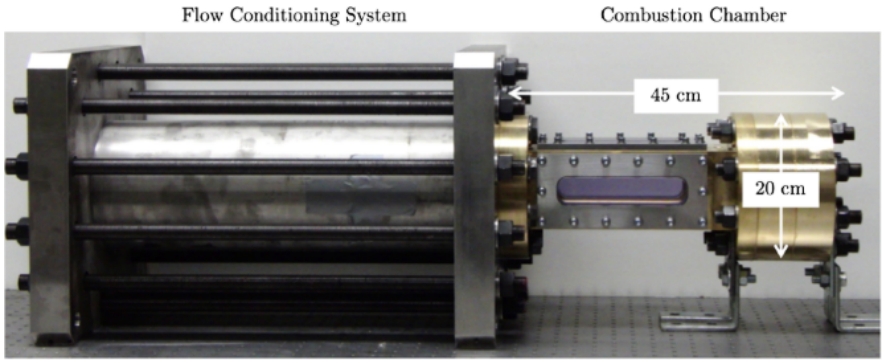

Figure 2.10 Research setup at Stanford University [104]. With permissions.

Finally, University of Calgary [13, 106, 107] has recently developed a slab burner operated at atmospheric pressure with GOx and paraffin wax. In addition to high-speed cameras and the Schlieren technique, they implemented flame spectrometry analysis. By doping regions of the fuel at different depths with magnesium oxide, the spectrometer detects MgO-specific light

emission in the exhaust gas plume. Thus, the regression rate measured by spectrometry is compared to the regression rate measured optically. They also studied the effect of 3D-printed fuel support in a lattice geometry on the regression rate. They found that the regression rate can be tailored using different lattice density.

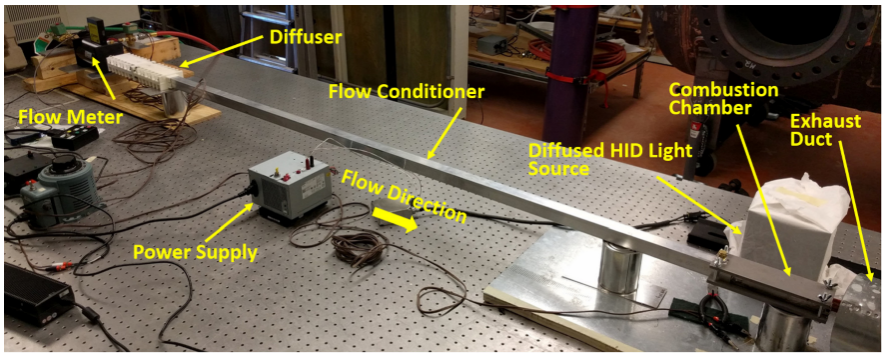

Figure 2.11 Research setup at the University of Calgary [13]. With permissions.

Overall, almost all visualization test facilities are using GOx as the oxidizer and various liquefying and non-liquefying hydrocarbons or polymers as the fuel. Side windows, and sometimes a top window, allow flow visualization using color or monochrome high-speed cameras, OH* and CH* chemiluminescence or the Schlieren imaging technique. These diagnostic techniques are discussed in more detail in Section 2.3.2. For safety and operational reasons, combustion at atmospheric pressure is preferred. However, although the regression rate of paraffin is independent of the combustion pressure, some research groups have found that the entrainment effect, flame instabilities and flame location can be affected. These studies highlight the suitability of slab burners as an excellent choice to experimentally understand the underlying mechanisms of hybrid rocket combustion. It should also be noted that hypergolic testing in a slab burner, either the ignition portion or the sustained combustion portion, has not been reported in the literature. Many of the slab burners presented here are not compatible with such tests, either because of the materials, such as brass, which are not compatible with hypergolic oxidizers, or because of the design, such as a long stabilization chamber. As discussed earlier, there is a need to visualize hypergolic ignition in engine-like configurations that is similar to the need to visualize combustion dynamics in slab burners. A hypergolic slab burner would be the ideal candidate to study both aspects. However, it requires that material and design choices be considered as early as possible in the design phase.

Table 2.4 Summary of existing slab burner research setup. Adapted from [104] and [108].

Research Center	Propellants	Data Acquisition System[a]	Pressure [MPa]	G_{ox} [kg/m^{2}s]	Fuel (L x W x T) [mm]	Year	Ignition System	Cross Section [mm]	Ref.
UTC	PMMA / GOx	P, T, Schlieren	Atmospheric	5.62 - 56.2	152.4 x 25.4 x 6.35	1963-1964	Spark plug igniter	44.45 x 44.45	[78,79]
Jet Propulsion Laboratory	HTPB + Al + Coal / GOx	P, T	1.38 (200 psia)	2.8 - 35	414.0 x 67.3 x 12.7	1992-1993	Spark plugs w. CH_4 flow	76.2 x 76.2	[80,81]
Pennsylvania State University	HTPB + Carbon Black + ULAF[e] / GOx	P, T, instantaneous X-ray radiography, ultrasonic pulse-echo	1.2 (170 psia) - 5.5 (800psia)	112.5 - 457.0	584.2 x 76.2 x 44.5	1995-2001	Solid propellant w. nichrome wire	76.2 x 76.2	[21,82–84]
NASA Ames Research Center	-	-	Elevated pressure	-	-	2003	-	-	[85]
ONERA	Paraffin / H_2 + O_2	P, T, ultrasonic pulse-echo, PIV	1.0 - 3.0	50 - 300	350 x 40 x 24.8	2009-2012	Electric device	-	[10,86]
Tokai University	Paraffin + EVA / GOx	P, T	Atmospheric	10 - 30	100 x 10 x 10	2009-2011	Nichrome wire	10 x 20	[25,26,87]
Korea Aerospace University	Paraffin + LDPE / GOx	P	Atmospheric	3.8 - 14.4	- x 50 x 50	2010-2015	-	-	[23,24]
Akita University	PMMA + Paraffin / GOx	High-speed camera w. infrared filter	Up to 2.0	50	100 x 40 x 20	2013	Electrical spark wire	-	[88]

DLR[b]/ SPLab[c,d]	Paraffin / GOx	P, T, Schlieren, PIV, gas probing, CH* chemiluminescence	Atmospheric and elevated pressure	50 - 100	180 x 90 x 18	2013-2019	GOx/hydrogen torch igniter	-	[11, 89–98]
Stanford University	Paraffin + PMMA + HDPE + HTPB / GOx	P, T, OH* chemiluminescence, Schlieren	Up to 1.5 (220 psia)	20 - 73	127 x 25.4 x 9.5	2012-2019	Nichrome wire	50.8 x 50.8	[7, 85, 100–104]
SPLab[c]	Paraffin + gelled wax + Nano-Al + metal hydrides / GOx	P	1.5	100 - 350	50 x 10 x 4	2013	Pyrotechnic ignition device	-	[99]
University of Calgary	Paraffin / GOx	P, Schlieren, Flame spectrometry	Atmospheric	8 - 16	73 x 12.7 x 9	2018-2019	Hot wire	25.4 x 25.4	[13, 106, 107]
Research Center	Propellants	Data Acquisition System[a]	Pressure [MPa]	G_{ox} [kg/m^{2}s]	Fuel (L x W x T) [mm]	Year	Ignition System	Cross Section [mm]	Ref.
University of Kwa-Zulu Natal	Paraffin + Al / N2O	-	Atmospheric	38	150 x 30 x 15	2017	Copper wire	32 x 47	[109]
Northwestern Polytechnical University	HTPB + paraffin / GOx	P, high-speed camera, Schlieren	Up to 2.5	Up to 265	100 x - x 12	2022-2023	Methane/GOx torch igniter	-	[12, 110, 111]
Université libre de Bruxelles	Paraffin / GOx or N_2O	P, T, high-speed camera, chemiluminescence, Schlieren	Up to 1.0	Up to 365	110 x 40 x 30	2022-2023	Propane/GOx torch igniter	-	[112]

[a] P and T are pressure and temperature respectively, [b] German Aerospace Center, [c] Space Propulsion Laboratory of Politecnico di Milano, [d] Joint research between the two research groups, [e] Ultrafine activated aluminum powder

2.3.2 Optical diagnostic techniques

Schlieren imaging

Schlieren imaging is widely used for the observation of shock waves [113–115]. The operating principle of Schlieren imaging is simple and is based on the fact that a change in temperature or density (which can be caused by a change in temperature or composition) changes the refractive index of a transparent medium. This effect can be used to visualize temperature or density gradients using an optical arrangement in which a light source, ideally a small point source, is collimated by a lens to produce parallel beams of light. This can be achieved by various configurations, as demonstrated in Figure 2.12. A secondary lens focuses the parallel light onto a knife edge. The knife edge partially cuts the light before it enters the camera. The test section must be between the lenses, within the sections illuminated by parallel light rays. The light deviates from its trajectory when a change in temperature or density occurs, and this deviated light is blocked by the edge. In this configuration, the test area is limited by the diameter of the lenses used.

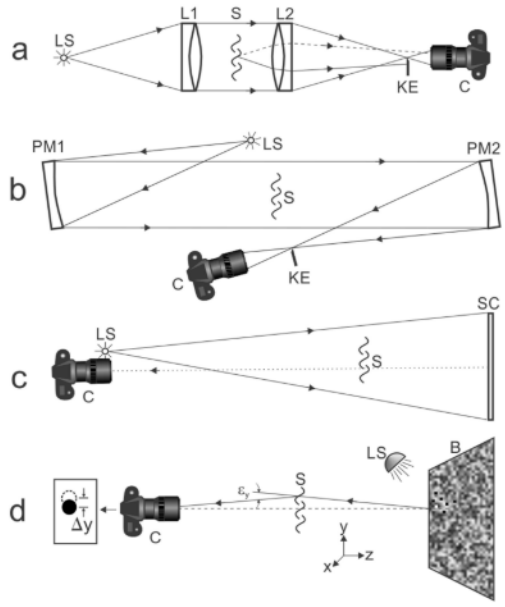

Figure 2.12 Schematic representation of different Schlieren techniques from [114]. a) Refractive system. b) z-type Schlieren system with parabolic mirrors. c) Direct shadowgraphy d) Background-oriented Schlieren (BOS). LS = light source, L = Lens, KE = knife edge, S = Testing area, PM = Parabolic mirror, SC = Projection screen. With permissions.

The second configuration (Figure 2.12b), the z-type Schlieren system, uses parabolic mirrors instead of lenses. By using mirrors, the experimental setup can be in the form of a *Z*, which has a smaller footprint in a laboratory. Again, the first parabolic mirror converts the light

emitted by the source into a parallel beam that is then focused on a knife edge before entering the camera.

The third system is not Schlieren imaging *per se*, but leads to similar data being acquired. A light source, close to the camera, is projected onto a screen. The object in the test area casts its shadow on the screen. The light emitted from the screen is then captured by the camera. By subtracting the acquired images from the reference frame, shock wave contours and transient phenomena can be observed. However, unlike Schlieren imaging, quantitative temperature/density measurements cannot be made.

Finally, a recently developed Schlieren technique is called *background-oriented Schlieren* (BOS) and finds similarities with PIV. A screen with a random dot pattern is illuminated by a light source far away from the test area. By recording the experiment in front of the screen and comparing the images from the background without any experiment, small distortions of the dot pattern are visible. This allows the software to calculate the refractive index of the transparent medium. The detection of small distortions is done with an image correlation algorithm similar to PIV techniques, hence the similarities between the two visualization tools.

The Schlieren technique is primarily used for boundary layer visualization when used in slab burners. Using automated edge detection software, the thickness of the thermal boundary layer is measured for various fuels. Stanford University observed that the fuel composition (PMMA, HPDE, Paraffin) does not affect the thickness of the thermal layer [13,102–104]. An example of a Schlieren image obtained in a slab burner is shown in Figure 2.13 and pictures the thermal boundary layer over the fuel surface.

Recent investigations done at Polytechnique Montréal, involving the author of this thesis as a collaborator, have combined the Schlieren imaging technique with hypergolic droplet ignition tests [19,22]. The first study showed that small gas releases in the form of jets occurred prior to hypergolic ignition of AB/paraffin fuels using WFNA as the oxidizer. The second study used the Schlieren technique to demonstrate that much more AB reacts prior to ignition with a sorbitol binder than with a paraffin binder. The two studies demonstrate that the Schlieren technique is an interesting tool to use in conjunction with high-speed color imaging when conducting droplet ignition experiments.

OH* and CH* chemiluminescence

OH* and CH* Chemiluminescence techniques are well suited for flame diagnostic experiments. They are easy to implement when optical access to the combustion region is possible.

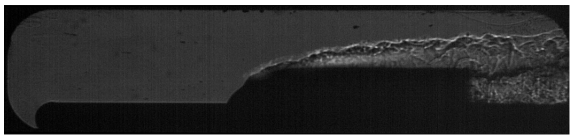

Figure 2.13 Example of Schlieren image inside a slab burner showing the thermal boundary layer. Oxidizer flow is from left to right [103]. With permissions.

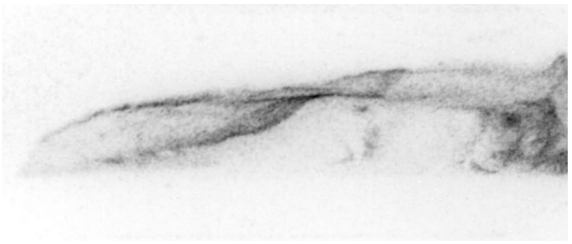

Figure 2.14 Example of OH* chemiluminescence image inside a slab burner. Oxidizer flow is from left to right and the image is inverted for clarity, with darker regions representing more intense chemical reactions [103]. With permissions.

When electronically excited species (such as OH or CH in flames) relax to a lower energy state, a photon is emitted. Depending on the species, the frequency of the emitted photon is well known. For example, the excited OH radical, denoted OH*, emits a photon in the near UV at about 307 nm, while an excited photon emitted by the CH* radical has a wavelength of 431 nm [116]. Using UV intensifiers and cameras, the photon emission is recorded in the form of images. The use of appropriate post-processing software leads to the identification of reaction zones that are correlated by the intensity of the signal.

Due to the short lifetime of the excited radicals, an instantaneous mapping of the reaction rate can be recorded. Chemiluminescence intensity signals are correlated with combustion conditions such as pressure, equivalence ratio, reaction rates and heat release [117–119]. However, detailed combustion reaction mechanisms must be known to extract much of the information.

In the context of hybrid rocket fuel characterization, Jens et al. [103, 104] and Petrarolo et al. [97] used OH* and CH* chemiluminescence as a means of accurately locating the position of the flame. Furthermore, a correlation between pressure and OH* intensity was observed by Jens et al., as well as a proportional correlation between the fuel burn rate and the signal intensity. An example of an OH* chemiluminescence image obtained in a slab burner is shown in Figure 2.14 and pictures the intensity of the excited OH species.

CHAPTER 3 OBJECTIVES AND PROJECT STRUCTURE

The literature review in Chapter 2 highlighted a number of challenges associated with hypergolic and non-hypergolic hybrid combustion. It presented the current state of the art for research on fuel and hypergolic additives for hybrid rocket applications. A major breakthrough in the early 2000s, i.e., liquefying fuels to achieve high regression rates, redefined the possibilities associated with this type of rocket propulsion. Since then, several studies have been conducted on paraffin waxes as fuel matrices.

The identification of paraffin wax as a potential fuel for future hybrid propulsion systems led to another research challenge: paraffin waxes have poor structural properties. Researchers identified additives that could increase the tensile and compressive strength of the fuels. Polymerized hydrocarbons such as EVA, Vybar, HDPE and LDPE are well suited for this application. However, they also increase the viscosity of the fuel, which reduces the regression rate.

Although still an emerging area of research, hypergolicity in hybrid engines has shown promising results in some space applications such as satellite maneuvering, spacecraft orbit control, and further simplifies the ignition sequence of hybrid engines. Since ignition tests are usually conducted using droplet ignition experiments, they do not represent the real operating conditions of a typical engine. For example, some phenomena related to high pressure, turbulent mixing, high temperature, oxidizer spray injection and re-ignition cannot be observed. Full-scale engines, or at least laboratory-scale slab burners, are required to evaluate the full spectrum of parameter dependencies involved in the hypergolic ignition of hybrid fuels. The evaluation of additives such as ammonia borane, sodium borohydride and metal-organic frameworks is just beginning, and their behavior under realistic combustion conditions remains to be fully understood.

Laboratory- and full-scale engines are used to characterize the regression rate of a solid fuel. However, some research groups have opted to conduct tests using a combustion visualization facility, where advanced diagnostic tools can be used. A visualization experiment, such as a slab burner, allows researchers to measure spatially and temporally the regression rate. Moreover, flame location, droplet entrainment, liquid film instabilities of the melt layer and the thermal boundary layer thickness can be observed in a way that is not possible with an engine configuration. These measurements are essential for an in-depth understanding of the fundamental combustion process taking place in a hybrid rocket combustion chamber. Several combustion visualization facilities exist, but they mainly use gaseous oxygen as the

oxidizer. The literature review supports the fact that hypergolic hybrid engines could help reduce the cost and complexity of this means of propulsion. It also demonstrated that little to no engine-scale or small-scale experiments have been conducted on the ignition and combustion dynamics of hypergolic fuels. Further investigation with various hypergolic-triggering oxidizers such as high-test peroxide or WFNA is required. It will lead to the ultimate goal of this proposed research, which is to bring the benefits of an advanced visualization facility to the study of research hypergolic hybrid fuels.

Considering the aforementioned research needs, the general objective defined for this thesis is to support the development of hypergolic hybrid rocket engines by conducting small-scale experiments and providing experimental results. Therefore, it is necessary to measure combustion properties, such as the regression rate, ignition delay and combustion instabilities, of paraffin-based and hypergolic fuels for hybrid rocket engines.

3.1 Specific research objectives

To answer to the general objective, four specifics objectives are defined:

1. Design, develop and instrument a laboratory-scale slab burner rig that replicates realistic combustion conditions (pressure, temperature, turbulence and velocity profile) encountered in a full-scale hybrid engine.

2. Identify suitable fuel additives for hybrid rocket applications that allow control over the ignition delay, regression rate and specific impulse of paraffin-based fuels.

3. Evaluate the ignition performance of hypergolic additives under the injection of sprayed liquid oxidizers.

4. Develop an injection system that supports the use of liquid and hypergolic oxidizers in the laboratory-scale test facility.

3.2 Project structure and coherence between the articles

The results of this thesis are presented in the form of scientific journal articles and address the specific objectives described in §3.1. As the thesis is presented in the form of separate articles, each with its own literature review, the reader may find information repeated in Chapter 2.

Article 1: Time-resolved regression rate measurement of paraffin wax alpha-olefin hybrid rocket fuels in a slab burner

This article addresses to the first and second specific objectives described in §3.1. First, it presents the design and validation of the slab burner developed through this thesis. The design rationale is discussed. It presents the results of a hot-wire anemometry test campaign aimed at characterizing the flow inside the combustion chamber and evaluating the turbulence intensity. The combustion experiments performed show the influence of alpha-olefin, also known by its brand name *Vybar*, on the regression rate of paraffin fuel. The regression rate is resolved temporally and spatially using an in-house algorithm that analyzes videos captured by a high-speed camera. Finally, a novel approach to measure the primary oscillation in hybrid rocket combustion systems is discussed.

The manuscript has been submitted to the *Aerospace Science and Technology* journal (Elsevier, 2022 Impact Factor (IF): 5.6) on November 8, 2023. The author of this thesis developed the idea for article by designing and instrumenting the slab burner used. He wrote the LabVIEW control and acquisition program, created the image analysis algorithm and prepared the sample for the tests. He performed the tests and curated the data, analyzed it and wrote 95% of the manuscript. B. Dumas helped curate the data and reviewed the article. Dumas also provided his valuable insight during the test campaign and data analysis. Professor É. Robert supervised the project, provided the funding and reviewed the manuscript.

Article 2: Metal-organic frameworks as hypergolic additives for hybrid rockets

This article tackles the second specific objective described in §3.1. It is part of a collaboration with colleagues from the Department of Chemistry at McGill University. It is the first scientific article to investigate the use of HMOFs for hybrid rocket applications. The article first presents experimental results, in the form of droplet ignition tests, on the ignition delay of pure HMOFs, namely Co(**VIm**)$_2$, Zn(**VIm**)$_2$, and Co(**AIm**)$_2$. Then, mixtures of paraffin and HMOFs are ignited, again in droplet ignition tests, under three fuel configurations: powder or pellet mixtures, fuel pellets coated with HMOFs and fuel pellets with HMOFs located in a hole in the center. Next, the article presents the theoretical performance of the HMOFs and paraffin fuels computed by the NASA-CEA program. The values needed for the calculations (the heat of formation of each HMOF), are found using periodic density functional theory computations. Finally, the use of HMOFs, as opposed to other hypergolic additives such as AB, is discussed.

The manuscript has been published in *Chemical Science* (Royal Society of Chemistry, 2022 IF: 8.4) on February 28, 2022 [120]. The author of this thesis led the project between Poly-

technique Montréal and McGill University. He carried out the theoretical performance of the HMOFs. Together with H.M. Titi and C. Mottillo, he curated the data by conducting droplet ignition experiments. He analyzed the data from this investigation. J.M. Marrett prepared the HMOFs. Professor M. Arhangelskis performed the periodic DFT calculations and wrote tthe calculations section of the manuscript. Professor R.D. Rogers reviewed the manuscript. B. Elzein helped to write the early parts of the manuscript Professors T. Friščić and É. Robert helped in the conceptualization of the experiment, supervised the project, provided the funding and reviewed the manuscript.

Article 3: Hypergolic ignition of paraffin-based hybrid rocket fuels by sprays of liquid oxidizer

This scientific article answers the third specific objective described in §3.1, by presenting the results of hypergolic ignition experiments using sprays of oxidizers. In this experiment, paraffin and AB fuels, in the form of pellets, are subjected to different oxidizer spray conditions. By changing the injection pressure, the injector diameter, and the position of the fuel pellets, the initial ignition conditions experienced by the pellet are varied. The sprays are characterized using a phase-doppler anemometer system that measures the size and the velocity distributions of the droplets in the jet. High-speed color imaging, high-speed Schlieren imaging and high-speed infrared imaging techniques are used to determine the ignition delay and the surface temperature prior to the ignition.

The manuscript has been published in the *Proceedings of the Combustion Institute* (Elsevier on behalf of The Combustion Institute, 2022 IF: 3.4) on October 17, 2022 [121]. This journal article followed a presentation at the peer-reviewed 39$^{\text{th}}$ International Symposium on Combustion held in July 2022 in Vancouver, Canada. A two-round peer review process is required to be accepted for presentation at the conference. If accepted, the manuscript is then forwarded to the journal editors for consideration for publication in the journal, with no guarantee of acceptance. Another round of peer review is required for journal acceptance. The author of this thesis developed the idea for the article. He performed the tests and curated the data, analyzed it and wrote 95% of the manuscript. B. Dumas helped in curating the data, preparing the fuel samples and reviewing the manuscript. J. Zahlawi prepared the fuel samples. M. Chartray-Pronovost reviewed the manuscript. Professor É. Robert participated in the conceptualization of the experiment, supervised the project, provided the funding and reviewed the manuscript.

Article 4: Hypergolic ignition of hybrid rocket fuels in a slab burner experiment

This scientific article addresses both the third and fourth specific objectives described in §3.1, first by adapting the slab burner test facility to accommodate the use of liquid oxidizer, and then by using it to evaluate the hypergolic performance of AB-paraffin fuel under engine conditions. The oxidizer spray is again characterized using a phase-doppler anemometer system. This system is also used to characterize the velocity field in the combustion chamber. Two modes of operation are envisioned for this test facility. The first one uses only nitric acid as the oxidizer for both parts of the burn, i.e, the hypergolic ignition and the sustained combustion. The second mode uses the hypergolic ignition capability of nitric acid-AB to ignite a paraffin-AB fuel slab with GOx as the main oxidizer.

The manuscript will be submitted before the thesis defense. The author of this thesis developed the idea for this article by designing and instrumenting the hypergolic slab burner used. He adapted the LabVIEW control and acquisition program created for the first specific objective and prepared the sample. He performed the tests, curated and analyzed the data, and wrote 95% of the manuscript. M. Chartray-Pronovost helped to curate the data and reviewed the article. W. Kaprolat also helped curate the data and reviewed the article, as well as helped to prepare the fuel sample. Professor É. Robert supervised the project, provided the funding and reviewed the manuscript.

CHAPTER 4 METHODOLOGY

This chapter describes the various methods implemented to conduct the research. The purpose of this chapter is not to repeat the information provided in the methodology section of the articles, but rather to provide further details on the context and how the experiments were conducted. Throughout this chapter, safety is often discussed either by mentioning the personal protective equipment worn while performing the tests, in the presentation of the various test procedures or in the design of the control software. However, these mentions are not a perfect guarantee of safety and should not be blindly followed without a good understanding of the experiments.

In this chapter, the droplet ignition tests and the diagnostic techniques are first described in detail. Then, this methodology is adapted to perform ignition tests using sprays of oxidizer. The design rationale of the slab burner is also presented in more detail than in Chapter 5. Finally, the design and test methodology of the hypergolic slab burner are explained.

4.1 Droplet ignition tests

The droplet ignition tests conducted for the experiment presented in Chapter 6, although simple in appearance, must be performed carefully for various safety reasons. The oxidizer used is WFNA, a strong oxidizer that reacts with a wide variety of materials such as aluminum, nitrile gloves (they catch fire), and carbon steel. Stainless steels are suitable for use with concentrated nitric acid. The droplet ignition tests are always conducted in a chemical fume hood, with the test operators wearing a full-face respirator mask with organic vapor filter cartridges and acid-resistant gloves.

A small amount of nitric acid, approximately 5 ml, is drawn in a small airtight glass syringe. The syringe contains and dispenses the acid. The use of a syringe pump helps to slowly dispense a single droplet of oxidizer with a repeatable diameter. In the case of the experiments presented Chapter 6, the syringe is controlled manually. A schematic representation of this experiment is shown on Figure 4.1.

The syringe is placed above the fuel pellet. As discussed in Chapter 2, the height of the syringe affects the ignition delay due to a faster or slower impact velocity on the pellet. To allow comparison of results, the height of the syringe is measured and kept constant throughout the tests.

A high-speed camera is required to measure the ignition delay. The camera (Fastcam Mini

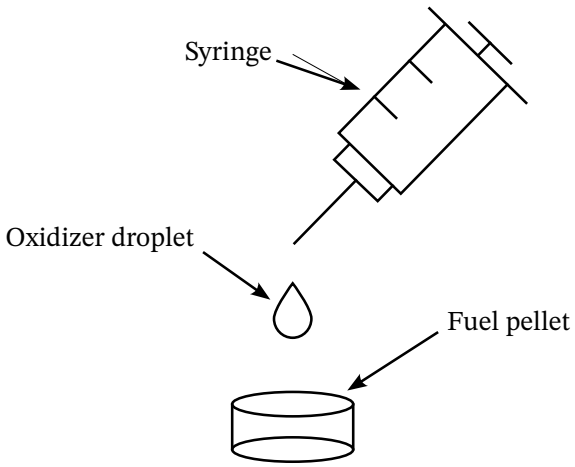

Figure 4.1 Schematic representation of the droplet ignition experiment.

AX200, Photron, Japan) is triggered manually using a dedicated software and computer. The camera is triggered before the droplet exits the tip of the syringe to ensure that the fall of the droplet, its impact on the sample and the ignition are fully captured. With experienced operators and a well set up camera, multiple tests (>30) can be performed in a single day, provided that samples are readily available.

4.2 Spray ignition tests

The spray ignition tests conducted for the experiment presented in Chapter 7 are similar to the droplet ignition tests, but require more preparation and operations. It is worth noting that this type of experiment was not found in the literature before it was conducted at Polytechnique Montréal. Thus, the methodology was developed with the knowledge and experience gained from the previous droplet ignition tests.

4.2.1 Spray generation

Since the goal of this study is to identify injector-related parameters that affect the ignition delay, several injectors need to be tested. Finding injectors with very low flow rates (down to ≈ 5 ml/s) that were compatible with the concentrated nitric acid was a challenge in itself. Several injectors marketed as "stainless steel" turned out to contain brass or nickel-plated brass components. Within seconds, the acid would oxidize the brass and the acid would turn from a bright yellow to a green-blue color.

As before, the spray injectors are placed above the fuel samples, with the small oxidizer droplets impacting the pellet surface directly, as schematically represented in Figure 7.2 b)

and c). The droplet concentration, diameter, and velocity within the spray change depending on the location, meaning that it is possible to perform a parametric sweep study with a single injector. Spray conditions also change as a function of oxidizer pressure. Thus, performing a complete parametric study, with repeatable results, can be a tedious task and the number of tests required can quickly reach several hundred. The injector parameters that need to be accounted for are: the x, y, z positions in the spray (although an axisymmetric hypothesis can be applied to reduce the number of positions by half), the injector pressure and the injector diameter. In addition, the number of additives, their concentration, the fuel binder formulation and the oxidizer can also be changed. In the experiment presented in Chapter 7, the author of this thesis decided to focus on the injector parameters with a fixed additive loading (20 wt.% AB in a paraffin binder) and a single oxidizer (WFNA).

First, the oxidizer needs to be pressurized in a closed vessel. Here, because of the small amount of oxidizer required to perform a single ignition test (up to $\approx$ 5 ml/s for a 2-3 second spray), a pressure tank is not used. Instead, a long stainless steel tube (SS-T4-S-035 1/4" O.D. tube, Swagelok, USA) is filled with the oxidizer and then pressurized. The acid is dispensed into the tube using an airtight glass syringe. A cap is then secured onto the tube. A pressurized gas is connected to the tube and a pressure regulator controls the oxidizer pressure. Finally, the spray begins when a valve located between the acid tube and the injector is opened. Pressurizing only the necessary amount of acid for each test proved to be time-consuming and involved many steps (filling the syringe, filling the tube, cleaning the syringe, rinsing the tube, securing the tube cap), but was considered safer in case of spillage or leakage of oxidizer. All experiments are performed in a chemical fume hood using the same personal protective equipment as for the droplet ignition tests.

4.2.2 Phase doppler anemometry

Because the oxidizer is delivered in a spray, the thousands of droplets produced by the injector have different diameters and velocities depending on their location. A Phase Doppler Anemometry (PDA) system is the primary scientific instrument used to study such a spray. The basic principle of a PDA system is based on laser light scattering. It uses a laser source to generate a coherent beam of light. This laser beam is split into two beams: the reference beam and the measurement beam. The measurement beam is directed to the measurement area. As the laser beam interacts with the droplets, it scatters light in different directions. Each droplet acts as a point scatterer, contributing in both reflected and refracted light components. This scattered light is collected by an optical detector positioned at a specific angle relative to the incident laser beam. When the two laser beams interact with the scattered light, they

create an interference pattern. This pattern is formed due to the phase difference between the two beams. The interference pattern is analyzed by the PDA system to provide information about the position and velocity of the droplets within the measurement volume. The system calculates the phase shift between the reference and measurement beams, which is directly related to the particle velocity. By taking into account the angle of the detectors and the wavelength of the laser light, the PDA system can determine the particle size from the diffraction pattern produced.

The PDA system is considered a calibration-free measurement technique. However, it is easy to obtain results that do not reflect the real conditions in the spray. Therefore, it is important to understand the interaction of parameters such as laser power, gain, and laser voltage on the measurement to verify that the chosen values of these three parameters do not affect the measured diameter and velocity distributions. In general, this task is accomplished by gradually increasing each parameter until the distribution does not change.

4.2.3 Camera acquisition systems

This experiment uses three different cameras. First, a high-speed color camera (Fastcam Mini AX200, Photron, Japan) captures the ignition delay and the ignition of the pellet. A Schlieren system, developed by the author and B. Dumas, co-author of the article presented in Chapter 7, is also used to capture pre-ignition events. A thermal infrared camera (MS FAST M350, Telops, Canada) is also used to measure the surface temperature of the sample prior to ignition. The Schlieren imaging system consists of two 107.95mm diameter parabolic mirrors with a focal length of 1143 mm (#50-051, Edmund Optics, USA), a fiber optic halogen lamp as the light source (#OSL2, Thorlabs, USA), a mechanical iris (#M-ID-1.0, Newport, USA) as the knife edge and a planar mirror to redirect the light beam into a monochrome high-speed camera (Phantom V310, Vision Research, USA). The Schlieren system is mounted in a Z-type configuration (see Figure 2.12 b). The initial goal of the Schlieren system was to record the pre-ignition events in the same manner as in the experiment of Elzein et al. [22]. However, the large number of small droplets in the spray, as well as the fuming coming from the acid itself, generate a considerable amount of gas that is opaque in the Schlieren images. This effect limits the number of events that can be measured, but the Schlieren images prove to be an excellent way to measure the precise moment at which the first droplets of a spray impact the pellet surface. Finally, the thermal infrared camera is positioned so that it can observe the entire surface of the sample and record its temperature. The three cameras are triggered simultaneously to synchronize their acquired images. The high-speed color camera sends a signal, in the form of a +5V logic signal, to the other cameras via BNC cables.

4.3 Slab burner tests

The slab burner designed for this project has two modes of operation. The first one uses a gaseous oxidizer and the second uses a liquid oxidizer. Prior to the start of this thesis, only a preliminary design of the slab burner and material study had been done by the author as an undergraduate project. The final design, the test procedure, the control and data acquisition system had to be developed from scratch within the framework of this PhD. This section covers the design and validation of the slab burner operating with gaseous oxidizer, while Section 4.4 covers the adaptation of the burner for accommodating a liquid oxidizer.

4.3.1 Design of the slab burner

The slab burner design requirements are as follow:

- Allow the visualization of the combustion of hybrid rocket fuels;
- Handle a range of combustion pressure typically associated with hybrid rocket engines;
- Cover a range of G_{ox};
- Reusable;
- Compatible with oxidizers such as nitric acid, HTP, GOx;
- Provide repeatable testing conditions.

The slab burner is designed to cover a wide range of combustion conditions. The operating pressure is up to 2.41 MPa (350 psig) and is made of stainless steel 304L to prevent oxidation. The oxidizer mass flux, in $kg/m^2 \cdot s$, can be changed by varying the mass flow of oxidizer by increasing its pressure (up to 20 g/s of GOx). In addition, three optical accesses allow visualization through quartz windows. The slab burner is designed to be reusable with as few operations as possible between tests. Finally, an oxidizer stabilization chamber is located upstream of the combustion chamber to provide repeatable test conditions.

The slab burner is divided into three sections: the flow stabilization chamber, the combustion chamber and the exit section. The sections are identified in the picture and the 3D CAD design are respectively presented on Figures 4.2 and 4.3.

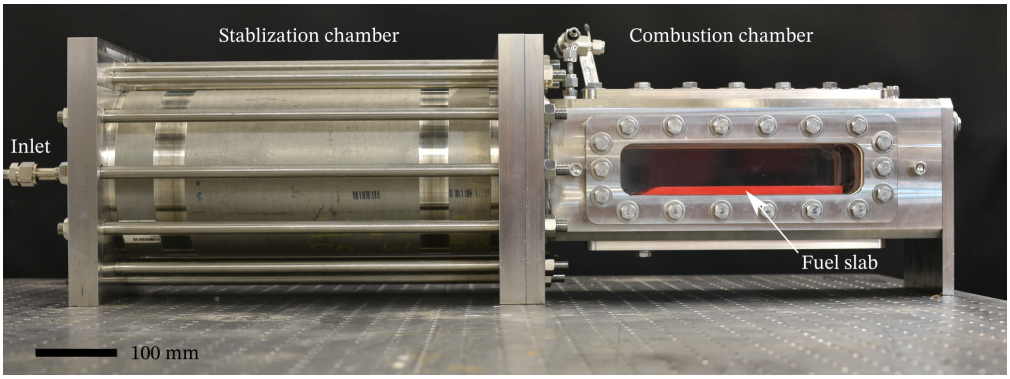

Figure 4.2 Picture of the slab burner apparatus.

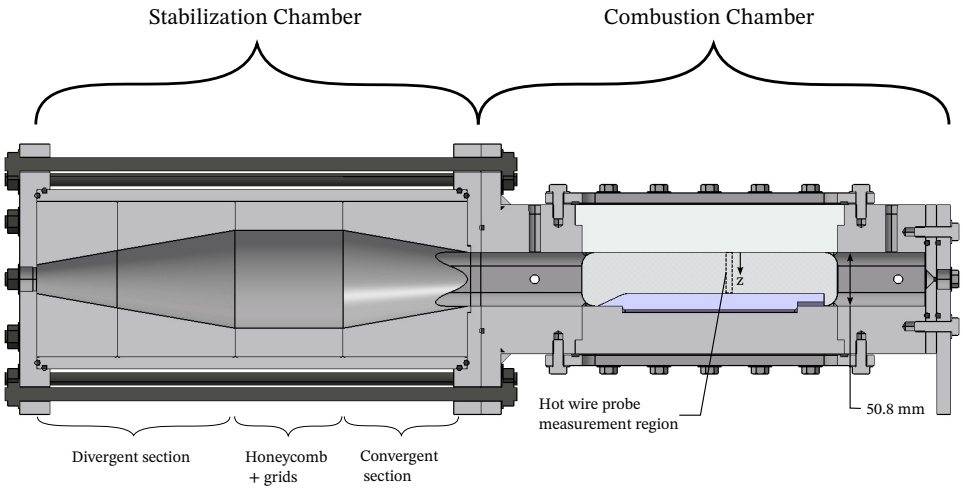

Figure 4.3 Sectional view of the 3D CAD design of the slab burner.

Stabilization chamber

The stabilization chamber presented here is inspired by the work of Chandler [7]. Its main role is to uniformize and straighten the oxidizer flow before it enters the combustion chamber. The objective is to ensure that the velocity profile and turbulence intensity are known and controlled, to enable predictable and repeatable boundary layer development over the burning fuel slab. The design rationale is based on standard practice for low-velocity wind tunnel facility. The inlet velocity of the gaseous oxygen entering the combustion chamber is ranging from 0.25 m/s to 5 m/s depending on the combustion pressure for a mass flow of up to 20 g/s. Several researchers investigated the use of screens and honeycombs, coupled with divergent and convergent sections to reduce turbulence in a flow field as well as experimental techniques to measure their effectiveness [122–125].

The stabilization chamber consists of a long stainless tube into which several parts are in-

serted. As seen on the sectional view on Figure 4.3, two diverging sections are followed by a straight section. Finally, a convergent section is placed before the combustion chamber. The divergent angle is 10° and the area ratio is 4.0, as suggested by Mehta et al. [122, 124]. Honeycombs are placed in the straight section to inhibit lateral turbulence of the flow. Two stainless steel meshes are also placed immediately before and after the straight section. The exit section also has an angle of 10° and an area ratio of 3.3.

Flow field characterization

The flow field is characterized to evaluate the effectiveness of the stabilization chamber to provide a repeatable flow. To do so, a test campaign is performed using the hot wire anemometer technique. The hot wire anemometer measures the velocity and its fluctuation, i.e., the turbulence. The anemometer consists of a probe mounted on a holder (Probe #55P11, Dantec Dynamics, Denmark). The holder is connected to a signal analyzer system (Multichannel CTA #54N80, Dantec Dynamics, Denmark), which also heats the wire and keeps it at a constant temperature. Convective heat transfer cools the hot wire and its temperature drops. To compensate, the system increases the current flowing through the wire, which in turn increases the temperature of the wire due to the Joule effect. Using a hot wire anemometer, it is possible to relate the current required to keep the temperature constant to the velocity around the hot wire probe. This method of measurement is very sensitive and allows small variations in velocity to be measured, which in turn allows turbulence in the flow field to be resolved.

The system is calibrated prior to measurement. During the calibration campaign, the probe is mounted next to a pitot tube (PAC-3-KL, United Sensor Corp., USA) connected to a differential pressure sensor (699.C17221110, Huba Control, Switzerland). The signal from the wire probe is plotted against the velocity measured by the pitot tube as shown in Figure 4.4. The signal represents the average of 100,000 data points. A calibration law correlating the voltage measured by the wire probe to the velocity of the flow is then calculated and is given by the following equation:

$$E^2 = A + BU^n \tag{4.1}$$

where E is the hot wire voltage , A and B are constants to be determined, U is the velocity measured by the pitot tube and n is a constant generally approximated by $n = 0.5$ for hot wire measurements. The constants A and B are determined by taking the intercept and the slope, respectively, from the plot of E^2 vs. U^n . The velocity measured by the hot wire is

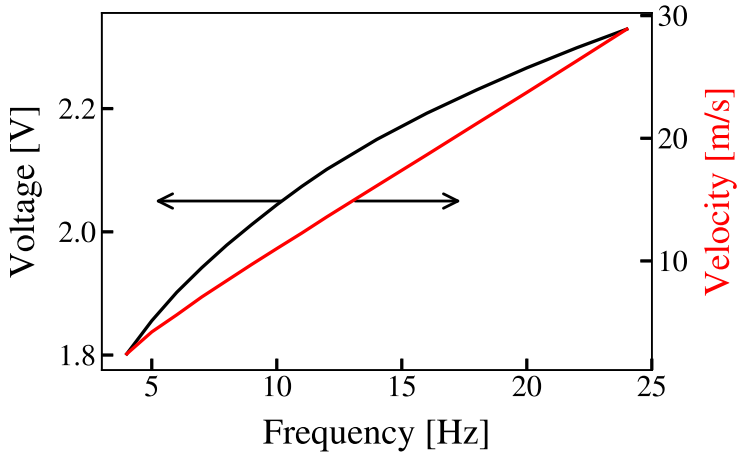

Figure 4.4 Signals obtained during the calibration of the hot wire system. The x axis represents different motor frequencies that drives the flow in the calibration channel.

then found using:

$$U = \left(\frac{E^2 - A}{B} \right)^2 \tag{4.2}$$

The hot wire technique provides a reliable measurement of the turbulence intensity in a given fluid flow. The variation of the velocity signal is given by

$$U' = U - \bar{U} \tag{4.3}$$

where U' is the fluctuation, U is the measured velocity signal and $\bar{U}$ is the mean of the velocity. It is then possible to compute the variance of the velocity fluctuation:

$$\sigma^2 = \frac{1}{n} \sum_{i=0}^{n} \left(U_i' - \bar{U} \right)^2 \tag{4.4}$$

where σ^2 is variance of the velocity fluctuation, n is the number of data point in the velocity signal. The root mean square (RMS) of the velocity signal is given by:

$$U_{RMS} = \sqrt{\sigma^2} \tag{4.5}$$

Finally, the turbulence intensity of the flow is given by:

$$I_{turbulence} = \frac{U_{RMS}}{\bar{U}} \tag{4.6}$$

The results of the test campaign are presented further in Chapter 5.

Combustion chamber

The design of the combustion chamber is presented in Figures 4.2 and 4.3 and a cross section is shown in Figure 4.5. The chamber is 419.1 mm (16.5 in) long and has a square cross section of 50.8 mm (2 in). The windows are made of quartz to provide optical access to the combustion region on both sides and at the top. Quartz is used for its ability to transmit near UV wavelengths and to allow the use of OH* chemiluminescence. By touching the sides of the fuel slab, the windows also prevent the fuel from burning on its lateral surfaces, thus making it easier to observe the combustion of the top surface of the fuel. Two holes on the top of the chamber are used for instrumentation. In this project, a pressure sensor and a pressure relief valve are placed, but in the future, the holes could be used to collect the combustion products or to measure the flame temperature using a thermocouple. The fuel is inserted through the bottom of the combustion chamber. Its shape is similar to that usually reported in the literature, with a forward facing ramp of 25°, which reduces the instabilities and recirculation zones that could appear if the leading edge of the fuel was abrupt with an angle of 90° In the case of non-hypergolic tests, i.e., using GOx as the oxidizer, the fuel is ignited by a small acetone-soaked cotton ball placed at the leading edge. An electric arc igniter is placed in the cotton ball, with its wire passing under the fuel slab and exiting the combustion chamber through its nozzle. The electric arc ignites the cotton ball and begins to melt the paraffin. The flame then propagates to the other end of the fuel slab.

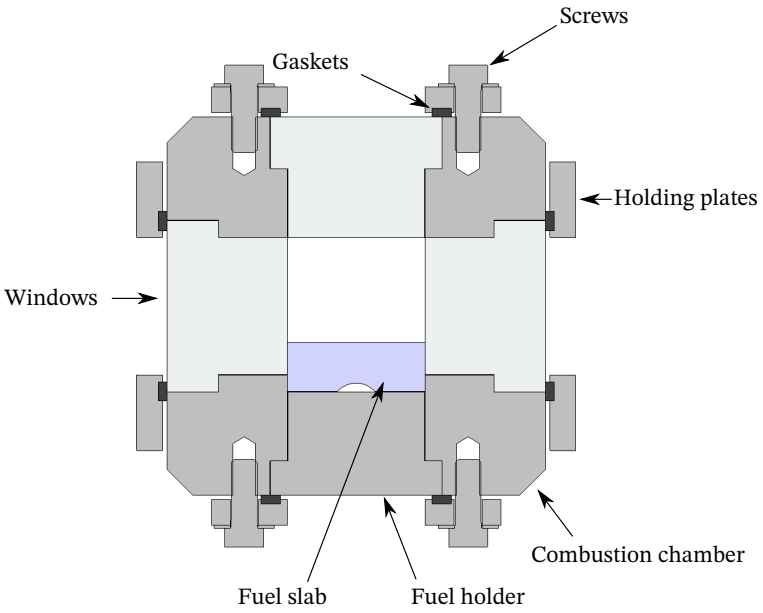

Figure 4.5 Cross sectional view of the combustion chamber.

The first series of tests in this slab burner implemented an ignition system using a nichrome

wire, similar to the ignition system used at Stanford or at University of Calgary [7, 107]. In this project, the use of a nichrome wire did not always result in ignition of the paraffin wax. In addition, using a nichrome wire involved a significant number of steps such as cutting the desired length of wire, soldering the extremities, and securing the wire to the top of the slab. Finally, after switching to the cotton ball igniter, it was found that the use of the nichrome wire increased the measured regression rate of the fuel. The main hypothesis here is that the wire acted as an obstacle increasing the turbulence inside the combustion chamber and thus increasing the regression rate. This observation is consistent with the use of passive mixing devices to further increase the regression rate of hybrid rocket fuels [126].

4.3.2 Piping, instrumentation and data acquisition in the slab burner

The slab burner apparatus features several sensors and control valves. The piping and instrumentation diagram (P&ID) is shown in Figure 4.6 (the same figure is also presented in Chapter 5, but is also shown here for clarity). Three separate fluid lines are required: the GOx line that delivers the oxidizer to the stabilization chamber, the air line needed to open the main oxidizer valve, and the N_2 line to purge and extinguish the flame after the test.

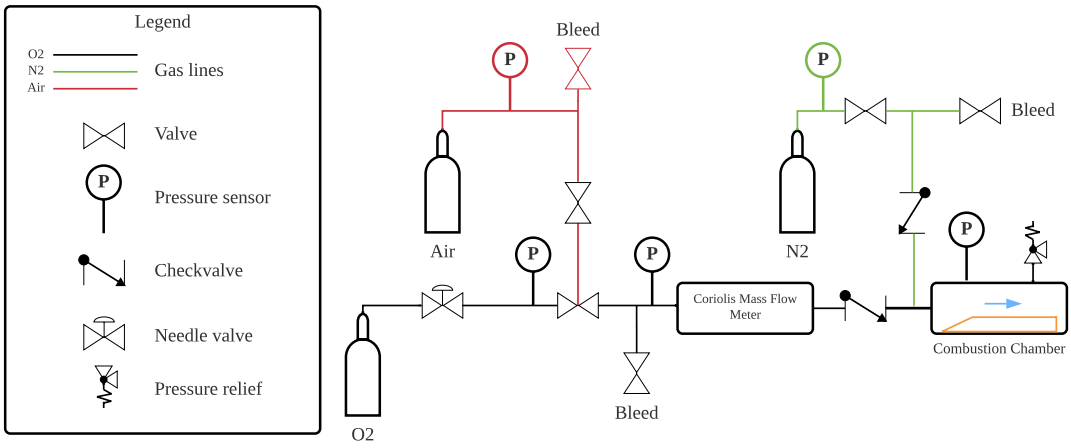

Figure 4.6 Piping & instrumentation diagram of the slab burner.

First, a pressure regulator (SR-4J, Victor, USA) is connected to a pressurized O_2 tank. The pressure is adjusted to obtain the desired oxygen mass flow. A needle valve (SS-4BK, Swagelok, USA) follows the regulator to precisely adjust the mass flow. The main oxidizer valve (SC-43GS4-31CJ, Swagelok, USA) is located immediately downstream. This valve is opened by compressed air and controlled by a solenoid valve. A mechanical emergency stop button is connected to the valve in case the test needs to be aborted. When the main oxidizer valve is opened, the oxygen enters the Coriolis mass flow meter (mini CORI-FLOW™ M15,

Bronkhorst, Netherlands), followed by the stabilization chamber and then the combustion chamber. A check valve (SS-4C-1, Swagelok, USA) is placed after the mass flow meter to prevent gas from flowing back into the line and potentially damaging the meter, or to prevent hot combustion gases from entering the oxygen tank. During testing, the oxidizer mass flow is not actively controlled, but is measured by the Coriolis mass flow meter. To change the amount of oxygen entering the combustion chamber, the static pressure of the oxidizer is adjusted beforehand by the pressure regulator connected to the oxygen tank. The oxidizer mass flow is linearly proportional to the static pressure, as revealed by the various tests performed. The correlation between the two parameters is shown in Figure 4.7. In addition, pressure sensors (MLH01KPSB01A, Honeywell, USA) are placed in the oxygen line. One is placed before the main valve to assess the static pressure of the oxygen. Another one is placed after the main valve and the last one is placed in the combustion chamber to measure the combustion pressure. A pressure relief valve (SS-4R3A, Swagelok, USA) set at 280 psi is mounted on the combustion chamber to prevent pressure build-up that could exceed the slab burner operating pressure. Finally, a bleed valve (H22G9DCM, Peter Paul, USA) is also placed on the line to purge any excess oxygen that may remain.

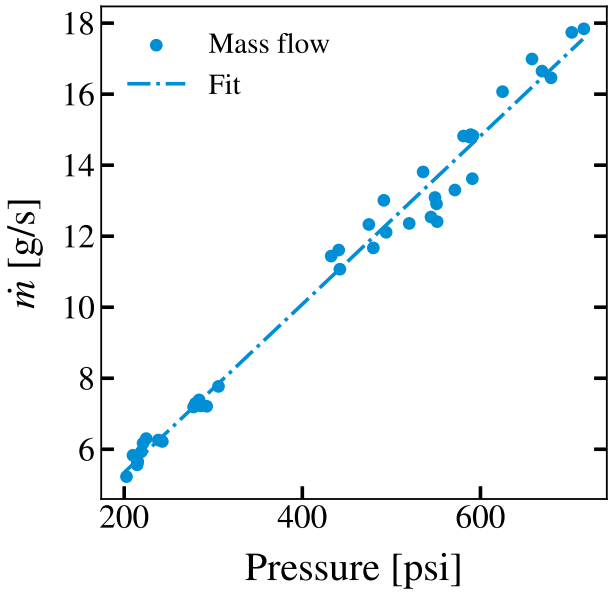

Figure 4.7 O_2 mass flow as a function of the O_2 static pressure tank. y = 0.0237x + 0.6036, R^2 = 0.985.

Second, an air line is connected directly to Polytechnique Montréal's compressed air lines. A valve (H22G9DCM, Peter Paul, USA) is placed in the main line before it enters the main oxidizer valve. This valve acts as a mechanical safety device, as it must be activated by the test operator before the main valve can be opened. A bleed valve (H22G9DCM, Peter Paul,

USA) and a pressure sensor (MLH01KPSB01A, Honeywell, USA) are also placed in the air line to purge the air at the end of the test and to monitor the air pressure.

Finally, another pressure regulator (SR-4J, Victor, USA) is connected to a pressurized N_2 tank. The pressure is usually set to about 2.76 MPa (400 psi) and monitored by a pressure sensor (MLH01KPSB01A, Honeywell, USA). A valve (H22G9DCM, Peter Paul, USA) controls the opening and closing of the N_2 in the stabilization chamber. A check valve (SS-4C-1, Swagelok, USA) is again placed to prevent combustion gas from returning to the N_2 line in case of major instabilities. A bleed valve (H22G9DCM, Peter Paul, USA) is also placed to purge excess gas in the line.

The data is acquired using a data acquisition (DAQ) card (NI-6351, National Instruments, USA) consisting of 16 analog input channels and up to 24 digital output channels. The pressure sensors are connected directly to the analog inputs, while the valves are controlled by the digital output channels.

4.3.3 Control and acquisition software

The slab burner is operated by a LabVIEW control and acquisition software developed by the author of this thesis. The software runs on LabVIEW V2018 using a laptop computer (ThinkPad W540, Lenovo, China). The program is based on a state machine architecture. The program contains a main while loop in which a case structure corresponds to the *state* of the program. The state is changed according to the operations that need to be performed.

First, the program initializes the data acquisition (DAQ) card and the mass flow meter, it enters an *initializing* state. In this state, several security checks are performed such as verifying the open/close status of each valve and digitally locking the state of these valves, meaning that the user must click an *unlock* button before being able to change the state of the valves. It then switches to an *idle* state where it continuously collects data, displays the measurements, and allows the user to activate the various control valves. The *recording* state creates the log files in which the data is written each time a block of data is acquired. Finally, the *stop* state closes all the valves that need to be closed, stops the data acquisition, and safely closes the communication tasks with the mass flow meter and the DAQ cards. Figure 4.8 schematically represents the various states and functions of the program and their respective tasks.

The program operates in two modes: manual or automatic. In the first mode, the operator can freely control each valve of the slab burner. In the second mode, a specific test sequence is automatically piloted - each valve is automatically opened and closed according to the

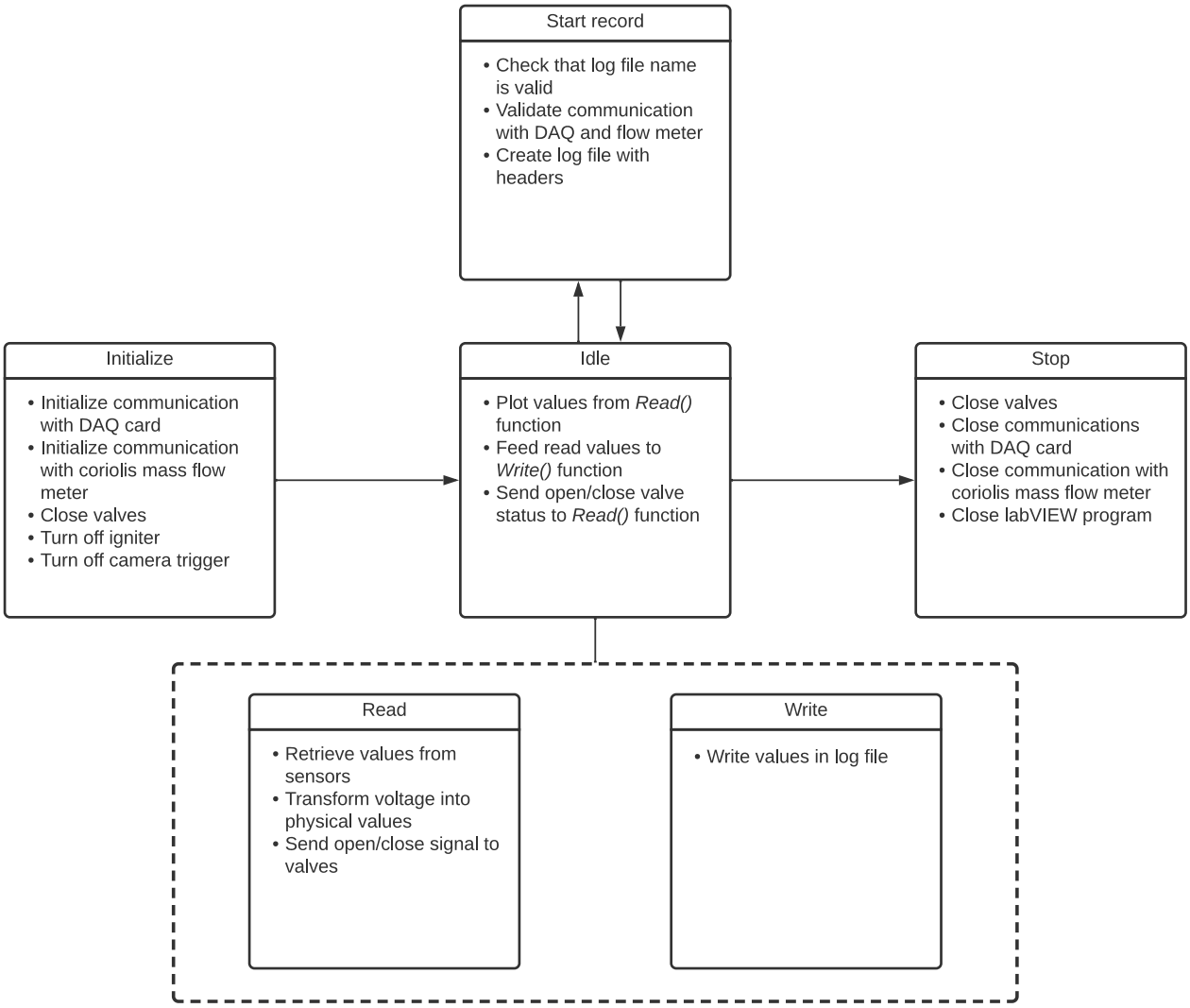

Figure 4.8 Block diagram of the LabVIEW program and its different functions.

test sequence and the test duration chosen by the operator. On top of the state machine architecture, a control sequence is programmed, where the operator only needs to input the duration of each part of the tests.

4.3.4 Test operations

The automatic non-hypergolic tests in the slab burner goes as follow. First, the stabilization and combustion chambers are filled with GOx by opening the main oxygen valve. The duration of the filling steps is determined by the operator and inputted on the graphical user interface of the software. Typically, the filling time is set to 5 seconds. Note that this time is arbitrary and has been found to always allow a reliable ignition. Then, the acetone-soaked

cotton ball igniter is triggered, initiating the combustion. At the same time, a +5V TTL signal is sent to the high-speed camera (Fastcam Mini AX200, Photron, Japan) via a BNC cable. The igniter is activated for approximately 1 second before being manually turned off while the test continues. The high-speed videos reveal that the acetone-soaked cotton ball is usually ignited in less than a few milliseconds after the igniter and camera are activated. The test duration is also chosen by the test operator and inputted on the graphical user interface of the software. In the context of this project, the test duration is set between 7.5 and 10 seconds, depending on the test being performed. The time limitation is mainly due to the onboard memory of the high-speed camera, which allows only a few seconds of video to be recorded, depending on its acquisition rate and the video resolution. Finally, the main oxidizer valve is closed and the purge valve is opened 250 ms later. The purge gas is N_2. It effectively quenches the flame a few seconds after its introduction into the combustion chamber. The test operations are performed according to the checklist presented in Appendix A.

4.4 Hypergolic slab burner tests

The slab burner is adapted to allow the use of liquid oxidizers. This allows a whole new range of tests to be performed, especially hypergolic tests. Most of the work presented in §4.3 is reused and adapted, namely the LabVIEW program, the control valves, the acquisition sensors, and the cameras. This version of the slab burner will be referred to as the *hypergolic slab burner*. The hypergolic slab burner is operated in two different configurations. In the first, a GOx flow passes through the stabilization chamber before entering the combustion chamber as in the non-hypergolic version. However, the hypergolic ignition is made by the injection of nitric acid from the injector, into the combustion chamber. In the second configuration, only nitric acid is injected in the chamber.

4.4.1 Design of the injection system

To inject the liquid oxidizer directly into the combustion chamber, a new part is designed and is placed between the stabilization and the combustion chambers. A picture of the hypergolic slab burner is shown in Figure 4.9 and the 3D CAD design is shown in Figure 4.10. The injection plate is a square measuring 254 mm by 254 mm and 31.8 mm thick. It has a square opening in the center that corresponds to the size of the combustion chamber inside dimensions, i.e., a square of 50.8 by 50.8 mm. It is made of 304L stainless steel, as are the other parts of the slab burner. At the top of the plate and in the center of the central opening, a hole allows the insertion of a tube (SS-T4-S-035 1/4" O.D. tube, Swagelok, USA)

through which the liquid oxidizer flows. To ensure that the assembly remains gas-tight, a fitting (SS-400-1-8, Swagelok, USA) is secured onto the injection plate. The inside of the fitting is drilled to allow the tube to cross the fitting. A union fitting (SS-400-6, Swagelok, USA) is mounted flush with the edge of the central orifice to easily change the length of the injection tube inside the combustion chamber. The tube is bent at a 90° angle. Finally, the inside of the end of the injection tube is tapped to secure on the injector (MC41024, Mistcooling, USA). The injector is 0.3 mm in diameter and the flow pattern follows a full cone spray. This method allows the injection tube and injector to be as small as possible. An alternative would have been to use injectors with large thread diameters, such as 1/8 or 1/4 NPT like the ones used in the spray injector experiment, but their relative size compared to the cross section of the combustion chamber would have been too large.

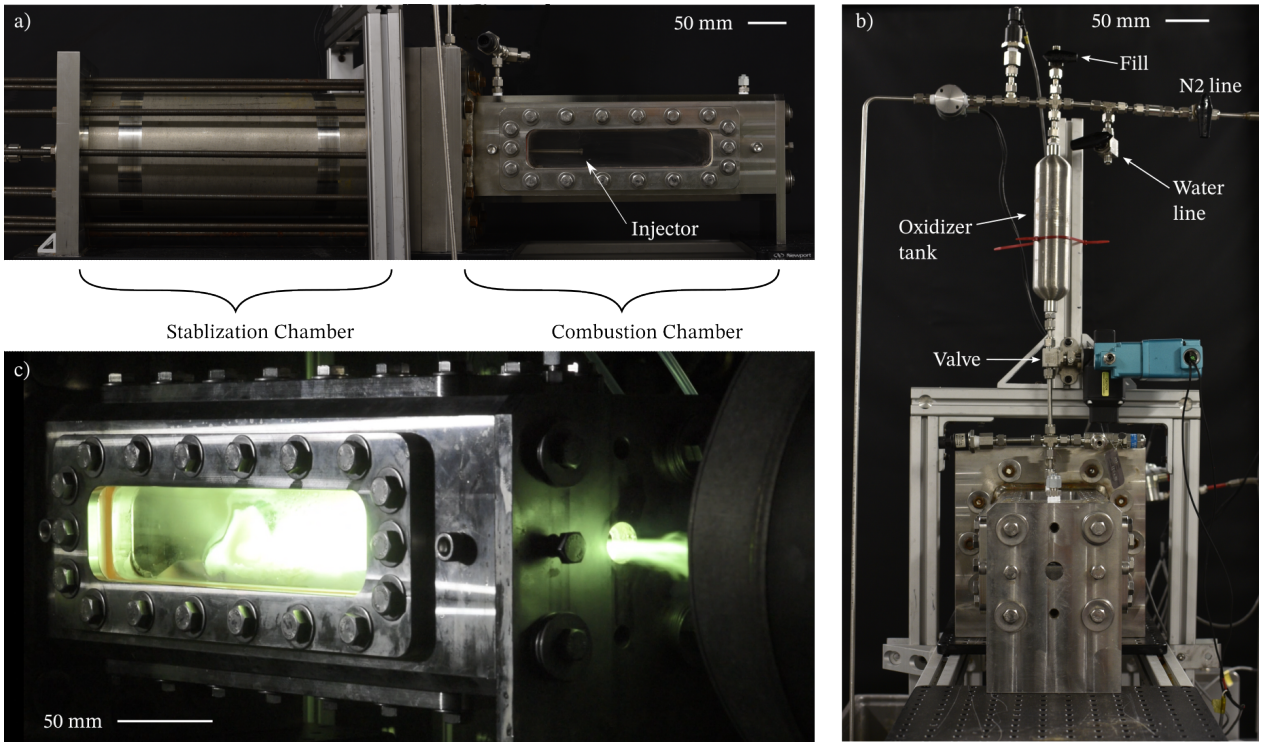

Figure 4.9 a) Side view of the hypergolic slab burner. b) Front view of the burner. c) A test in the hypergolic slab burner.

4.4.2 Piping, instrumentation and data acquisition in the hypergolic slab burner

The same pressure sensors and control valves are reused as in the non-hypergolic version of the slab burner. The P&ID of the hypergolic version of the slab burner is shown in Figure 4.11. This version uses five liquid lines instead of three. First, a nitric acid line runs from

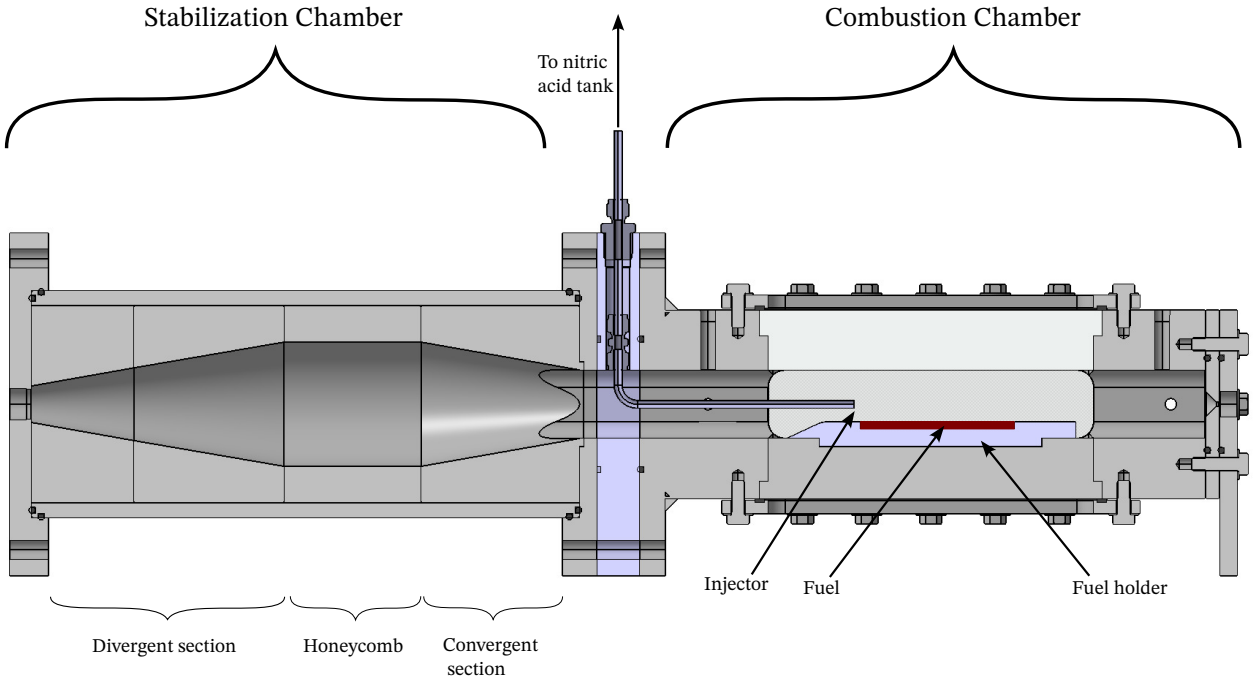

Figure 4.10 Sectional view of the 3D CAD design of the hypergolic slab burner.

the acid tank to the top of the injection plate. The nitric acid is pressurized by a N_2 tank. An air reservoir is connected to the main pneumatic valve to control it. The air is also connected to a water tank that is used to rinse and flush the nitric acid line after each test. Another N_2 tank, this time connected to the stabilization chamber, is used to flush ambient air before the hypergolic tests and to quench the flame after the tests. Finally, in the case of the test performed using GOx and nitric acid, an O_2 pressurized tank is also connected to the stabilization chamber. The Coriolis mass flow meter is placed in this line to monitor the GOx mass flow.

4.4.3 Control and acquisition software of the hypergolic slab burner

The hypergolic slab burner is controlled by an adapted version of the program developed for the non-hypergolic slab burner. The acquisition system is also the same except for the sensor and valve locations within the lines, as shown in the previous section. For these tests, the operator enters the duration of the nitric acid injection, and the GOx injection time if needed. Finally, the operator selects the duration of the automatic N_2 flush after the test. The other safety functions, the camera trigger and the recording functions are reused from the previous version.

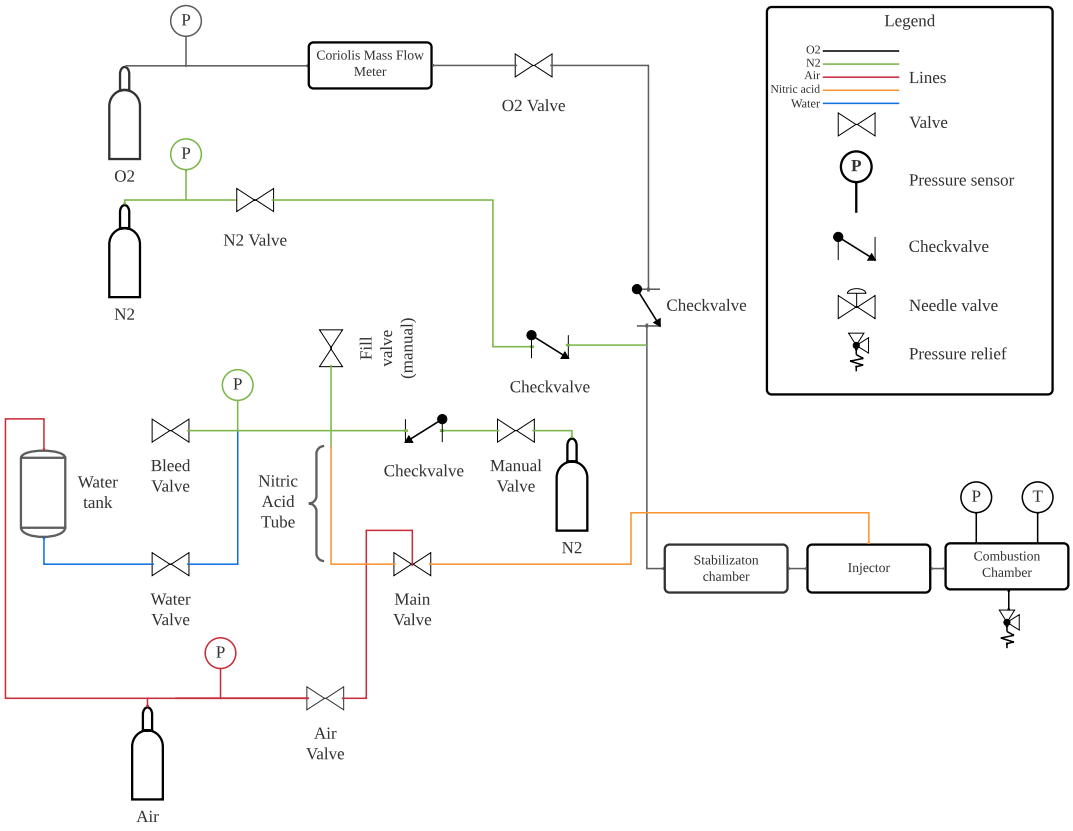

Figure 4.11 Piping & instrumentation diagram of the slab burner.

4.4.4 Test operations of the hypergolic slab burner

Hypergolic tests are performed by trained operators due to the high risk factor associated with this experiment. Fuming nitric acid (90% concentrated) is a strong and corrosive oxidizing agent that reacts with many materials. Its fumes are also toxic and should not be inhaled. Due to the nature of the experiment, it must be pressurized to be sprayed into the chamber. Therefore, the lower the amount of acid used, the better and easier it was to mitigate the risks.

The tests are always performed by two operators. They wear acid-resistant boots, gloves, a full-face respirator with organic vapor filter cartridges, and a full TYCHEM® 5000 suit. They wear this equipment for all aspects of the tests, whether it is inserting the sample into the chamber, loading the nitric acid, testing, or cleaning the test room.

First, the fuel sample is glued to the fuel holder, the design of which is presented in Chapter 8. The fuel is inserted into the combustion chamber from the bottom. A large plastic container (41195T58, McMaster-Carr, USA) filled with about 200L of water is already placed under the slab burner. This is placed in case nitric acid leaks from the combustion chamber. If it

does, it drips into the container where it is diluted to a safe concentration. The nitric acid is then transferred to the nitric acid tank on the injection plate. The transfer is done with a gas-tight glass syringe (HAM81530, Hamilton Company, USA), 5 ml at a time. The N_2 tank is opened at the desired injection pressure. The operators leave the test room and the test is performed according to the checklist presented in Appendix B. After the burn, the valve in the water line is opened to flush the nitric acid reservoir and injector, and to dilute any unreacted oxidizer remaining in the combustion chamber. The hypergolic slab burner is disassembled and all parts are thoroughly rinsed with water.

CHAPTER 5 ARTICLE 1: TIME-RESOLVED REGRESSION RATE MEASUREMENT OF PARAFFIN WAX ALPHA-OLEFIN HYBRID ROCKET FUELS IN A SLAB BURNER

Submitted to *Aerospace Science and Technology* journal on November 8, 2023.

By

Olivier Jobin, Benoît Dumas and Étienne Robert

5.1 Abstract

The design of a slab burner for hybrid rocket fire testing is presented and a novel tool is introduced to obtain spatially and temporally-resolved measurements of regression rate of the fuels. Videos recorded by a high-speed camera are used, based on color and edge detection. The algorithm is presented in detail using the results of a test campaign aimed at studying the influence of the addition of alpha-olefin to a paraffin fuel on the regression rate. Multiple tests at different oxidizer mass fluxes are conducted using neat paraffin and a mixture of 20 wt.% alpha-olefin and 80 wt.% paraffin wax. The addition of 20 wt.% of alpha-olefin is found to reduce the regression rate by 20.6 % compared to neat paraffin. In addition, the spectral content of the flame oscillations observed during the burn tests is analyzed using a Fast Fourier Transform of the flame intensity signal from the high-speed videos. Peaks are found to be in good agreement with the predicted primary hybrid oscillation frequency. Finally, a theoretical performance analysis is performed and the results show that alpha-olefin could improve the specific impulse of paraffin-based fuels, without affecting the optimal oxidizer-to-fuel ratio.

5.2 Introduction

The pioneering work by Karabeyoglu et al. [9,105] on liquefying fuels initiated a new research era on the topic of hybrid rocket propulsion. The simplicity and inherent safety of hybrid rocket motors, compared to liquid engines and solid rocket motors, respectively, remain at the core of the advantages they bring in space propulsion. However, their use as propulsion systems has been hampered by several challenges, namely, a limited understanding of the fundamental combustion processes at play in the engine, hard-to-predict fuel regression rates, poor mechanical integrity of the fuel grain and a general lack of major large-scale projects using hybrid rocket technologies. A large number of studies have proposed solutions, either

mechanical or chemical, to address the issues associated with regression rates. In some cases, the desired goal is to increase the regression rate of a given fuel to further increase the power output of the engine. In this perspective, Glaser et al. [112] proposed increasing the turbulence intensity and mixing in the combustion chamber by using stepped fuel grains, with an observed increase in the regression rate of high-density polyethylene (HDPE) fuels.

However, higher regression rates generally require the design of combustion chambers with larger diameters to overcome the fast rate of fuel consumption and achieve the same burn time as a low regression fuel. Moreover, in large size grains the mechanical properties of the fuel matrix becomes important to maintain consistent and predictable combustion. Some applications can therefore require a reduced the regression rate to accommodate the engine design, especially with fuels having a low viscosity in the melted state and a brittle character in the solid phase, such as paraffin wax. Low-density polyethylene (LDPE) has been thoroughly investigated as an additive to neat paraffin wax [23, 24]. By modifying the viscosity of the melt layer, LDPE reduces the regression rate of combined LDPE/paraffin fuels. Another extensively studied additive is ethylene vinyl-acetate copolymer (EVA) [25–28]. EVA is known to be soluble in paraffin wax and offers superior mechanical properties at the cost of a lower regression rate. Bilge et al. [29] also identified a class of additives, known as tackifier resins, capable of increasing the mechanical properties without affecting the viscosity of the fuel. Recent studies at Polytechnique Montréal have investigated the use of alpha-olefin, also known as *Vybar*, as an additive to increase the viscosity and the compressive mechanical properties of paraffin wax. Elzein et al. [22] reported that the addition of 20 wt.% of alpha-olefin to a paraffin matrix nearly doubled its compressive strength, while more than doubling the viscosity of the melted fuel. In addition, they reported that increasing the viscosity of the melt layer reduced the ignition delay of paraffin enriched with hypergolic additives. However, the suitability of alpha-olefin as an additive for paraffin fuels needs to be further investigated as its effect on the regression rate is unknown. This is the subject of the present work.

One way to assess the regression rate of hybrid fuels is through the use of visualization experiments in optically-accessible combustion chambers mimicking engine conditions. Such experiments are essential for the analysis of the underlying combustion mechanisms. They can also be used, in conjunction with image analysis techniques, to measure the regression rate of fuels [11, 13, 106, 112]. Two classes of experiments are typically used: optically accessible engines and slab burners. The first type usually consists of a lab-scale motor configuration with optical access, while the second type usually relies on a laboratory-scale rectangular combustion chamber that reproduces the main features of the hybrid engine configuration, i.e., a grazing flow of oxidant over a solid fuel surface. This is conventionally achieved by placing a slab of solid fuel on one side of the combustion chamber while providing optical access

through the other walls. Over the years, multiple slab burners have been designed, covering a large range of oxidizer mass fluxes, G_{ox}. The advantages of such experimental apparatus over an engine configuration are mainly related to the improved optical access that they provide. Using lateral windows, one may track the real-time regression rate [13, 106], Kelvin-Helmholtz (K-H) liquid layer instabilities [11, 96, 98], soot production [127], fuel droplet entrainment [12, 110, 111] and flame propagation phenomena by filming the combustion with high-speed cameras. The use of slab burners is also motivated by the need to obtain experimental data sets to validate numerical models. However, they are limited to lower oxidizer mass fluxes compared to hybrid engines. Spatially and temporally-resolved regression rate measurement are also often not provided due to the difficulty of obtaining clear images with high temporal resolution and of developing image analysis software capable of monitoring the fuel consumption.

Chandler et al. and Jens et al. [7, 85, 100–104] from Stanford University also developed a slab burner to visualize the entrainment effect, i.e., the formation droplets in the melt layer the breaking of K-H instabilities, from paraffin-based fuel burning with gaseous oxygen (GOx). In their case, the regression rate is measured either by using an empirical power law ($\dot{r} = aG_{ox}^{n}$, where $\dot{r}$ is the regression rate, G_{ox} is the oxidizer mass flux and a and n are empirical constants), by measuring the mass difference over the test duration or by comparing the height difference of the fuel before and after the test. Researchers from the German Aerospace Center (DLR) [11, 90–96, 98] also developed a slab burner in which they studied K-H instabilities of the liquefying layer on top of hybrid fuels, and linked the wavelengths and excited frequencies to the regression rate of the fuel. Their slab burner has also been used for the characterization of different propellant formulations. Their regression rate measurements are space and time-averaged and are obtained by weighing the fuel before and after the tests. Knowing the surface area, the regression rate values are computed.

Researchers at Tokai University [25, 26, 87] and Korea Aerospace University [23, 24] each designed a similar test bench. They operated it at atmospheric pressure and investigated the addition of EVA (Tokai University) and LDPE (Korea Aerospace University) on the regression rate of paraffin wax. In this experiment, the regression rate is obtained by measuring the time between two vertical lines set 5 mm apart from the fuel surface. This makes the measurement time-averaged at a single point along the length of the fuel. Liu and colleagues [12,110,111] investigated the influence of hydroxyl-terminated polybutadiene (HTPB) on droplet entrainment in the combustion of paraffin wax using a slab burner. The results indicated that the melted liquid layer promotes K-H instabilities. The addition of HTPB to the fuel reduced the production of droplets due to a carbonized layer forming on the fuel surface. Moreover, they observed a periodic oscillation of the diffusion flame that they

suggested originates from K-H instabilities.

More recently, a research team from University of Calgary [13, 106, 107] developed a slab burner operated at atmospheric pressure using GOx and paraffin wax. In addition to high-speed cameras, they implemented flame spectrometry analysis. By doping regions of fuels at different depths with magnesium oxide, MgO-specific light emission is acquired by the spectrometer in the exhaust plume. Thus, the regression rate obtained by spectrometry is compared to the optically measured regression rate. Additionally, they were able to spatially and temporally measure the regression rate, using a combination of backlit saturated images and an image processing algorithm to monitor the top edge of the fuel, resulting in a direct, and spatially resolved, measurement of the regression rate. Finally, Glaser et al. [112] used a slab burner to complement the results of a lab-scale hybrid rocket motor that tested the effect of a stepped fuel grain on the regression rate of hybrid fuels. They found that a stepped fuel increases the turbulence and mixing, thus increasing the regression rate. To analyze the images captured by a high-speed camera, they used a moving average of multiple 100 images. They found that the intensity of the image at a given location was correlated to the local regression rate of the fuel.

Overall, almost all slab burners are using GOx as the oxidizer and various liquefying and non-liquefying hydrocarbons and polymers as the fuel. Side windows, and sometimes a top window, allow for the visualization of the flow using high-speed cameras. However, for most experiments found in the literature the regression rate is determined by measuring the height of the slab before and after the test or by weighing it, thus obtaining time-averaged values. Very few slab burners implement a time-resolved or spatially-resolved regression rate measurement technique. The focus of this article is to assess the effect of the addition of alpha-olefin on the burning rate of paraffin-based hybrid fuels. For this experiment, a slab burner has been designed at Polytechnique Montréal. The regression rate of paraffin-based fuels is spatially and temporally measured using a newly developed color identification algorithm on images from a high-speed camera. Analysis of the images also revealed interesting information on the combustion dynamics of hybrid fuels, in particular on the so-called blocking effect, which is believed to occur in all hybrid rockets. Finally, a theoretical performance analysis of such fuel blends is also reported, completing the evaluation of alpha-olefin as a potential additive for tailoring the regression rate of paraffin fuels.

5.3 Methodology

5.3.1 Experiment Setup

The slab burner is designed to provide direct optical access to the burning samples, thus allowing analysis of the flame and burning rate. It is mainly inspired by the work of Chandler et al. [7, 100] in the early 2010s, at Stanford University. Our implementation is intended to be used with hybrid rocket fuels such as paraffin wax, HDPE or LDPE and gaseous oxygen as the oxidizer. The burner is made of 304L stainless steel to prevent oxidation. The slab burner consists of three parts: an injection system that also contains a flow straightener, a combustion chamber with windows that allows for combustion visualization and a nozzle to adjust the combustion pressure. A picture and a detailed section view is shown in Figs. 5.1 and 5.2. The combustion chamber features three windows, two on the sides and one on the top, to enable the visualization of the fuel combustion along two orthogonal axes.

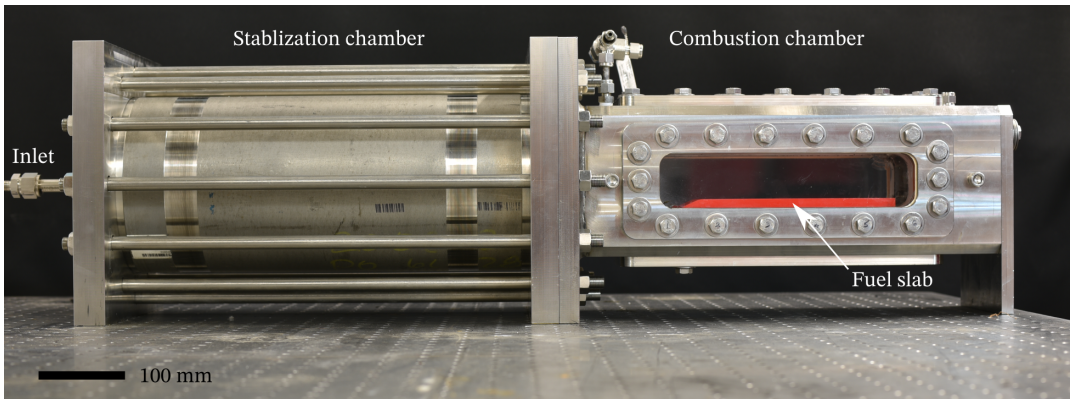

Figure 5.1 The slab burner developed at Polytechnique Montréal.

5.3.2 Injection chamber

The injection chamber is based on low-velocity wind tunnel design rules and ensures a repeatable and uniform inlet flow to the combustion chamber. The first section consists of a diffuser with an angle of 10.0 degrees and an area ratio of 4.0 as suggested by Mehta et al. [122, 124]. This allows the flow to expand before entering the next straight section, featuring a honeycomb to inhibit radial turbulent vortices. The last section is made up of a low-angle convergent section that also serves to transition from a circular inlet to a square combustion chamber cross-section. The angle is 10.0 degrees and the area ratio is 3.3.

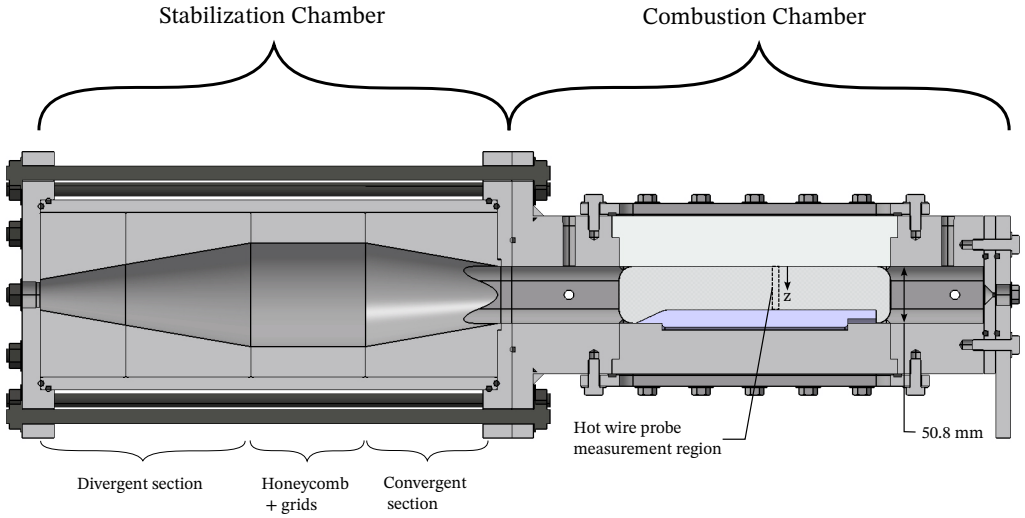

Figure 5.2 Detailed section view of the slab burner.

5.3.3 Combustion chamber

The combustion chamber features a square 50.8 x 50.8 mm cross-section and a length of 419.1 mm. Three windows of a thickness of 46.2 mm and a length of 253.7 mm are placed on the sides and on the top of the chamber to provide optical access. Quartz is used as the window material for its ability to let near UV wavelengths pass through and for its compatibility to withstand high-temperature gradients and harsh oxidative environments. The chamber is designed to withstand an internal pressure of up to 2.41 MPa, but the results shown here were all gathered at near atmospheric pressure. The fuel slab is placed in the center of the combustion chamber, on the bottom. The geometry of the fuel can be modified according to the type of experiments performed. However, in the framework of this research, a fuel slab geometry of 213.4 mm in length and 12.0 mm in thickness with a forward-facing ramp of 25 degrees is used. The design of the windows and the width of the fuel slab prevent lateral burning of the fuel and reduce the complexity of the image processing.

5.3.4 Flow field characterization

To verify that the flow is well stabilized and repeatable, measurements inside the combustion chamber are performed using hot wire anemometry. The probe is placed at various positions on top of an inert fuel slab to capture the velocity and turbulence intensity of the oxidizer stream. The hot wire probe is put into the combustion chamber at the same streamwise positions where videos are recorded and its height is varied along the z axis with increments of 0.4 mm, as shown on Fig. 5.2.

The hot wire anemometry system is calibrated in a wind tunnel with air as the fluid. Results are compared based on G_{ox} to ensure coherence with experiments using gaseous oxygen. The probe is a tungsten filament of 5 µm diameter mounted on straight prongs (Probe #55P11, Dantec Dynamics, Denmark), connected to a control box (Multichannel CTA #54N80, Dantec Dynamics, Denmark) that ensures that the temperature of the sensor is kept constant throughout the tests. The signal is then acquired at a frequency of 10 kHz on a 24-bit analog card (NI PXI-4495, National Instruments, United States) connected to a data acquisition system (NI PXI-1042, National Instruments, United-Sates) monitored using a LabVIEW program.

The velocity profile inside the combustion chamber is measured with and without the use of a fuel blank slab to assess the influence of the fuel geometry on the flow field inside the chamber. The results of the hot wire anemometry test campaign are shown in Fig. 5.3 a), with the turbulence intensity in Fig. 5.3 b). The addition of a blank fuel in the chamber increases the velocity measured since it reduces the cross-section area through which the fluid passes through. However, in both scenarios, the velocity profile remains symmetrical. For a given mass flow, the turbulence intensity remains relatively constant as a function of height above the slab, meaning that there is no drastic change in flow conditions close to the surface of the fuel. The range of measured turbulence intensity is between 15 to 25%.

With regard to the results presented, it has been shown that the stabilization chamber provides a repeatable oxidizer inflow to the combustion chamber of the slab burner. However, it is worth noting that during the measurement at $G_{ox_2} = 4.30 kg/m^2 s$ using the blank fuel, the turbulence intensity near the surface increased from 20% to 25%. This effect may be due to boundary layer detachment or to the limitations of the hot wire used here. A drawback of this technique is the inability to measure zero velocity at the wall, since the probe cannot be placed in contact with it. In addition, the probe itself can disturb the flow and generate velocity fluctuations that result in higher turbulence intensity values. Moreover, as the probe approaches the wall, the effect of the natural convection on the wire increases as the velocity of the flow decreases.

5.3.5 Test procedure

Prior to each test, a fuel slab is prepared by first melting paraffin wax (FR5560, Candlewic, United States) in an oven, and by slowly pouring it in a silicon mold. The slab is then inspected to ensure that no bubbles are trapped as the fuel cooled. In the case of mixtures of paraffin wax and alpha-olefin (Vybar 103, Baker Hughes, United States), the two components are first weighed according to the mixture ratio before melting them together while stirring.

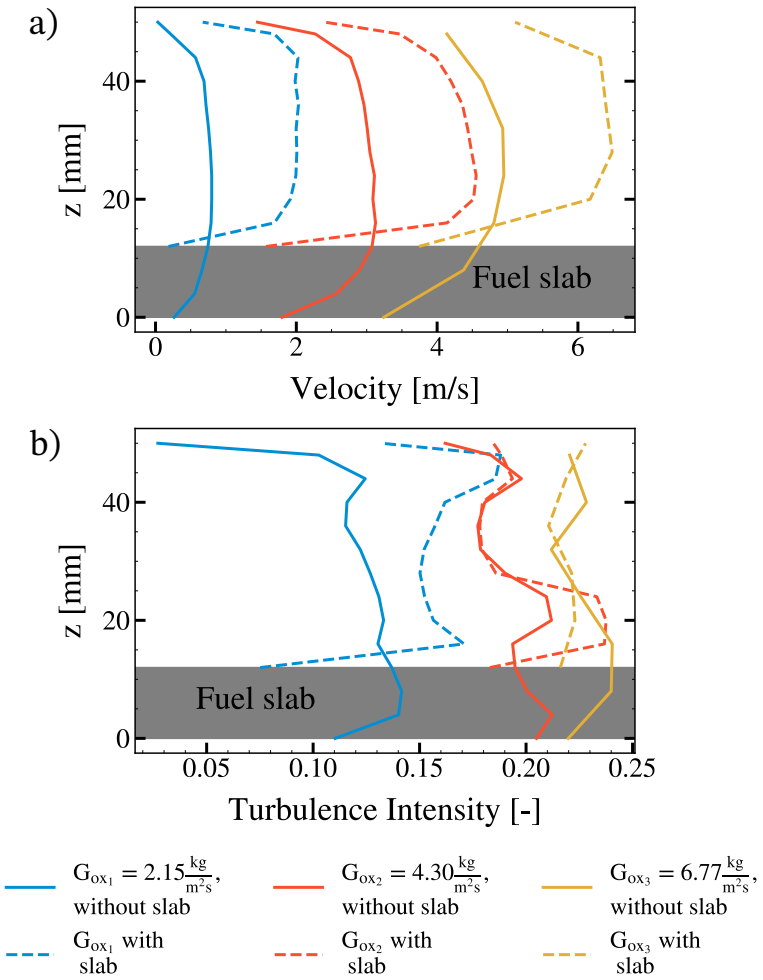

Figure 5.3 Velocity and turbulence profiles inside the slab burner. The dark area indicates where the height of the fuel slab.

The fuel slab is weighed before each test.

The ignition system consists of an acetone-soaked cotton ball placed on the front end of the fuel grain. An electric igniter, which produces a low current but high voltage arc, is placed on the cotton ball. When turned on, the arc ignites the cotton ball in a few milliseconds. The flame then propagates to the end of the fuel slab. After the igniter is inserted and armed, the oxygen and nitrogen gas cylinders are opened. The test operators exit the test room and the rest of the procedure is operated from an adjacent control room. The data acquisition system and the test control software are programmed using LabVIEW based on a state machine design architecture. The LabVIEW program controls the opening and closing of the valves, acquires the data, triggers the igniter and the camera and automatically shuts down the test following the duration entered by the operator. The piping & instrumentation diagram (P&ID) of the slab burner is shown in Fig. 5.4 while the test and firing sequence is

shown in Fig. 5.5. The oxidizer flow is accurately measured using a Coriolis mass flow meter (mini CORI-FLOW^{TM} M15, Bronkhorst, The Netherlands).

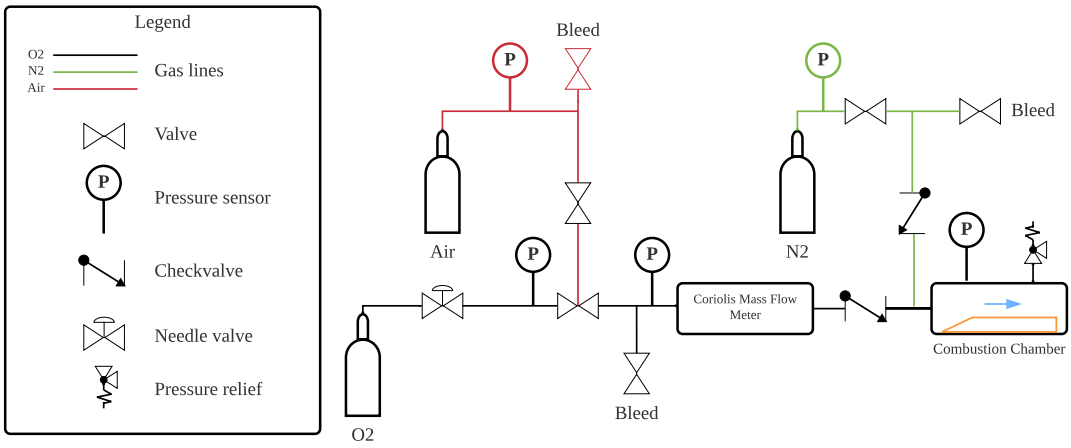

Figure 5.4 Piping & instrumentation diagram of the slab burner.

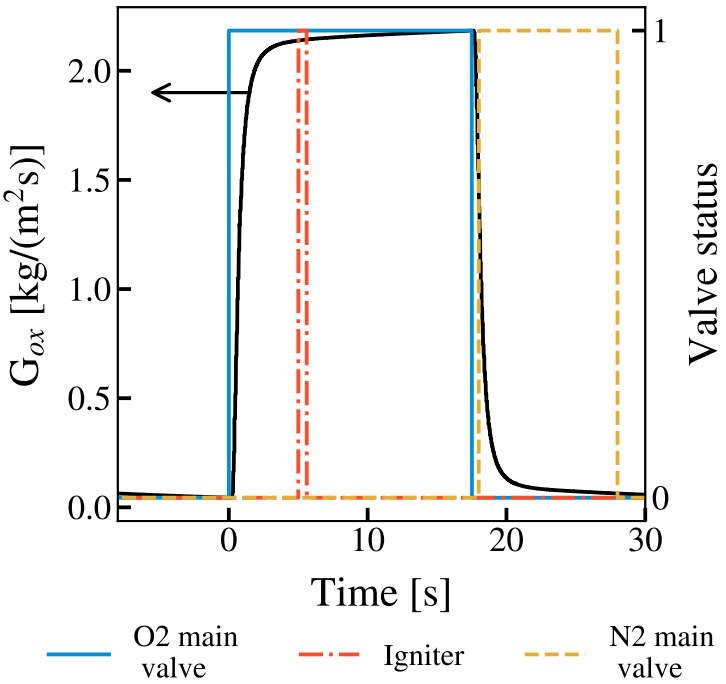

Figure 5.5 Sequence of operations during a typical slab burner test with a burn time of 12.75 seconds.

First, the main oxygen valve is opened for 5 seconds before the igniter is triggered. Initial tests have shown that injecting oxygen before firing the igniter increases the reliability of ignition to a 100% success rate. Then, both the igniter and the camera are triggered. The

duration of the test is typically 10 seconds due to the onboard memory limitations of the high-speed camera. Finally, the main oxygen valve is closed and the nitrogen purge is opened for at least 10 seconds. After each test, the remaining fuel slab is weighed to measure the amount of paraffin burned. The chamber is then cleaned and the procedure is repeated. Considering all the steps, a maximum of 3 tests per day is considered reasonable.

5.3.6 Image acquisition

The combustion tests are filmed using a high-speed camera (Fastcam Mini AX200, Photron, Japan) operating at 5,000 frames per second (fps) with a 105 mm Sigma lens, set to an F-number of 1.4 and an exposure time of 1/20,000 s. Due to the high F-number and the low exposure time, a powerful light source is required to obtain adequate illumination of the paraffin slab. A high-intensity LED light source (Varsa, Nila, United States) is placed beside the camera, oriented toward the side of the fuel slab. The use of side illumination provides high contrast between the dark background, the white paraffin slab and the blue and orange flames. Some tests were also performed using an ombroscopy technique with back illumination, but this approach was found to dim the flame structure captured by the camera. Therefore, all results presented in this paper are obtained using the first light source arrangement described here.

5.4 Image processing algorithm

An edge detection algorithm is implemented to measure the regression rate of the fuel burning. The technique used here is based on the color identification of the fuel slab. As the test progresses and the fuel burns, the edge of the identified fuel slab is extracted, and its thickness is determined. The difference in thickness between two consecutive frames is then linked to the regression rate by knowing the time interval between those frames. The following sections explain each step of the process.

5.4.1 Moving average

First, a moving average of 50 frames is computed on the entire video sequence to accentuate the edge of the paraffin, with an example shown in Fig. 5.6 b). The 50 frames are averaged pixel by pixel to create an image similar to one taken with a camera using a longer shutter speed. During this pre-processing step, the discrete details of the flame structure are lost, but the overall flame thickness, flame height, and top surface of the fuel are clearly revealed, allowing for easier image processing. This process is repeated for N-50 frames, where N is

the number of frames acquired during the test.

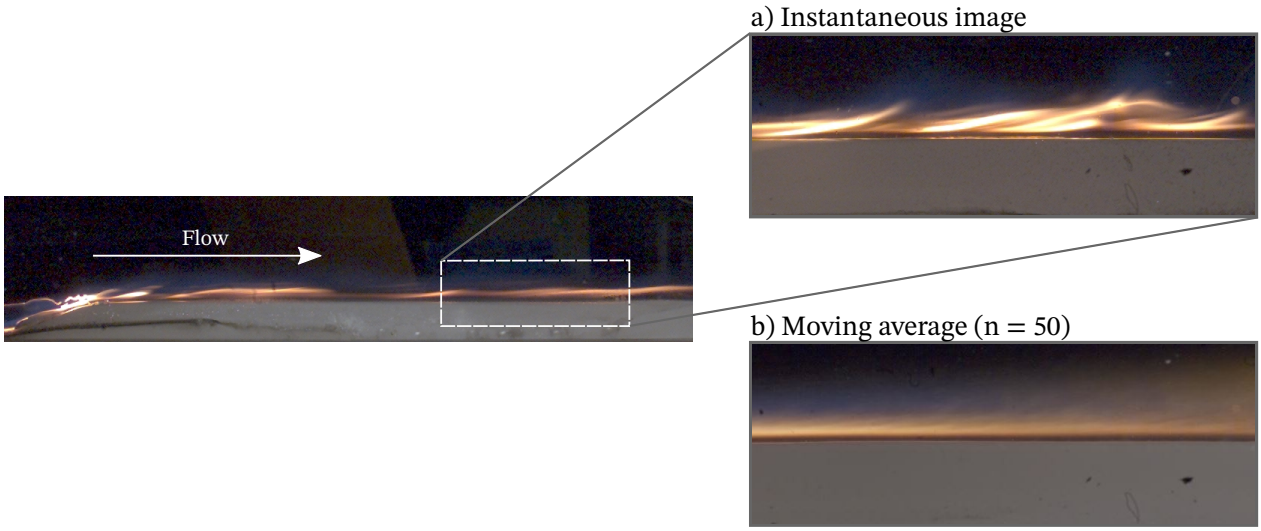

Figure 5.6 Snapshots of video during a slab burner experiment. a) Example of an instantaneous image of a zoomed portion. b) Example of a moving average of 50 frames. Supplemental videos available on the online version.

5.4.2 Masking

For each selected averaged frame, a region of interest mask is defined that includes only the initial fuel slab for color reference. The colors in this mask are stored and compared to other features in the image using the formulas presented in the next section. As presented in Section 5.5.1, the algorithm is quite robust in identifying the color of the fuel due to its uniformity along the length of the slab.

5.4.3 Color identification

The edge detection algorithm mainly relies on color identification. The paraffin used has a white color very different compared to the black background and the orange flame. This makes it possible to search for all the features in the image that are approximately the same color as the paraffin and classify them as corresponding to the fuel.

To perform color segmentation and detection techniques, the CIELAB, or $L^*a^*b^*$, color space is better suited than alternatives, such as the typical RGB (red, green, and blue). The CIELAB space was created in 1976 by the *Commission internationale de l'éclairage* (CIE), the international authority on light and color, to provide a perceptually uniform color space

for the typical human eye. It is often used for color tolerance in the manufacturing and printing industries [128].

Similar to the RGB space, the CIELAB is a three-dimensional color space that covers the range of colors perceived by the human eye. Its first parameter, L^*, defines black and white shades, while the parameters a^* and b^* define green to red and blue to yellow colors, respectively. A unique color is thus a combination of the three parameters. Due to the uniformity of the CIELAB color space, it is possible to compute the difference between two colors, ΔE, by taking the Euclidean distance between two color coordinates:

$$\Delta E = \sqrt{(L_1^* - L_2^*)^2 + (a_1^* - a_2^*)^2 + (b_1^* - b_2^*)^2} \tag{5.1}$$

where L_1^*, a_1^* and b_1^* are the coordinates of the first color in the CIELAB space and L_2^*, a_2^* and b_2^* are the coordinates of the second color in the same color space. This formula is also known as the CIE76 color difference formula [128].

The averaged RGB images are first transformed in the CIELAB space in terms of the parameters L^*, a^* and b^* as shown in Fig. 5.7. The average parameters of the slab colors within the mask are then computed; L^*_{mean}, a^*_{mean} and b^*_{mean}. Using Eq. 5.1, the color of each pixel in the image is compared against the average color in the mask. An image where each pixel of the picture contains a value of ΔE is thus created, as shown in Fig. 5.8, where the dark regions represent the areas in which ΔE is close to zero. In other words, where the color is in better agreement with the color of the fuel slab. The entirety of the fuel slab presents ΔE values close to zero. However, other regions of the flame also match the fuel colors and need to be filtered out in subsequent steps.

Finally, to select only the regions of the frame containing the same colors as the fuel, a tolerance on ΔE is introduced:

$$tolerance = \overline{\Delta E}_{masked} + 2\sigma \tag{5.2}$$

where $\overline{\Delta E}_{masked}$ is the average value of ΔE within the mask and σ is the standard deviation of ΔE also within the mask. This allows the background of the frame and most of the flame to be filtered out while accounting for the variability of fuel colors. The initial illumination provided by the light source appears to vary along the length of the fuel slab, which is also accounted for by adding σ in the tolerance equation. Additionally, as the flame develops during the test, the color of the fuel shifts from bright white toward orange and red due to the translucency of the fuel. This phenomenon is also accounted for by updating the value

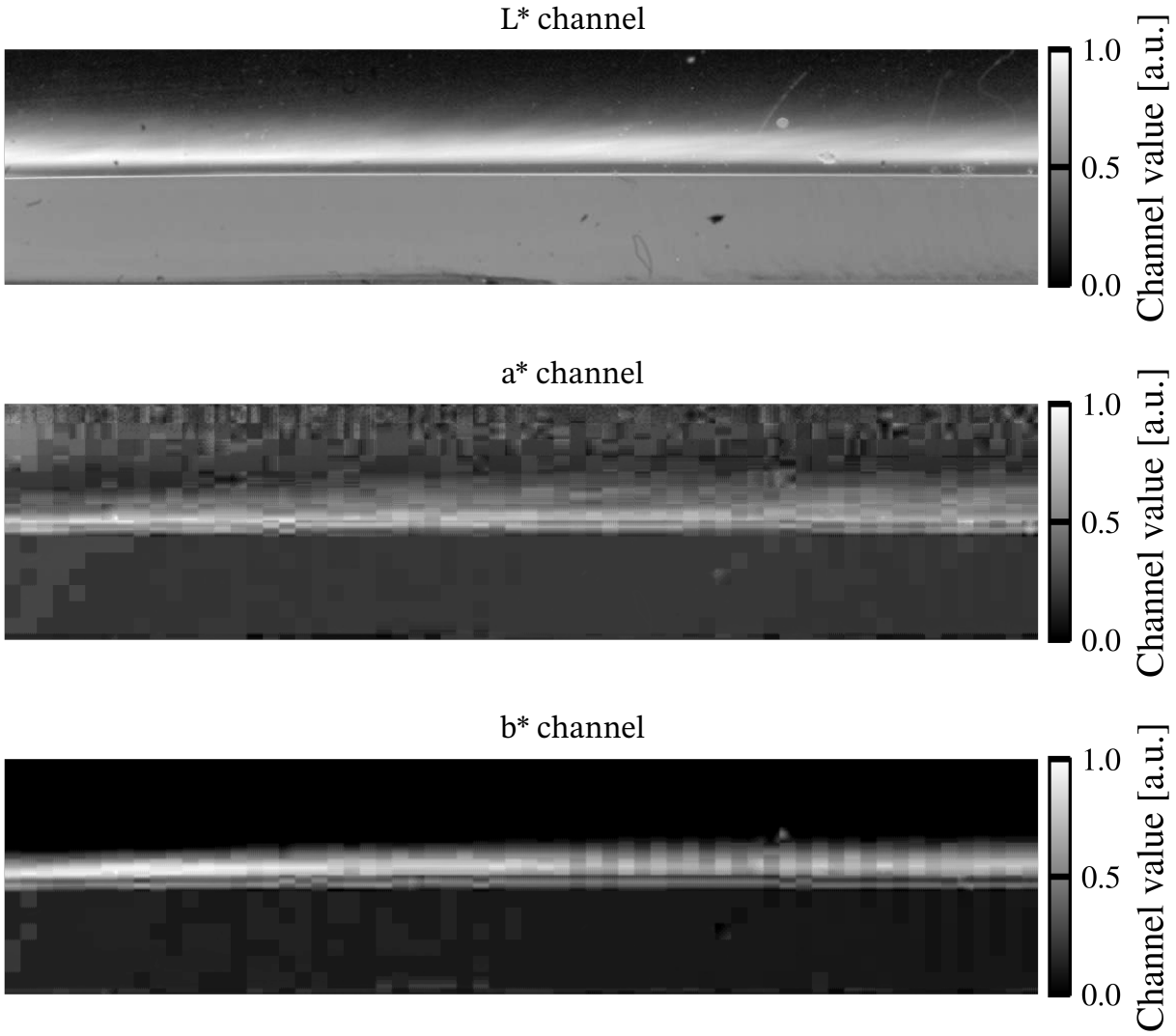

Figure 5.7 Example of the L^*, a^* and b^* component of the image.

of $\overline{\Delta E}_{masked}$ as the test progresses.

Fig. 5.9 shows an example of the histogram values of ΔE for a given frame. On the left side of the tolerance line is the signal corresponding to the fuel color and on the right side, is the signal that is filtered out. The red line corresponds to the region of the image within the initial mask, while the blue signal corresponds to the entire image. Most of the pixels within the mask are identified as having the same color as the fuel. However, a small portion of the region within the mask appears outside of the tolerance line and is filtered out. This portion of the signal generally consists of the top edge of the fuel slab which is usually included when the user roughly draws the initial mask, and of the black soot that may appear on the side of the slab.

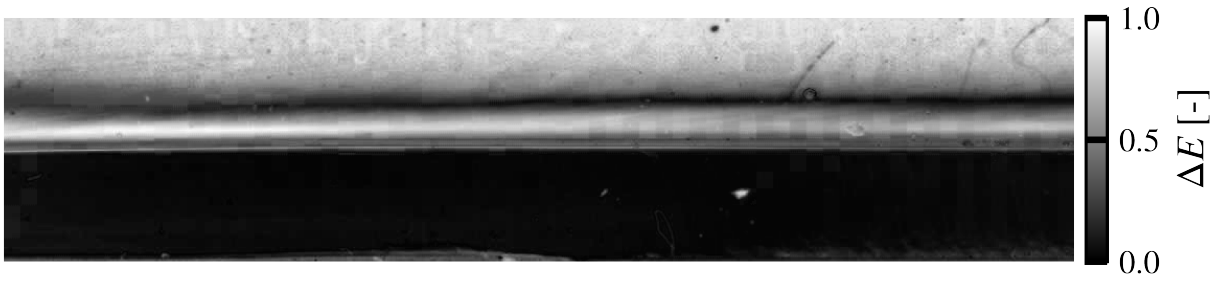

Figure 5.8 ΔE color correlation scale with the color inside the mask (fuel slab color). Darker values indicate a better agreement with the color in the mask.

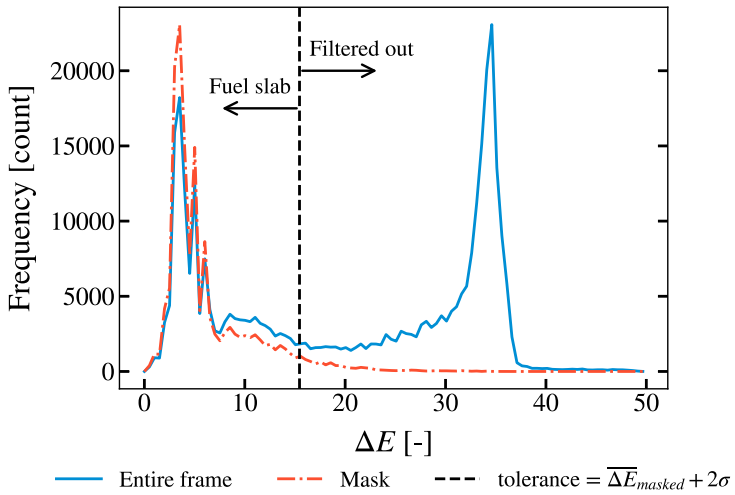

Figure 5.9 Example of a histogram of the ΔE value over the entire image shown in Fig. 5.8.

5.4.4 Edge extraction

The regions identified where the color is within tolerance are used to create another binary mask, namely the matching color mask, as opposed to the initial mask used for color reference. Since regions of the flame colors are close to the color of the fuel slab, the matching color mask initially contains areas of the flame that need to be filtered out, as shown in Fig. 5.10 a). Connected components in the binary mask are identified and those with less than 10,000 pixels are removed, leaving only the fuel slab (Fig. 5.10 b). Finally, the top surface of the fuel is retrieved by using a Sobel edge detection algorithm (Fig. 5.10 c). This whole process is repeated for the entire duration if the burn to track the location of the paraffin surface over time.

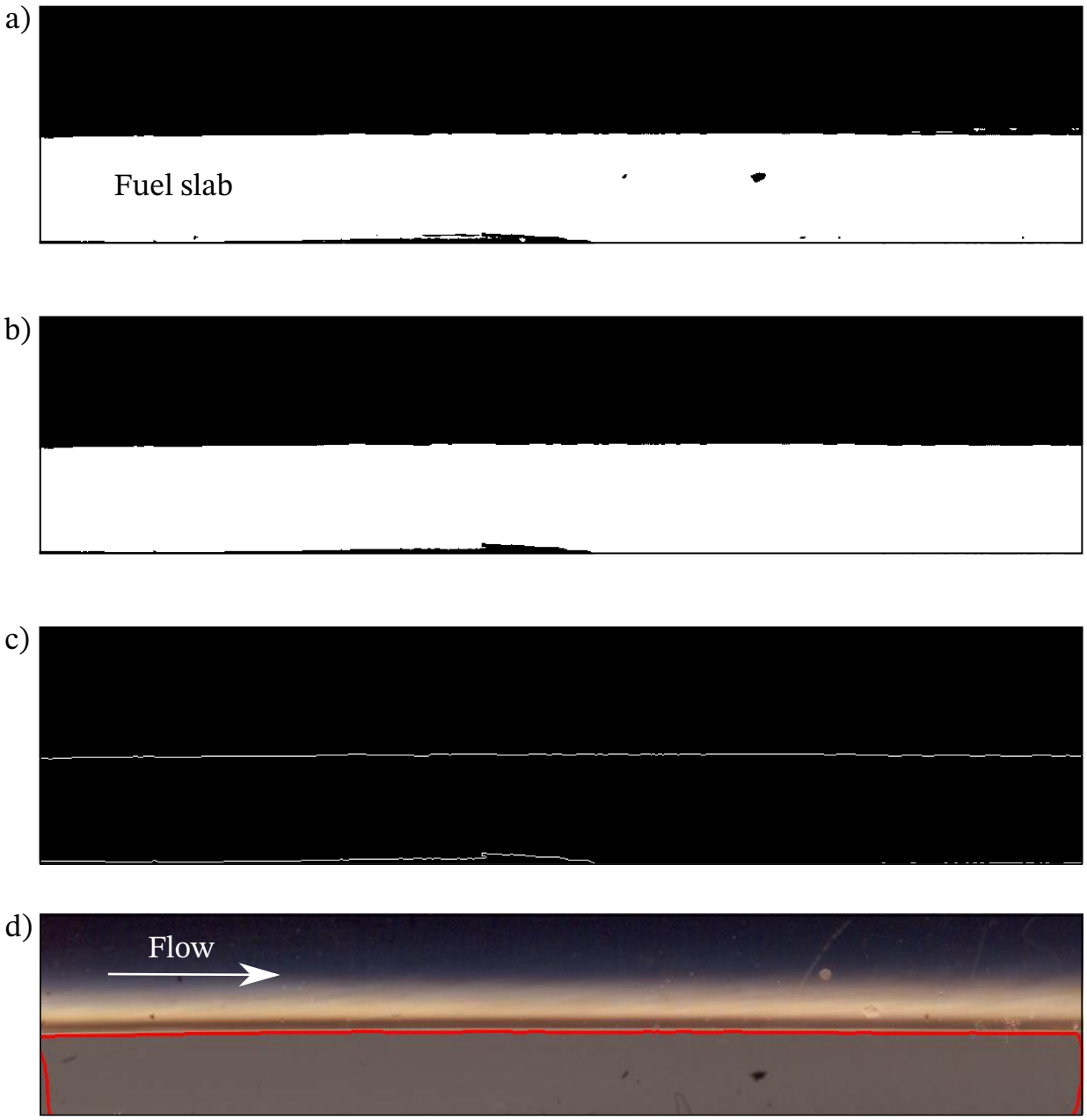

Figure 5.10 Image processing steps. a) White regions represent the pixels within the *tolerance* color value of the fuel slab. b) Smaller regions with less than 10,000 pixels are filtered. c) Extracted edge of the geometry in b). d) Overlay of the analyzed image and the extracted edge in red.

5.5 Results and Discussion

5.5.1 Edge tracking

All tests performed in the slab burner are analyzed using the edge detection algorithm. An example of a sequence of processing steps is shown in Fig. 5.11. The color shift of the fuel slab from the bright white in the first frame to the darker colors in subsequent ones does not affect the ability of the algorithm to distinguish the slab from the other objects in the image. This color shift occurred in the majority of the tests and is mainly due to soot trapped in the small gap of less than 1 mm between the side of the fuel slab and the windows. The darkening of the slab was more noticeable with alpha-olefin present in the fuel. The major limitation of the fuel edge tracking algorithm is when fuel droplets splash on the windows and block the camera's field of view. Depending on the size and color of the fuel deposited on the windows, either discontinuities appear in the identified fuel edge or the obstructions are not recognized as part of the slab, resulting in a temporary important decrease in the height of the fuel. Additionally, the tests performed at lower oxidizer mass flow, $\dot{m}_{ox} \approx 7$ g/s, produced more soot on the sides of the channel. This may be explained by the longer residence time for the fuel droplets in the slab burner due to the lower velocity and by the richer flame conditions.

To overcome these obstacles and to remain as consistent as possible in the analysis between each test, the videos are analyzed until artifacts appear in the edge tracking. For the majority of the tests, a run length of 5 seconds is analyzed before such artifacts appear.

5.5.2 Regression rate

The influence of alpha-olefin (*Vybar*) in a paraffin-based hybrid fuel on the regression rate has been investigated and is reported here. Multiple tests (14 tests for neat paraffin and 10 tests for 20 wt.% alpha-olefin and 80 wt.% paraffin mixture) have been performed over a range of mass flows, from 7 to 17 g/s of O_2, corresponding to an oxidizer mass flux range of 2.15 to 6.90 kg/m^{2}s. Using the boundary of the fuel identified by the edge detection algorithm, the relative distance from the top of the frame to the fuel surface is computed at multiple locations along the length of the fuel, as shown in Fig. 5.12. This process is repeated for each moving averaged frame on which the algorithm is applied. The distance is then plotted against time and the slope gives the regression rate. The oxidizer mass flux is determined by the following equation:

$$G_{ox} = \dot{m}_{ox}/A_{cs} \tag{5.3}$$

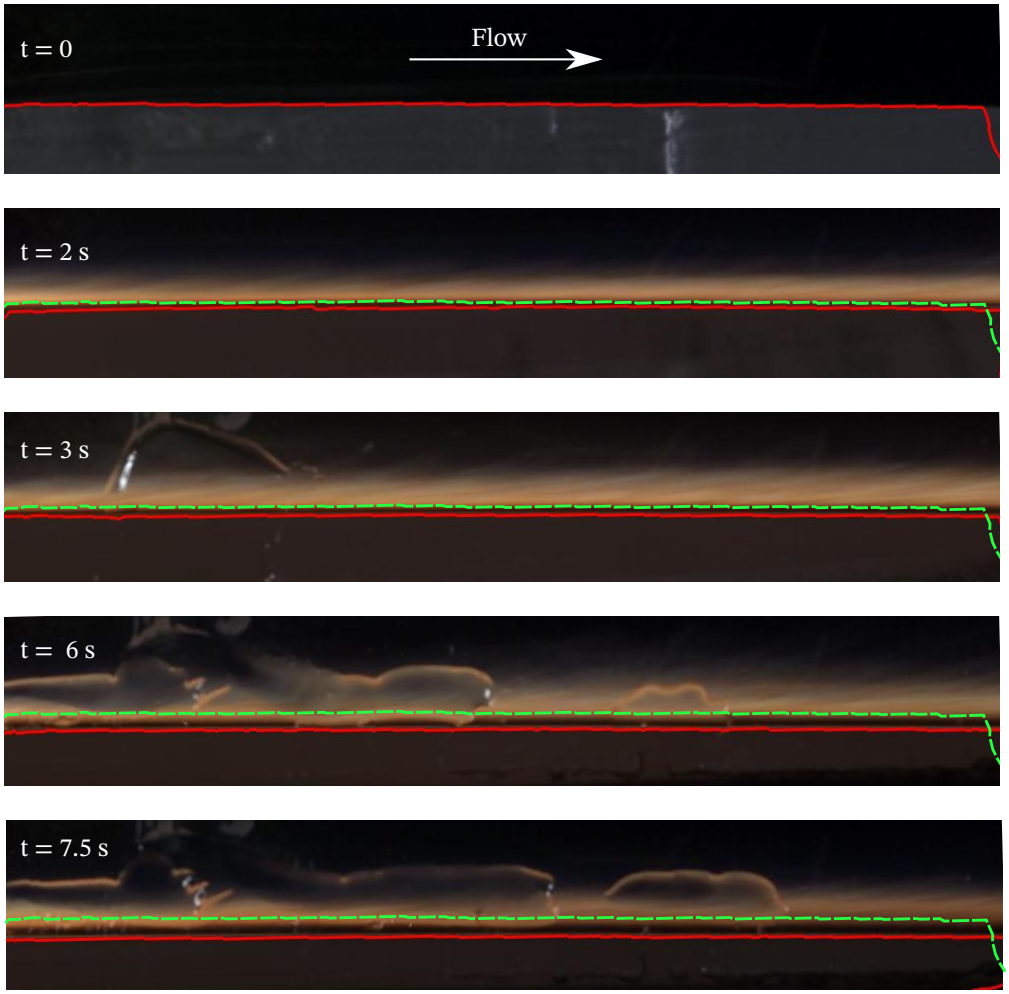

Figure 5.11 Edge tracking sequence of a 100 wt.% paraffin test at G_{ox} = 5.76 kg/m^{2}s. The dashed green line corresponds to the initial edge of the fuel slab.

where A_{cs} is the cross-section area of the combustion chamber without the fuel slab, i.e., 2.581e-3 m^2. The change in the slab height over the duration of the burn is neglected to facilitate comparison between tests. Since the regression values are generally comprised between 0.10 and 0.25 mm/s with a burn time of up to 10 seconds, the difference between the initial and final cross-section area is only on the order of 5%.

Spatially-resolved regression rate

The regression rate is spatially resolved by tracking the boundary at several locations from the leading edge of the fuel slab. Fig. 5.13 shows an example of the distance of the slab height as a function of time for 4 locations. As can be seen from the overlay of the four plots, the combustion follows a similar behavior at these different locations. The fact that the

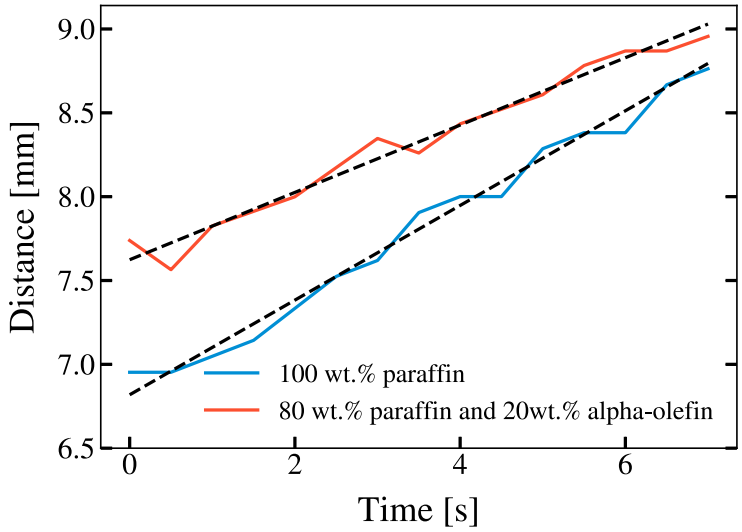

Figure 5.12 Example of the distance from the top of the frame and the edge of the fuel slab for a test of the two fuel mixtures. The dashed lines are the best least-squares fits. The slope of the fit is the regression rate.

regression rate values do not change drastically is also a good indicator that the fuel burning is rather constant or only slightly decreasing as the test progress. Regression rate profiles are also extracted with an example shown in Fig. 5.14. The profiles are further discussed when compared to the light intensity of the flame in Section 5.5.3.

Temporally-resolved regression rate

Due to the low range of oxidizer mass flux tested, the regression rate values are small. A low fuel burn rate does not justify tracking the fuel slab edge at very high frequencies. The results in Fig. 5.13 are taken at 5 Hz and discrete jumps in the signal can be seen. This pixelisation is a result of the limited spatial resolution of the camera and lens. However, this also indicates that regular video cameras could be used to measure the regression rate in slab burners.

To verify the linearity of the regression rate over the whole burn time, the distance versus time signal is derived to obtain an instantaneous regression rate signal as a function of time. First, a second-order interpolation function is fitted through the raw data, as shown in Fig. 5.15 a). A moving average with a window of 2 points is also computed to smooth the data before it is derived for comparison purposes. The interpolated signal is then derived using a second order finite difference approximation. An example of an instantaneous regression rate signal is shown in Fig. 5.15 b) and is compared with the time-averaged regression rate value

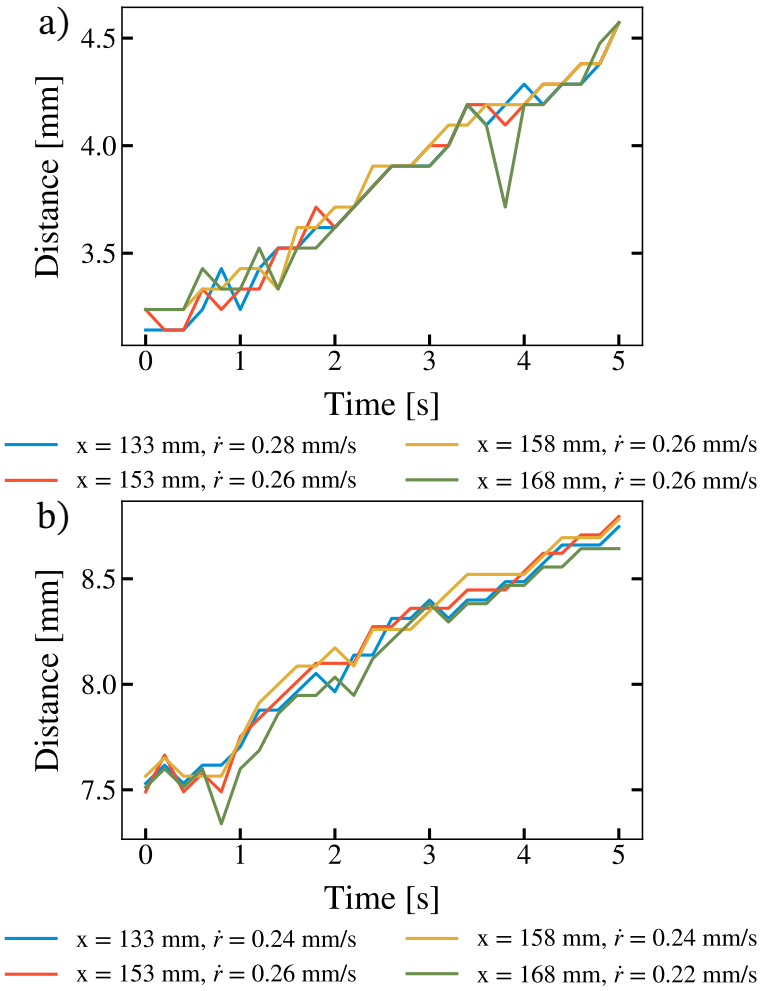

Figure 5.13 Distance to the edge of the fuel slab for locations along the fuel slab length. a) 100 wt.% paraffin FR5560. b) 80 wt.% paraffin FR5560 and 20 wt.% alpha-olefin.

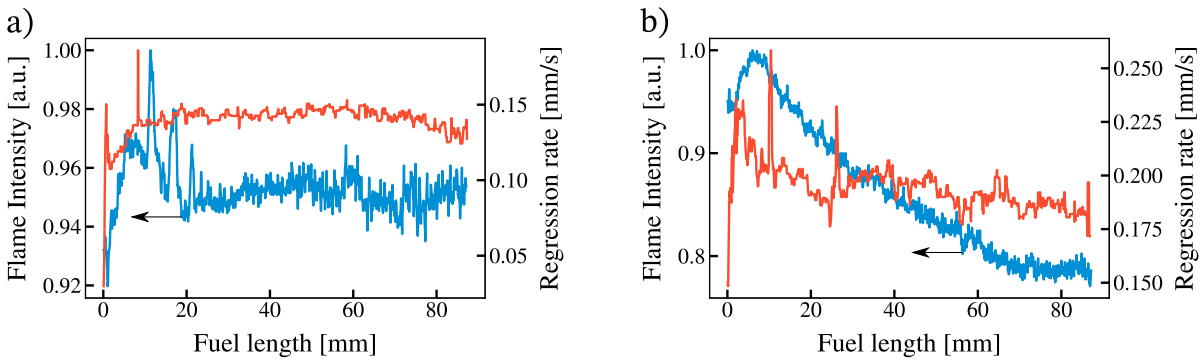

Figure 5.14 Flame and regression rate profiles for two tests. a) An example of a test where the flame intensity and regression rate are constant. b) An example of a test where the flame intensity gradually decreases but the regression rate remains approximately constant.

obtained from a linear fit. In general, the signal oscillates around the time-averaged value. Applying a moving average step to the distance signal allows the instantaneous regression rate signal to be smoothed. However, this smoothed signal still oscillates around the time-averaged $\dot{r}$ value, but its oscillation amplitudes are smaller than the raw interpolated signal. The observed oscillations are mainly due to the scarcity of the original signal and its stepped shape. Figures 5.15 c) and d) show the regression rate at the positions shown in Fig. 5.13. In some cases, such as the example shown in Fig. 5.15 c), the instantaneous value of the regression rate peaks in the first second of a test. This phenomenon is explained by the edge tracking algorithm suddenly "moving" during the ignition phase, where a large ignition kernel moves from the leading edge to downstream of the slab.

The linearity of the regression rate over the burn time is further assessed by looking at the coefficient of determination (R^2) of the linear regression of the data. For the example of the signals in Fig. 5.13, the R^2 values are all above 0.92, with most values around 0.97.

Both methods seem to indicate that the measured regression rate for the tests conducted for this study is approximately constant with time. This effect also suggests that the oxidizer mass flow, G_{ox}, can be considered constant during our slab burner tests, since the regression rate is directly related to the oxidizer mass flux. Finally, the use of linear regression also helps to overcome some of the drawbacks of the edge-tracking algorithm. For example, in one case in Fig. 5.13 a), at $x = 168$ mm, the value drops off abruptly. This behavior generally occurs when a black spot of soot is trapped on the side of the fuel slab. In this case, the edge tracking algorithm fails to follow the surface and is fooled by the sudden color change from white to black. The effect of these numerical artifacts is not significant because the regression rate is taken from the slope of the best-fit linear trend to the distance signal.

Effect of alpha-olefin on the regression rate

The results from the test campaign are presented in Fig. 5.16. For both fuels, a curve fit for a power law in the form of $\dot{r} = aG_{ox}^{n}$ is calculated using the least-square method. The $\dot{r}$ values are taken at 9 different longitudinal positions along the fuel slab and are then averaged. The error bars in Fig. 5.16 represent the standard deviation of these 9 different locations.

The addition of alpha-olefin into the paraffin fuel matrix decreases the measured regression rate due to to the higher viscosity of the resulting melt layer. Elzein et al. [22] reported a viscosity of 6.37 mPa·s for neat paraffin and a viscosity of 17.3 mPa·s for a 20 wt.% alpha-olefin and 80 wt.% paraffin mixture. The increased viscosity of the fuel inhibits the droplet entrainment mechanism responsible for the high-regression rate of liquefying fuels such as paraffin wax. The results presented here show that the addition of 20 wt.% alpha-olefin into

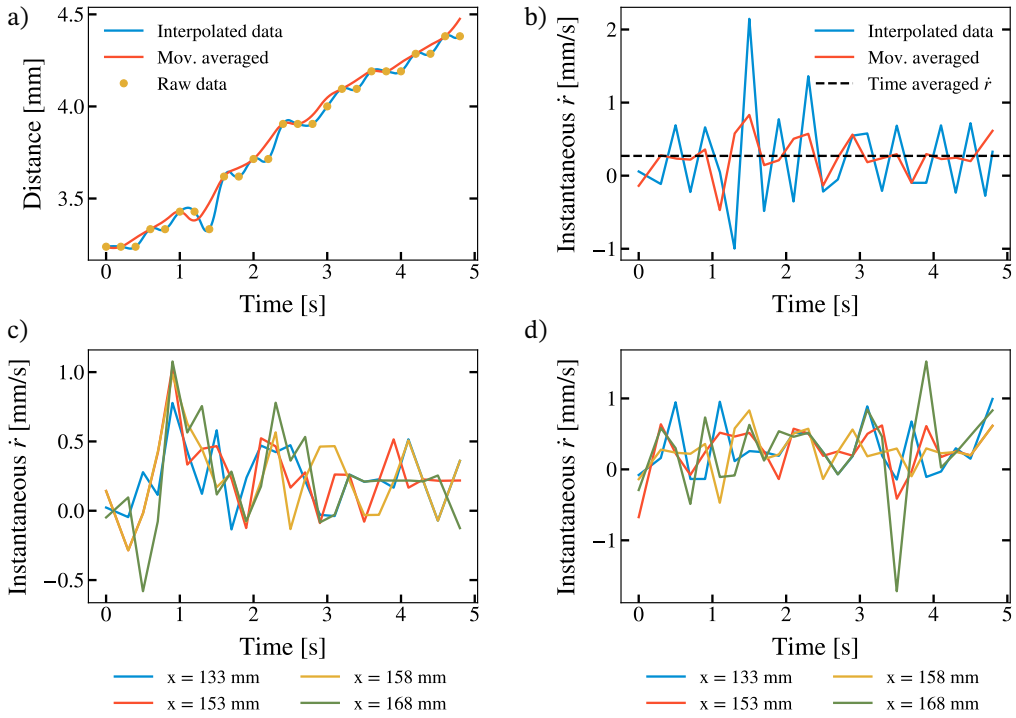

Figure 5.15 a) An example of the distance between the top of the chamber and the fuel as a function of time and its interpolated signal. b) Instantaneous regression rate of the signals shows in a). c) Instantaneous regression rate of the signals in Figure 5.13 a). d) Instantaneous regression rate of the signals in Figure 5.13 b).

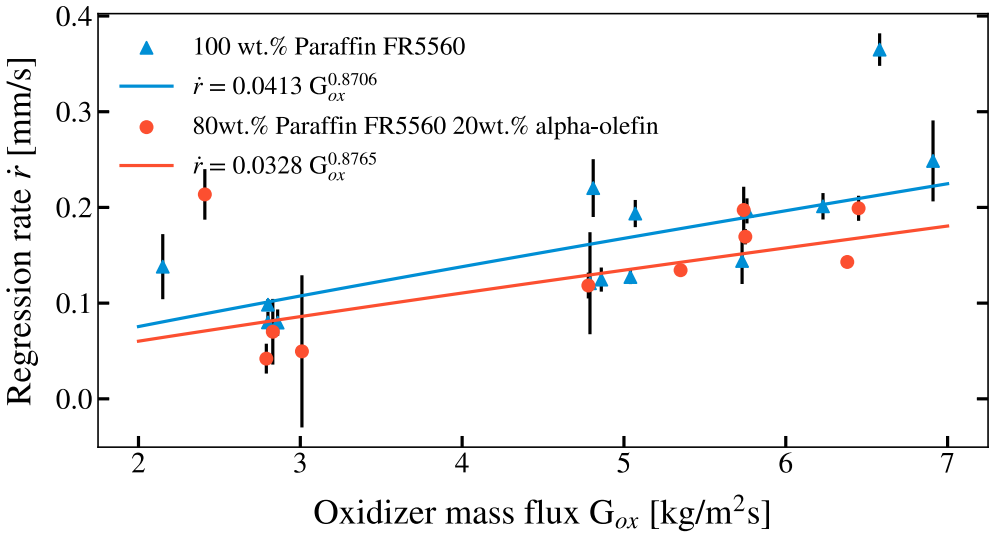

Figure 5.16 Regression rate measured using the of 100 wt.% paraffin FR5560 and 80 wt.% paraffin FR5560 and 20 wt.% alpha-olefin as a function of the oxidizer mass flux. The error bars correspond to the regression rate standard deviation for the 9 positions measured along the length of the fuel slab.

a paraffin fuel matrix reduces the coefficient a by 20.6 % and does not affect the coefficient n in the regression rate correlation.

A small spatial variability is observed in the regression rate measurement in any given test, as demonstrated by the small error bars in Fig. 5.16. However, some tests exhibit an unusually high regression rate behavior, well outside of these error bar ranges. This is notably the case for both tests conducted at the lowest G_{ox}. This high variability is also observed in the results of Petrarolo et al. [11, 98], for experiments conducted in a range of G_{ox} from 2.5 to 22.5 kg/m^{2}s. This observation, made in both experiments, seems to indicate that as the oxidizer mass flux decreases, the variability in the regression rate value increases. It could also suggest that at very low mass fluxes some other parameters overcome the effect of G_{ox} on the regression rate. For instance, in the experiments presented here, at about $G_{ox} = 2$ kg/m^{2}s, the melted paraffin starts to flow back toward the stabilization chamber from the leading edge. The oxidizer velocity is not sufficiently high to push the paraffin downstream against the slope on the leading edge of the slab. This may indicate unexpected combustion behavior at low G_{ox} values, which might not accurately reflect the typical combustion conditions in hybrid engines. This unexpected behavior could occur in nearly stagnant conditions, where the low flow of oxidizer does not dissipate heat by convection. To verify if this variability is also present in engine conditions, tests conducted at very low oxidizer mass fluxes in model engines could be performed and compared with the results presented here. In addition, it is

worth noting that the outlier tests never show a regression rate lower than expected. This points to causes that can increase the regression rate, such as porosity in the fuel plate, increased turbulence in the flow, or an uneven fuel surface.

Nevertheless, the results presented here suggest that alpha-olefin could be a useful additive to reduce the regression rate while increasing the structural integrity of the fuel. To fully evaluate the effect of alpha-olefin addition on regression rate, experiments at higher oxidizer mass flows are required.

5.5.3 Visual assessment of the combustion

Although measuring regression rate may not warrant the use of a high-speed camera, analyzing these videos visually reveals interesting flame behavior. Fig. 5.6 a) illustrates an example of the type of flame observed during the combustion of both fuel mixtures. The flame is made of long filament-like structures entrained by the oxidizer flow. In these filament structures, zones of high combustion activity and low combustion activity are seen with apparent periodicity, which are further analyzed in Section 5.5.4.

The intensity of the flame has been identified to be linked to the regression rate. For example, Jens et al. [103] and Glaser et al. [112] respectively observed a direct correlation between the OH^* intensity and the regression rate of the fuel and the CH^* and visible light intensity with localized regions of higher regression rate using stepped fuel slabs.

To verify this link between both parameters, vertical flame intensity slices of 5 pixels width are extracted from the frames to create an intensity profile along the length of the fuel using the methodology proposed by Glaser et al. [112]. The intensity profile is computed using the following equations:

$$I\left(x\right) = \sum_{t=0}^{t=t_{burn}} \sum_{y=0}^{y=y_{max}} I(x,y,t) \tag{5.4}$$

$$\bar{I}\left(x\right) = \frac{I\left(x\right)}{max\left(I\left(x\right)\right)} \tag{5.5}$$

where I is the grayscale value of the pixel in the frame, on a scale from 0 to 255, t is the time, y is the y-axis of the frame and $\bar{I}$ is the normalized intensity. An example of two intensity profiles along the slab length is shown on Fig. 5.14, revealing that the intensity of the flame is generally higher toward the upstream end of the fuel slab. In the first case, the normalized intensity over the length of the slab remains fairly stable after the initial intensity peaks, while the second case shows a gradually decreasing normalized intensity over the length. Additionally, in the second case, the regression rate decreases from values between 0.200 and 0.225 mm/s in the first 13 mm of the image to values below 0.200 mm/s in the remaining

part of the frame.

In 75% of the tests, the light intensity profiles decrease along the fuel length, while a similar decreasing trend is observed for the regression rate in 66% of the tests. Only 42% of the tests indicate matching decreasing trends for both parameters, and two tests (8% of the data set) have both increasing intensity and regression rate profiles. The remaining 50% of the tests show inverse trends, either decreasing or stable regression rate and increasing light intensity, or vice versa. Additionally, Fig. 5.17 reveals an interesting observation: the light intensity gradually decreases as the test progresses at a specific position over the fuel length. This behavior is opposite to the regression rate value, which was found to be constant over time.

Possible explanations are that a portion of the fuel is expelled without completely burning, explaining decreasing flame intensity compared to increasing or stable regression rate. In addition, the ignition point at the front of the fuel slab results in a lengthier combustion time for the upstream fuel compared to the downstream end. Even if the camera is positioned away from the upstream end, the left side of the image experiences a longer burning time due to the flame propagation from the ignition site to the downstream end. This may ultimately lead to falsely high flame intensity values.

The link between the regression rate and the flame intensity does not always follow the conclusions of the aforementioned studies. The results shown here highlight that one must be careful when attempting to determine the regression rate using the flame intensity signal as a proxy. To obtain this information, direct regression rate measurement techniques, such as the edge detection algorithm presented here, are a more reliable approach than utilizing indirect measurement based on light intensity signals.

Finally, in addition to the filament-like flame structure, several fuel droplets are observed being expelled from the surface and entering the reaction zone. This mass transfer mechanism was theorized by Karabeyoglu et al. [9, 105] and has been observed experimentally in many other slab burner experiments [12, 24, 100, 104, 110, 111]. It is the main cause of the high regression rate of liquefying fuels due to the increased mass transfer into the flame by the breakup of K-H instabilities of the liquid layer forming on top of the fuel slab. In the experiments presented here, bursting events expel the droplets into the reaction zone in large quantities. This observation is consistent for both fuel mixtures. Efforts to automatically locate and track the fuel droplets were not pursued due to the sporadic nature of the bursting events.

5.5.4 Flame oscillations

The filament structure of the flame contains both high and low combustion activity regions moving in a periodic manner as seen on Fig. 5.6 a). To evaluate the periodicity of the oscillations, a method based on a Fast Fourier Transform (FFT) using a Hanning window of the flame intensity signal is used. Four positions along the length of the fuel are selected and four intensity slices are extracted using Eq. 5.4, without summing for the temporal variable t. A signal $I(x,t)$ is thus computed at the four x positions. An example of the signal is shown on Fig. 5.17. Finally, the FFT is computed on each intensity slice as also shown on Fig. 5.17.

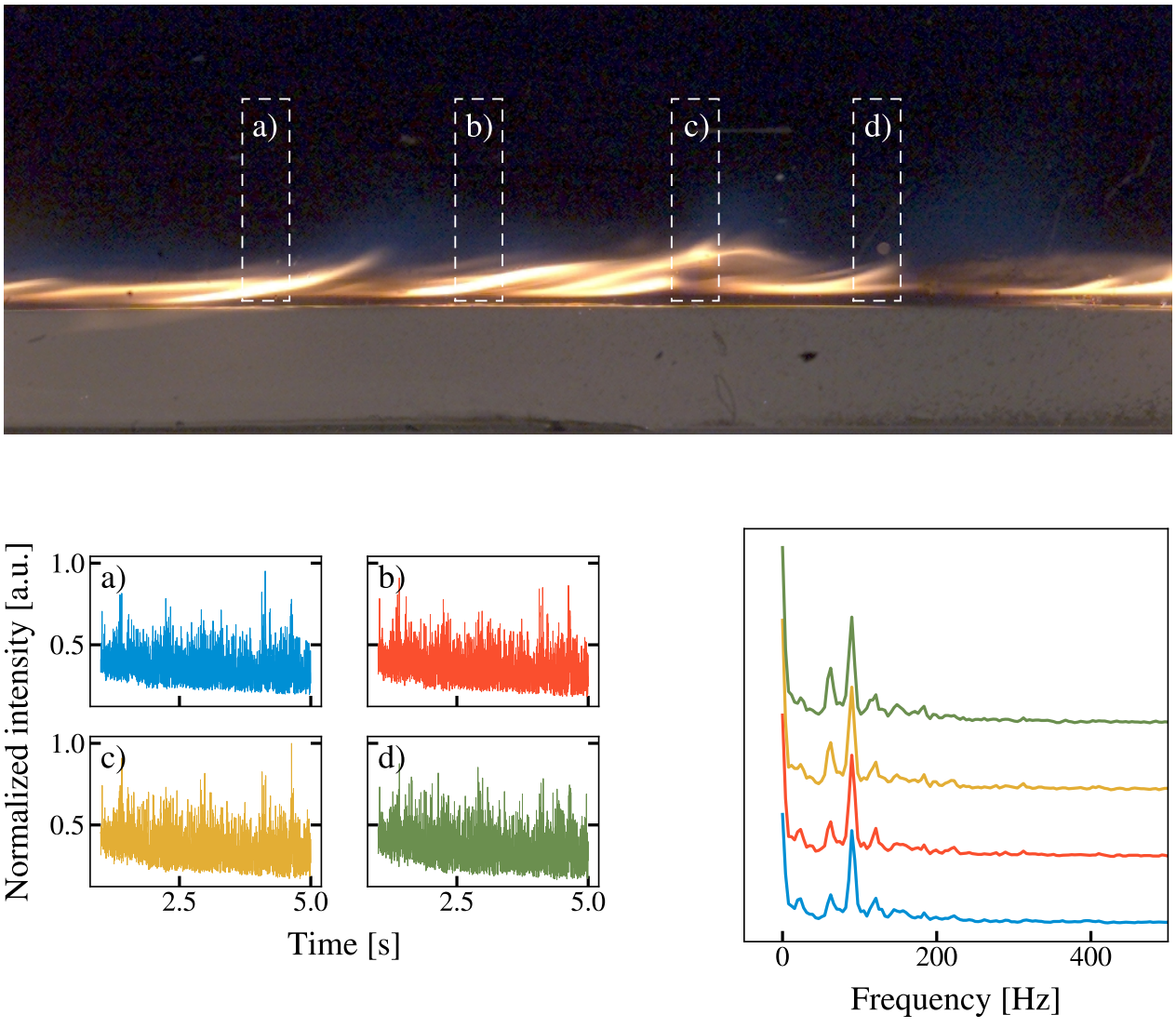

Figure 5.17 Example of an intensity signal obtained at 4 different locations in the flame and the corresponding FFT spectrum.

In general, the FFT spectrum does not change at the different x positions, indicating that the flame intensity fluctuations do not change in nature over the length of the fuel slab. As shown in Fig. 5.17, neglecting the peak around 0 Hz, up to 3 frequencies below 100 Hz are generally excited for all tests performed here. A clear trend can not be observed regarding the scaling of the excited frequency as a function of the oxidizer mass flux or of the regression rate of the fuel. However, it is worth mentioning that for each test, one of the three frequency peaks is closely linked to the primary hybrid oscillation frequency computed with the universal scaling law proposed by Karabeyoglu et al. [15]:

$$f = 0.2341 \left(2 + \frac{1}{O/F}\right) \frac{G_{ox} R T_{av}}{L P_c} \tag{5.6}$$

where f is the primary hybrid oscillation frequency in Hz, $RT_{av} = 6.38\text{e+}5$ $(\text{m/s})^2$ for gaseous oxygen systems, L is the length of the fuel slab in meters and P_c is the combustion pressure in Pa. This empirical scaling law is assumed to be valid for all hybrid systems [15]. This instability is due to multiple complex phenomena, namely, the coupling of thermal heat transfers in the solid fuel and the blocking effect of the heat transfer between the boundary layer and the solid fuel. This instability is usually measured by computing the FFT spectrum of the pressure chamber signal, but it originates from physical phenomena that can be observed visually. Karabeyoglu et al. [15] postulated that the instability could be directly observed in a circular motor as the radial oscillations of the flame in the boundary layer. The slab burner makes it possible to observe this phenomenon and the presence of the primary hybrid oscillation frequency in the spectrum is a possible explanation for the observed behavior. Fig. 5.18 shows the frequency of the excited peak nearest to the primary hybrid oscillation frequency as a function of the G_{ox} for tested conditions. The average error between the frequency estimated using Eq. 5.6 and the nearest peak is 12.1%. It is also worth noting that the frequency obtained using our image processing approach is always lower than the estimated primary hybrid oscillation frequency, which was originally captured through the fluctuation of the pressure measured in the chamber in the study of Karabeyoglu et al. [15]. A possible explanation is the fact that the chamber pressure signal is not spatially resolved and constitutes an integration of all the phenomena in the chamber, whereas the frequency measured here is spatially resolved to a known position in the chamber.

Another explanation that should be considered for the flame oscillations is the turbulence and oxidizer flow velocity. A spectral analysis is therefore also performed on the signals measured using the hot wire anemometry system. For the positions and flow velocities tested, a dual peak generally appears for frequencies much higher than those observed for the fluctuation in combustion intensity, between 500 and 1000 Hz. This hints that the turbulence and flow

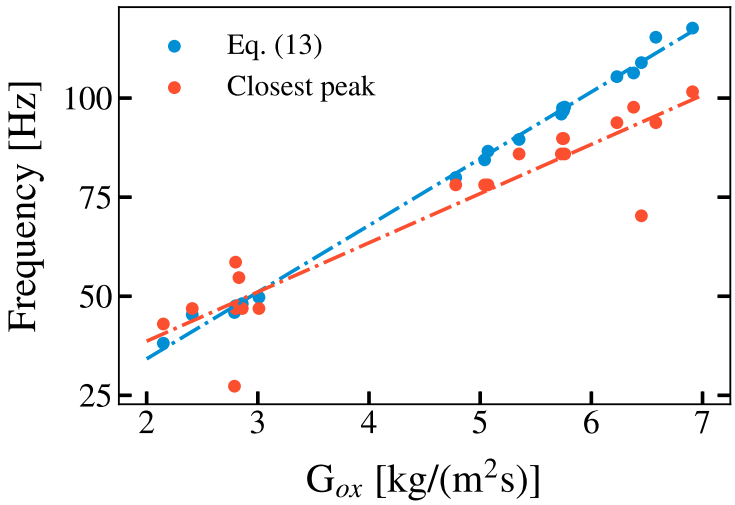

Figure 5.18 Primary hybrid oscillation frequency predicted by Eq. 5.6 compared to the nearest of the three excited frequencies of the intensity signal.

velocity are likely not responsible for the onset of the observed flame oscillations.

5.5.5 Theoretical performance

In addition to reducing the regression rate and allowing its tuning, alpha-olefin can also be used to enhance the performance of hybrid rocket fuels. A theoretical performance analysis is carried out using the NASA Chemical Equilibrium with Applications (CEA) program [129]. This program uses the fuel and oxidizer properties, the combustion chamber pressure as well as the O/F, to compute the specific impulse (I_{sp}). The fuels used in this study are neat paraffin wax, neat alpha-olefin and an 80-20 wt.% paraffin-alpha-olefin mixture. The oxidizer is always GOx. The combustion chamber pressure is set to 2.41 MPa (350 psi) and the O/F is varied from 1.0 to 7.0 with 100 steps. The exhaust gases are perfectly expanded to atmospheric conditions. The paraffin and GOx properties are taken directly from the CEA program, while the alpha-olefin properties are taken from Elzein et al. [22]. The heat of formation of the alpha-olefin is -1494.0 kJ/mol and the chemical formula is $(C_{20}H_{40})_{15}$.

Interestingly, alpha-olefin fuel has a higher I_{sp} than paraffin wax, with a maximum I_{sp} of 275.8s compared to paraffin wax's maximum value of 266.6s. Both fuels have a similar O/F value at their maximum I_{sp}; 2.26 for alpha-olefin and 2.32 for paraffin wax. When alpha-olefin is added to paraffin wax in an 80-20% weight ratio, it slightly improves the performance of pure paraffin, increasing its I_{sp} from 266.6s to 268.4s, without affecting the optimal O/F value. This suggests that alpha-olefin can be used in hybrid motors with paraffin wax and

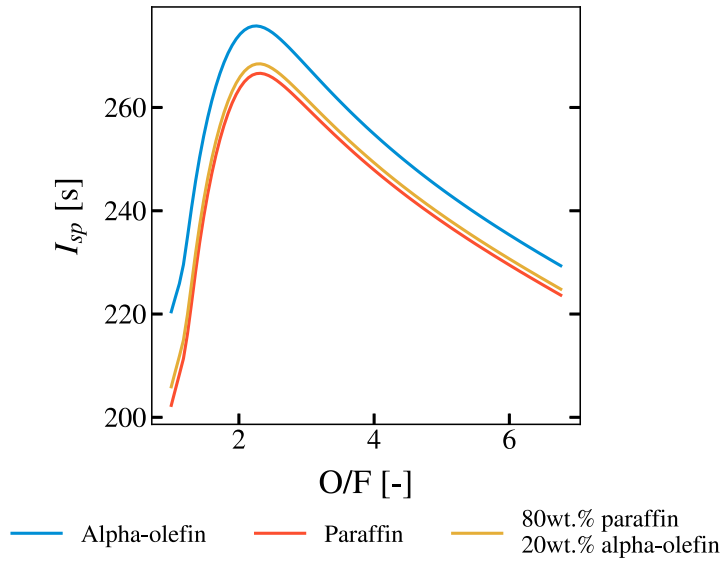

Figure 5.19 Theoretical performance of paraffin wax, alpha-olefin and 80 wt.% paraffin wax 20 wt.% alpha-olefin mixture.

GOx propellants without requiring a complete redesign. Moreover, this finding highlights that alpha-olefin additive, such as *Vybar 103*, is a promising option for reducing the regression rate of paraffin wax while maintaining its performance.

5.6 Conclusions

The results presented here are the first test campaign conducted on the new slab burner developed at Polytechnique Montréal. The design of the slab burner was presented as well as a hot-wire anemometry test campaign characterizing the flow and turbulence inside the combustion chamber. In addition, an algorithm based on color detection in the CIELAB color space was developed to spatially and temporally measure the regression rate of hybrid rocket fuels. Two fuels were analyzed: neat paraffin wax and a blend of 80 wt.% paraffin wax and 20 wt.% alpha-olefin. The results show that alpha-olefin, such as the brand name *Vybar 103*, is a suitable additive for paraffin-based hybrid fuels that could be used to increase the structural integrity of paraffin fuels and reduce the regression rate. The addition of 20 wt.% alpha-olefin reduced the regression rate by 20.6%. The tests showed a filament-like flame structure that appeared to oscillate from regions of high to low combustion activity. By extracting intensity slices in the flame and performing a fast Fourier transform on the intensity signal, excited frequencies were extracted, with one peak closely matching the primary hybrid oscillation frequency postulated to be present in all hybrid systems. The slab burner is an

attractive test platform to further investigate the effect of additives on the regression rate of paraffin fuels. Further studies should be conducted to determine suitable additives for hybrid space propulsion. Finally, other experiments such as the influence of chamber pressure on combustion dynamics and novel ignition systems will be interesting to study in the slab burner.

Author contributions

Olivier Jobin: Conceptualization, Methodology, Software, Investigation, Writing - Original Draft. **Benoît Dumas:** Investigation, Writing - Review & Editing. **Étienne Robert:** Conceptualization, Writing - Review & Editing

Conflicts of interest

The authors declare that they have no known competing financial interests or personal relationships that could have appeared to influence the work reported in this paper.

Acknowledgements

This work was supported by the Natural Sciences and Engineering Research Council of Canada (NSERC) Discovery Grant RGPIN-2022-05071; NSERC CGS M (to O.J. and B.D.), and ES D scholarships (to O.J.) and the Canadian Space Agency Flights and Fieldwork for the Advancement of Science and Technology (FAST) funding initiative grant 18FAPOLB17. The authors would also like to thank Professor Jérôme Vétel for his help using the hot wire anemometry system.

Supporting Information Available

Data is available upon request. Supplemental videos available on the online version of the article.

CHAPTER 6 ARTICLE 2: METAL-ORGANIC FRAMEWORKS AS HYPERGOLIC ADDITIVES FOR HYBRID ROCKETS

Published in *Chemical Science*, Issue 12, 2022, pp. 3424-3436 on February 28, 2022 [120].

By

Olivier Jobin, Cristina Mottillo, Hatem M. Titi, Joseph M. Marrett, Mihails Arhangelskis, Robin D. Rogers, Bachar Elzein, Tomislav Friščić and Étienne Robert

6.1 Abstract

Hybrid rocket propulsion can contribute to reduce launch costs by simplifying engine design and operation. Hypergolic propellants, i.e. igniting spontaneously and immediately upon contact between fuel and oxidizer, further simplify system integration by removing the need for an ignition system. Such hybrid engines could also replace currently popular hypergolic propulsion approaches based on extremely toxic and carcinogenic hydrazines. Here we present the first demonstration for the use of hypergolic metal-organic frameworks (HMOFs) as additives to trigger hypergolic ignition in conventional paraffin-based hybrid engine fuels. HMOFS are a recently introduced class of stable and safe hypergolic materials, used here as a platform to bring readily tunable ignition and combustion properties to hydrocarbon fuels. We present an experimental investigation of the ignition delay (ID, the time from first contact with an oxidizer to ignition) of blends of HMOFs with paraffin, using White Fuming Nitric Acid (WFNA) as the oxidizer. The majority of measured IDs are under 10 ms, significantly below the upper limit of 50 ms required for functional hypergolic propellant, and within the ultrafast ignition range. A theoretical analysis of the performance of HMOFs-containing fuels in a hybrid launcher engine scenario also reveals the effect of the HMOF mass fraction on the specific impulse (I_{sp}) and density impulse (ρI_{sp}). The use of HMOFs to produce paraffin-based hypergolic fuels results in a slight decrease of the I_{sp} and ρI_{sp} compared to that of pure paraffin, similar to the effect observed with Ammonia Borane (AB), a popular hypergolic additive. HMOFs however have a much higher thermal stability, allowing for convenient mixing with hot liquid paraffin, making the manufacturing processes simpler and safer compared to other hypergolic additives such as AB.

6.2 Introduction

For small space technology companies, designing engines based on well established, albeit reliable, propellants is not always an attractive option, either due to their high toxicity, or requirements for complex engine designs. For example, hydrazine and its derivatives monomethylhydrazine (MMH) and unsymmetrical dimethylhydrazine (UDMH) [130] have been used for over 60 years as both satellite and rocket fuels due to their reliable combustion properties. However, their extreme toxicity and difficult handling represent significant challenges and have motivated a future ban for the use of these propellants in the European Union [131]. Other propellants systems, using liquid oxygen as the oxidizer and hydrogen or RP-1 as the fuel, are less toxic or non-toxic, but still require costly storage techniques and involve complex liquid-fueled cryogenic engines [132]. The cost of developing and using engines based on such propellants is an obstacle for the companies aiming to democratize access to space and serve the burgeoning microsatellite industry. The desire to mitigate the impact of this emergent space industry on the environment, while making launches simpler, safer and less costly, calls for the development of innovative solutions to propulsion challenges adapted to small-scale launchers [133]. Recently developed propulsion approaches such as ion thrusters [134], water-splitting [135], and solar-powered engines [136] are simpler and safer than chemical propulsion, but are not suitable for all applications. For instance, ground-to-orbit missions as well as rapid-response spacecraft orbital manoeuvring and attitude correction require high thrust that these novel propulsion approaches cannot provide (*e.g.* the International Space Station carries ca. 1 ton of hypergolic hydrazines [137]). Consequently, chemical propulsion is still the choice for rocket launchers or in-orbit maneuvering [138, 139], with hybrid engines an attractive alternative to complex, and therefore more costly, liquid-fueled engines [140]. To replace polluting propellants and enable competitive small-scale launchers, new technologies [33, 51, 53, 57, 141–154] should match or exceed the performance metrics of currently used propulsion approaches. For instance, the characteristic velocity (C^*) is a measure of the combustion performance of a rocket propulsion system, independent of its nozzle. The typical C^* value for liquid oxygen and RP-1 is approximately 1774 m/s at an optimal oxidizer-to-fuel ratio (O/F) of 2.24, while it is of 1711 m/s for the hypergolic, but highly toxic, combination of dinitrogen tetroxide (N_2O_4) and a mixture of 50% UDMH with 50% hydrazine at an O/F of 2.00 [130]. Another important performance metric is the specific impulse (I_{sp}), which is the change in velocity per unit of propellant consumed. Typical I_{sp} values for commonly used propellant mixtures for liquid and solid engines are listed in Table 6.1. The cryogenically stored propellant mixture of liquid oxygen (LOx) and liquid hydrogen (LH_2) has a theoretical I_{sp} of 386 s, which is generally considered to be the upper limit in

chemical propulsion [130]. For comparison, solid rocket boosters (SRBs), the simplest rocket propulsion approach, can provide I_{sp} values of approximately 260-265 s when mixtures of hydroxyl-terminated polybutadiene (HTPB), aluminum powder (Al) and the oxidizer ammonium perchlorate (AP) are used [130,155,156]. These values are comparable to hypergolic hydrazine fuels, but the thrust of SRBs cannot be stopped nor throttled.

Table 6.1 Theoretical maximum I_{sp} values for common propellants [130].

Fuel/Oxidizer	I_{sp} [s]	Type of engines
LOx/Liquid hydrogen (LH_2)	386	Liquid
N_2O_4/UDMH	278	Liquid, hypergolic
RP-1/O_2	285	Liquid
HTPB-AP-Al	260-265	Solid
AMF-M315E	231-248 [155]	Monopropellant, hypergolic
SHP163	276 [156]	Monopropellant, hypergolic

To fulfill its potential of reduced development costs and improving mechanical simplicity, hybrid rocket propulsion is in need of novel propellant systems to be competitive for launch vehicle applications, especially regarding specific and density impulses. This can be achieved with energy-dense additives in fuel grains made of solid hydrocarbons, including metal or organic hydrides and crystalline metals [20, 30]. As an example, the incorporation of aluminum particles has been shown to improve the specific impulse of hybrid propellants relying on relatively weak oxidizers such as hydrogen peroxide or nitrous oxide [20]. Another way of making hybrid rockets more interesting is by inducing the hypergolic ignition of its fuel. Additives such as ammonia borane (AB) can be included in a fuel matrix [22, 30, 51, 53]. On contact with the oxidizer, white fuming nitric acid (WFNA) for example, AB spontaneously ignites. A critical parameter here is the time elapsed from the first contact between the oxidizer and the fuel to the appearance of flames. This is called the ignition delay (ID) and low values are essential to ensure proper operation in hypergolic engines.

Here, we present a proof-of-principle demonstration of experimental and theoretical performance characteristics of a new class of hypergols based on a metal-organic framework (MOF) design [35–38]. We have recently demonstrated how the combination of metal nodes such as Zn^{2+} and Co^{2+}, with linkers based on suitably substituted imidazoles (e.g. 2-vinyl and 2-acetylene-substituted imidazoles, H**VIm** and H**AIm**, respectively, Figure 6.1a), results in zeolitic imidazolate frameworks (ZIFs) [39, 157] exhibiting hypergolic behavior (Figure 6.1b, c).

Specifically, these hypergolic MOFs (HMOFs) were found to exhibit ultrashort IDs (below 50 ms, and often below 5 ms) when in contact with traditional oxidizers such as white and red

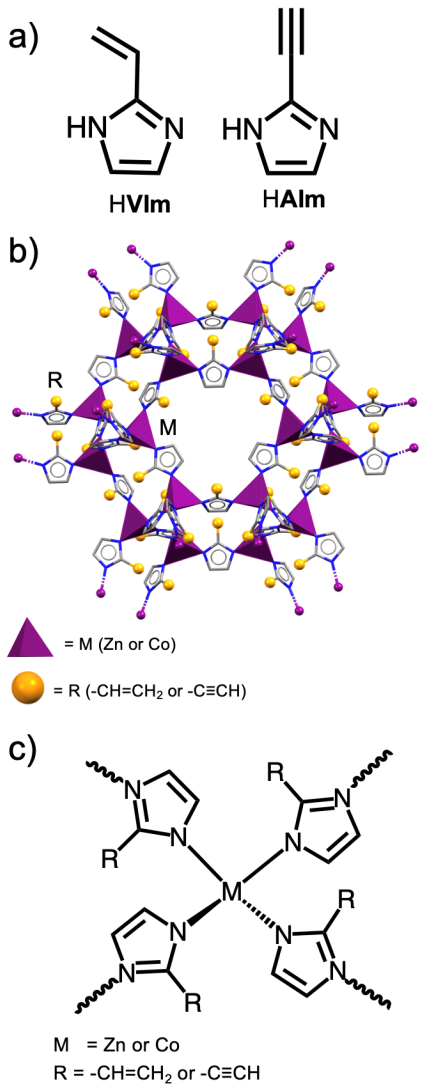

Figure 6.1 a) Schematic representation of the ligand used in this study. b) A general illustration of the HMOFs. c) A schematic diagram of the assembly of metal ions and organic linkers to form HMOFs.

fuming nitric acids (WFNA, RFNA, respectively), along with heats of combustion (ΔH_C) around -8700 kJ/mol, with volumetric energy density (E_v) of 36.3 kJ/cm^3 [157]. While these values are higher than for MMH (ΔH_C = -1304 kJ/mol; E_v = 24.7 kJ/cm^3) or UDMH (ΔH_C = -1979 kJ/mol; E_v = 25.9 kJ/cm^3) [157,158], HMOFs are also attractive as readily handled solids. They are stable in extended storage and do not exhibit ignition below at least 250-325 ^{o}C [39], compared to AB who can self-ignites at temperature as low as 75 ^{o}C [159].

As the next step in developing MOFs as a platform for new hypergolic systems, we demonstrate here that these HMOFs are highly effective additives to induce hypergolicity into con-

ventional, non-hypergolic hybrid engine paraffin fuels. The hypergolic and energetic properties of HMOFs will be compared against additives currently used to bring these characteristics to hybrid fuels; AB and Al [160], respectively.

6.3 Materials and methods

6.3.1 Hypergolic additives

The HMOFs used in this study were selected based on their hypergolic character. To ensure the safe operation of rocket engines using hypergolic propellants, an ID below 50 ms [161] is generally considered desirable, with ID below 10 ms required for dynamic altitude control systems [30]. However, with the hybrid propulsion approach, less stringent threshold can be used as the fuel is in a solid state and in a predetermined geometry. As a result, flooding of the engine is harder to achieve compared to a liquid engine, decreasing the likelihood of dramatic consequence in case of a high ID. It is not possible to add more fuel in the chamber than the exposed surface of the grain, making them safer than hypergolic liquid engines.

The IDs of hypergolic hybrid additives documented in the literature, including the HMOFs used here, are provided in Table 6.2. Previously reported RFNA and WFNA ignition drop tests on pure HMOFs samples revealed that the materials generated from H**AIm** exhibit the shortest ID values, at or below 5.0 ms. The HMOFs based on H**VIm** exhibit longer IDs, with Co(**VIm**)$_2$ at 11.0(5.0) ms, and its zinc and cadmium analogues above 10 ms. These values compare advantageously with those of currently available hypergolic propellants or additives used for blending in hydrocarbon or polymeric matrices. More specifically, the H**AIm**-based HMOFs exhibit IDs matching that of hydrazines and AB. Even the worst-performing Cd(**VIm**)$_2$ exhibits an ID of 35.0(1.0) ms at atmospheric pressure, notably shorter than the 50 ms target [39]. Other new HMOFs technologies, namely ZZU-362 and ZZU-363, were recently explored by Wang et al. [162] where hypergolic metal clusters were assembled with energetic ligands to create high density HMOFs, with IDs in the range of 26 to 60 ms.

6.3.2 Experimental section

Sample preparation

Hypergolic ignition tests on mixtures of HMOFs and paraffin were performed using Co(**VIm**)$_2$, Zn(**VIm**)$_2$ and Co(**AIm**)$_2$ as the hypergolic ignition additive, and FR5560 paraffin wax (The Candlewic Company, USA) as the matrix. The fuel samples were in the form of cylindrical pellets of approximately 300 mg, exposed to a single droplet of WFNA (10 μL volume)

Table 6.2 Ignition delays of hypergolic additives and HMOFs with WFNA as the oxidizer.

Category	Additive	Avg. Ignition Delay [ms]	Standard Deviation [ms]	Ref.
Common hypergolic additive	AB	2.0	-	[33]
	Hydrazine	3.1	-	[163]
	Lithium-Aluminum-Hydride†	31.3	7.2	[63]
Metal-Organic Framework	ZZU-362	59.0	-	[162]
	ZZU-363	26.0	-	[162]
	Co(**VIm**)$_2$	11.0	5.0	[39]
	Zn(**VIm**)$_2$	29.0	1.0	-
	Co(**AIm**)$_2$	2.0	1.0	[39]
	Zn(**AIm**)$_2$	2.0	1.0	[39]

† Test conducted at a pressure of 0.10 MPa with analytical reagent-grade nitric acid (69.3 wt.%)

Table 6.3 Selected properties of HMOFs used here for comparison.

Fuel Additive	Chemical Formula	Density [g/cm^3]	ΔH_f^0 [kJ/mol]
Co(**VIm**)$_2$	Co($C_5H_5N_2$)$_2$	0.944	-1.3
Zn(**VIm**)$_2$	Zn($C_5H_5N_2$)$_2$	0.976	-51.5
Co(**AIm**)$_2$	Co($C_5H_3N_2$)$_2$	0.985	445.8
Zn(**AIm**)$_2$	Zn($C_5H_3N_2$)$_2$	0.996	397.1

supplied using a glass syringe held approximately 150 mm above the pellets.

Ignition was investigated for three different sample configurations (Configuration I, II and III), differing in how the HMOF and the FR5560 wax are combined. Configuration I was based on a fuel pellet made from homogeneous blend of 80 wt.% FR5560 wax paraffin and 20 wt.% HMOF. Configuration II consisted of a fuel pellet with a thin layer (ca. 10 mg by weight) of a HMOFs placed on top of it. In Configuration III, a central hole was drilled in the pellets and filled with ca. 10 mg of a HMOF.

Samples for ignition testing in Configuration I were made by melting the paraffin on a hot plate, followed by addition of a HMOF and gentle stirring until a homogeneous liquid is obtained. The blend was then poured into an aluminum mold and hand-pressed. Before ignition tests, the pellet surface was sanded using 80-grit sandpaper to ensure a consistent contact surface and exposure of hypergolic additives to the oxidizer droplet. Pellets were made one by one and, unless otherwise specified, ignition tests were performed in triplicate.

Samples for ignition testing in Configuration II were prepared following the same steps as Configuration I, followed by of pressing ca. 10 mg of a HMOF powder on the top surface

of the pellet. Samples in Configuration III were prepared by following the same steps as for Configuration I. After solidification, a small hole of ca. 2 mm diameter and a depth of 4 mm was drilled in the center of the pellet, into which 10 mg of HMOFs powder was placed and gently pressed. Pellets for studies in Configurations II and III were based either on pure paraffin, or on a mixture containing 20 wt.% HMOFs with 80 wt.% paraffin. In the latter case, both propellants were mixed together in the same way as for Configuration I.

Droplet ignition tests

The ID was measured from the sequence of events following the impact of an oxidizer droplet on fuel samples, recorded using a Fastcam Mini AX200 high-speed camera (Photron, Japan) operating at 10,000 frames per second (fps). A 105 mm Sigma lens was used, set at an F-number of 1.4, with an exposure of 1/10,000 s and an OSL2 high-intensity light source (Thorlabs, USA). The ID was measured as the time interval between the initial contact of the droplet with the upper surface of a fuel pellet and the visible first emission of light. Previous experiments comparing visible light emission and OH* chemiluminescence in droplet ignition tests have revealed that the former can reliably be used to capture the onset of combustion [22].

Ignition of mixtures of HMOFs and paraffin

A sequence of images representative of the ignition of samples of pure HMOFs is illustrated in Figure 6.2. In each sequences, the second image captures the first contact between the oxidizer droplet and the sample, while the image directly after represents the first recorded frame where ignition is visible. Any subsequent images are shown as a means to illustrate the intensity and character of the flame. In the case of Zn(**VIm**)$_2$ (Figure 6.2b), only small sparks were perceptible, in contrast to the sustained flames observed with the two other HMOFs.

For the ignition tests conducted on samples containing the paraffin and a HMOF, the results are summarized in Table 6.4.

Periodic DFT calculations

Periodic density functional theory (DFT) calculations were used to determine the standard enthalpies of formation (ΔH_f^0) of ZIF materials. In order to calculate the ΔH_f^0 values, electronic energies of elements in their standard states (Zn and Co metals, graphite, H_2, N_2 and O_2 gases) had to be combined with the electronic energies of ZIF structures from

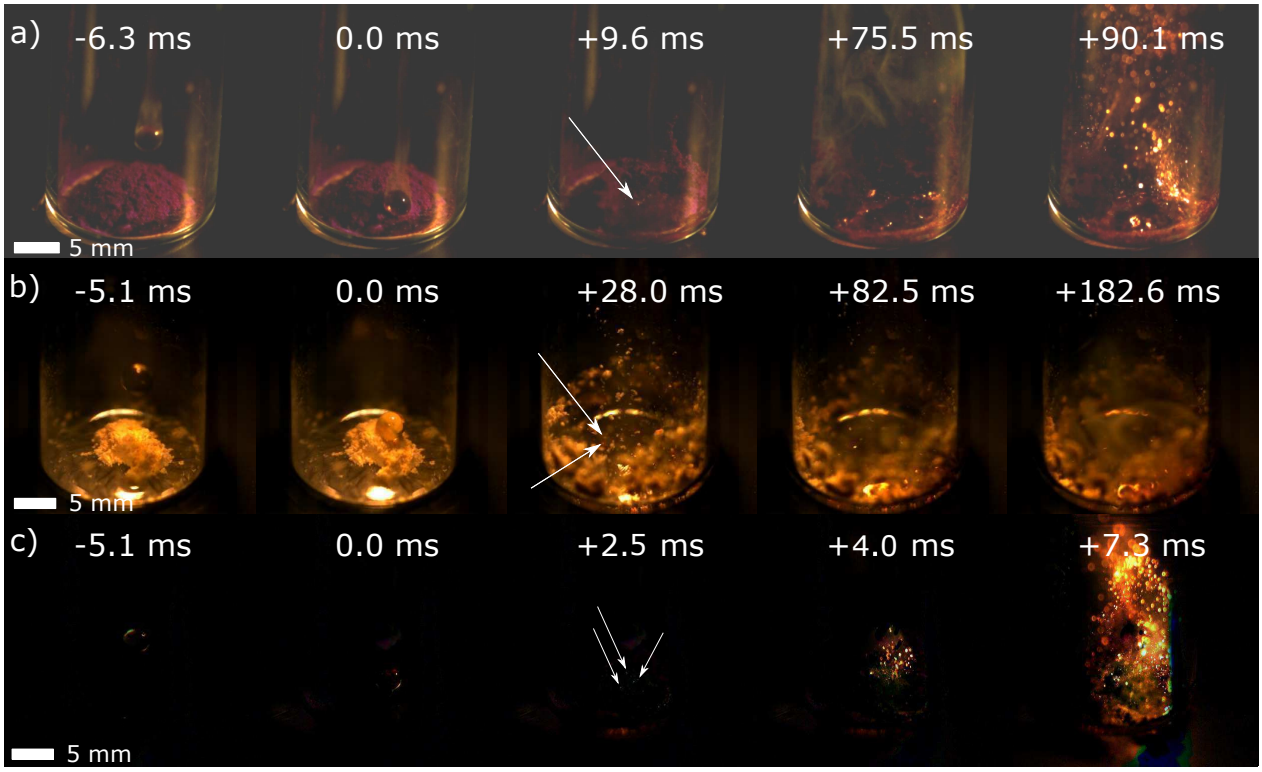

Figure 6.2 Droplet ignition tests on a) pure Co(**VIm**)$_2$, b) pure Zn (**VIm**)$_2$, and c) pure Co(**AIm**)$_2$ using ca. 10 mg of HMOF powder samples and WFNA as the oxidizer. The location of the first ignition is marked with the white arrow. Picture in c) were digitally modified to remove reflections on the glass vial. The original videos are available online as supplemental material.

our previous publication [39]. Calculations were performed with the plane wave DFT code CASTEP 16.1 [164]. The crystal structures of ZIFs, Zn, Co and Cd metals were converted into CASTEP input format using the program CIF2Cell [165]. For the elements present in the gas phase under standard conditions (H_2, N_2) the respective molecules were placed in a 30x30x30 Å cubic box, sufficiently large to prevent the interaction for the periodic images of gas molecules. Calculations were performed using a PBE [166] functional combined with Grimme D2 dispersion correction [167]. The plane-wave basis set was truncated at 750 eV cutoff, and norm-conserving pseudopotentials were used to attenuate the core regions of electron density. In the case of crystal structures, optimization involved relaxation of atom coordinates and unit cell parameters, subject to the symmetry constraints of the corresponding space groups. In the case of gas phase molecules, the dimensions of the cubic box were kept fixed throughout the optimization. The optimization was deemed converged upon satisfying the following criteria: a maximum energy change of 10-5 eV/atom, a maximum force on atom of 0.01 eV/Å, a maximum atom displacement of 0.001 Å, and a residual stress of 0.05 GPa (only for

Table 6.4 Ignition delay of tested fuel formulations and configuration using WFNA as the oxidizer. Configuration I = Fuel pellet, Configuration II = HMOF powder layer on fuel pellet, Configuration III = HMOF powder-filled hole in fuel pellet. NT = Not Tested. - = No ignition.

MOF	Configuration	Pellet Content	Avg. Ignition Delay [ms]	Standard Deviation [ms]
Co(**VIm**)$_2$	I	80 wt.% FR5560 wax/ 20 wt.% Co(**VIm**)$_2$	-	-
		50 wt.% FR5560 wax/ 50 wt.% Co(**VIm**)$_2$	-	-
	II	100 wt.% FR5560 wax	12.9	10.7
		80 wt.% FR5560 wax/ 20 wt.% Co(**VIm**)$_2$	13.3	5.3
	III	100 wt.% FR5560 wax	6.3	1.6
		80 wt.% FR5560 wax/ 20 wt.% Co(**VIm**)$_2$	8.3	0.1
Zn(**VIm**)$_2$	I	80 wt.% FR5560 wax/ 20 wt.% Zn(**VIm**)$_2$	NT	NT
		50 wt.% FR5560 wax/ 50 wt.% Zn(**VIm**)$_2$	-	-
	II	100 wt.% FR5560 wax	-	-
		80 wt.% FR5560 wax/ 20 wt.% Zn(**VIm**)$_2$	-	-
	III	100 wt.% FR5560 wax	-	-
		80 wt.% FR5560 wax/ 20 wt.% Zn(**VIm**)$_2$	-	-
Co(**AIm**)$_2$	I	80 wt.% FR5560 wax/ 20 wt.% Co(**AIm**)$_2$	-	-
		50 wt.% FR5560 wax/ 50 wt.% Co(**AIm**)$_2$	7.0‡	1.8‡
	II	100 wt.% FR5560 wax	2.3	0.1
		80 wt.% FR5560 wax/ 20 wt.% Co(**AIm**)$_2$	NT	NT
	III	100 wt.% FR5560 wax	1.8	0.7
		80 wt.% FR5560 wax/ 20 wt.% Co(**AIm**)$_2$	NT	NT

‡ Tested in the form of powder since the mixture was too brittle to form a pellet.

variable cell optimization for crystal structures).

The resulting energies were used to compute the enthalpies of formation according to the following reaction equations:

$$Co(\mathbf{VIm})_2 :\ Co_{(s)} + 10C_{(s)} + 2N_{2(g)} + 5H_{2(g)} \rightarrow Co(C_5H_5N_2)_{2(s)} \tag{6.1}$$

$$Zn(\mathbf{VIm})_2 :\ Zn_{(s)} + 10C_{(s)} + 2N_{2(g)} + 5H_{2(g)} \rightarrow Zn(C_5H_5N_2)_{2(s)} \tag{6.2}$$

$$Co(\mathbf{AIm})_2 :\ Co_{(s)} + 10C_{(s)} + 2N_{2(g)} + 3H_{2(g)} \rightarrow Co(C_5H_3N_2)_{2(s)} \tag{6.3}$$

$$Zn(\mathbf{AIm})_2 :\ Zn_{(s)} + 10C_{(s)} + 2N_{2(g)} + 3H_{2(g)} \rightarrow Zn(C_5H_3N_2)_{2(s)} \tag{6.4}$$

6.3.3 Ignition results and discussion

Ignition tests of blends with Co(VIm)$_2$

Drop tests on pellets containing 20 wt.% Co(**VIm**)$_2$ with 80 wt.% paraffin in Configuration I generated only discrete, small sparks on the pellet surface, with no definitive ignition. Moreover, the sparks were difficult to distinguish from light reflection on the surface of the

WFNA droplet, preventing the clear measurement of IDs. This difficulty to observe flames in Configuration I is most likely caused by the very fine granulometry of the HMOF powders used to prepare the samples, with an average particle size on the order of 0.1 μm [39]. When embedded in a paraffin matrix, the weak outgassing produced by these very small particles is quenched by the oxidizer layer resting on top of the fuel pellet.

To achieve ignition, we explored using a single pellet containing 50 wt.% Co(**VIm**)$_2$ and 50 wt.% paraffin wax. In this case, a strong reaction occurred on the surface of the pellets, with bubbles and gas generation 100.8 ms after the first contact with the WFNA droplet. The herein used pellet fabrication method, in which the HMOFs are mixed with melted paraffin, could hinder hypergolic ignition at low loadings, due to the paraffin completely coating the very fine particles and shielding them from the oxidant. Ignition of paraffin requires vaporization through the exothermic hypergolic ignition upon contact of the HMOF with WFNA. In Configuration I, the heat produced from the weak outgassing is lost to the WFNA liquid layer resting on top of the pellet. Several seconds after the test, each pellet was thoroughly examined: a black layer of burned HMOFs was present on its surface, hinting that some HMOFs reacted with the oxidant, but that this reaction was indeed quenched before triggering the combustion of paraffin.

Drop tests in Configuration II revealed ignition in all cases, accompanied with large bursts of flame visible in half of all the tests performed. Bursts of flame occurred mainly on top of the pellets and are attributed to the hypergolic ignition of the HMOF upon contact with WFNA. Overall, the experiments suggest that the HMOF flame did not transition to a paraffin flame and that the paraffin did not react with WFNA. The hypergolic ignition in this case also does not appear to generate enough heat to melt the paraffin and create a sustained flame, most likely because of the small particle size in the HMOF layer. Due to the impact of the WFNA droplet, part of the HMOF layer was expelled away from of the paraffin pellet, which decreased the opportunity for ignition of the paraffin. In this configuration, and using Co(**VIm**)$_2$ as the HMOF, a large variation in IDs was observed, which we believe might be related to other factors not evaluated here, such as the compactness or the uniformity of the HMOF layer. These two parameters will affect the spreading of the HMOF layer upon impact with the oxidizer droplet.

To test the hypothesis of HMOF particles being too small, we explored hypergolic ignition in Configuration III. In 5 out of 6 cases, using either neat paraffin or a blend of paraffin and Co(**VIm**)$_2$ in respective weight ratio 80:20, sparks were produced, followed by bursts of flames resembling those observed for Configuration II. However, the bursts of flame in Configuration III were also followed by continuous combustion (up to 2.5 s) that was attributed to the

paraffin, first reacting with the leftover WFNA and then with ambient air. This interesting result indicated that the addition of HMOFs in the fuel matrix did not significantly hinder the ignition of the paraffin, thus confirming that combustion is not affected after the hypergolic reaction. Using 5 mg Co(**VIm**)$_2$ instead of 10 mg in this configuration did not lead to the ignition of the paraffin.

Notably, the ignition with Co(**VIm**)$_2$ in Configuration III, using either pure paraffin and or HMOF-paraffin blends as the pellet material, produced remarkably short average IDs of respectively 6.3(1.6) ms and 8.3(0.1) ms. These values are 52% and 37% shorter, respectively, than the IDs seen in Configuration II, confirming that spatially concentrated HMOF not only enable paraffin ignition, but also reduce the ID value. One of the major differences between both configurations is the reduction of the amount of HMOF particles expelled from the pellet upon contact with the droplet in Configuration III. Concentrated in the center of the pellet, the HMOF flame contributed more to the vaporization of the paraffin through longer flame and direct contact with the edges of the hole. Furthermore, eight out of twelve tests in Configurations II and III were observed to ignite with IDs below 10 ms, which is considered to be the target value for dynamic altitude control systems [30].

Ignition tests on blends with Zn(VIm)$_2$

Tests carried with Zn(**VIm**)$_2$ did not lead to the ignition of the pellets in any of the three configurations. In some cases, mostly under configurations II and III, a reaction occurred on the surface of the pellet: fumes were generated and a layer of black material was observed to form. Furthermore, small sparks similar to those observed on pure Zn(**VIm**)$_2$ powder (Figure 6.2c) were observed. However, due to the difficulty of distinguishing the light emitted by the sparks from the light refracted by the WFNA droplet, ID values are not reported.

A single droplet test was performed with a pellet containing 50 wt.% paraffin wax and 50 wt.% Zn(**VIm**)$_2$ under configuration I. Since sparks were not observed in that case, ignition of mixtures containing 20 wt.% of Zn(**VIm**)$_2$ was not tested.

The poor hypergolic performance of Zn(**VIm**)$_2$-paraffin blends compared to those based on Co(**VIm**)$_2$ did not warrant further experiments. This result was consistent with our previous observation [39] of lower hypergolic reactivity for HMOFs based on zinc, compared to cobalt.

Ignition tests on blends with Co(AIm)$_2$

As Co(**AIm**)$_2$ has previously been demonstrated to be the most rapidly igniting HMOF so far, tests were conducted only in Configurations II and III, using a neat paraffin wax pellet.

Tests in Configuration I could not be done using a pellet, as the mixture of HMOF and paraffin was too brittle after being pressed by hand. Consequently, the drop ignition tests in this configuration were conducted on a mixture of Co(**AIm**)$_2$ and paraffin powder. Out of the three tests carried that way, two led to hypergolic ignition lasting approximately 2 seconds, making Co(**AIm**)$_2$ the only HMOF that readily ignited even in a homogeneous powder mixture with paraffin (Figure 6.3).

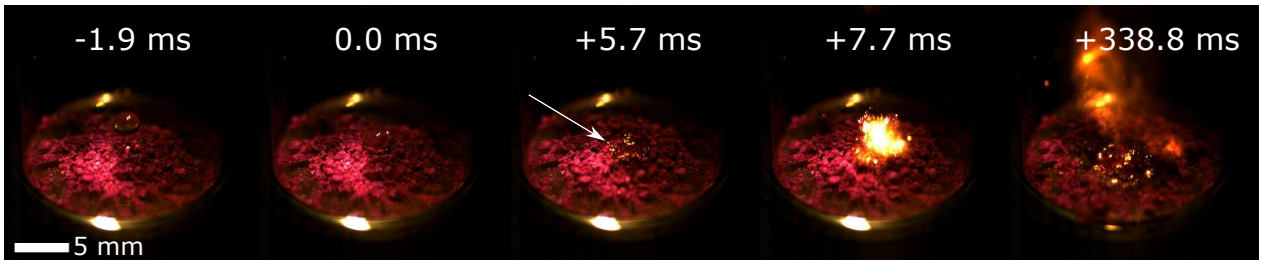

Figure 6.3 Example of a ignition drop test on 50 wt.% FR5560 wax / 50 wt.% Co(**AIm**)$_2$ using WFNA as the oxidizer. The location of the first ignition is marked with the white arrow. Full sequence available on supplement material.

Tests carried with Co(**AIm**)$_2$ in Configuration II all revealed rapid ignition, with an average ID of 2.3(0.1) ms, which corresponds to a reduction of 82% compared to Co(**VIm**)$_2$ in the same configuration. In addition to a remarkably short ID values, well under the 10 ms target value, paraffin ignition and burning was observed in two out of three tests (Figure 6.4). Compared to Co(**VIm**)$_2$, the herein observed ignition of paraffin bearing a thin layer of Co(**AIm**)$_2$ may be attributed to a faster hypergolic reaction with WFNA, leading to more heat being transferred to the paraffin before the HMOF particles were expelled from the surface. Overall, these results clearly demonstrate that the heat released by hypergolic ignition of a thin layer of Co(**AIm**)$_2$ can be used to ignite solid paraffin fuel underneath.

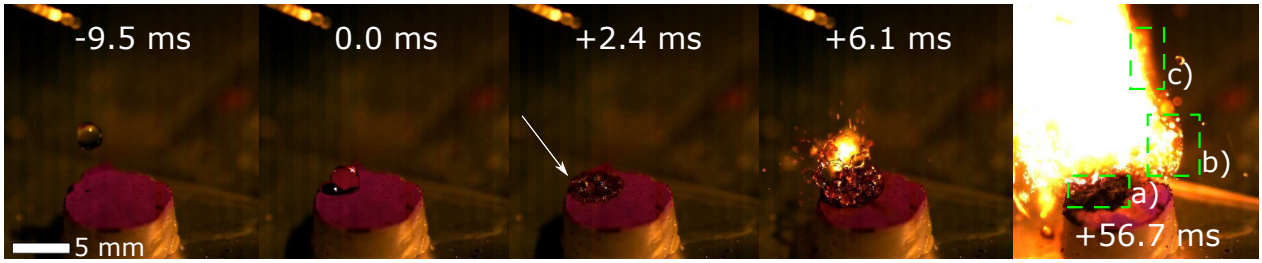

Figure 6.4 Example of an ignition drop test on a FR5560 wax pellet covered with a thin 10 mg layer of Co(**AIm**)2 (Configuration II) , using WFNA as the oxidizer. The location of the first ignition is marked with the white arrow. a) Burned paraffin and HMOFs. b) Burning HMOF. c) Paraffin flame. Full sequence available in supplemental material.

Ignition drop tests with Co(**AIm**)$_2$ in Configuration III gave the shortest ID values, leading to an average of 1.8(0.7) ms. This value represents a decrease of 71% compared to the results obtained with Co(**VIm**)$_2$ in the same configuration. Notably, following the initial hypergolic ignition of Co(**AIm**)$_2$, paraffin ignition was observed in all cases (Figure 6.5).

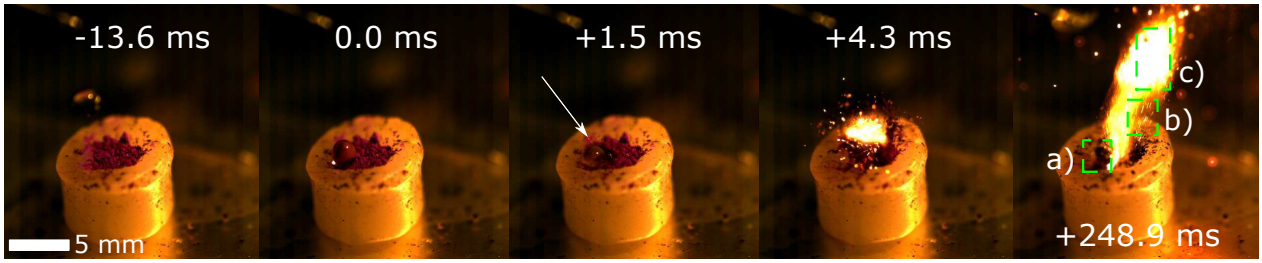

Figure 6.5 Drop tests on neat paraffin wax pellet with a 10 mg of Co(**AIm**)$_2$ located in a hole in the center, using WFNA as the oxidizer. The location of the first ignition is marked with the white arrow. a) Burned paraffin and HMOF. b) Burning HMOF powder. c) Paraffin flame. Full sequence available in supplemental material.

6.4 Theoretical performance

The use of MOFs as modular propellant fuels and additives is contingent upon their projected performance as components of fuel blends useful for practical engine designs. In that context, we present here the theoretical performance of HMOFs as additives for hypergolic ignition in hybrid propulsion systems based on paraffin fuel. The thermo-chemical simulations considered solid paraffin wax for the fuel grain matrix, and the performance characteristics were calculated for variable HMOF additive mass fractions and O/F ratios. A paraffin-based propellant system was selected for modeling as its liquefying characteristics results in the high regression rates needed for high-thrust hybrid rocket engines.

The I_{sp} and density specific impulse (ρI_{sp}) are propulsive performance parameters heavily dependent on a variety of physical factors such as engine and nozzle geometries as well as on the fuels and oxidizers used. The exhaust gas velocity V_e is a critical parameter in the calculation of the I_{sp}. So it is a function of the temperature of combustion T_c, the mean molecular weight of the exhaust gas M_W, the ratio of the exit pressure and combustion pressure $\frac{P_e}{P_c}$ and the ratio of specific heat γ:

$$I_{sp} = \frac{V_e}{g} = \frac{1}{g}\sqrt{\frac{2\gamma R_u T_c}{(\gamma - 1)\, M_W}\left(1 - \frac{P_e}{P_c}\right)^{\frac{\gamma-1}{\gamma}}} \tag{6.5}$$

Thus, the higher the combustion pressure and temperature, and the lower the molecular

weight of the combustion gas, the higher the performance of the engine will be.

The density specific impulse measures the performance of a given propellant by taking into account its density, with higher density specific impulse associated with higher engine performance for a given volume of propellant. It is defined by:

$$\rho I_{sp} = \rho_{propellant} \cdot I_{sp} \tag{6.6}$$

with $\rho_{propellant}$ defined as:

$$\rho_{propellant} = \frac{\rho_{ox} \cdot \rho_{fuel}\,(1 + O/F)}{\rho_{fuel} \cdot O/F + \rho_{ox}} \tag{6.7}$$

where ρ_{ox} is the density of the oxidizer and ρ_{ox} is the density of the fuel. The density specific impulse is determined at the optimal O/F for each fuel and oxidizer formulation.

Finally, the C^* values are a mean to assess the combustion independently of the nozzle efficiency or performance. The value of C^* is proportional to the I_{sp} and is defined by:

$$C^* = \frac{P_c \cdot A_t}{\dot{m}} \tag{6.8}$$

where A_t is the throat area of the nozzle and $\dot{m}$ is the average mass flow of the engine.

The I_{sp} and ρI_{sp} of hybrid paraffin-based fuel mixtures containing HMOFs were calculated using the NASA-CEA software [129]. The values obtained were then compared to those for paraffin fuels containing AB and aluminum for reference. AB in a paraffin matrix can yield hypergolic ignition [22,33,57], just as our proposed use of HMOFs. Although aluminum particles as fuel additives do not yield hypergolicity, they were considered here for comparison as energetic rocket fuel additives [160]. The oxidizers investigated were WFNA, LOx and high-test peroxide (HTP, H_2O_2 at 90 wt.% concentration in H_2O). The absolute combustion chamber pressure considered was 6.89 MPa (1000 psia) and the exhaust gases were assumed to be in chemical equilibrium conditions and perfectly expanded to atmospheric pressure. The properties of the oxidizers were retrieved from NASA-CEA, with the densities used for calculations being 1.141 g/cm^3 for LOx, 1.513 g/cm^3 for WFNA and 1.392 g/cm^3 for HTP. The chemical formula of the paraffin used for the analysis is $C_{32}H_{66}$ with an approximate density of 0.90 g/cm^3. The properties of paraffin, aluminum and AB were extracted from the NASA-CEA library whereas those of the HMOFs were measured experimentally and reported earlier in Table 6.3.

6.4.1 Performance of pure HMOFs

For comparison purposes, theoretical performances of pure fuel matrices made of paraffin and HTPB without energetic or hypergolic additives are shown in Figure 6.6 and Table 6.5, as a function of the O/F ratio for various oxidizers. When used as the oxidizer, LOx used as oxidizer provides the best specific impulse among those presented with a maximal value of approximately 300s. The use of WFNA allowed maximal values of I_{sp} of approximately 265s whereas engines using H_2O_2 could achieve an I_{sp} of almost 290s.

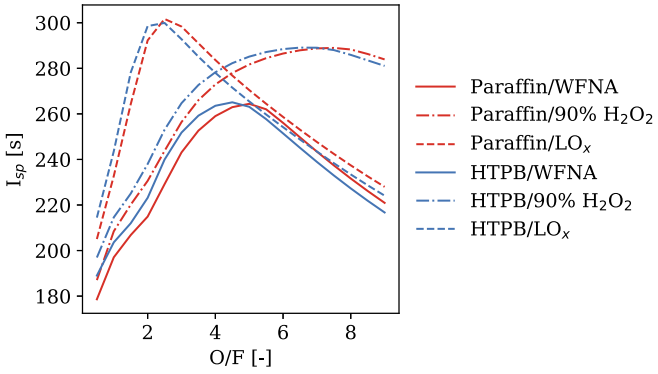

Figure 6.6 Theoretical performances of common propellants and oxidizers used in hybrid rocket engines. Equilibrium conditions, chamber pressure of 6.89 MPa and perfect expansion to atmospheric conditions.

Table 6.5 Theoretical performances of commonly used fuels and oxidizer combinations at their optimum O/F ratio.

Fuel	Oxidizer	O/F	I_{sp} [s]	ρI_{sp} [sg/cm^3]
HTPB	WFNA	4.5	265.1	360.0
HTPB	LOx	2.3	301.2	321.5
HTPB	H_2O_2 90 wt.%	6.7	289.2	378.1
Paraffin	WFNA	5.0	264.4	359.3
Paraffin	LOx	2.6	301.8	321.0
Paraffin	H_2O_2 90 wt.%	7.4	289.0	377.7

Before assessing the performances of HMOFs within a paraffin fuel matrix, the I_{sp} was calculated for their pure form and was compared to the values for aluminum and AB. These results are presented for Co(**AIm**)$_2$ and Co(**VIm**)$_2$ in Table 6.6. With all oxidizers studied, pure AB always presented the highest specific impulse. Pure Co(**AIm**)$_2$ and Co(**VIm**)$_2$ had slightly lower I_{sp} values compared to AB but were always higher than pure aluminum. As expected, aluminum yielded a higher ρI_{sp} compared to AB and the selected HMOFs because

of its high density. Interestingly, the ρI_{sp} of Co(**AIm**)$_2$ and Co(**VIm**)$_2$ was higher than AB when WFNA or HTP were used as the oxidizer.

Table 6.6 Theoretical performances of pure MOFs, aluminum and ammonia borane. Equilibrium conditions, chamber pressure of 6.89 MPa and perfect expansion to atmospheric conditions are assumed.

Oxidizer	Fuel	O/F	I_{sp} [s]	ρI_{sp} [sg/cm^3]
WFNA	AB	1.00	288.67	297.14
	Aluminum	2.00	231.88	411.05
	Co(**VIm**)$_2$	2.50	242.01	312.35
	Zn(**VIm**)$_2$	2.50	241.83	316.17
	Co(**AIm**)$_2$	2.25	245.24	318.50
LOx	AB	1.75	316.62	309.22
	Aluminum	2.25	228.32	316.79
	Co(**VIm**)$_2$	1.25	261.16	272.69
	Zn(**VIm**)$_2$	1.25	264.04	280.21
	Co(**AIm**)$_2$	1.25	263.48	280.86
H_2O_2 90 wt.%	AB	1.25	298.04	307.61
	Aluminum	2.75	269.86	431.37
	Co(**VIm**)$_2$	3.75	271.13	343.13
	Zn(**VIm**)$_2$	3.75	270.95	346.10
	Co(**AIm**)$_2$	3.50	272.80	347.81

6.4.2 Performance of HMOFs/Paraffin fuels

In Table 6.7, the results for HMOF-containing fuels are shown side-by-side with the values calculated for fuel blends containing AB or aluminum. Figures 6.7a and 6.7b present the I_{sp} and ρI_{sp} of paraffin-based fuels as a function of additive mass loading, with WFNA as the oxidizer. For each additive mass fraction, calculations were done over a broad range of O/F ratios and the one yielding the highest I_{sp} was chosen as optimal and reported in the figures and in Table 6.7. A solid additive mass loading range of 5 wt.% to 50 wt.% was considered; the upper-bound was selected because homogeneous blends were experimentally achieved up to 50 wt.% for a wide variety of additives [20] with higher concentration yielding very brittle fuel blends. However, in practical applications with paraffin fuel matrices, desirable burning characteristics may only be present over a reduced mass loading range. At high mass loads, the inclusion of additives could lead to decreased performances and fuel regression rates. For instance, using AB as an hypergolic additive, Weismiller *et al.* reported that at concentration over 20% by mass in a paraffin or a HTPB fuel matrix, the regression rate was reduced due to a condensed phase created on the surface of the fuel grain during the combustion process [57].

Condensed phase products on the surface of the pellets were also observed with all HMOFs investigated in this paper. This reduction in regression rate is therefore also expected with HMOFs. For this reason, a moderate mass loading of 20 wt.% was selected to investigate the effect of the O/F ratio on the I_{sp}, with results presented in Table 6.7 and in Figure 6.7c when WFNA is used as the oxidizer.

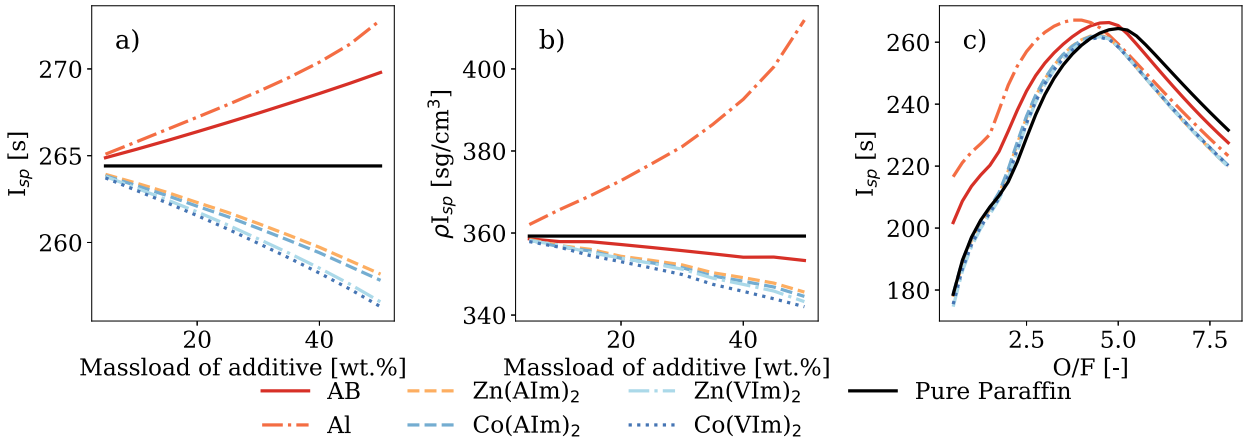

Figure 6.7 a) Specific impulse as a function of the mass load of additive in a paraffin-based fuel matrix at the optimal O/F ratio, b) density specific impulse as a function of the mass load of additive in a paraffin-based fuel matrix and c) theoretical performance at 20 wt.%, as a function of oxidizer-to-fuel ratio. Calculated using WFNA as the oxidizer.

As shown in Figures 6.7a and 6.7b, both I_{sp} and ρI_{sp} are slightly lower when HMOFs were added to the fuel mixture compared to pure paraffin reacting with WFNA, decreasing approximately linearly with increasing MOF loading. This contrasts with the use of AB, which resulted in a slight increase in I_{sp}. The addition of aluminum also yielded an increase in I_{sp}, an effect scaling approximately linearly with increased additive mass loading (an increase of 3.3% at a mass load of 50 wt.%). Although there was a minor reduction in I_{sp} on the order of 2.0% at a mass load of 50 wt.% for the HMOF-containing fuels compared to pure paraffin as well as paraffin-AB or -Al mixtures, this modest performance tradeoff implied that HMOFs could be useful as additives to impart hypergolicity to an otherwise non-hypergolic fuel.

The performance parameters were also calculated using LOx as an oxidizer, with the results shown in Figure 6.8a, yielding higher values compared to WFNA. Additionally, the decrease in I_{sp} and ρI_{sp} values associated with increasing the HMOF mass loading was less pronounced when LOx was used in calculations. For instance, when using LOx the decrease of I_{sp} for Zn(**AIm**)$_2$ at a fixed mass load of 20 wt.%, was 2.15% and 1.18% compared to AB and Al, respectively. Corresponding values were 1.53% and 1.84%, respectively, when WFNA was used. Interestingly, behavior of the calculated I_{sp} as a function of the O/F ratio for the

HMOFs revealed a very similar combustion behavior to the fuel blends using AB and Al as additives, again considering a case with 20% mass loading (Figure 6.8c). The curves were all similar in profile, with maxima close to an O/F ratio of 2.5 in all cases. Notably, the I_{sp} values for Zn(**AIm**)$_2$ and AB are almost equal and just under 300 s at an O/F ratio of approximately 2.5.

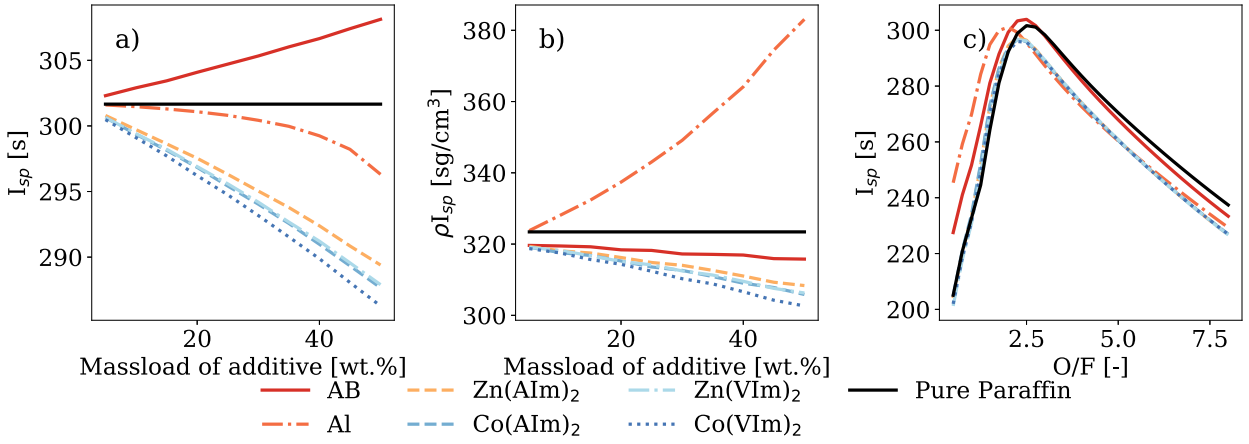

Figure 6.8 a) Specific impulse as a function of the mass load of additive in a paraffin-based fuel matrix at the optimal O/F ratio, b) density specific impulse as a function of the mass load of additive in a paraffin-based fuel matrix and c) theoretical performance at 20 wt.%, as a function of oxidizer-to-fuel ratio. Calculated using LOx as the oxidizer.

Finally, the same parameters were calculated using HTP as an oxidizer (Figure 6.9). Overall, the I_{sp} of the hypergols was similar to those obtained when using LOx as an oxidizer. However, there was a smaller drop in I_{sp} with increasing HMOF mass loading. At a mass loading of 20 wt.%, the decrease was of 0.98% and of 1.07% when compared to AB and Al, respectively, at the same mass loading. However, the ρI_{sp} with 90% HTP was higher than that when using WFNA as the oxidizer. The trends for the variation of the I_{sp} as a function of the O/F again showed very similar combustion behavior between the HMOFs, AB and Al additives.

In addition to the I_{sp} and ρI_{sp} calculated using the NASA-CEA software, the C* values were also computed. The values are reported in Table 6.7 for a mass loading of 20 wt.% in a paraffin matrix, in each case for the O/F ratio that provides the maximum C* value. The combustion temperature corresponds to the temperature inside the combustion chamber, whereas the molecular weight was computed at the exit of the nozzle and took into account products in condensed phases.

The results presented here showed that for the HMOF considered, the C* and optimal O/F were similar. The latter was also comparable to the optimal O/F when AB was used as

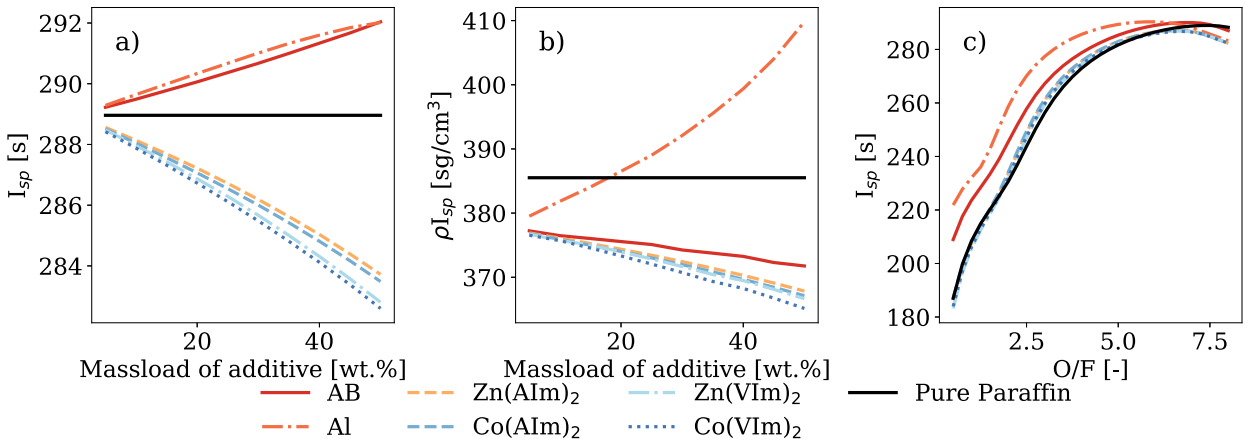

Figure 6.9 a) Specific impulse as a function of the mass load of additive in a paraffin-based fuel matrix at the optimal O/F ratio, b) density specific impulse as a function of the mass load of additive in a paraffin-based fuel matrix and c) theoretical performance at 20 wt.%, as a function of oxidizer-to-fuel ratio. Calculated using 90 wt.% H_2O_2 as the oxidizer.

Table 6.7 Combustion characteristics of AB, Al and HMOFs additives in a paraffin matrix at a mass loading of 20 wt.%. Equilibrium conditions, chamber pressure of 6.89 MPa and perfect expansion to atmospheric conditions are assumed.

Oxidizer	Additive	O/F	C* [m/s]	T_C [K]	M_W [g/mol]
WFNA	AB	4.1	1616.1	3105.95	24.729
	Aluminum	3.4	1614.5	2905.89	23.916
	Co(**VIm**)$_2$	4.5	1571.8	3131.48	27.299
	Zn(**VIm**)$_2$	4.5	1573.9	3139.94	27.351
	Co(**AIm**)$_2$	4.0	1585.8	3123.26	26.029
LOx	AB	2.1	1836.1	3503.93	21.942
	Aluminum	1.7	1814.9	3623.51	22.662
	Co(**VIm**)$_2$	2.4	1771.5	3660.30	26.021
	Zn(**VIm**)$_2$	2.3	1781.9	3652.10	25.388
	Co(**AIm**)$_2$	2.1	1789.9	3594.36	24.232
H_2O_2 90 wt.%	AB	5.8	1754.4	3065.08	20.805
	Aluminum	5.0	1749.0	3164.18	21.496
	Co(**VIm**)$_2$	5.7	1730.1	3062.22	21.441
	Zn(**VIm**)$_2$	5.7	1732.4	3070.17	21.467
	Co(**AIm**)$_2$	5.7	1732.2	3075.78	21.538

the additive. Interestingly, when LOx was used as the oxidizer, every paraffin-additive mixtures had a higher C* than the previously mentioned RP1-LOx (1774 m/s) and N_2O_4-UMDH/Hydrazine (1711 m/s) fuel-oxidizer combinations. When considering 90% HTP as the oxidizer, the C* values for the HMOFS were also higher than for the N_2O_4-UMDH/Hydrazine

combinations.

In general, combustion of paraffin and HMOFs yielded a higher combustion temperature compared to AB, while surpassing aluminum when WFNA was used as the oxidizer. Even though the temperature of combustion of HMOFs was higher than AB, the specific impulse of the latter was higher, primarily due to the lower molecular weight of the exhaust gases.

6.5 Discussion

The presented results demonstrate significant potential of HMOFs as solid, safe to handle and hydrazine- or aminoborane-free additives that can provide hypergolicity to inexpensive, safe and energy-dense solid hydrocarbon fuels required for use in hybrid rocket engines, such as paraffin. The I_{sp} values calculated are closed to those obtained when aluminum metal or AB is included in the paraffin matrix. For instance, with a moderate mass loading of 20 wt.% for which good combustion efficiency and regression rates are expected, the relative penalty in I_{sp} is not more than 2.15%, compared to the use of hypergolic AB or non-hypergolic Al additives, when LOx is used as the oxidizer. This slightly higher specific impulse for the hypergolic AB - WNFA combination compared to the HMOFs investigated here is explained by the very high hydrogen content of the former resulting in a lower molecular weight of the combustion products, even though HMOFs have a large heat of combustion. Another minor disadvantage for the use of HMOFs as fuel additives compared to AB or Al is the slightly narrower range of O/F ratios over which the I_{sp} is close to its optimal value. This means that with HMOF additives in hybrid engines, the oxidizer supply would need to be more carefully controlled and evenly distributed over the fuel grain to ensure optimal combustion, especially when using WFNA. As shown in Figure 6.7c, the I_{sp} as a function of the O/F ratio for HMOF-based paraffin mixtures features a slightly sharper peak between 3.50 and 4.25, as opposed to the broader peaks observed both AB and aluminum additives. However, this difference between the behavior of the additives is much less pronounced when LOx or 90% HTP are used as oxidizers.

A hybrid engine relying on HMOFs to provide hypergolicity to paraffin or other hydrocarbon fuel matrices would therefore lose slightly in I_{sp}, but gains in having a simple ignition, eliminating the need for more complex external ignition systems. Hypergolic propellants can also add flexibility with regards to possible mission profiles, as they could enable reliable restartability, a feature not possible for solid rockets and adding complexity to non-hypergolic hybrids. A caveat is the difficult ignition observed when the very fine HMOF powders were evenly mixed with paraffin. In droplet ignitions test shown here, the mixture composition surrounding MOF particles immersed in the fuel matrix is very lean and as a result the hot

outgassing that might initiate the combustion can be quenched by the local overabundance of oxidizer. In engine conditions, careful tuning of the O/F ratio during the transient ignition phase of operation could avoid this problem, but this observation highlights the necessity to carefully assess the importance of granulometry of the additives on the hypergolic ignition phenomena in hybrid engines.

Compared to the reference hypergolic additive for hybrid rocket propulsion, AB, HMOFs have the potential to be much easier to mix with paraffin and other hydrocarbons. This is explained by the presence of organic ligands and by their much higher temperature of decomposition, determined by thermogravimetric analysis to be 250-325 °C [39] for the HMOFs considered here, and 80-100 °C for AB [159]. HMOFs also have lower toxicity compared to hypergolic fuels based on hydrazine, meaning they offer a safer and less toxic alternative additive that is easier to handle. Finally, HMOFs have the ability to be tailored as needed by including other metals or chemical compounds in their porous structure, making them suitable for a wide range of needs.

6.6 Conclusions

We have outlined the development of a new materials platform for hypergolic hybrid rocket propulsion, based on metal-organic frameworks (MOFs) as a recently emerged class of hypergolic materials. The hypergolic MOFs exhibit ignition delays and energy content competitive with currently used fuels and additives, and this case study has shown that the presence of Co(**AIm**)$_2$ and Co(**VIm**)$_2$ can enable reliable and short ignition delays (below 10 ms) for otherwise non-hypergolic paraffin-based fuel. Thermo-chemical simulations reveal that the herein explored hypergolic MOFs could potentially closely match the theoretical specific impulse values of currently used hybrid rocket additives. The values, calculated for paraffin as the fuel matrix in combination with three popular different oxidizers (WFNA, LOx and HTP), were compared to the performance achieved with currently used hypergolic (AB) and non-hypergolic fuel additives (aluminum). Although the calculated I_{sp} values were found to generally slightly decrease with the increase of the mass loading of HMOF in the paraffin fuel matrix, evaluating the change in I_{sp} as a function of oxidizer-to-fuel ratio revealed performance characteristics similar to those predicted for AB- and Al-containing fuel mixtures. The decrease in I_{sp} was found to be no more than 2.15% for a HMOF mass loading of 20 wt.%. This minuscule decrease in performance is a very small cost for using a material that is much more thermally stable than AB as a means to enable hypergolicity within the rocket engine. Further studies will investigate the effect of the hypergolic MOF particle size on the ignition process and its implication on the range of additive mass loadings for which low

ignition delays and reliable combustion can be achieved without a significant change in the regression rate of the paraffin fuel.

Author contributions

Olivier Jobin: Conceptualization, Investigation (Ignition experiments, Performance computations), Writing - Original Draft. **Cristina Mottillo**: Conceptualization, Investigation (Ignition experiments), Writing - Original Draft. **Hatem M. Titi**: Conceptualization, Investigation (Ignition experiments), Writing - Original Draft. **Joseph M. Marrett**: Investigation (HMOF preparation). **Mihails Arhangelskis**: Investigation (Periodic DFT calculation), Writing - Original Draft. **Robin D. Rogers**: Writing - Review & Editing. **Bachar Elzein**: Writing - Original Draft. **Tomislav Friščić**: Conceptualization, Writing - Review & Editing . **Étienne Robert**: Conceptualization, Writing - Review & Editing

Conflicts of interest

T.F., R.D.R., H.M.T., J.M.M. are inventors on patent application (no. 62/730,590, from 13 September 2018) related to hypergolic MOFs, which is assigned to ACSYNAM Inc. (Montreal, H1P 1W1, Canada) with T.F., C.M. and R.D.R. as co-owners.

Acknowledgements

This work was supported by NSERC Discovery Grant RGPIN-03622-2014; NSERC CGS M, and ES D scholarships (to O.J.); Canadian Space Agency Flights and Fieldwork for the Advancement of Science and Technology (FAST) funding initiative (grant 18FAPOLB17); NCN Sonata grant 2018/31/D/ST5/03619; NSERC RGPIN-2017-06467; NSERC E. W. R. Steacie Memorial Fund (NSERC SMFSU 507347-17); Tier-1 Canada Research Chair Program (to T.F.). We further acknowledge WestGrid (www.westgrid.ca) and Compute Canada (www.computecanada.ca) for providing access to the Cedar supercomputer.

CHAPTER 7 ARTICLE 3: HYPERGOLIC IGNITION OF PARAFFIN-BASED HYBRID ROCKET FUELS BY SPRAYS OF LIQUID OXIDIZER

Published in *Proceedings of the Combustion Institute*, Vol. 39(4), 2023, pp. 5073-5082 on October 17, 2022 [121].

By

Olivier Jobin, Benoît Dumas, Joanna Zahlawi, Mathieu Chartray-Pronovost, Étienne Robert

7.1 Abstract

An experimental study is conducted to measure the ignition delay of ammonia borane doped paraffin wax with sprays of white fuming nitric acid as oxidizer. The injection pressure and injector diameter are varied to investigate the effects of spray characteristics on the ignition dynamics. A range of Weber (We) number for the oxidizer jet covering $100 < We < 2700$ and Reynolds (Re) number $1300 < Re < 8900$ is investigated, whereas the We number at the droplet scale varies from $0.8 < We_{drop} < 24.1$. The sprays are characterized using phase-doppler anemometry to obtain the size and speed distribution of the oxidizer droplets across multiple positions. In addition to conventional high-speed imaging, the hypergolic ignition is also observed using Schlieren imaging and a high-speed mid-infrared camera. The results show that the ignition delay of a hypergolic hybrid fuel under spray conditions is unaffected by the mean droplet size of the oxidizer. The ignition delay decreases with increasing We number at the droplet scale and increasing droplet velocity. The variability in the ignition delay also decreases with Weber number and droplet velocity. The values obtained for the ignition delay when using a spray are generally higher than those from simple oxidizer drop experiments, highlighting the need to investigate the hypergolic ignition in configurations representative of engine conditions.

7.2 Introduction

The growing interest in hybrid rockets is mainly driven by their safety compared to liquid and solid rockets. They however bring advantages, such as throttleability, unavailable for solid motors, and anticipated lower launch cost due to reduced mechanical complexity, when compared to liquid-fueled engines [22]. Such space-bound propulsion systems often rely

on hypergolic propellant combinations, i.e., fuels and oxidizers that spontaneously ignite on contact. This removes the need for separate ignition systems which add weight and complexity.

A considerable number of studies have been conducted on the characterization of the ignition delay (ID) of hypergolic hybrid rockets [22, 168] with low IDs required for fast and reliable engine control. A target ID of 50 ms is usually considered for the ignition of hypergolic liquid rocket engines and this value is also extended to hybrid rocket engines [161], with a more demanding target of 10 ms for dynamic altitude control systems [30]. These values (ID target) are used as safety constraints for liquid engines due to the risk of engine flooding leading to mechanical failure following late ignition. However, hypergolic hybrid engines are considered safer than hypergolic bi-liquid engines because the mixing of the oxidizer and the fuel is limited by the solid state of the fuel due to its finite exposed surface, thus preventing flooding. The ID criterion is therefore less critical for safe hybrid engine operations, but is still necessary to achieve precise control systems. Typical hybrid rocket fuels include paraffin wax, hydroxyl-terminated polybutadiene (HTPB), and polyethylene. Hypergolicity in such fuels can be achieved through the use of hypergolic additives. The most commonly tested are ammonia borane (AB) [22,30,168], lithium-aluminum-hydride (LAH) [63], sodium borohydride ($NaBH_4$) [169,170], sodium amide ($NaNH_2$) [73], metal organic-frameworks [120] and amine-boranes [33]. The most common liquid hypergolic oxidizers are hydrogen peroxide (H_2O_2), nitrogen tetroxide (NTO), mixed oxides of nitrogen (MON), and white fuming nitric acid (WFNA).

The experimental measurement of the ID in hypergolic solid-liquid propellant systems is typically carried out simply by filming the events following a large oxidizer droplet impacting a solid fuel pellet containing hypergolic additives. The time between the initial droplet-pellet contact and the first light emission is thus measured. Although useful to determine whether or not propellants can reach the ID criteria of < 50 ms, these experiments do not reflect the conditions encountered in hybrid rocket engines, where liquid oxidizer droplets are likely to be very small, fast and delivered in large number as a spray.

As a first step toward full-scale fire testing of hypergolic hybrid rocket engines, Padwal et al. [169] compared the ID of droplet ignition tests and oxidizer sprays in a hollow fuel grain using H_2O_2 as the oxidizer and a fuel mixture containing boron, paraffin wax, and $NaBH_4$. They showed that the IDs were similar between the two test configurations but did not characterize the oxidizer spray parameters. Benhidjeb-Carayon et al. [73] characterized the hypergolic ignition and re-ignition of a 2 inch diameter lab-scale motor burning paraffin doped with $NaNH_2$ additives and sprayed MON as the oxidizer. They successfully demonstrated

the relight of their hybrid rocket motor using a configuration where the upstream extremity of the fuel grain is highly concentrated in hypergolic additives. However, to date, no study has investigated the effect of spray characteristics on the ID of hypergolic hybrid propellants such as the size distribution of the droplets, the Weber number (We) of the spray, or its Reynolds number (Re).

Spray characteristics are however often studied for hypergolic liquid rocket systems. To characterize the propellant sprays and jets, experimental investigations often rely on the high-speed recording of the atomization process, image analysis or Phase-Doppler Anemometry (PDA) measurement [171–173]. For example, Kooij et al. [174] demonstrated that the We number could predict the size distribution of various injectors. Other physical parameters influence the droplet generation mechanism, but the viscosity of the fluid has been shown to not affect the median droplet size in the spray [174]. The most important factors were found to be the surface tension of the fluid (related to the We number), its pressure of injection (linked to the Re number), and the densities of the fluid and the surrounding media [174–178].

Indiana et al. [179, 180] studied different configurations of impinging-jet injectors in a small-scale liquid rocket engine burning hydrogen peroxide and ethyl-alcohol. They were able to study the effect of the We and Re numbers on mixing and combustion efficiency in their impinging jets. Using a PDA system, they characterized the size distribution of droplets in the jets using water as an accessible surrogate to avoid potentially damaging the PDA system. To ensure that the size distribution was the same between the water and the propellants, the We and Re numbers were kept constant. Zhang et al. [181] investigated the hypergolic ignition of a colliding pair of liquid fuel and oxidizer droplets. They observed that as the We increases from 30 to 200, the ID decreases due to better mixing, higher deformation, and faster evaporation of the propellants. These studies demonstrated that the effect of spray characteristics on the ignition of liquid propellants is well documented, but whether these trends remain maintained in conditions relevant for hybrid rocket engines remains unknown.

The study presented here focuses on the use of liquid-fed injectors to atomize the oxidizer over solid hypergolic fuel pellets; a configuration closer to hybrid rocket engine conditions where the liquid oxidizer is injected into the combustion chamber as a spray. Using a PDA system and high-speed imaging techniques, three showerhead injectors were characterized at different injection pressures to determine the influence of the Weber number, the Reynolds number, and the droplet size on the hypergolic ignition of AB-doped paraffin wax and WFNA.

7.3 Experimental methods

7.3.1 Injector characterization

Three stainless steel full-cone injectors (Mist-Jet® Type AM # 0.37 (Inj1), 0.75 (Inj2) and 1.50 (Inj3), Steinen, USA, with the number corresponding to the nominal flow rate in gph at 0.28 MPa) with a spray angle of 70 ° are selected, with the discharge coefficients (C_d) calculated via mass flow rate measurements. The diameters are 0.229 mm, 0.305 mm and 0.508 mm for Inj1, Inj2 and Inj3 respectively. Water is pressurized with Helium in a range of 0.14 to 1.72 MPa as shown schematically in Figure 7.2 and the flow rate is measured using a Coriolis mass flow meter (mini CORI-FLOW™ M15, Bronkhorst, Netherlands). For each pressure, the mass flow rate is acquired for three minutes to ensure that a steady state is achieved. As expected, all three injectors follow a power law , with the mass flow rate approximately proportional to the square-root of the pressure with R^2 values above 0.99 (**Figure 7.1a**). The C_d are calculated using the following equations:

$$\dot{m}_{id} = A_{inj} \left(2\rho\Delta P\right)^{0.5} \tag{7.1}$$

$$C_d = \dot{m}_{measured}/\dot{m}_{id} \tag{7.2}$$

where $\dot{m}_{id}$ is the lossless mass flow, A_{inj} is the area of injection, ρ is the density, P is the pressure and $\dot{m}_{measured}$ is the measured mass flow.

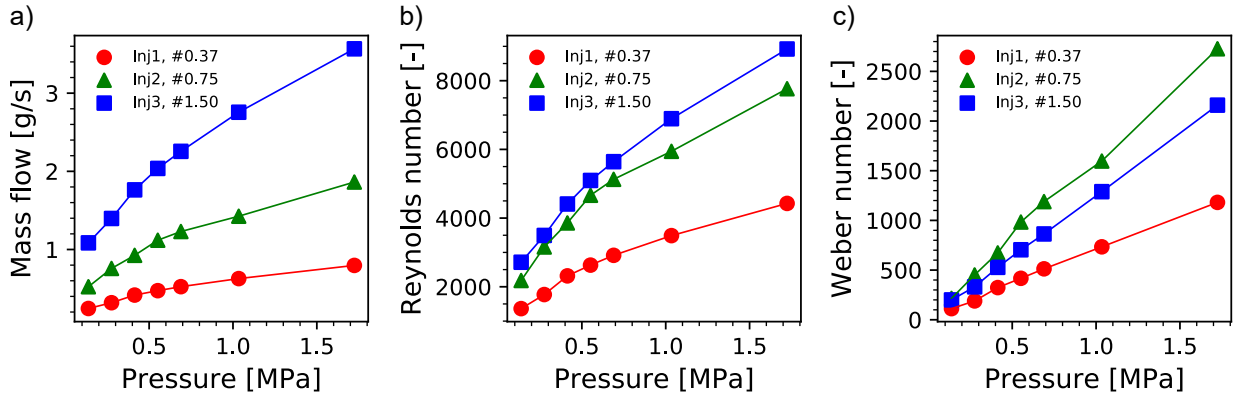

Figure 7.1 Measured spray parameters using water. a) Mass flow. b) Re number of the jet. c) We number of the jet.

For the range of pressures considered, the C_d are found to be constant with values of 0.34 ± 0.01, 0.44 ± 0.01 and 0.30 ± 0.01 for Inj1, Inj2 and Inj3, respectively.

Additionally, since the Reynolds and Weber numbers of the jets are the main non-dimensional

parameters affecting the atomization processes, they are calculated for the different liquid pressure applied (**Figure 7.1b** and **c**) using the following equations:

$$Re = \frac{\rho U d_{inj}}{\mu} \tag{7.3}$$

$$We = \frac{\rho U^2 d_{inj}}{\sigma} \tag{7.4}$$

with $U = 4\dot{V}/\pi d_{inj}^2$ and $\dot{V} = \dot{m}/\rho$, U is the velocity of the jet exiting the injector, d_{inj} is the diameter of the injector, μ is the dynamic viscosity, σ is the surface tension between the liquid and the ambient media, and $\dot{V}$ is the volumetric flow rate. Note that the We and Re numbers can be expressed for the entire jet as it exits the injector or for the individual droplets using the droplet diameters and their velocities. In the latter case, the subscript $_{drop}$ is added. The range of Re numbers varied from 1300 to 8900, with Inj1 achieving the lowest values and Inj3 the highest. However, Inj2 has the highest We numbers because it has the highest C_d. The range of Weber numbers measured varied from 100 to 2700.

Phase-Doppler anemometry measurements

PDA measurements are carried out on the sprays exiting the injectors to enable the investigation of the effect of the droplet size and velocity distribution on the hypergolic ignition. Due to safety concerns with WFNA, the PDA measurements are done using water. The spray characterization is performed in an open environment at ambient (NTP) conditions. The methodology used by Indiana et al. [179], relying on Weber and Reynolds numbers similitude, is implemented to estimate the size and velocity distributions of the WFNA droplets. First, the exit velocity of the jet is calculated using the Bernoulli equation for a range of pressures:

$$U = (2\Delta P/\rho)^{0.5} \tag{7.5}$$

Then, knowing the physical properties of water and WFNA, the Re and We numbers are calculated. This enables the identification of water injection pressures that will result in similar Re or We number for the WFNA sprays used in the combustion tests. Due to the lower surface tension between air and WFNA (0.0412 N/m) compared to water (0.073 N/m) and the higher density of WFNA (1410 kg/m^3) compared to water (998 kg/m^3), WFNA requires lower injection pressures to achieve the same We and Re numbers as water. The We number corresponding to 4 injection pressures for WFNA (0.28, 0.41, 0.55, and 0.69 MPa) are first calculated, and then the 4 corresponding water injection pressures are chosen to match the We number of the WFNA (0.49, 0.63, 0,97, and 1.21 MPa). PDA measurements

are performed on the water sprays at these pressures. The We number is used, as opposed to the Re number, since it was identified as the more relevant similarity parameter for the atomization process [175].

The PDA (112 mm Fiber PDA and FlowExplorer laser, Dantec Dynamics, Denmark) is mounted on a traverse system (Lightweight Traverse, ISEL, Germany) to allow a scan in the r-z plane of the injector, as shown in **Figure 7.2**, with increments of $\Delta r = \Delta z = 10$ mm, for a total of 5 positions in the r direction and 7 positions in the z direction . The scans are performed at each point in space for 60 seconds or for 50,000 detected droplets, whichever comes first. The PDA is operated in forward scattering mode, with an angle set to 30°, using a 300 mm lens for the laser and a 310 mm lens for the detector. Prior to each measurement, a verification of the PDA parameters is performed, with optimal values found to be 150 mW, 800V, and 18 dB for respectively the power of the laser, the anode voltage, and the gain of the detector, as shown in **Figure S1 and Figure S2**. This ensured reliable assessment of particle size with spherical and burst validations of over 80%, covering the 0 to 60 µm size range.

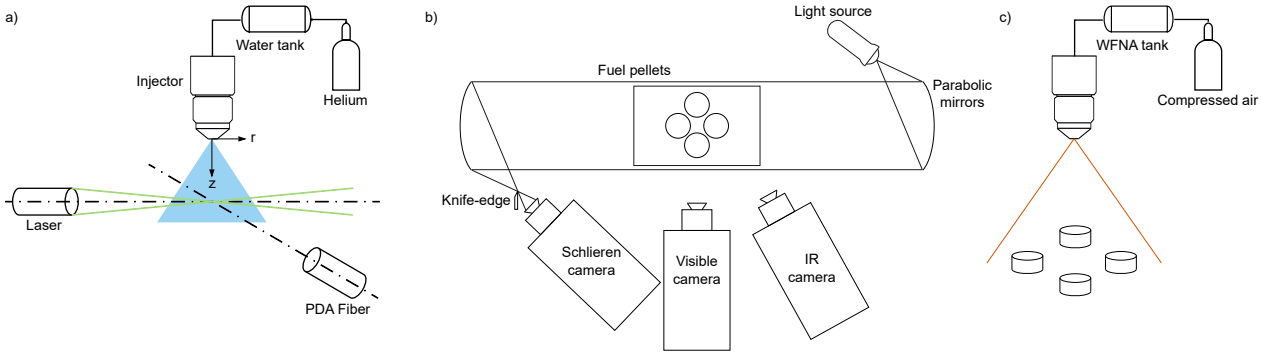

Figure 7.2 Schematic of the test setups. a) PDA measurements for spray characterization. b) Combustion tests - top view. c) Combustion tests - front view.

7.3.2 Combustion tests

Combustion experiments are carried out to assess the effect of droplet size, Weber number, Reynolds number, size distribution, and velocity of the oxidizer droplets on the ID of hypergolic hybrid fuel. Due to differences in the oxidizer droplet size distribution and local mass flux as a function of the position in the spray, both radially and axially, a fuel pellet experiences different conditions depending on its location. The PDA system directly measures the size distribution of the particles. To find the local oxidizer mass flux, the mass of each detected particle is calculated and summed over the time of the measurement, assuming

spherical droplets, with the effective sampled area calculated from the minor and major axis given by the PDA software for the detection volume. To allow the investigation of particle size and velocity uncoupled from the mass flux, pairs of conditions (pressure, injector and position) resulting in an equivalent mass flux but with different size distributions were identified. As such, the spray parameters over the fuel samples can be tested independently.

For the tests where the radial position was more than 10 mm from the center-line of the jet, up to 4 samples are placed and ignited at the same time to assess the repeatability of the ignition delay under the same conditions. For each radial position, a minimum of 4 pellets were ignited. This minimum distance was chosen to prevent the direct fire spread from one pellet to another. The fuel pellets are placed in a 3D-printed holder to expose only the top surface of the fuel and prevent the ignition from the sides.

Additionally, using the PDA measurements, the droplet Stokes number, computed using the pellet diameter as the characteristic length, varied from 0.1 to 1.2. Since this number is on the order of 1, most of the droplets are expected to follow their ballistic trajectory and impact the pellets surface, as can be seen in the Supplemental Video prior to ignition.

Image acquisition

To measure the ID, three different acquisition systems are used. The first is a high-speed camera (Fastcam Mini AX200, Photron, Japan) operating at 5,000 frames per second (fps) with an 85 mm Sigma lens, set at an F-number of 1.4 and an exposure of 1/20,000 s. This camera is mainly used to obtain color images of the ignition processes, and to identify the presence of the green flame attributed to Boron oxidation upon ignition. This camera triggers the two others by sending a TTL signal through BNC cables to ensure proper synchronization of the three acquisition systems. This camera is triggered manually before each test.

The second is a Schlieren apparatus used to clearly identify the first contact between the WFNA droplets and the fuel, as well as to reveal pre-ignition events as identified by Elzein et al. [22]. The apparatus consists of two parabolic mirrors of 107.95mm in diameter with an effective focal length of 1143mm (#50-051, Edmund Optics, USA). The light source is a fiber illuminator halogen lamp (#OSL2, Thorlabs, USA). An iris is placed in front of the source, with a 1.5mm aperture (#M-ID-1.0, Newport, USA). The images are recorded using a monochrome high-speed camera (Phantom V310, Vision Research, USA) with a 105 mm lens operated at 5,000 fps, set at an F-number of 1.4 and exposure of 1/5,000 s. The time difference between the first contact identified by the Schlieren apparatus and the first light emission recorded by the high-speed camera is the measured ID.

Finally, a mid-infrared high-speed camera (MS FAST M350, Telops, Canada) is used for *in-situ* measurement of the fuel surface temperature prior to the hypergolic ignition. The camera is operated at 700 fps with a 50 mm lens, with a low exposure of 1/20,000 s to prevent saturation. The results are analyzed by taking into account all pixels contained within the surface of the pellet, and thus computing an average surface temperature.

Pellet fabrication

To make the fuel pellets, paraffin wax is grounded to obtain a powder, which is then sifted with a sieve shaker to obtain a granulometric range between 212 and 500 µm. The AB is also grounded and sifted manually to obtain a granulometric range between 250-600 µm. The powdered AB is mixed with the powdered paraffin to obtain a mass concentration of 20% AB in the fuel. A custom aluminum die and mold set is used to compress the fuel mixture with a pressure of ca. 10 MPa. The pellets formed with this process have a thickness of 6 mm and a diameter of 9.5 mm.

7.4 Results and discussion

7.4.1 Spray characterization

The three injectors show similar trends in their droplet size distribution. For all tested pressures, the PDA measurements show a smaller D_{50} at the center-line compared to the edge of the conical jet. At $r = 10$ mm, the size distribution follows a log-normal law (**Figure 7.3a**). At $r = 20$ mm, the spray begins to transition to a bi-modal distribution (**Figure 7.3b**). At $r = 40$ mm, the bi-modal distribution is well defined, with a small cluster around ca. 15 µm and a larger peak at ca. 45 µm (**Figure 7.3c**). The velocity magnitude (w) of the droplets also shifted from higher velocities near the center of the jet, to lower velocities at the edges of the spray (**Figure 7.3**). The results clearly show that, for all the radial positions, the bigger droplets have a higher total velocity than smaller droplets.

The median droplet diameter (D_{50}) is used for comparisons here as Kooij et al. [174] showed a direct link between this parameter, the We number, and the injector dimensions. The injection pressure, as well as the radial and axial distances from the injector, affect the D_{50} across the spray. As the axial distance from the injector increases, the droplet size also increases at the center of the spray. This is likely due to the recombination and agglomeration of smaller droplets into larger ones, converging to the same size observed on the spray edges (**Figure 7.4**a). Increases in the injection pressure are found to decrease the diameter of the droplets (**Figure 7.4**b). The complete data of the D_{50} for each injector r and z positions is

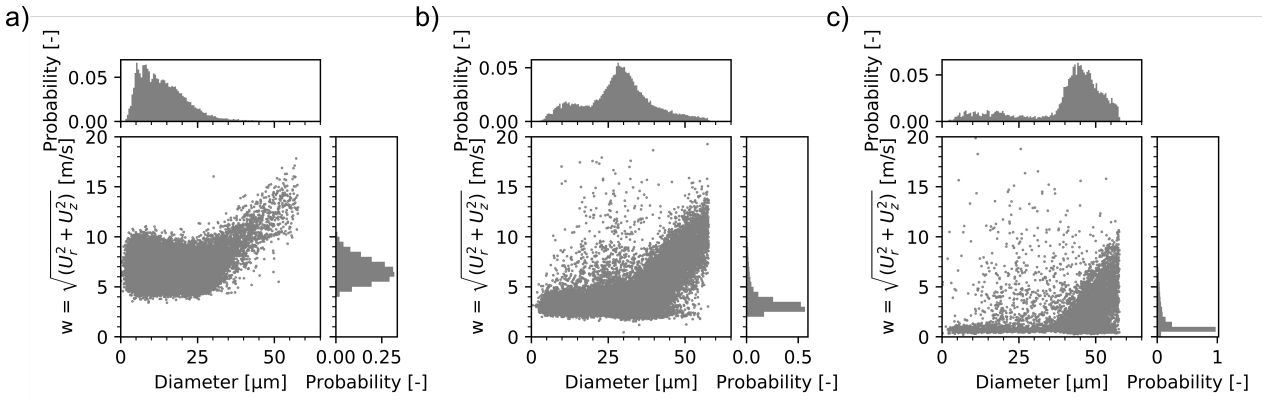

Figure 7.3 Velocity magnitude (w) and diameter of the droplets and their probability distribution. P = 0.73 MPa and z = 70 mm using water. a) r = 10 mm. b) r = 20 mm. c) r = 40 mm.

presented in Figure S3 through Figure S9.

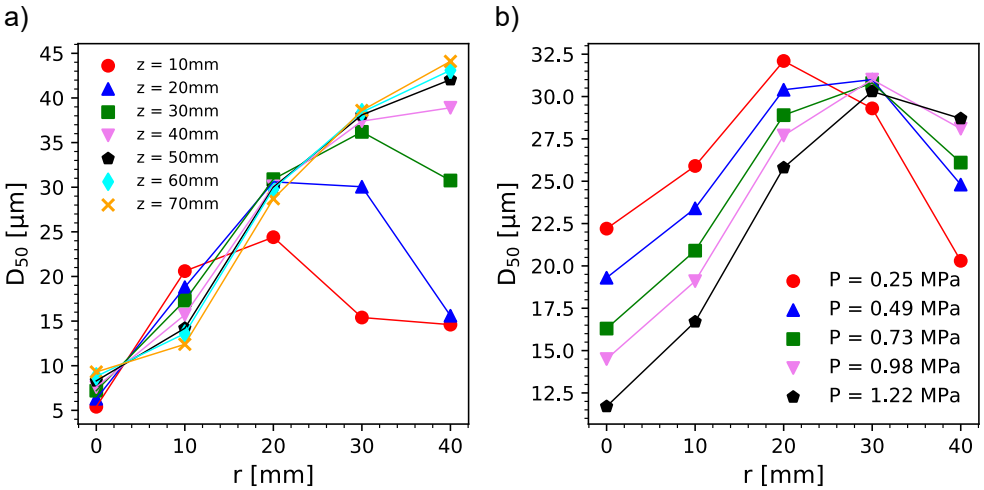

Figure 7.4 a) Effect of the radial and axial injection distances on the droplet size across the spray at P = 0.73 MPa for Inj3 using water. b) Effect of the injection pressure on the droplet size at z = 50 mm for Inj3 using water.

Using the droplet size as well as the r- and z-axis velocities, allowed the calculation of the droplet Weber and Reynolds numbers, using Eqs. 7.3 and 7.4. The range of We_{drop} calculated varies is from 0.8 to 24.1.

7.4.2 Ignition delay

The identification of the first contact between the oxidizer and the fuel is done using the Schlieren images, providing high contrast between the individual droplets and the relatively uniform background. The moment of ignition, defined as the first appearance of a green flame, is found using the color images. An example of each sequence obtained is presented in **Figure 7.5** showing 4 pellets at $r = 30$ mm and $z = 50$ mm with the oxidizer injected at a pressure of 0.41 MPa and $We_{drop} = 1.02$. The images obtained with the Schlieren apparatus during the combustion phase are obstructed by the large number of droplets sprayed on the sample, thus limiting the amount of image analysis that could be done. In some cases, the ignition is still discernible, and depending on the intensity of the sustained combustion afterward, the flame may or may not be seen.

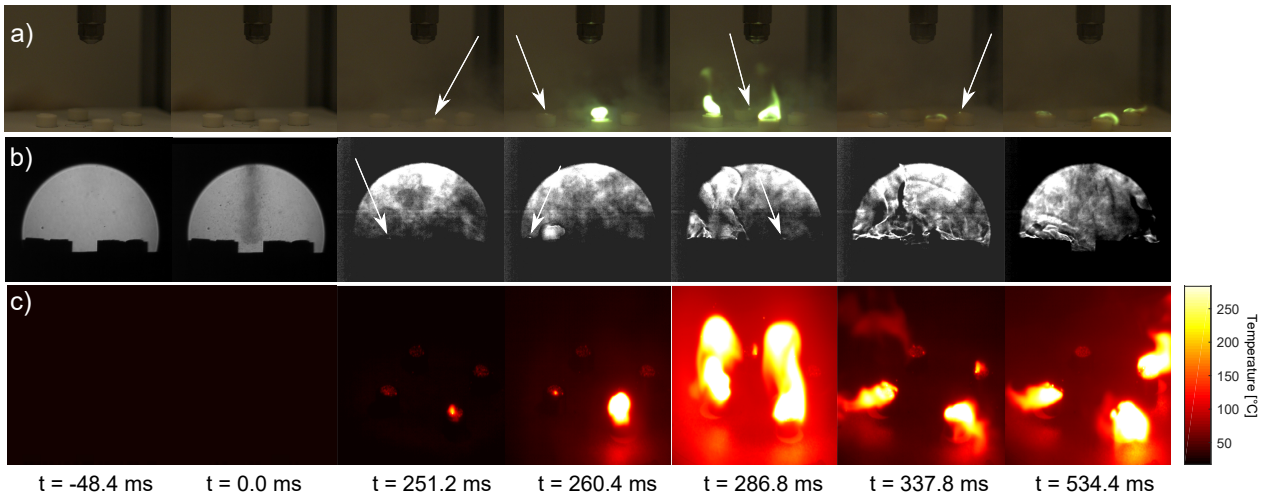

Figure 7.5 Hypergolic ignition of paraffin-AB fuel samples using a spray of WFNA. The locations of ignition are identified with the arrow. a) Color images. b) Schlieren images c) Temperature map recorded by the IR camera. Note that the viewing axis is not the same and is shifted of ca. 90° between a) and b).

For the majority of the combinations of spray parameters tested, i.e., pressure, axial and radial positions, and injectors, the IDs were superior to the ones obtained with a conventional oxidizer drop ignition test. For fuel samples containing 20 wt.% AB, an ID of 41.7(8.8) ms in drop ignition tests was measured, a value comparable with previous experiments [22]. The ID of the same fuel samples under the WFNA sprays varied from 24.2(5.9) to 1138.7(352.4) ms (**Figure 7.6**). While the majority of these tests did not reach the 50ms target value for the ID, it is known that other parameters, not evaluated here, such as the additives granulometry, increased rigidity of the fuel, catalyst addition to the fuel matrix and mass loading of additives, are efficient strategies to further reduce the ID [22,182]. Such strategies

could easily be implemented in this test configuration. Among the configuration evaluated, a clear trend could not be observed between the ID and the local mass flux or the D_{50}. The ignition delay appeared independent of these two parameters, at least within the range tested (1.9e-3 to 8.1e-2 kg/m^2·s). Other spray parameters were found to have an effect on ignition delay. These parameters are : the Re and We numbers of the jet, the Re and We numbers of the droplets, the total mass flow of the jet, and the velocity of the droplets (**Figure 7.6**). In each case, as the parameter of interest increases, the ID tends to decrease. Additionally, lower values of these parameters lead to higher variability in the ID values. This indicates that the hypergolic ignition may be less reliable at low Re and We numbers, and low droplet velocities.

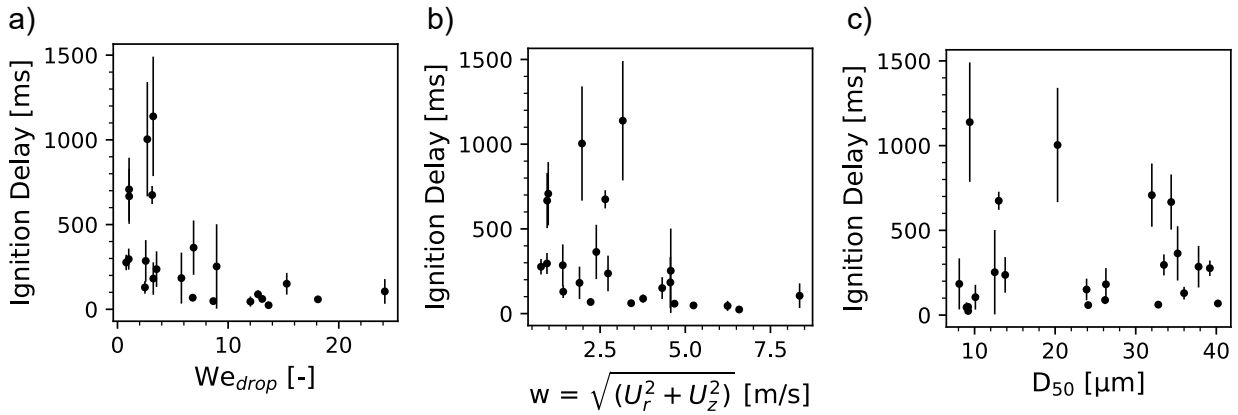

Figure 7.6 Influence of spray characteristics on the ID. The vertical lines represent the standard deviation of four pellet ignitions. a) We_{drop}. b) Total velocity. c) Median droplet diameter.

The We number reveals the combined effect of speed and diameter of the droplets on the hypergolic ignition. As the We_{drop} increases, the ID decreases asymptotically (**Figure 7.6 a**). At We_{drop} >12.0, the ID of the samples is approximately 100 ms and only further decreases by a few ms at higher values. The We_{drop} includes the combined effect of the diameter of the droplets and their velocity. These results show that the decrease in the ID with increasing We_{drop} is mainly due to the velocity of the oxidizer droplets impacting the samples rather than their diameter (**Figure 7.6b and c**). This trend was also observed by Clements et al. in drop ignition tests [64]. In their case, they hypothesized that a droplet with a higher velocity could more easily overcome the gas layer expelled by the reaction between WFNA and AB that inhibits contact between the hypergolic reactants. A higher velocity thus penetrates that protective gas layer and reduces the ID. In the experiments presented here another hypothesis is proposed, as the reaction is less violent and the combustion dynamic is different than during drop ignition tests. The higher velocity could allow the droplet to

cover more surface upon impact with the sample. This effect increases the chance of an AB grain being covered by WFNA and initiating the hypergolic ignition, thus decreasing the ID. Moreover, the asymptotic behavior reveals that at a sufficiently high We number, the hypergolic ignition is no longer controlled by the characteristics of the spray, but rather by the chemical reactions between the oxidizer and the hypergolic additive. This observation was also made by Zhang et al. [181] in the case of hypergolic liquid propellants. In their experiments, they showed that the ID decreased as the We increased until it reached a minimum value. Finally, at low We numbers the results show greater variability in the ID values. This poor repeatability is not desirable for a hybrid rocket engine using this hypergolic system, meaning that extreme care must be given to minimize the spread of measured ID values when designing such propellants. A summary of the positions tested, as well as their given results in regard to D_{50}, We_{drop} and ID is given in Table 7.1.

Table 7.1 Combustion test summary and results using WFNA and paraffin pellets with 20 wt.% AB. The ID on each line corresponds to the mean values of 4 tests. The numbers in parenthesis correspond to the standard deviation of the ID.

r [mm]	z [mm]	P [MPa]	Injector #	D_{50} [μm]	We	Re	w [m/s]	We_{drop}	Re_{drop}	ID [ms]
10	30	0.41	1	8.1	540.7	3590.0	4.56	5.78	69.84	184.0(150.6)
10	60	0.41	1	9.4	540.7	3590.0	3.17	3.23	56.24	1138.7(352.4)
20	40	0.55	1	26.3	721.0	4145.3	1.90	3.24	94.21	181.4(95.8)
20	50	0.41	1	13.8	540.7	3590.0	2.73	3.53	71.27	237.1(105.1)
20	60	0.41	1	13	540.7	3590.0	2.65	3.13	65.13	674.6(53.5)
20	70	0.69	1	20.3	901.2	4634.6	1.97	2.70	75.53	1003.8(337.2)
30	30	0.41	1	35.2	540.7	3590.0	2.39	6.88	158.88	364.0(160.3)
30	40	0.28	1	39.2	360.5	2931.2	0.77	0.79	56.71	276.6(45.6)
30	50	0.41	1	33.5	540.7	3590.0	0.94	1.02	59.55	296.1(62.0)
30	60	0.41	1	34.4	540.7	3590.0	0.95	1.05	61.46	667.0(162.7)
30	70	0.28	1	32.0	360.5	2931.2	0.98	1.05	59.12	707.8(186.6)
10	30	0.41	2	9.0	1202.7	6182.2	6.24	12.01	106.17	45.7(29.7)
10	30	0.69	2	9.2	2004.5	7981.1	6.58	13.66	114.45	24.2(5.9)
10	50	0.28	2	9.2	801.8	5047.7	5.24	8.66	91.14	48.4(18.3)
20	70	0.41	2	12.5	1202.7	6182.2	4.57	8.96	108.05	253.0(249.0)
30	50	0.28	2	36	801.8	5047.7	1.42	2.48	96.48	129.3(37.3)
40	70	0.41	2	37.8	1202.7	6182.2	1.40	2.55	100.33	285.5(122.9)
10	60	0.69	3	10.1	1562.9	9098.1	8.36	24.16	159.51	105.5(73.0)
20	30	0.28	3	32.8	625.2	5754.2	3.41	13.08	211.50	61.4(9.6)
20	50	0.69	3	24.1	1562.9	9098.1	4.68	18.11	213.34	58.8(10.9)
20	60	0.69	3	23.9	1562.9	9098.1	4.32	15.30	195.23	150.9(64.0)
20	60	0.55	3	26.2	1250.3	8137.6	3.76	12.70	186.25	88.5(23.8)
40	60	0.69	3	40.2	1562.9	9098.1	2.22	6.80	168.81	68.4(20.4)

Finally, the temperature measurements from the mid-IR camera revealed that the temperature increases as soon as the first droplets impinged the surface of the pellets. Regardless of the spray conditions, the average temperature usually reached a value of ca. 50 °C before ignition (**Figure 7.7**). Although an exact reaction mechanism of solid AB-liquid WFNA combustion is still not available in the literature, references showed that AB undergoes exothermic dehydrogenation when mixed with acids [168, 183]. Baier et al. [168] also observed the production of HBO_2 prior to the ignition of AB pellets and nitric acid. Thus, this heat release

may be attributed to the exothermic dehydrogenation of AB through AB-WFNA reactions. After the slow temperature increase, a sudden spike is measured, followed by a decrease. This increase corresponds to the first emitted green light due to the AB reacting with the WFNA. At this stage, the paraffin does not burn and HBO_2, BO_2, BO and H_2 are produced. If the combustion is sustained, the temperature gradually increased, whereas it quickly decreased when the reaction of the AB failed to ignite the paraffin matrix. Interestingly, the discrete aspect of the hypergolic ignition is revealed with the IR measurements by observing isolated hot spots on the surface achieving temperatures as high as 80°C in a few milliseconds before the first flame appeared (**Figure 7.7**). This important result confirms that only a small concentrated amount of AB is needed, or even one single AB crystal, to drive the ignition of the fuel. Furthermore, this result supports the fact that a droplet covering more surface upon impact, due to a higher velocity, will increase the likelihood of touching AB particles, and thus igniting the sample.

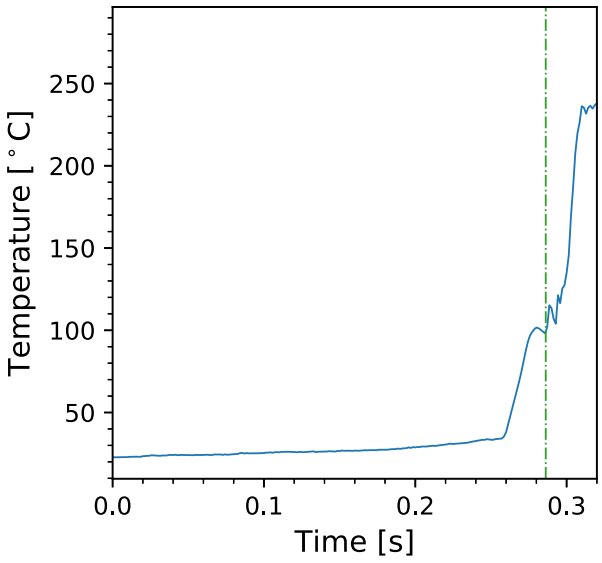

Figure 7.7 Example of the average temperature profile at the surface of the pellet measured by the mid-IR camera. The dashed vertical line represents the first visible ignition.

7.5 Conclusion

The use of hypergolic hybrid rockets for space missions is contingent on a better understanding of the ignition mechanisms which remain incomplete for liquid oxidizers and solid fuels. In this study, the combined use of spray characterization instruments (PDA system and mass flow meter) and of high-speed imaging techniques (color high-speed and Schlieren

imaging) allowed the investigation of the ignition delay (ID) of paraffin wax doped with ammonia borane, a hypergolic additive, using white fuming nitric acid as the oxidizer. The spray characteristics can greatly reduce the ID, mainly the combined effect of the droplets' velocity and diameter, characterized by Weber number. As the We number is increased, the ID decreased from values between 300 to 1100 ms until reaching a plateau at approximately 100 ms, hinting that beyond a critical We value, the hypergolic ignition is driven by other factors than the oxidizer spray. The ID of sprayed oxidizer was higher than the ID measured with conventional droplet ignition experiments. The ID values using sprayed WFNA is also higher than the 50 ms target typically deemed suitable for hypergolic additives in hybrid rocket propulsion. These results indicate that the ignition of hypergolic propellant formulation must be investigated in realistic engine conditions and that the spraying of liquid oxidizer must be further improved for hypergolic hybrid rockets, to allow for lower ID.

7.6 Acknowledgements

This work was supported by the Natural Sciences and Engineering Research Council of Canada (NSERC) Discovery Grant RGPIN-03622-2014; NSERC CGS M (to O.J. and B.D.), and ES D scholarships (to O.J.); Canadian Space Agency Flights and Fieldwork for the Advancement of Science and Technology (FAST) funding initiative grant 18FAPOLB17.

7.7 Supplementary material

Supplementary material and videos associated with this article can be found in the online version.

CHAPTER 8 HYPERGOLIC IGNITION OF HYBRID ROCKET FUELS IN A SLAB BURNER EXPERIMENT

8.1 Summary of the chapter

Hypergolic ignition systems, where combustion is initiated nearly instantaneously upon contact between the oxidizer and the fuel, can improve the reliability, safety, and simplicity of hybrid rocket engines. Hypergolic performance, namely the ignition delay, is of critical importance as it determines the response time of the propulsion system. To evaluate this performance metric, a novel slab burner experiment is developed to study the hypergolic behavior of hybrid rocket propellants in an engine-like configuration. The liquid oxidizer injection system and the flow conditions implemented in this slab burner are characterized in detail. Two types of experiments are presented. In the first, nitric acid is used essentially for ignition and is injected into a combustion chamber containing a paraffin-based fuel slab doped with ammonia borane and filled with gaseous oxygen. Rapid hypergolic ignition with nitric acid and sustained combustion with gaseous oxygen are observed. In the second experiment, concentrated nitric acid is injected into a combustion chamber under an inert atmosphere resulting in significantly slower ignition. The experiments are filmed with a high-speed camera to measure the hypergolic ignition delays and their locations. In addition, the reignition capability of these two systems is evaluated. Successful reignitions are observed with delays greater than the initial hypergolic ignition.

8.2 Context of the work

Hybrid rocket engines have the potential to ease access to space through their inherent safety and simplicity of operation compared to solid or liquid rocket engines. One way to further enhance the simplicity and reliability of hybrid propulsion is through the use of hypergolic ignition systems. Such systems allow the elimination of complex and heavy ignition systems such as spark igniters or pyrotechnics. In addition, a hypergolic ignition system gives the engine re-ignition capability, which is desirable for various missions and operations, such as in-space propulsion for intermediary burns, orbital correction maneuvers, and reaction control systems (RCS).

The introduction of hypergolicity into hybrid rocket engines is typically accomplished by

embedding additives in a fuel binder. These additives exhibit hypergolic behavior with the oxidizer, ideally achieving ignition within milliseconds of initial contact between the reactants. Notable hypergolic additives include ammonia borane (AB, BH_3NH_3) [19,22,33,51,61,64,121], metal-organic frameworks [39, 40, 120], sodium amide ($NaNH_2$) [69], sodium borohydride ($NaBH_4$) [52, 65, 66] and potassium bis(trimethylsilyl)amide (PBTSA, $KSI_2C_6NH_{18}$) [69]. For hybrid propulsion systems, they are usually incorporated into a fuel such as paraffin wax, low or high-density polyethylene (LDPE or HDPE, respectively), or sorbitol. Investigated oxidizers are mainly some type of nitric acid (HNO_3) such as concentrated nitric acid, white fuming nitric acid (WFNA) or red fuming nitric acid (RFNA), concentrated hydrogen peroxide (H_2O_2), nitrogen tetroxide (NTO, N_2O_4) or mixed oxides of nitrogen (MON).

Droplet ignition tests are simple and convenient experiment for evaluating the hypergolic behavior of fuel-oxidizer combinations. In this test configuration, a large oxidizer droplet is generated from a syringe and is released from a fixed height, ultimately impacting a fuel pellet containing the hypergolic additives. The ignition is usually recorded with a high-speed camera to measure the delay between the first contact of both propellants and the first visible flame. In this configuration, interesting parameters such as droplet velocity, diameter, fuel surface roughness, storage conditions, additive content in the fuel, and ambient pressure have been identified as influencing the ignition delay [64,66]. Although useful for evaluating the ignition delay, this type of experiment does not reflect the conditions encountered in hybrid engines, namely oxidizer injection as a gas or through multiple small droplets, shear flow at the fuel surface, turbulence, and the enclosed volume. In fact, droplet ignition experiments are often conducted under ambient atmosphere with air as the surrounding gas. As highlighted by Nath et al. [66], the medium in which the experiments are conducted greatly affects the ignition delay of hypergolic fuels. For example, they showed that the ignition delay was reduced by 48 % when argon was used as the surrounding gas, as opposed to air, and that helium completely inhibited the ignition, likely as a result of its high thermal diffusivity.

Recent studies have begun to evaluate hypergolic performance under engine-like conditions. A previous study by Jobin et al. [121] and the work of Nath et al. [77] investigated the hypergolic ignition of hybrid fuels under oxidizer sprayed from injectors, as can be the case in an engine. Both groups reported higher ignition delays compared to droplet ignition tests. Nath et al. used an additive content of 25 wt.% $NABH_4$ in a HDPE fuel matrix and 90% hydrogen peroxide injected at a rate of 2.5 ml/s. They performed a single ignition test in which they observed multiple ignition kernels lasting 3 to 5 ms, but no sustained flame. In our previous experiments using AB and paraffin fuel samples and concentrated nitric acid as the oxidizer, the results showed a relationship between the ignition delay and the droplet Weber number of the sprayed oxidizer [121]. In this case, a Phase Doppler Anemometer

(PDA) system was used to measure the conditions across the spray from three different injection nozzles. An increase in velocity tended to decrease the ignition delay, likely due to the droplets covering more of the surface with a thinner layer of liquid as they hit the sample. In these experiments, ignition delays ranging from 24 to 1138 ms were measured depending on the spray conditions with most of the sample undergoing sustained combustion.

Two recent investigations have tested a hypergolic ignition system in an engine-like configuration. Benhidjed-Carayon et al. [73] designed and tested a 2-in diameter engine to evaluate the combustion and ignition performance of a paraffin-based fuel with either sodium amide or PBTSA as the hypergolic additive and MON-3 as the oxidizer. They reported stable combustion, high performance and low ignition delays on the order of 100 to 200 ms. The additive content varied throughout the length of the fuel, with the first section where the oxidizer directly impinges on the fuel having a 90 wt.% hypergolic additive content. In addition, they were able to successfully demonstrate the reignitability of the engine. However, having such a high additive content resulted in a locally excessively high regression rate. They concluded that in this configuration, a combustion time greater than 2 seconds would not be sustainable due to increased instabilities, necessitating the need for other additives with lower regression rates or an improved ignition segment geometry and design.

Jeong et al. [54] designed a 25 wt.%AB, 1 wt.% Pd-C and 74 wt.% paraffin igniter for a laboratory-scale hybrid rocket engine using 95 wt.% H_2O_2 as the oxidizer. The igniter was placed in the upstream section of an optically accessible poly(methyl methacrylate) (PMMA) engine. The palladium-carbon material helps to reduce the ignition delay due to the catalytic properties of Pd with hydrogen peroxide. Thus, this igniter relies on both the hypergolic reaction between AB and H_2O_2 as well as the catalyzed thermal decomposition of H_2O_2 when in contact with the palladium.

The use of laboratory-scale engines, as in these two studies, is a valuable method for evaluating rocket performance parameters such as specific impulse (I_{sp}) or characteristic velocity. However, in the first investigation, the lack of optical access prevents the visualization and further study of the hypergolic ignition in an engine configuration. In the study performed by Jeong et al. [54], although their engines were optically accessible due to the translucency of PMMA, the igniters burned out completely after only a few seconds, making engine relighting impossible. These observations therefore justify the need to perform visually accessible hypergolic tests in an engine-like configuration, which is the focus of this paper.

The first objective of this study is to design a novel hypergolic slab burner that allows the visualization of the ignition process in a configuration closer to those encountered in a hybrid engine. It implements an injection system that accommodates a liquid oxidizer. In this

case, the oxidizer used is 90 wt.% concentrated nitric acid, whereas the fuel is paraffin wax with ammonia borane (AB) as the hypergolic additive. The spray ignition is characterized in detail using a PDA system. The hypergolic slab burner can be operated in two modes, representing different scenarios. The first is the use of nitric acid for ignition, in conjunction with a secondary oxidizer, gaseous oxygen (GOx) in this case, to sustain combustion of the paraffin-based fuel. The second mode of operation is to provide only the liquid oxidizer in the combustion chamber, both to initiate the combustion and to sustain it. The novel research facility is then used to observe and characterize the hypergolic ignition process, quantifying critical parameters such as the ignition delay and its location along the fuel slab. The location is compared against the results from the spray injector characterization campaign. The flame intensity and its location over the fuel length is also discussed. The reignition of the fuel slabs is investigated and successfully demonstrated. Finally, the regression rate of the fuels compositions is presented.

8.3 Materials and methods

8.3.1 Slab burner visualization experiment

The slab burner used for this work is adapted from previous experiments conducted at Polytechnique Montréal (see Chapter 5). The test facility consists of three sections: a stabilization chamber and a combustion chamber, with a new spray injection section introduced between them. A picture and a schematic representation of the slab burner are shown in Figures 8.1 and 8.2. The design of the stabilization and the combustion chambers are already discussed in a previous research article (see Chapter 5), but the injection section is discussed in further details here since it is part of the novelty of this work.

The injection plate is a square measuring 254 mm by 254 mm and is 31.8 mm thick. It has an opening in the center with the same dimensions as the combustion chamber, i.e., a square cross-section of 50.8 by 50.8 mm. The part is made of the same material as the other parts of the slab burner, 304L stainless steel. On the top of the square channel, a 101.6 mm (4 in.) long hole extends from the opening to the top of the plate. A 1/4 in. diameter stainless steel tube (Swagelok, USA) is inserted into this hole. The tube is secured to the top with an NPT tube fitting, and its other end is bent at a 90-degree angle to enter the combustion chamber. An injector (MC41024, Mistcooling, USA) is secured onto the end of the tube. It has a diameter of 0.3 mm and the flow pattern results in a full cone spray. This injector was selected for its small outside diameter, low flow rate, and compatibility with concentrated nitric acid. Since the injector is placed directly in the flow coming out of the stabilization

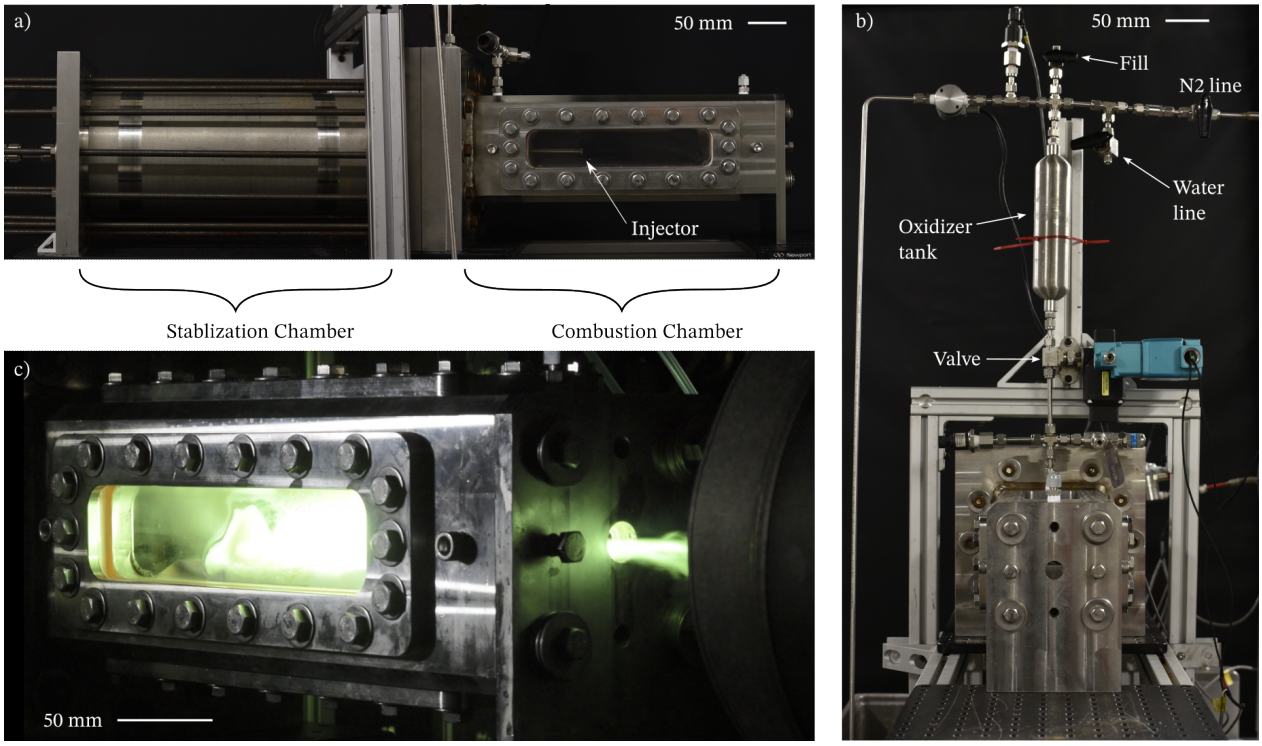

Figure 8.1 a) Side view of the hypergolic slab burner. b) Front view of the burner. c) A test in the hypergolic slab burner.

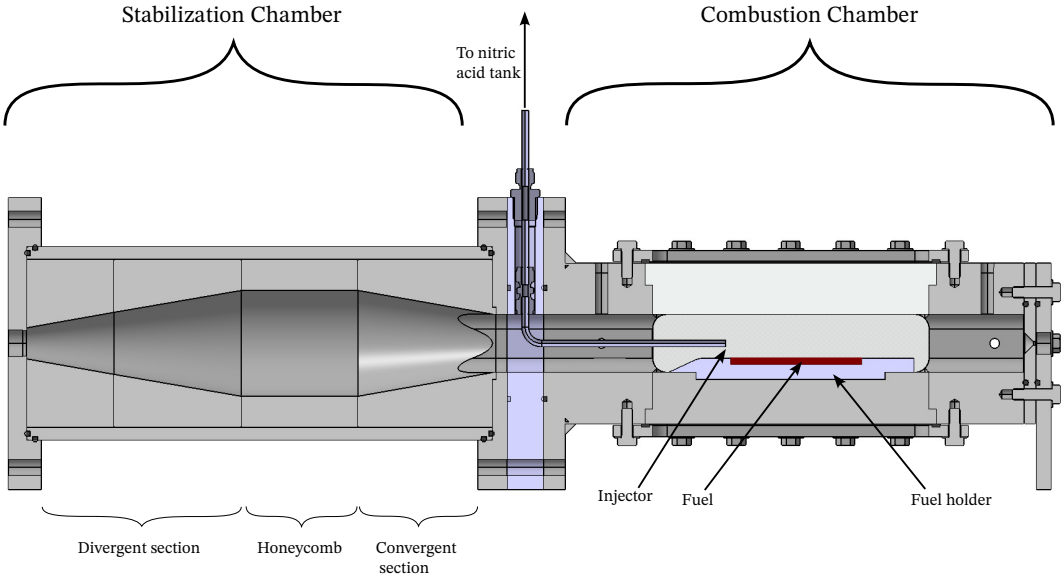

Figure 8.2 Detailed section view of the hypergolic slab burner.

chamber, its diameter footprint had to be as small as possible to avoid large turbulent flow structures induced by its presence. Section 8.4.2 covers the characterization of the flow field in

the presence of the injection system. Finally, the injection tube is connected to a pressurized nitric acid tank as shown in the Piping and Instrumentation Diagram (P&ID) in Figure 8.3. The mass flow rate of nitric acid is controlled by changing its static pressure in the tank.

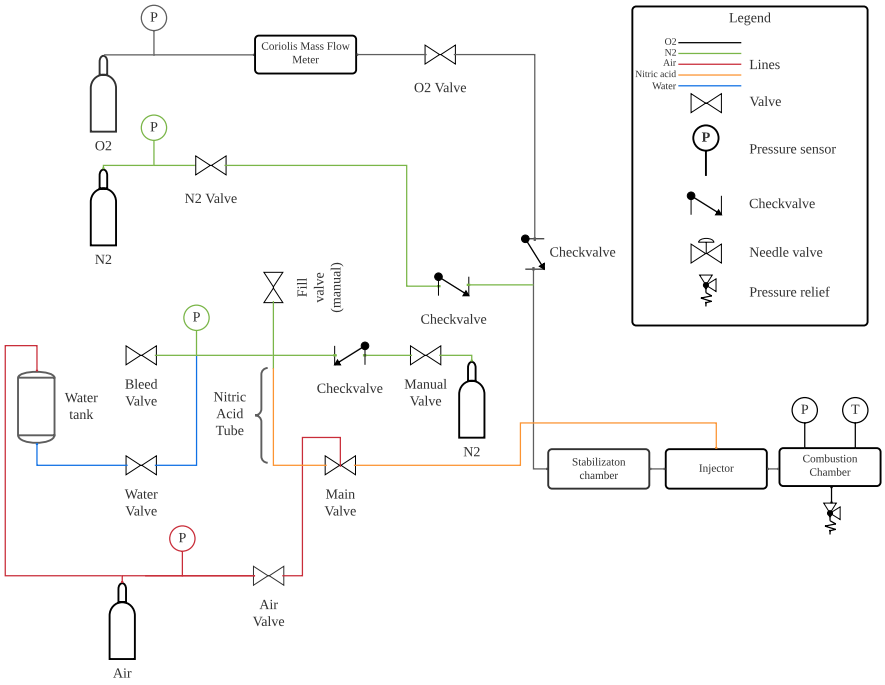

Figure 8.3 Piping & instrumentation diagram of the hypergolic slab burner.

8.3.2 Fuel preparation

The fuel is composed of paraffin wax (FR5560, Candlewic, USA) and ammonia borane (#900-1016, Boron Specialties LLC, USA). The paraffin is received in slabs while AB is purchased in powder form. The paraffin is ground into powder using a standard electric blade grinder, into which a small amount of dry ice is mixed to the paraffin. The dry ice prevents powdered paraffin to reagglomerate due to the heat generate by friction of the blades. Both powders are then sieved through meshes to obtain a granulometry of 212-500 µm. The components are weighed using a milligram scale (NewClassic MF MS304S/03, Mettler Toledo, Switzerland) and thoroughly mixed in a custom Y-mixer to the desired mass ratio. Approximately 25 g of the fuel mixture is placed in a rectangular press mold measuring 114.3 mm (4.5 inches) by 50.8 mm (2.0 inches) with a thickness of 12.7 mm (0.5 inches). The mold is placed and pressed in a 20-ton hydraulic press (Model M, Carver Laboratory Press, USA). Prior to insertion into the slab burner, the fuel slab surface is lightly brushed to remove any remaining powder or impurities on the surface. The surface is left intact, neither cut nor sanded. The fuel slab

is glued to a 304L stainless steel fuel holder. The fuel holder has a shape similar to what is commonly reported in the literature with a forward facing ramp of 25 degrees, which reduces instabilities and recirculation zones as opposed to a sharp leading edge [104, 112]. The fuel holder design is shown in Figure 8.4.

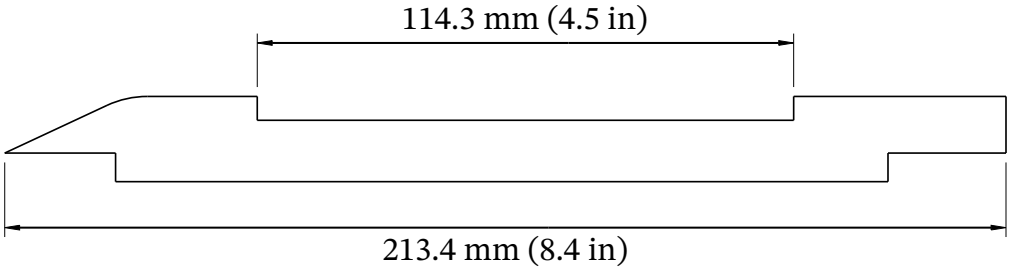

Figure 8.4 Side view of the design of the fuel holder. The width of the piece is 50.8 mm (2 in), same as that of the combustion chamber.

8.3.3 Video acquisition and analysis

The experiments are filmed with a high-speed camera (Fastcam Mini AX200, Photron, Japan). The camera is pointed toward the inside of the combustion chamber, covering the entire fuel slab. A 105 mm lens is mounted on the camera, which typically results in a spatial resolution of approximately 10 pixels per mm. The high-speed camera video is analyzed to determine the ignition delay, defined as the time between the first droplets exiting the nozzle and the first flame, with a typical first contact time of approximately 3 to 5 ms. The location of the first ignition kernel is also identified to correlate ignition with oxidizer spray dynamics.

8.3.4 Tests procedure

First, the hypergolic slab burner is used to evaluate the suitability of a hypergolic igniter system in a paraffin/oxygen hybrid engine. In this case, an oxygen flow is stabilized in the test section by supplying oxygen for a few seconds before a small amount of nitric acid, 5 to 10 ml, is sprayed through the injector. The hypergolic reaction between AB and the nitric acid is sufficient to melt the paraffin and start the slab combustion. After a set time, usually 3 seconds, the nitric acid spray is stopped and the fuel reacts only with gaseous oxygen. After the test, the nitric acid tank is refilled and pressurized to reignite the fuel sample by performing the test procedure a second time.

In the second test configuration, the combustion chamber is filled with nitrogen prior to nitric acid injection to ensure that ambient air does not contribute to the ignition or to the

sustained combustion. The pressurized nitric acid is then sprayed into the chamber, initiating hypergolic ignition. Combustion is maintained as long as the nitric acid continues to be sprayed. The test is terminated after 10 seconds when the injection of oxidizer is stopped. Reignition is also evaluated by performing the test procedure a second time without removing the fuel slab from the chamber.

In both cases, the flame is quenched by purging the stabilization and combustion chambers with nitrogen at the end of the test. Before removing the fuel sample, the nitric acid tank and injector are rinsed with distilled water. Extensive safety precautions are taken during the tests, including the wearing of acid-resistant gloves, boots, and a protective hazmat suit (Tychem 5000, DuPont, USA) sealed with nitric acid-resistant tape, and a face shield with organic vapor cartridges.

8.4 Results

8.4.1 Spray characterization

The oxidizer injector mass flow is first characterized at three different pressures (0.68 MPa, 1.72 MPa and 3.45 MPa) using water as a surrogate for nitric acid due to its highly corrosive nature. This method allows the mass flow to be estimated using only the acid pressure, without the use of a flow meter. First, the water is pressurized with nitrogen to a given pressure. A valve located between the injector and the water tank is then opened. The mass flow is measured using a Coriolis mass flow meter (mini CORI-FLOW^{TM} M15, Bronkhorst, The Netherlands). The valve is left opened for a few seconds to allow the mass flow signal to stabilize and the procedure is repeated for all pressures with the results are shown in Figure 8.5 a). A fitted curve in the form of $y = mx^n$ is calculated with an R^2 value of 0.981 and an exponent n equal to 0.49. Finally, the results are converted from a water mass flow rate to a nitric acid flow rate using the following equation:

$$\dot{m} = C_d A \sqrt{2\rho\Delta P} \tag{8.1}$$

where $\dot{m}$ is the mass flow, C_d is the discharge coefficient, A is the injector area, ρ is the density of the fluid, and ΔP is the static pressure difference between ambient conditions and the water tank pressure. When water is used as the fluid, C_d is calculated knowing all the other parameters. For the tested injector, C_d is 0.318 $\pm$ 0.012 and is constant over the tested pressure range. For a pressure swirl injector, C_d is independent of the Reynolds number (Re) for values above 3000, which is the case for the test conditions here. [175].

Thus, using this discharge coefficient value, the steady-state water mass flow is converted in a steady-state nitric acid mass flow by knowing its density and pressure during the slab burner tests. This allows the mass flow to be obtained even though the acid is not compatible with the Coriolis flow meter. The Re and Weber (We) numbers are also calculated as they are important non-dimensional parameters related to spray atomization, calculated using the following equations:

$$Re = \frac{\rho U d_{inj}}{\mu} \tag{8.2}$$

$$We = \frac{\rho U^2 d_{inj}}{\sigma} \tag{8.3}$$

with $U = 4\dot{V}/\pi d_{inj}^2$ and $\dot{V} = \dot{m}/\rho$, U is the velocity of the spray exiting the injector, d_{inj} is the diameter of the injector, μ is the dynamic viscosity, σ is the surface tension between the liquid and the surrounding media, and $\dot{V}$ is the volumetric flow rate.

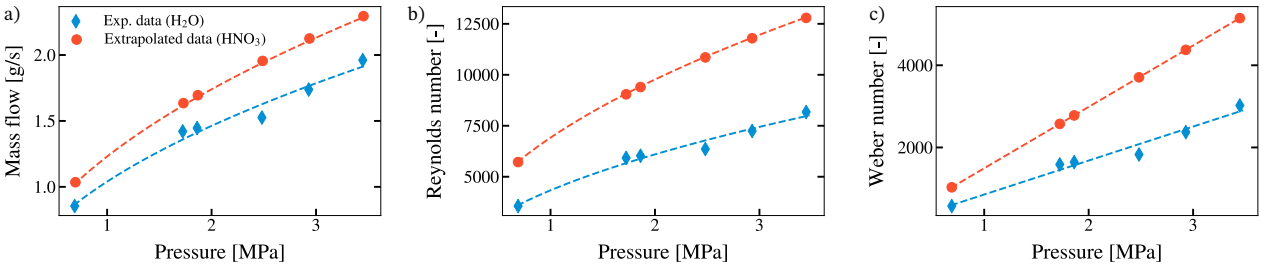

Figure 8.5 Experimental results using the mass flow meter. a) The mass flow as a function of the tank static pressure. b) Reynolds number as a function of the tank static pressure. c) Weber number as a function of the tank static pressure

A PDA system (112 mm Fiber PDA and FlowExplorer laser, Dantec Dynamics, Denmark) is also used to characterize the spray parameters. Measurements are taken with water and with the injector inside the combustion chamber of the slab burner, with and without the use of an oxidizer co-flow. They are conducted at the center of the spray coming out of the injector at a fixed height. This height corresponds to the fuel height, i.e., the location where the oxidizer droplets hit the fuel surface and subsequently lead to hypergolic ignition. The rationale of these measure is to determine the droplet conditions that lead to ignition. The PDA is mounted on a traverse system (Lightweight Traverse, ISEL, Germany) to allow scanning in the longitudinal directions. The scans are performed at each point in space for 180 seconds or for 5,000 detected droplets, whichever comes first. The PDA is operated in forward scattering mode, with an angle set to 30°, using a 300 mm lens for the laser and a 310 mm lens for the detector. Six longitudinal positions are measured for each pressure. The measured median velocities and median droplet diameters (D_{50}) are shown in Figure 8.6.

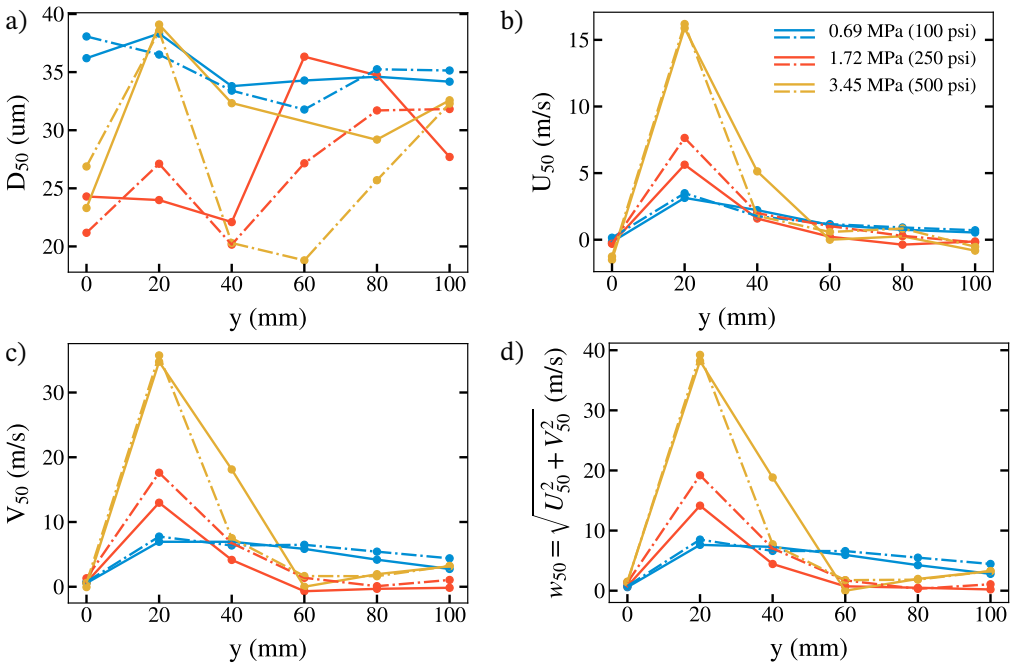

Figure 8.6 Spray results from the PDA system. a) Median diameter b) Median horizontal velocity. c) Median vertical velocity d) Median total velocity. ━━━ refers to the tests when GOx is used, ┅┅┅ refers to the conditions when only nitric acid is used.

Figure 8.6 a) reveals that the median droplet diameter is largest at an injection pressure of 0.69 MPa (100 psi) and remains constant along the length of the fuel. As the injection pressure is increased, a variation of D_{50} is observed along the length of the fuel and is smaller than at 0.69 MPa (100 psi). This is due to the spray exiting the injector at a higher velocity, resulting in a higher We number and increased atomization efficiency. Adding the GOx co-flow does not drastically change the D_{50} values. The median droplet diameter is approximately 37 µm for a water injection pressure of 0.69 MPa (100 psi) and between 20 and 40 for pressures varying from 1.72 MPa (250 psi) to 3.45 MPa (500 psi). Figure 8.6 b) to 8.6 d) clearly illustrate the region where the droplets hit the fuel slab at the highest velocity. The median total droplet velocity (w_{50}) is maximum at 20 mm from the injector tip and reaches values of 7.6, 14.1, and 38.2 m/s at water pressures of 0.69 MPa (100 psi), 1.72 MPa (250 psi), and 3.45 MPa (500 psi), respectively, without the GOx co-flow. The addition of the co-flow slightly increases w_{50} to maximum values of 8.5, 19.2, and 39.2 m/s.

To directly compare the results from the PDA system using water to nitric acid as the fluid, a similarity study is performed. This method relies on comparing results based on the Weber number, as opposed to the Re number, since the former is a more relevant similarity parameter for the atomization process [175]. The Weber number similarity comparison follows

the methodology used by Indiana et al. [179] to estimate the size and velocity distributions of the nitric acid droplets in the spray.

First, the spray velocity of a nitric acid is calculated using the Bernoulli equation for a range of pressures:

$$U = (2\Delta P/\rho)^{0.5} \tag{8.4}$$

using the physical properties of density, dynamic viscosity, and surface tension of nitric acid. A corresponding Re and We are computed using Eqs. 8.2 and 8.3, where the previously computed velocity is factored by the discharge coefficient of the injector. Finally, water and nitric acid static pressures which give the same Re and We are identified and are shown in Table 8.1. The droplet diameter and velocity in the spray is expected to follow the same behavior, i.e., the same D_{50} and w_{50}, at the same Weber number, regardless of the fluid. This methodology allows spray characterization studies to be performed in a safer manner by using water instead of nitric acid to conduct these experiments.

HNO_3 Pressure [MPa (psi)]	Equivalent H_2O pressure [MPa (psi)]	
	Re similarity	We similarity
0.34 (50)	0.88 (127)	0.70 (101)
0.69 (100)	1.76 (255)	1.40 (203)
1.38 (200)	3.52 (510)	2.79 (405)
1.72 (250)	4.39 (637)	3.50 (507)

Table 8.1 Equivalent water pressure required to match the Re or We numbers of the nitric acid pressure.

8.4.2 Flow field characterization

The presence of the injector tube in the combustion chamber can create unwanted turbulence in the flow and act as a passive turbulent device that increases the regression rate of the fuel [126] when tests are conducted using GOx. It is then not possible to use previous velocity and turbulence intensity profiles obtained using hot wire anemometry in the combustion chamber and reported in Jobin et al. (see Chapter 5). Furthermore, the presence of the tube inside the chamber complicates the use of a hot wire anemometry probe to extract velocity measurements. Therefore, the velocity measurements are also performed using the PDA system with the configuration parameters presented above. First, the flow is seeded with Di-Ethyl-Hexyl-Sebacat (DEHS) aerosol droplets with a mean diameter of 0.8 µm produced by an aerosol generator (Atomizer Aerosol Generator ATM 221, Topas GmbH, Germany). The aerosol is injected before entering the stabilization chamber. These droplets are good

tracers for velocity measurements since they follow the streamlines of the flow due to their small diameter.

The PDA system is used to measure the velocity of each DEHS droplet passing through a measurement volume. The PDA is also mounted on a traverse, this time to allow scanning in both the fuel length and vertical directions. The scan sheets are taken at the mid-plane of the lateral direction of the combustion chamber. In total, 252 spatial positions are scanned, with 14 positions in the fuel length direction and 18 positions in the vertical direction, corresponding to spatial increments of 10 mm and 2 mm, respectively. The scans are performed at each spatial position for 60 seconds or for 10,000 detected droplets, whichever comes first. The turbulence in the flow is also quantified by the relative turbulence intensity, which is calculated using the following equation:

$$T = \frac{V_{rms}}{\bar{V}} \tag{8.5}$$

where V_{rms} is the root mean square of the velocity and $\bar{V}$ is the average velocity at a given y position. In total, 2 velocity maps are measured corresponding to different oxidizer velocities, which in turn are related to two static pressures of GOx, i.e., 0.69 MPa (100 psi) and 1.38 MPa (200 psi). The results show that the presence of the injector affects the flow around it. The velocity downstream of the injector approaches zero immediately after it and gradually increases as shown in Figure 8.7. This behavior is less pronounced when the fuel holder is placed in the combustion chamber. The flow stabilizes more quickly compared to when it is not present. In addition, the turbulence intensity is at its maximum values around the injector and decreases as the flow stabilizes. Again, the presence of the fuel geometry also tends to slightly reduce the turbulence intensity as shown in Figure 8.8. The flow velocity is about 0.4 m/s at a static pressure of 0.69 MPa (100 psi) and approximately 0.7 m/s at a static pressure of 1.38 MPa (200 psi). The turbulence intensity is about 5% at a co-flow pressure of 0.69 MPa (100 psi), and between 10% to 15% at 1.38 MPa (200 psi).

8.4.3 Hypergolic tests using GOx and nitric acid

The objective of this first experiment is to measure the hypergolic performance of a paraffin-AB fuel, with gaseous oxygen as the oxidizer and nitric acid only initially to induce hypergolic ignition. This configuration is interesting because paraffin/GOx hybrid engines are one of the most studied hybrid propellants combinations. The idea is to provide information on a useful ignition system that could be implemented in existing engines as it requires minimal design changes. Two additive concentrations in the fuel are tested in this configuration, 20 wt.% and

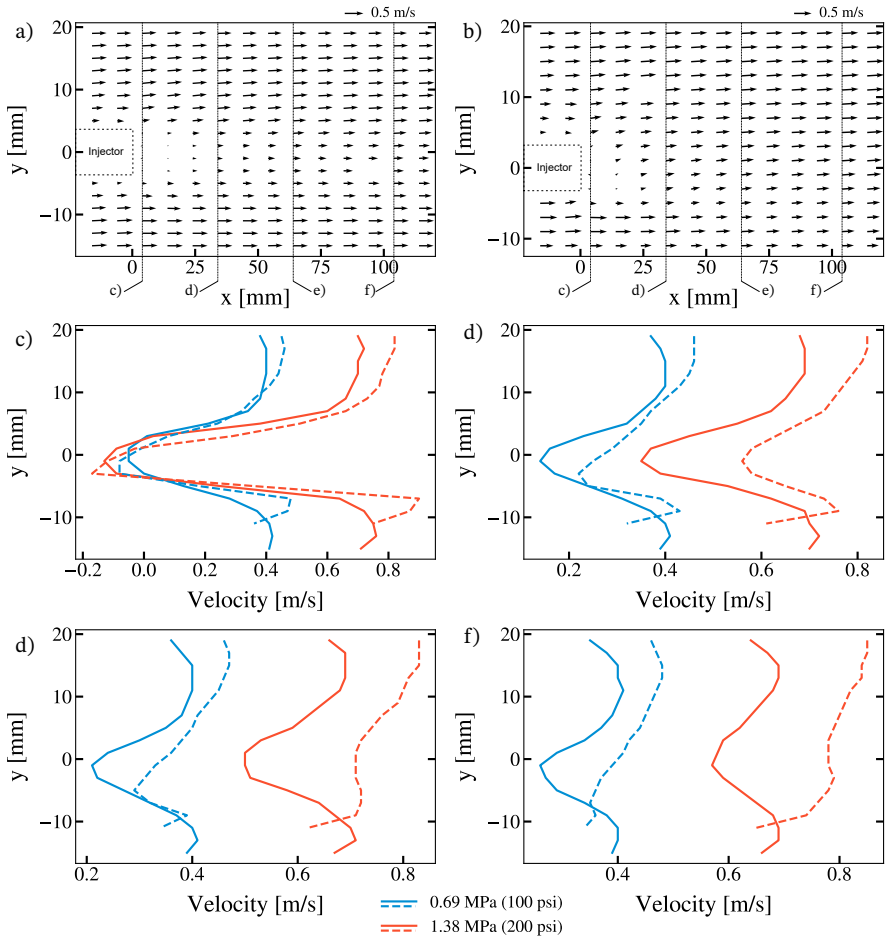

Figure 8.7 Flow field and velocity slices in the combustion chamber at two GOx co-flow static pressures. $x = 0$ mm is positioned at the tip of the nozzle. a) Flow field at 0.69 MPa (100 psi), without slab. b) Flow field at 0.69 MPa (100 psi), with slab. c) Velocity slice at $x = 4$ mm. d) Velocity slice at $x = 34$ mm. e) Velocity slice at $x = 64$ mm. f) Velocity slice at $x = 104$ mm. ━━━ refers to experiments conducted without a slab fuel, ------ refers to experiments conducted with a slab fuel.

40 wt.%, and the nitric acid injection pressure is set at 1.38 MPa (200 psi), corresponding to a mass flow of 1.45 g/s.

Visual assessment

A visual assessment of the ignition is first performed. As soon as nitric acid is injected, droplets hit the surface and begin to agglomerate to form a larger pool of oxidizer (Figure 8.9 b). Surface reactions between the nitric acid and the AB in the fuel heat the small pool of oxidizer lead to bubble formation (Figure 8.9 c). This is likely due to dehydrogenation of the ammonia borane, as discussed in Section 8.5. After reaching either a critical temperature or

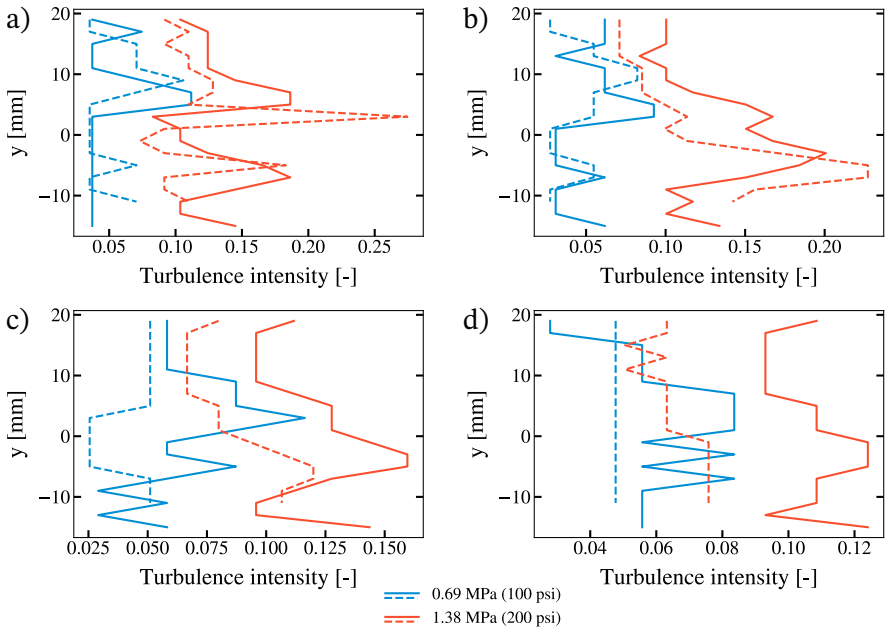

Figure 8.8 Turbulence intensity slices in the combustion chamber. The pressure is the GOx co-flow pressure. $x = 0$ mm is positioned at the tip of the nozzle. a) $x = 4$ mm. b) $x = 34$ mm. c) $x = 64$ mm. d) $x = 104$ mm. ━━━ refers to experiments conducted without a slab fuel, ------ refers to experiments conducted with a slab fuel.

concentration, a large ignition kernel, easily observed by its bright green flame color, appears (Figure 8.9 d) and propagates (Figure 8.9 e-f) in the chamber. The combustion is sustained throughout the test, even when the nitric acid injection is stopped (Figure 8.9 g).

To support the visual assessment, the intensity of the green flame is quantified using the green channel of the RGB (red, green and blue) color images. The intensity is calculated both spatially and temporally to provide time and space resolved data. Vertical flame intensity slices of 1 pixel width are extracted from the frames using the following equations:

$$I\left(t\right) = \sum_{x=0}^{x=x_{max}} \sum_{y=0}^{y=y_{max}} I(x,y) \tag{8.6}$$

$$\bar{I}\left(t\right) = \frac{I\left(t\right)}{max\left(I\left(t\right)\right)} \tag{8.7}$$

where I is the green channel value of the pixel in the frame, on a scale from 0 to 255, x is the x-axis in the fuel length direction, y is the y-axis of the frame, i.e, the normal direction of the fuel edge, t is the time, and $\bar{I}$ is the normalized intensity.

Using the light intensity as a proxy, these equations allow the evolution of the combustion to be tracked. For example, Figure 8.10 shows the intensity signal over the fuel length for various

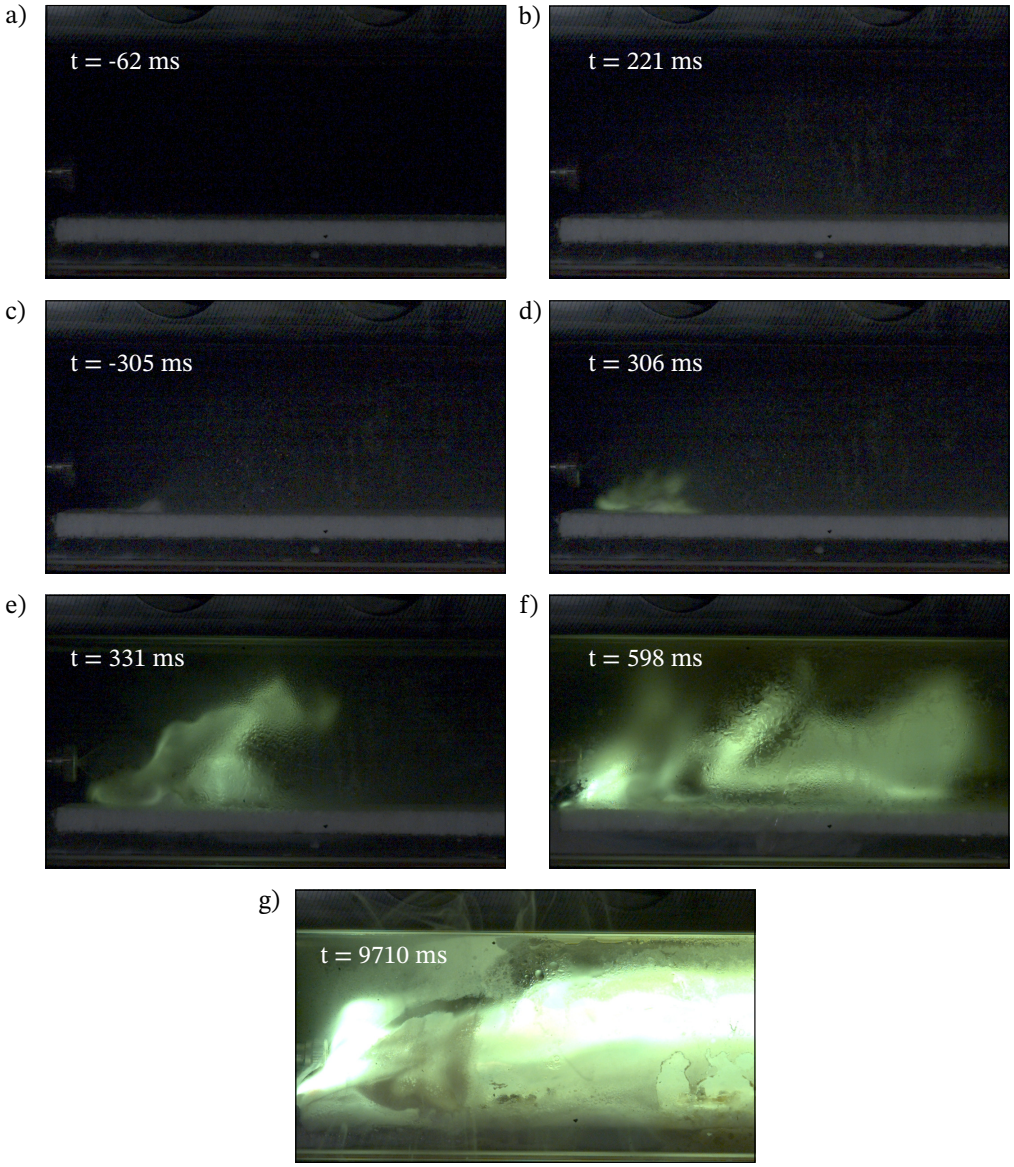

Figure 8.9 Typical ignition sequence of the tests using nitric acid and GOx as the oxidizer.

tests a both additive concentrations. The intensity signal slightly increases when nitric acid is sprayed in the chamber. Then, a sudden and maintained increase is visible, associated to the green flame from ignition. In general, the intensity decreases rapidly after ignition and stabilize afterward. Instabilities are observed, likely coming from the combination of combustion instabilities, and windows being gradually blocked by fuel deposits.

The intensity signal is also observed at different locations along the length of the fuel. The intensity signals follow the same trends regardless of location, as shown in the example provided in Figure 8.11. These intensity signals are taken from a test in which the AB

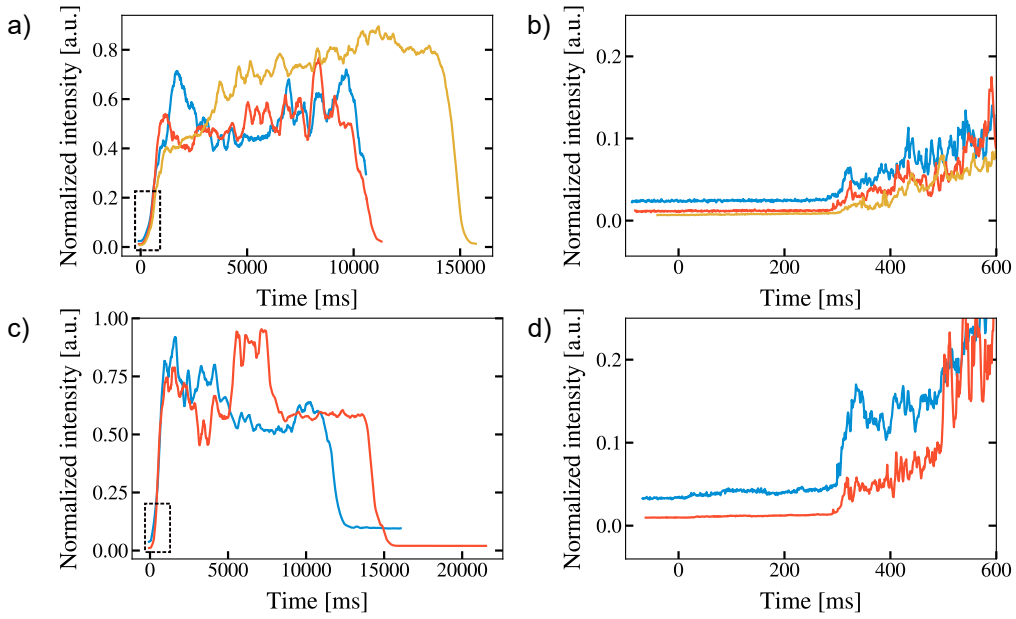

Figure 8.10 Normalized flame intensity as a function of time. Each color represents a different test. a) 40 wt.% AB - 60 wt.% paraffin. b) Zoom of frame a). c) 20 wt.% AB - 80 wt.% paraffin. d) Zoom of frame c).

concentration is 20 wt.%. The intensity measured at $x = 20.5$mm shows an initial peak due to the initial ignition of the fuel. The other instabilities appear mostly at each x position, indicating even combustion of the fuel along its length.

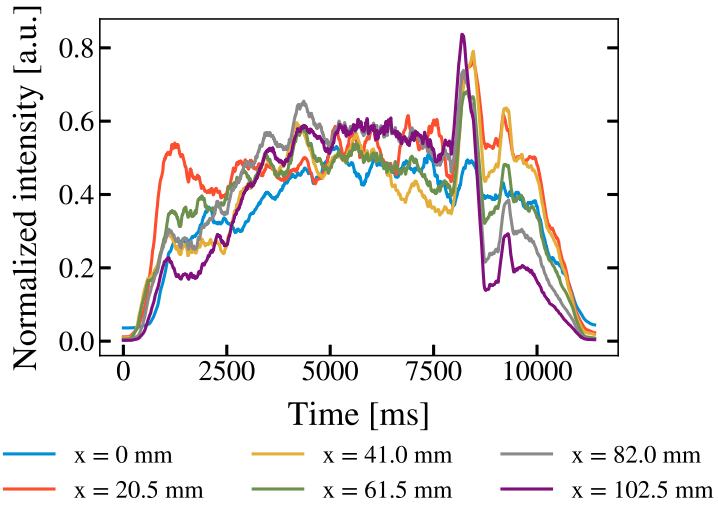

Figure 8.11 Normalized flame intensity at various fuel length location as a function of time.

The intensity of the flame is also evaluated spatially. The equations are similar than Eqs.

8.6 and 8.7, but the values are summed for the time instead of the fuel length:

$$I\left(x\right) = \sum_{t=0}^{t=t_{burn}} \sum_{y=0}^{y=y_{max}} I(t,y) \tag{8.8}$$

$$\bar{I}\left(x\right) = \frac{I\left(x\right)}{max\left(I\left(x\right)\right)} \tag{8.9}$$

where the variables are similar than described above.

This light intensity signal allows to compare the flame intensity along the fuel length over the entire burn duration. An example of this signal is shown in Figure 8.12 for tests with fuel slabs containing 40 wt.% AB content. In general, the intensity profiles follow the same trend. The flame intensity increases further downstream of the combustion chamber, corresponding to a region of higher combustion activity. A drop in the signal is observed between $x =$ 18 mm and 40 mm, corresponding to the location where the nitric acid spray impinges the windows. It is also at this location that the view is the most obstructed by paraffin and combustion products.

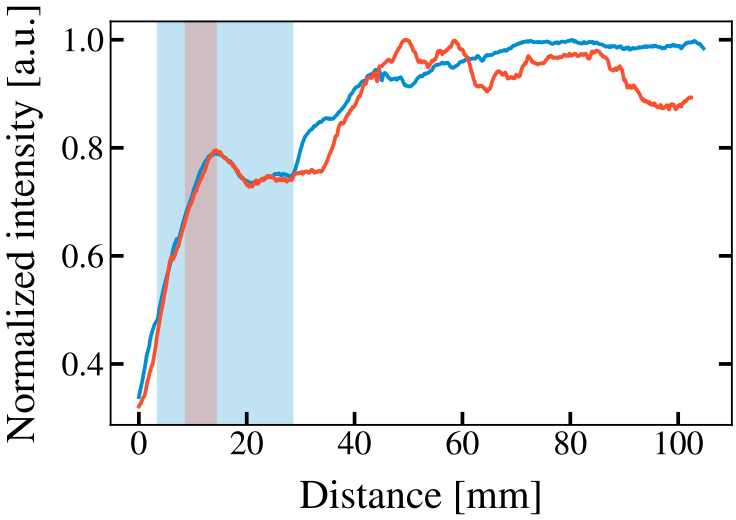

Figure 8.12 Normalized flame intensity as a function of the fuel length for fuel slabs with a 40 wt.% AB content. Each color represents a different test. The shadow zones are the projected area of the first ignition kernel.

The location and size of the first observable ignition kernel of each tests is also studied, indicated by the shadow zones in Figure 8.12. The start and end points of the ignition location are obtained by taking the projected area of the kernel on the fuel slab. This measure has been made for all slab burner tests in this configuration. The average length

of these ignition zones are 15.1 ± 1.1 mm and 14.8 ± 9.8 mm for the 20 wt.% AB and 40 wt.% AB tests, respectively. The larger size uncertainty in the latter can be attributed to the higher AB content in the fuel. A larger amount of AB on the surface of the fuel may introduce more variability in the size of the initial ignition. The location of the projected ignition is constrained within $x = 3.5$ and 11.1 mm, with average distances of 9.0 ± 2.6 mm and 7.2 ± 3.2 mm for the 20 wt.% AB and 40 wt.% AB tests, respectively.

Finally, since the nitric acid pressure for these tests is 1.38 MPa (200 psi), the Weber number similarity results in Table 8.1 indicate that the corresponding water pressure is 2.76 MPa (400 psi) for We = 2059. Using the results obtained from the PDA (Figures 8.6 a) through 8.6 d), the nitric acid droplets that led to the first ignition kernel have a median diameter D_{50} between 20 and 40 µm with a median total velocity w_{50} between 3 and 35 m/s. The droplet size is comparable to those reported in our previous spray ignition experiment [121]. However, the median total velocity is higher in the slab burner compared to up to 8 m/s in our previous experiment.

Ignition delay

Both additive contents show a similar mean ignition delay, 278 ± 10 ms for the 20 wt.% content and 286 ± 17 ms for the 40 wt.% content. All tests successfully ignited and sustained combustion for the full test duration. In addition, the small standard deviation is interesting because it directly correlates with the reliability of the ignition system, which is highly desirable for hypergolic ignition. From these results, and in this configuration, the ignition delay is not influenced by the additive concentration in the fuel. In fact, the limiting factor may be related to the nitric acid injection itself, such as the droplet velocities, as is also the case in droplet ignition tests [64] and in oxidizer spray ignition experiments [77, 121].

8.4.4 Hypergolic tests using only nitric acid

The second set of experiments focuses on the use of nitric acid as the only oxidizer with AB-doped paraffin as the fuel. This engine configuration may be of interest for in-space propulsion, small satellites, or reaction control systems as opposed to booster engines due to the toxicity and environmental hazard of nitric acid and nitrogen oxides resulting from nitric acid decomposition and combustion. This configuration has the advantage of only having to carry nitric acid for engine operation, as opposed to carrying oxygen as well. In this case, the injection mass flow rate, is varied from 1.02 g/s at 0.69 MPa (100 psi) to 2.04 g/s at 2.76 MPa (400 psi), while keeping the AB content in the fuel slab constant at 40 wt.%.

Visual assessment

The combustion dynamics are very different from the tests in which GOx is also used along with nitric acid. In this second test configuration, impinging nitric acid droplets also agglomerate to form a larger pool of oxidizer (Figure 8.13 b). Exothermic surface reactions also heat the oxidizer on the fuel surface where bubbles form (Figure 8.13 c). Unlike the first set of experiments however, oxidizer is scarce in the gas phase. When bubbles escape from the nitric acid, a dark orange gas fills the combustion chamber (Figure 8.13 d). This gas color is due to nitrogen dioxide (NO_2) formed by the thermal decomposition of the nitric acid, in addition to water and oxygen. The hot oxygen is then available to burn with the gaseous products of the initial surface reactions, probably hydrogen as mentioned in section 8.5. Ignition is however much slower than in the case where O_2 is present. After a few seconds, a small ignition kernel finally appears (Figure 8.13 e) and propagates, with sustained combustion (Figure 8.13 f) until the end of the test (Figure 8.13 g). As can be seen from the images in Figure 8.13, the fuel surface is severely degraded as the test progresses and swelling is seen. Figure 8.15 b) shows the top view of the sample burned for the test shown in Figure 8.13.

To support the visual assessment, the intensity of the green channel of the RGB signal is also evaluated in this case. Due to the different combustion dynamics, a different type of intensity profile is observed as shown in Figure 8.14. In this case, both the nitric acid decomposition and the ignition are captured while previously only ignition was discussed. First, the optical signal increases for about 500 ms until it reaches a small plateau, maintained for 1000 ms. Although being captured in the green channel signal, it is not related to the ignition itself, but rather to the light reflection from the oxidizer droplets. When compared to the high-speed camera images, this sequence coincides with the gradual deposition of oxidizer droplets on the windows. A sharp increase is then observed due to the production of NO_2 from the thermal decomposition of nitric acid. The signal decreases after approximately 1500 ms and then gradually increases and oscillates as the hypergolic ignition is triggered. The moment of ignition is determined by the frames from the high-speed camera. Interestingly, regardless of the oxidizer mass flow, the onset of nitric acid thermal decomposition and its duration are very similar, even though the ignition delays are not the same, as shown in the next section. This suggests that the limiting factor preventing rapid ignition occurs after the thermal decomposition of the nitric acid. As observed earlier, the intensity signals over the length of the fuel also follow the same trend.

Unlike the tests conducted with GOx and nitric acid as the oxidizers, the location and size of the first ignition kernel cannot be measured due to the accumulation of residues on the slab

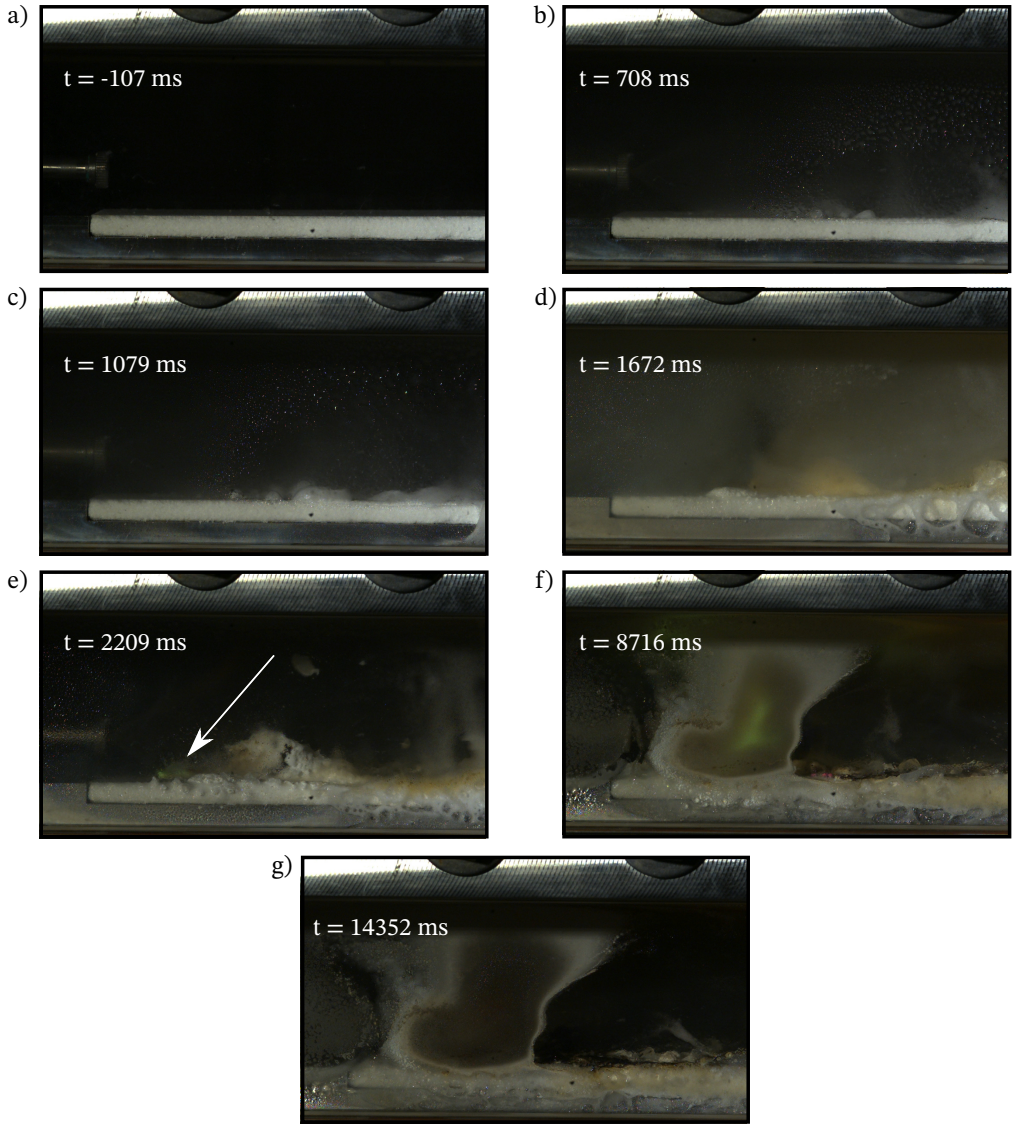

Figure 8.13 Typical ignition sequence of the hypergolic slab tests using only nitric acid as the oxidizer.

burner windows. These residues are likely a results of the nitric acid vapors as they tend to leave an opaque white film on materials. Due to the longer ignition delay compared to the first set of experiments and the lack of GOx flow, the ignition process is not well captured by the high-speed camera. However, the fuel samples at the end of the tests clearly show an area where most of the fuel was consumed. This is also the region where the first hypergolic ignition kernels are observed. An example of the fuel after a burn is shown in Figure 8.15. For the majority of tests, the fuel in this region was completely burned. However, it should be noted that after a test, for safety reasons, water is injected through the nozzle into the slab burner combustion chamber to dilute any remaining unreacted nitric acid. AB is known

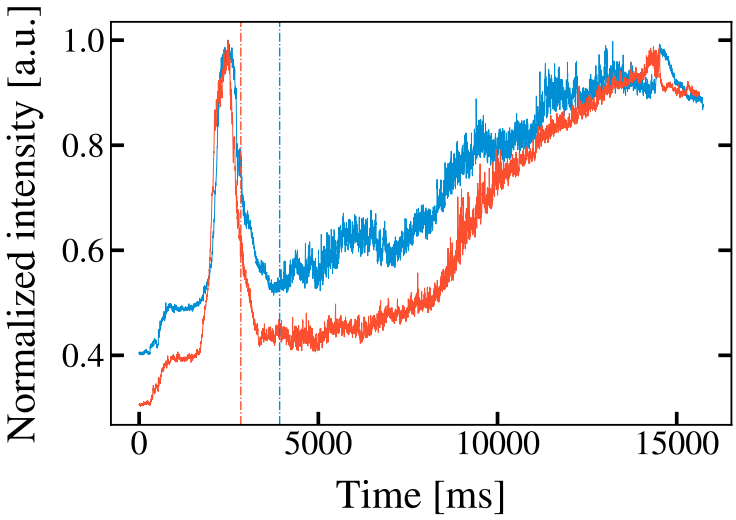

Figure 8.14 Normalized flame intensity as a function of time. Each color represents a different test. The dashed lines represent the moment of ignition.

to be soluble in water, so the condition of the fuel slab after the test may also be affected by the water, not just the nitric acid combustion.

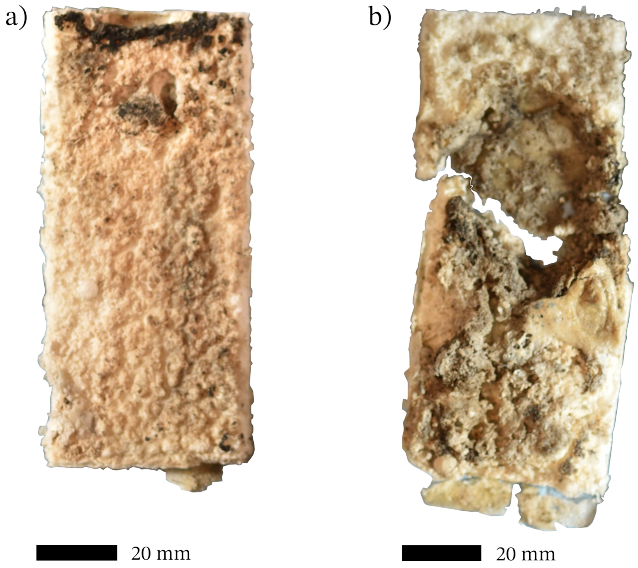

Figure 8.15 Top view of examples of the fuel slab after a hypergolic test. Flow is from top to bottom. a) A hypergolic test using nitric acid and GOx. b) A hypergolic test using only nitric acid.

This observation is further supported by comparing the intensity signal along the fuel length. As opposed to the first test configuration, the maximum value is located at the same position as the observed burn-through of the samples rather than downstream of the fuel. As can

be seen in Figure 8.16 a to c), the intensity profiles generally follow a very similar trend, showing great repeatability between tests.

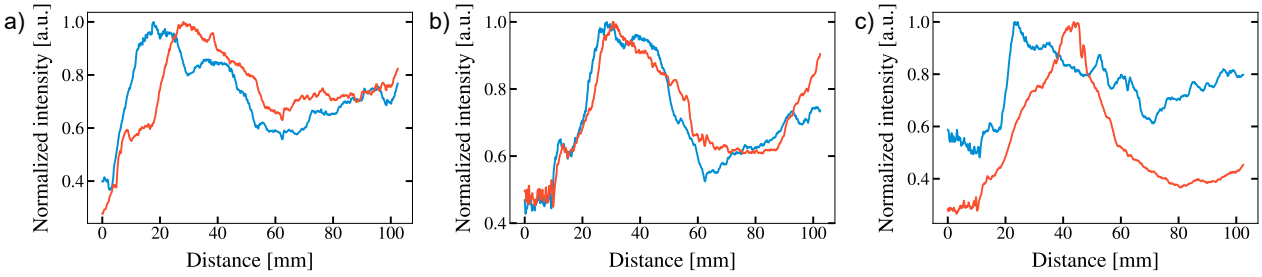

Figure 8.16 Normalized intensity as a function the distance. Each color represents a different test. Injection pressure = a) 0.69 MPa (100 psi). b) 1.38 MPa (200 psi). c) 2.76 MPa (400 psi).

Ignition delay

The ignition delay results are shown in Figure 8.17. Two tests are performed for each injection pressure. The first two oxidizer pressures show a fairly constant ignition delay at 2987 and 3379 ms for 0.69 MPa (100 psi) and 1.38 MPa (200 psi), respectively. However, at 2.76 MPa (400 psi) the ignition delay decreases by approximately 1 second (30%) to reach 1931 ms. The exact mechanism for this decrease in ignition delay is not known, but many hypotheses are proposed. First, the higher injection pressure increases oxidizer droplet velocity and flow rate. The increased droplet velocity has previously been shown to reduce the ignition delay of hypergolic hybrid fuels due to the increased surface coverage upon splashing of the droplets [64,77,121]. This increased surface contact between the nitric acid and AB increases the likelihood of meeting the conditions for hypergolic ignition. In addition to the increased surface area covered by the acid, the increased droplet momentum changes the dynamics of the agglomerated oxidizer pool. The pool appears to creep along the surface of the fuel, leaving a thin layer of oxidizer in its wake. The large variation in oxidizer thickness and amount on the fuel surface may also increase the likelihood of reaching hypergolic ignition conditions. Finally, it is also possible that under the first two pressure conditions, there is not enough oxidizer to successfully achieve ignition. However, if this explanation were the key factor in explaining the difference in ignition delay, there should have been a decrease in ignition delay between the 0.69 MPa (100 psi) tests and the 1.38 MPa (200 psi) tests, which is not the case here.

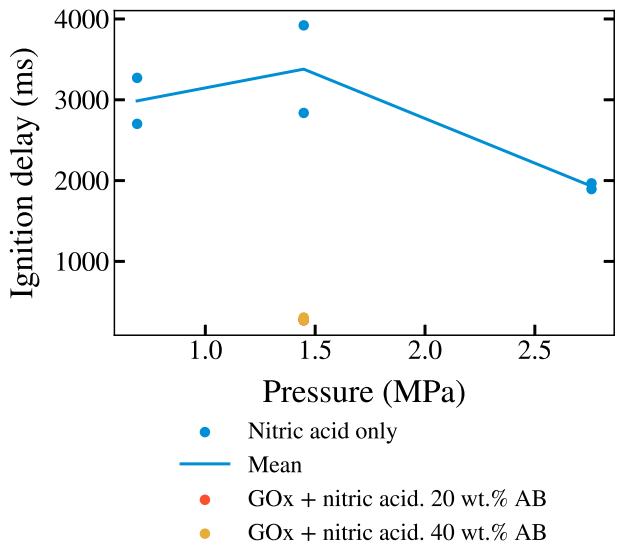

Figure 8.17 Ignition delay as a function of the injection pressure in the when only nitric acid is used as the oxidizer.

8.4.5 Reignition

One of the most important aspects of a hypergolic hybrid engine often discussed but rarely tested, either in droplet ignition tests or in engine conditions, is its reignition capability. In theory, a hypergolic hybrid engine could be shut down and reignited by simply closing and reopening the oxidizer flow into the combustion chamber. However, as several research studies show, during hypergolic ignition drop tests, ammonia borane and paraffin samples tend to form a black foam-like deposit on their surface, which can potentially reduce hypergolic performance during subsequent relights.

In the experiments conducted here, several reignition tests were performed. Among the tests performed when nitric acid is the sole oxidizer, 5 out of 6 tests were successfully reignited. However, the ignition delay for each reignition is much longer than the initial hypergolic ignition. The reignition delays are 6681, 4000, 3820, 2573 and 8379 ms for tests with injection pressures of 0.69 MPa (100 psi), 0.69 MPa (100 psi), 1.38 MPa (200 psi), 2.76 MPa (400 psi) and 2.76 MPa (400 psi), respectively. The longer ignition delay can be explained by the completely different fuel surface between the clean and the burned sample. After the initial hypergolic burn, the surface is irregular, with large peaks and valleys of melted paraffin that solidified between the two burns. Char and condensed combustion products are also observed sitting on the surface. In some cases, burn-through of the sample at the site of initial ignition is visible. The altered exposed surface is unlikely to maintain the same additive content as the initial burn, thus affecting the ignition delay. However, the altered conditions remain similar

to what the surface would be under real engine conditions. Thus, the ignition delay of the hypergolic reignition sample is something worth looking at in extended studies focused on this particular problem. This does not change the fact that the results are considered significant because they demonstrate the successful reignability behavior of paraffin/AB hypergolic fuels with sprayed nitric acid as the oxidizer.

In addition, reignition experiments were also performed on 3 tests when GOx is the main oxidizer following ignition. The measured IDs are 2492, 1796, and 278ms, with the first two tests containing 40 wt.% AB and the last containing 20 wt.% AB. The IDs are again lower than those when GOx is not used, but are still significantly higher than the first hypergolic ignition. These results indicate that GOx contributes to the reduction of the ignition delay even in the case of reignition. However, its addition to the reactants is not sufficient to overcome the fact that the exposed fuel surface seems to be the limiting factor inhibiting fast reignitions.

8.5 Discussion

8.5.1 Mechanisms of hypergolic ignition and comparison with droplet and spray ignition tests

It is believed that paraffin does not react with the oxidizer until it begins to evaporate after the hypergolic ignition. Its main role is to act as a binder for AB, but also act as a sink of the heat generated by the exothermic reactions between AB and nitric acid. Although not fully understood, the reaction of ammonia borane with nitric acid can be divided into three ways. First, upon contact, the nitric acid catalyzes the exothermic dehydrogenation of AB, releasing H^+ ions and a large amount of energy (about 800 kJ/mol at ambient conditions) [34]. This catalytic reaction also produces the reactive BH_3 species. In addition to catalytic dehydrogenation, AB undergoes an exothermic thermal decomposition that produces H_2 and other secondary species (H_2BNH_2, B_2H_6, NH_3, and $B_3H_6N_3$) [34, 184]. Finally, the species produced are then oxidized by the nitric acid, again releasing heat. A portion of this heat is transferred to the nitric acid, which decomposes into NO_2, water, and O_2. Baier et al. [168] experimentally observed the exothermic formation of HBO_2 prior to ignition, suggesting that it also contributes to the heat release that drives the decomposition of nitric acid. Moreover, their results suggest that HBO_2 is consumed at the flame front, possibly contributing to the green color of the flame as soon as the first visible ignition occurs.

The experiments using oxygen along with nitric acid for hypergolic ignition show much lower ignition delays than when using nitric acid alone. Filling the combustion chamber with

oxygen before injecting nitric acid reduced the ignition delay tenfold, from up to 3 seconds to about 280 ms. The major difference is that an oxidizing species (O_2) is already available to react with the species formed by the decomposition of AB, thus limiting the steps required to achieve ignition and bypassing the nitric acid thermal decomposition step when it is used as the sole oxidizer.

Nevertheless, the ignition delays measured using nitric acid as the sole oxidizer are surprisingly higher than the spray ignition tests (between 300 to 1100 ms, [121]) and droplet ignition tests of previous studies (between 20 to 45 ms, [22]). This is explained by the slower oxidizer supply to the fuel compared to when a large droplet impacts and covers the entire pellet surface. As previously observed, the conditions favorable for achieving hypergolic ignition need only be met at a discrete location on the fuel. The delivery of nitric acid in thousands of microscopic droplets delays the achievement of these conditions compared to when a droplet is in immediate contact with all the available AB on the fuel surface. However, the difference between the ignition delay measured previously in spray ignition tests (from 300 to 1100 ms [121]) and here (2000 to 4000 ms) may be due to the fact that the combustion chamber is filled with nitrogen as opposed to ambient air, which limits the amount of O_2 available in the environment to initiate the ignition. In addition, the fact that the injector is placed in the same direction as the fuel, as opposed to having its tip pointing directly at the sample as in the spray ignition tests, may reduce the splashing of the droplet hitting the surface. This would limit the surface area covered by nitric acid and delay the hypergolic ignition. The results presented here indicate that, in addition to the introduction of nitric acid into the combustion chamber, the introduction of gaseous oxidants such as GOx may be a suitable alternative to reduce the ignition delay of hypergolic hybrid engines.

8.5.2 Regression rate

Finally, the regression rate of the fuel was examined. Unfortunately, image analysis algorithms, such as those presented by Jobin et al.(see Chapter 5) or Dunn et al. [13], could not be implemented here to determine the regression rate due to the accumulation of oxidizer and melted paraffin on the windows. Even if the use of such an algorithm would have been possible, it is uncertain whether the results would have been of much value due to the fact that the fuel samples tend to swell during combustion, thus initially presenting a negative regression rate. This observation was also made by Pfeil in the combustion of a small WFNA-paraffin/AB hybrid engine [30].

In an effort to estimate this interesting metric, the regression rate is obtained by measuring the difference in mass before and after each test. The following equation is used to convert

the mass to a regression rate value:

$$\dot{r} = \frac{\Delta m}{\rho_{fuel} \cdot A \cdot t_b} \tag{8.10}$$

where $\dot{r}$ is the regression rate, Δm is the mass difference, ρ_{fuel} is the density of the fuel mixture, with 900 kg/m^3 as the density of paraffin and 780 kg/m^3 as the density of AB, $A = 114.3$ x 50.8 mm^2 is the area exposed to the fuel, and t_b is the burn time. However, as noted above, because water is injected into the chamber after each test to dilute the remaining nitric acid, the regression rate values may be higher than reality due to the reaction of AB with the fluid. In addition, this method relies on the ability of the test operators to retrieve each piece of fuel remaining in the combustion chamber. This has proven to be more difficult than anticipated due to the high degradation of fuel samples and their brittleness after combustion. The results are presented in Table 8.2. While the regression rate values may not be exact, the trends observed follow the expected behavior. First, when GOx and nitric acid are used, the consumed mass per second and the regression rate of the sample are higher when the fuel composition is 40 wt.% AB as opposed to 20 wt.%. This is expected due to the rapid hypergolic reactivity of AB and nitric acid. This observation is also consistent with the results of Benhidjeb-Carayon et al. [73], where they used a higher concentration of hypergolic additives in sections of the fuel in a 2-in hypergolic hybrid engine. The sections of the fuel grain containing the highest amount of additives were completely burned out after their tests, while fuel remained where less hypergolic additives were used. Finally, for the tests conducted when nitric acid is the sole oxidizer, the regression rate increases as the injection pressure also increases, which is consistent with the formulation commonly used for hybrid rocket fuels ($\dot{r} = aG_{ox}^n$). In both cases, the variability for the $\dot{r}$ values is impossible to quantifiy, due to the fact that only 2 tests were performed for the fuel composition pressures. These results should therefore be interpreted with great caution and the completion of the data set will be the subject of future studies.

8.6 Conclusions of the chapter

A novel hypergolic slab burner was developed to study the hypergolic ignition of hybrid rocket fuels in an engine-like configuration. The design of the slab burner and its injection system were presented. The spray from the injector was characterized using a Phase Doppler Anemometer system. Two sets of experiments were performed. In the first, paraffin-based fuels containing 20 or 40 wt. % of ammonia borane were used. The gaseous oxidizer was first introduced into the combustion chamber and then 90% concentrated nitric acid was injected

Oxidizer	Nitric acid pressure [MPa (psi)]	Fuel	Δm [g/s]	STD	$\dot{r}$ [mm/s]	STD
Nitric acid	1.38 (200)	40-60	0.41	0.06	0.08	0.01
+ GOx	1.38 (200)	20-80	0.36	0.05	0.07	0.01
	0.69 (100)	40-60	0.38	0.16	0.08	0.03
Nitric acid	1.38 (200)	40-60	0.57	0.08	0.12	0.02
	2.76 (400)	40-60	0.75	N/A	0.15	N/A

Table 8.2 Mass burned and regression rate of each tested configuration. 40-60 refers as 40 wt.% AB - 60 wt.% paraffin fuel mixture and 20-80 refers as 20 wt.% AB - 80 wt.% paraffin fuel mixture. STD stands for *standard deviation*.

for a few seconds to initiate combustion. In the second set of experiments, the combustion chamber was filled with nitrogen, then nitric acid was injected for the entire duration of the test. Both configurations successfully led to hypergolic ignition that transitioned to sustained combustion. The ignition delay of the first set of experiments was more than 10 times faster than that of the second set. Finally, the reignition of these fuels was investigated. All reignition tests conducted with the first experimental configuration successfully reignited, while the success rate in the second configuration was 83 %. In both configurations, the ignition delay is greater than when the sample was first ignited. This is attributed to the change in the exposed surface of the fuel, namely char deposition, melted paraffin coating the surface, and uneven additive content. This novel test apparatus paves the way for the study and understanding of the phenomena behind hypergolic ignition. Further testing with new instrumentation and other fuel/oxidizer combinations will be the focus of future studies. In addition, a method for spatially and temporally measuring the regression rate should be implemented to take full advantage of the slab burner.

Author contributions

Olivier Jobin: Conceptualization, Methodology, Software, Investigation, Writing - Original Draft. **Mathieu Chartray-Pronovost:** Investigation, Writing - Review & Editing. **William Kaprolat:** Investigation, Writing - Review & Editing. **Étienne Robert:** Conceptualization, Writing - Review & Editing

CHAPTER 9 GENERAL DISCUSSION

9.1 Slab burner

Chapter 5 addressed the first and second specific objectives of this thesis, which is to design, develop and instrument a laboratory-scale slab burner rig. The main focus of this article was to study the influence on the combustion of an additive, namely alpha-olefin (Vybar), identified in a previous study conducted by the author. To conduct this study, the slab burner was designed, instrumented and commissioned. An image analysis methodology was introduced to measure the regression rate of hybrid fuels, resolved both spatially and temporally.

To ensure valid results coming from this study, the flow entering the slab burner was carefully characterized by a hot wire anemometry test campaign. The characterization of the flow in slab burners found in the literature is often not validated or presented, although it is a critical first step for such a study. In the preliminary tests conducted on the slab burner, the ignition system relied on a tungsten wire to heat the top of the fuel slab, initiating combustion after a few seconds. In addition to the tedious and time-consuming task of sample preparation, the measured regression rate in these tests was highly variable and almost twice the values from the definitive tests presented in chapter 5. Induced turbulence in the wake of the wire was found to be the culprit. This justified finding another way to ignite the samples. This anecdote shows that even with a tidy design, small details can affect the results. The hot wire anemometry test campaign provided confidence in the regression rate results presented here by quantifying the turbulence intensity and velocity profiles and showing that the results are repeatable from test to test.

Image analysis is a science in itself, a statement that is even truer when automatic image analysis is part of the game. The large amount of images collected by the high-speed cameras did not allow for manual analysis, thus justifying the need for an automatic edge detection algorithm. The image analysis methodology was based on a color identification technique widely used in color research and industry to validate and quantify color deviations in manufactured products. The algorithm was developed and adapted to the type of images obtained during the tests. Its implementation led to the successful measurement of the regression rate of paraffin and alpha-olefin fuels, with high spatial and temporal resolution. This task cannot be performed in regular hot-fire tests of hybrid rocket engines. Because of the windows of the slab burner, the fuel edge can be tracked in its entirety for the entire duration of the burn.

The main novelty of this part of the thesis is the results of the regression rate when alpha-

olefin is added to a paraffin fuel matrix. Alpha-olefin was identified as a suitable candidate to reduce and tune the regression rate of paraffin rocket engines without sacrificing performance. The detailed presentation of the image analysis algorithm in this article may be useful to other researchers as it is easy to implement and was found to be reliable. In this type of study, the image analysis part is an auxiliary task, but difficult to implement. It is hoped that researchers will use the proposed methodology to accelerate their regression rate measurement development in slab burners.

9.2 Metal-organic frameworks as hypergolic additives

Chapter 6 tackled the second specific research objective of this thesis, which is the evaluation of suitable fuel additives for hybrid rocket applications. The main focus of this article was to investigate the suitability of novel metal-organic frameworks as hypergolic additives. The motivation for this work was mainly due to the creation of hypergolic MOFs by colleagues in the Department of Chemistry at McGill University. The hypergolic testing experience of the author and the chemical knowledge of his colleagues were combined and concluded in a rigorous experimental and theoretical study.

The experimental ignition results showed that Co(**VIm**)$_2$ and Co(**AIm**)$_2$ exhibit a strong hypergolic behavior with WFNA (fast ignition below 10 ms), while delivering the energy necessary to sustain paraffin combustion. The theoretical performance results showed that the hypergolic MOFs are suitable for hybrid rocket applications, since they allow to induce a hypergolic behavior to the fuel at the cost of a low (about 2 %) performance decrease (assessed through the I_{sp}). This cost may be justified by the ease of manipulation of these MOFs, as they are thermally stable well above the melting point of paraffin, unlike ammonia borane. This is of particular interest in the development of large hypergolic engines, where safety and operations will be a major concern.

The novelty of this work is easily demonstrated by the fact that it was the first time that MOFs were tested as hypergolic additives for hybrid rocket fuels. However, the novelty is not only due to the "first of its kind" aspect of these experiments. The results presented in this article were conclusive regarding the use of MOFs for their hypergolic behavior. Hypergolic MOFs are very interesting additives that can be tailored as needed. For example, by changing the metal or organic linkers to more energetic ones.

9.3 Hypergolic spray ignition tests

Chapter 7 addressed the third specific objective of this thesis, which is to evaluate the ignition performance of hypergolic additives under sprayed liquid oxidizer injection. The rationale for this experiment was to transition from traditional hypergolic droplet ignition tests to a test configuration more similar to rocket engine conditions. In addition, this step was necessary for the development of the hypergolic slab burner, which addresses the fourth and final specific objective of this thesis.

Due to the oxidizer being sprayed onto the fuel pellets, the oxidizer spray needed to be well characterized. The amount, and quality, of conclusions that can be drawn from oxidizer spray ignition tests are primarily limited by the spray diagnostic capabilities. In this work, the Phase Doppler Anemometer system was essential in providing insight into the oxidizer spray. Due to the inherent safety issues with reactive and strong oxidizing chemicals being sprayed in countless tiny droplets, surrogate tests were first performed using water as the fluid. The results were then converted to a nitric acid oxidizer spray using a Weber number similarity study. This methodology is similar to "cold" flow injector tests conducted in rocket testing, where the mass flow and spray characteristics of injectors are tested using water or other non-hazardous fluids.

The results from this study showed that the ignition delays measured in this test configuration were approximately an order of magnitude (>100 ms) greater than those measured in droplet ignition tests (<50 ms). The main factor driving the ignition delay was found to be the Weber number at the droplet scale, taking into account the droplet diameter and its velocity measured by the PDA system. By increasing the velocity of the impinging droplets, the ignition delay was successfully reduced. In addition, the high-speed infrared camera revealed that only a single location with a sufficient amount of hypergolic additives on the fuel pellet was required to initiate and sustain the combustion.

The novelty of this work is first in the implementation of the experimental methodology since no other hypergolic spray experiment focusing on the oxidizer spray conditions was found in the literature. In addition, the translation of the results from the PDA system to the ignition delay showed that the individual droplet velocity is an important parameter for achieving hypergolic ignition. Finally, among the aforementioned conclusions drawn, this study demonstrated the need to also evaluate the hypergolic ignition in a configuration closer to that of a rocket engine, as opposed to ignition droplet tests. The study of the influence of the oxidizer spray on the ignition delay is a first step towards a better understanding of the hypergolic ignition of hybrid rocket fuels. The author of this work hopes that other

researchers will implement these experimental techniques to further advance the knowledge on this topic.

9.4 Hypergolic slab burner

The last specific objective of this thesis, which is to develop an injection system to support the use of liquid oxidizers in the slab burner, was achieved and presented in Chapter 8. This was the last step of transitioning from droplet ignition tests to a configuration closer to full or lab-scale engines. This objective regrouped the experience and knowledge gained from the other specific objectives: the slab burner from the first objective, the droplet ignition knowledge obtained from the MOF ignition experiments, and the spray characterization methodology from the hypergolic spray experiments.

The spray in the combustion chamber of the slab burner was again characterized using the PDA system. This made it possible to quantify the diameter and velocity of the droplets hitting the fuel surface and to identify the conditions most likely to lead to rapid hypergolic ignition. Due to the presence of the injector in the combustion chamber, the flow field was also measured with the PDA system, allowing to quantify its effect on the turbulence in the chamber. This step is, again, important since it was observed that the turbulence plays a significant role in the combustion rate of the fuel. Two case studies were considered in this experiment. The first mode of operation utilized the hypergolic ability of nitric acid and ammonia borane to promote ignition in a paraffin/GOx combustion mode. This demonstrated that reliable hypergolic ignition can be achieved in less than 300 ms and is capable of initiating and sustaining combustion even when the nitric acid injection is turned off. The second mode of operation used only nitric acid as the oxidizer. It is envisioned that this system may be useful for smaller engines, such as those for space propulsion or for RCS systems. Longer ignition delays were observed compared to when GOx was also used in the combustion. With a high-speed camera looking through the slab burner windows, the location of the ignition was studied to relate it to the droplet conditions measured by the PDA system. Finally, hypergolic reignition was tested and achieved in both operating modes, confirming that it is indeed possible to ignite the engine multiple times.

To the best of the author's knowledge, this experiment represents the first hypergolic slab burner reported in the literature. The novel design of the liquid injection system may be useful to replicate by other researchers considering implementing such a system in their existing slab burner facilities. Again, it is hoped that the methodology linking spray characterization to hypergolic ignition location will be used by others. The goal would be to optimize spray injection of oxidizers as much as fuel compositions, surface roughness, and mass loading of

additives are studied and reported.

9.5 General impact

It is clear that hypergolic ignition systems for hybrid rocket engines need to be better understood before they can be widely adopted. This statement is also true for hybrid rocket engines in general, illustrating the low level of maturity of hypergolic systems. The work in this thesis has highlighted areas for improvement and generated ideas to increase the maturity level of such a system. The general impact of this work can be divided into two categories.

First, its impact is related to the methodological aspect of the experiments conducted for this thesis. A test methodology for hypergolic spray ignition tests was not available in the literature and had to be implemented from the ground up. The same is true for the hypergolic slab burner design and test methodology. In this regard, the work performed in this thesis paves the way for future experiments to further investigate the fundamentals of hypergolic ignition under engine-like conditions.

Second, the impact of this work is related to the results obtained. It is expected that future hybrid engines will implement additives such as hypergolic MOFs for the hypergolic additives, or alpha-olefin to adjust the regression rate of paraffin-based fuels. The suitability of hypergolic MOFs was evaluated, allowing researchers to evaluate and consider an entirely new class of materials for future ignition systems. It is also believed that the hypergolic community will begin to use experiments other than the traditional droplet ignition tests to evaluate hypergolic ignition. The results presented here have highlighted the fact that ignition using sprayed oxidizers is different from the ignition observed in droplet ignition tests. Future efforts will be needed to optimize the oxidizer spray to achieve more reliable and faster ignitions.

CHAPTER 10 CONCLUSION AND RECOMMENDATIONS

10.1 Summary of works

This thesis aims to contribute to the effort to further advance the knowledge of hypergolic ignition in hybrid rocket engines. Common experiments are conducted in environments far from ones in a real, full-scale engine. The lack of testing in engine environments makes the understanding of hypergolic ignition difficult and limited.

The general objective of this thesis was to support the development of hypergolic hybrid rocket engines by conducting small-scale experiments and providing experimental results. To achieve this objective, an experimental test rig had to be developed that would allow such small-scale investigations. A slab burner was designed and instrumented to observe the combustion dynamics of hybrid rocket fuel combustion. The test facility was first used to evaluate the regression rate and combustion dynamics of paraffin-based fuel into which alpha-olefin additive (Vybar) was mixed. This additive was identified in a previous study to increase the viscosity of the melted fuel and reduce the ignition delay when used with ammonia borane as the hypergolic additive. Its effect on the regression rate was assessed and it was found that a 20 wt.% alpha-olefin addition to paraffin can decrease the regression rate by approximately 20 %, with gaseous oxygen as the oxidizer, without impacting the specific impulse. An image analysis tool was developed to automatically process the images at a high-speed and return the spatially and temporally resolved regression rate.

In addition to alpha-olefin as a regression rate tailoring additive, other types of suitable additives were tested. Hypergolic metal-organic frameworks were evaluated for their newly engineered hypergolic capabilities. Mixtures of MOFs and paraffin were tested in various concentrations and configurations to assess the ignition delay with WFNA as the oxidizer. Fast and reliable ignition delays were measured, with most of the samples igniting in less than 10 ms. Moreover, a theoretical performance analysis was conducted and showed that these additives do not present a serious reduction in specific impulse compared to neat paraffin. However, they do have the advantage of being stable at higher temperatures compared to ammonia borane, which facilitates the manufacture of such fuel combinations.

Ammonia borane was also studied as a hypergolic additive when exposed to nitric acid sprays, as opposed to the hypergolic MOFs being tested in droplet ignition experiments. This experiment demonstrated that under more realistic conditions, i.e., a sprayed oxidizer versus a single oxidizer droplet, the ignition delay is influenced by the spray characteristics,

specifically the velocity at which the droplets impact the fuel pellets. This work was made possible by the use of a Phase Doppler Anemometer system to thoroughly measure the conditions (droplet size and velocity) across the spray.

The last experiment combined the methodology developed and employed in the other experiments to develop a hypergolic slab burner. An injection system consisting of a spray injector was designed and added to the slab burner developed in this thesis. This allowed the knowledge gained from the spray injection experiment to be applied to a slab burner experiment. The hypergolic phenomena were studied in two configurations, one where only nitric acid is used as the oxidizer and the other where GOx is the main oxidizer and nitric acid hypergolically ignites the engine. Both operating modes successfully ignited and reignited with a longer ignition delay compared to droplet ignition experiments. The experiments conducted with GOx resulted in much faster ignition (approximately 300 ms) than when only nitric acid was used (2000 to 3000 ms). In the former case, oxygen was readily available to react with the ammonia borane decomposition products, whereas in the latter case, nitric acid must thermally decompose into gaseous oxidative species before initiating the combustion.

Two major impacts are expected from this work. The first is in the methodologies employed and developed to enable such studies. It is believed that the hypergolic community will implement such methodologies to look further into the hypergolic ignition, either in spray ignition tests or in hypergolic slab burners. The second anticipated impact pertains to the results, notably the utilization of MOFs as hypergolic additives or alpha-olefin as a fuel additive, and the results indicating that oxidizer spray conditions affect hypergolic ignition.

10.2 Limitations and recommendations for future research

- **Investigate the effect of MOFs on the regression rate:** The slab burner has not been used with MOFs incorporated into the fuel. Their effect on the regression rate is unknown and should be investigated.
- **Study the regression rate at high pressures:** The slab burner has been designed to withstand combustion pressures up to 2.41 MPa (350 psi) but has only been used at atmospheric pressure due to the added complexity of designing nozzles capable of increasing the pressure. The regression rate of fuels based on paraffin, and potentially alpha-olefin, is independent of the combustion pressure. However, this is no longer the case when metallic additives are used. Further studies are therefore required to evaluate the effect of pressure on the regression rate, using AB and MOFs.
- **Perform slab burner tests at higher oxidizer mass fluxes:** The results in Chap-

ter 5 are limited to a low range of oxidizer mass flux, which may not relate to the range encountered in large scale engines. This would require a different test site with ventilation capable of handling such high combustion product flow rates.

- **Perform high pressure hypergolic slab burning tests:** Once a nozzle system is designed to increase the combustion pressure, further hypergolic experiments could be conducted at high pressure. The goal would be to verify that the results presented here at atmospheric pressure (mainly the effect of droplet velocity on ignition and its delay) hold true at higher pressures.

- **Measure spatially and temporally the regression rate in the hypergolic slab burner:** The tests conducted in the hypergolic slab burner did not allow the use of the automatic image analysis tools developed for the work presented in Chapter 5, resulting in the lack of spatial and temporal regression rate measurements. This was mainly due to the fact that nitric acid fumes residues, melted paraffin droplets and combustion products quickly came into contact with the windows and obstructed the view. Efforts should be put to develop a way to either limit the obstruction or to analyze the images in such a way that this is not a problem. For example, coatings that do not allow paraffin or combustion products to adhere could be researched and applied to the windows inside the combustion chamber. Other techniques based on artificial intelligence could be explored as it has begun to emerge in image processing for slab burners. Finally, techniques not based on image processing could also be tried such as doping the fuel with chemical tracers and probing for a given species or embedding resistances or thermocouples into the fuel.

- **Use other oxidizers to replace nitric acid:** The use of nitric acid in propulsion systems is a good first step in the transition from NTO and hydrazine-based systems to more environmentally friendly and less toxic alternatives. However, nitric acid also has toxicity and environmental hazards that it would be interesting, and certainly mandatory in the future, to eliminate. At the time of writing this thesis, hydrogen peroxide is under vigorous investigation as a high-performance oxidizer that presents hypergolic potential with a wide range of additives. It is believed that the MOFs studied here also exhibit hypergolic behavior due to their strong and fast reaction with nitric acid and the presence of their organic linkers. Therefore, further studies, in the form of droplet ignition tests, spray injection tests and hypergolic slab burner tests should focus on the use of high-test peroxide as an alternative to nitric acid. Additional safety measures would need to be implemented due to the risk of thermal and catalytic exothermic decomposition of hydrogen peroxide at high concentrations.

- **Perform PDA measurements of nitric acid sprays:** Much of the technical analysis performed with the PDA system is based on the Weber number similitude methodology. It would be interesting to perform tests using nitric acid as the injected fluid to verify the results of the water tests and the Weber number similitude studies. Much effort would be required to conduct this experiment safely.

- **Implement additional diagnostic tools:** A slab burner is a unique tool for investigating the fundamentals of hypergolic and non-hypergolic hybrid rocket combustion. With its multiple optical accesses, optical and laser-based diagnostic tools could be implemented. For example, Schlieren technique, OH* and CH* chemiluminescence could provide insight into the reaction rate, precise location of the combustion, and identification of pre-ignition events in the case of hypergolic tests. Laser-based techniques such as planar laser-induced fluorescence would be interesting to implement, as this type of experiment has not been reported in the literature for slab burners. Finally, using the PDA system during a hypergolic slab burner test would allow the droplet conditions to be measured individually for each test to account for potential variations. This technique is particularly worth investigating when hypergolic slab burner tests are performed at high pressures. In addition, the change in spray conditions as the temperature increases in the chamber prior to ignition could be captured.

REFERENCES

[1] "Types of chemical rocket engines," in *Science Learning Hub – Pokapū Akoranga Pūtaiao*, 2014. [Online]. Available: https://www.sciencelearn.org.nz/resources/393-types-of-chemical-rocket-engines

[2] G. Sutton and O. Biblarz, *Rocket Propulsion Elements*, 9th ed. New York, USA: John Wiley & Sons, 2016.

[3] G. Marxman, C. Wooldridge, and R. Muzzy, "Fundamentals of Hybrid Boundary Layer Combustion," presented at the Heterogeneous Combustion Conference. Palm Beach, FL: American Institute of Aeronautics and Astronautics, Dec. 11-13 1963. [Online]. Available: https://doi.org/10.2514/6.1963-505

[4] G. A. Marxman, "Combustion in the turbulent boundary layer on a vaporizing surface," *Symposium (International) on Combustion*, vol. 10, no. 1, pp. 1337–1349, 1965. [Online]. Available: https://doi.org/10.1016/S0082-0784(65)80268-5

[5] G. Marxman, "Boundary-layer combustion in propulsion," *Symposium (International) on Combustion*, vol. 11, no. 1, pp. 269–289, 1967. [Online]. Available: https://doi.org/10.1016/S0082-0784(67)80153-X

[6] M. A. Karabeyoglu, "Transient combustion in hybrid rockets," PhD dissertation, Stanford University, Stanford, CA, 1998. [Online]. Available: https://search.proquest.com/docview/304454044?accountid=40695

[7] A. Chandler, "An Investigation of Liquefying Hybrid Rocket Fuels With Applications To Solar System Exploration," PhD dissertation, Stanford University, 2012. [Online]. Available: http://purl.stanford.edu/bm524fh7508

[8] A. Karabeyoglu, B. J. Cantwell, and D. Altman, "Development and testing of paraffin-based hybrid rocket fuels," presented at the 37th Joint Propulsion Conference and Exhibit, Salt Lake City, UT, July 8-11 2001. [Online]. Available: https://doi.org/10.2514/6.2001-4503

[9] A. Karabeyoglu, D. Altman, and B. J. Cantwell, "Combustion of Liquefying Hybrid Propellants Part 1, General Theory," *Journal of Propulsion and Power*, vol. 18, no. 3, pp. 610–620, May 2002. [Online]. Available: https://doi.org/10.2514/2.5975

[10] N. Pelletier, "Étude des phénomènes de combustion dans un propulseur hybride : modélisation et analyse expérimentale de la régression des combustibles liquéfiables," PhD dissertation, Université de Toulouse - ISAE, Toulouse, France, 2009.

[11] A. Petrarolo, M. Kobald, and S. Schlechtriem, "Understanding Kelvin-Helmholtz Instability in Paraffin-based Hybrid Rocket Fuels," *Experiments in Fluids*, vol. 59, no. 4, p. 62, Mar. 2018. [Online]. Available: https://doi.org/10.1007/s00348-018-2516-1

[12] L.-l. Liu, T.-y. Zhang, Z.-b. Chen, X. He, and Z. Ji, "Boundary layer combustion of paraffin fuels for hybrid propulsion applications," *Acta Astronautica*, vol. 193, no. January, pp. 338–345, apr 2022. [Online]. Available: https://doi.org/10.1016/j.actaastro.2022.01.035

[13] C. Dunn, G. Gustafson, J. Edwards, T. Dunbrack, and C. Johansen, "Spatially and temporally resolved regression rate measurements for the combustion of paraffin wax for hybrid rocket motor applications," *Aerospace Science and Technology*, vol. 72, pp. 371–379, jan 2018. [Online]. Available: https://doi.org/10.1016/j.ast.2017.11.024

[14] A. Karabeyoglu, G. Zilliac, B. J. Cantwell, S. De Zilwa, and P. Castellucci, "Scale-up Tests of High Regression Rate Liquefying Hybrid Rocket Fuels," presented at the 41st Aerospace Sciences Meeting and Exhibit, Reno, NV, Jan. 6-9 2003. [Online]. Available: https://doi.org/10.2514/6.2003-1162

[15] M. A. Karabeyoglu, S. De Zilwa, B. Cantwell, and G. Zilliac, "Modeling of hybrid rocket low frequency instabilities," *Journal of Propulsion and Power*, vol. 21, no. 6, pp. 1107–1116, 2005. [Online]. Available: https://doi.org/10.2514/1.7792

[16] P. George, S. Krishnan, P. M. Varkey, M. Ravindran, and L. Ramachandran, "Fuel Regression Rate in Hydroxyl-Terminated-Polybutadiene/Gaseous-Oxygen Hybrid Rocket Motors," *Journal of Propulsion and Power*, vol. 17, no. 1, pp. 35–42, Jan. 2001. [Online]. Available: https://doi.org/10.2514/2.5704

[17] G. Zilliac and M. A. Karabeyoglu, "Hybrid rocket fuel regression rate data and modeling," presented at the 42nd AIAA/ASME/SAE/ASEE Joint Propulsion Conference, Sacramento, CA, July 9-12 2006. [Online]. Available: https://doi.org/10.2514/6.2006-4504

[18] K. Lohner, J. Dyer, E. Doran, Z. Dunn, and G. Zilliac, "Fuel regression rate characterization using a laboratory scale nitrous oxide hybrid propulsion system," presented at the 42nd AIAA/ASME/SAE/ASEE Joint Propulsion Conference &

Exhibit. Sacramento, CA: American Institute of Aeronautics and Astronautics, 9 - 12 July 2006. [Online]. Available: https://doi.org/10.2514/6.2006-4671

[19] B. Dumas, O. Jobin, W. Kaprolat, J. Zahlawi, and E. Robert, "Ignition delay and performance of sorbitol based hypergolic hybrid fuels," *Fuel*, vol. 349, p. 128417, 2023. [Online]. Available: https://doi.org/10.1016/j.fuel.2023.128417

[20] A. Karabeyoglu and U. Arkun, "Evaluation of Fuel Additives for Hybrid Rockets and SFRJ Systems," presented at the 50th AIAA/ASME/SAE/ASEE Joint Propulsion Conference. Cleveland, OH: American Institute of Aeronautics and Astronautics, July 28-30 2014, pp. 1–41. [Online]. Available: https://doi.org/10.2514/6.2014-3647

[21] B. Evans, E. Boyer, K. K. Kuo, G. Risha, and M. Chiaverini, "Hybrid rocket investigations at penn state university's high pressure combustion laboratory: Overview and recent results," presented at the 45th AIAA/ASME/SAE/ASEE Joint Propulsion Conference and Exhibit, Denver, CO, Aug. 2-5 2009, pp. 1–22.

[22] B. Elzein, O. Jobin, and E. Robert, "Reducing the ignition delay of hypergolic hybrid rocket fuels," *Journal of Propulsion and Power*, vol. 37, no. 1, pp. 77–85, 2021. [Online]. Available: https://doi.org/10.2514/1.B37918

[23] S. Kim, J. Lee, H. Moon, H. Sung, J. Kim, and J. Cho, "Effect of Paraffin-LDPE Blended Fuel on the Hybrid Rocket Motor," presented at the 46th AIAA/ASME/SAE/ASEE Joint Propulsion Conference & Exhibit. Nashville, TN: American Institute of Aeronautics and Astronautics, July 25-28 2010. [Online]. Available: https://doi.org/10.2514/6.2010-7031

[24] S. Kim, H. Moon, J. Kim, and J. Cho, "Evaluation of Paraffin–Polyethylene Blends as Novel Solid Fuel for Hybrid Rockets," *Journal of Propulsion and Power*, vol. 31, no. 6, pp. 1750–1760, nov 2015. [Online]. Available: https://doi.org/10.2514/1.B35565

[25] I. Nakagawa, S. Hikone, and T. Suzuki, "A Study on the Regression Rate of Parrafin-Based Hybrid Rocket Fuels," presented at the 45th AIAA/ASME/SAE/ASEE Joint Propulsion Conference & Exhibit. Denver, CO: American Institute of Aeronautics and Astronautics, Aug. 2-5 2009, pp. 1276–1279. [Online]. Available: https://doi.org/10.2514/6.2009-4935

[26] S. Maruyama, T. Ishiguro, K. Shinohara, and I. Nakagawa, "Study on Mechanical Characteristics of Paraffin-Based Fuel," presented at the 47th AIAA/ASME/SAE/ASEE Joint Propulsion Conference & Exhibit. San Diego, CA:

American Institute of Aeronautics and Astronautics, July 31 - Aug. 3 2011. [Online]. Available: https://doi.org/10.2514/6.2011-5678

[27] D. Mengu and R. Kumar, "Development of EVA-SEBS based wax fuel for hybrid rocket applications," *Acta Astronautica*, vol. 152, pp. 325–334, Nov. 2018. [Online]. Available: https://doi.org/10.1016/j.actaastro.2018.08.034

[28] T. Ishigaki and I. Nakagawa, "Improving Physical Properties of Wax-Based Fuels and Its Effect on Regression Rate," *Journal of Propulsion and Power*, pp. 1–6, Nov. 2019. [Online]. Available: https://doi.org/10.2514/1.B37613

[29] K. Bilge, U. Kokal, N. B. Emerce, U. C. Yildiz, M. Baysal, and A. Karabeyoglu, "Selection Criteria for Tackifier Addition to Paraffin Wax based Hybrid Rocket Fuels," presented at the AIAA Propulsion and Energy 2019 Forum. Indianapolis, IN: American Institute of Aeronautics and Astronautics, Aug. 19-22 2019. [Online]. Available: https://doi.org/10.2514/6.2019-3921

[30] M. Pfeil, "Solid amine-boranes as high performance hypergolic hybrid rocket fuels," PhD dissertation, Purdue University, oct 2014. [Online]. Available: https://docs.lib.purdue.edu/open_access_dissertations/347/

[31] T. R. Sippel, S. C. Shark, M. C. Hinkelman, T. L. Pourpoint, S. F. Son, and S. D. Heister, "Hypergolic Ignition of Metal Hydride-based Fuels with Hydrogen Peroxide," presented at the 7th US National Combustion Meeting, Atlanta, GA, March 20-23 2011, pp. 1–15. [Online]. Available: https://www.researchgate.net/publication/265727021

[32] K. J. Stober, A. Thomas, B. J. Evans, and B. J. Cantwell, "Investigation of Green Hypergolic Propellants for Hybrid Rockets," presented at the 52nd AIAA/SAE/ASEE Joint Propulsion Conference. Salt Lake City, UT: American Institute of Aeronautics and Astronautics, July 25-27 2016. [Online]. Available: https://doi.org/10.2514/6.2016-4991

[33] M. Pfeil, A. S. Kulkarni, P. V. Ramachandran, S. F. Son, and S. D. Heister, "Solid Amine–Boranes as High-Performance and Hypergolic Hybrid Rocket Fuels," *Journal of Propulsion and Power*, vol. 32, no. 1, pp. 23–31, jan 2016. [Online]. Available: https://doi.org/10.2514/1.B35591

[34] U. B. Demirci, "Ammonia borane , a material with exceptional properties for chemical hydrogen storage," *International Journal of Hydrogen Energy*, vol. 42, no. 15, pp. 9978–10 013, 2017. [Online]. Available: https://doi.org/10.1016/j.ijhydene.2017.01.154

[35] H.-C. J. Zhou and S. Kitagawa, "Metal–Organic Frameworks (MOFs)," *Chemical Society Reviews*, vol. 43, no. 16, pp. 5415–5418, jul 2014. [Online]. Available: https://doi.org/10.1039/C4CS90059F

[36] H.-C. Zhou, J. R. Long, and O. M. Yaghi, "Introduction to Metal–Organic Frameworks," *Chemical Reviews*, vol. 112, no. 2, pp. 673–674, feb 2012. [Online]. Available: https://doi.org/10.1021/cr300014x

[37] S. L. James, "Metal-organic frameworks," *Chemical Society Reviews*, vol. 32, no. 5, p. 276, aug 2003. [Online]. Available: https://doi.org/10.1039/b200393g

[38] Y. Cui, B. Li, H. He, W. Zhou, B. Chen, and G. Qian, "Metal–Organic Frameworks as Platforms for Functional Materials," *Accounts of Chemical Research*, vol. 49, no. 3, pp. 483–493, mar 2016. [Online]. Available: https://doi.org/10.1021/acs.accounts.5b00530

[39] H. M. Titi, J. M. Marrett, G. Dayaker, M. Arhangelskis, C. Mottillo, A. J. Morris, G. P. Rachiero, T. Friščić, and R. D. Rogers, "Hypergolic zeolitic imidazolate frameworks (ZIFs) as next-generation solid fuels: Unlocking the latent energetic behavior of ZIFs," *Science Advances*, vol. 5, no. 4, pp. 1–8, apr 2019. [Online]. Available: https://doi.org/10.1126/sciadv.aav9044

[40] K. Wang, Z. Wang, X. Zhao, X. Qi, S. Song, Y. Jin, and Q. Zhang, "Unearthing hidden hypergolic potential of energetic complexes with hydrogen peroxide," *Combustion and Flame*, vol. 244, p. 112235, 2022. [Online]. Available: https://doi.org/10.1016/j.combustflame.2022.112235

[41] Y.-J. Wang, X.-Y. Wang, H. Xu, W.-W. Ren, R. Pang, L. Yang, W.-C. Tong, Q.-Y. Wang, and S.-Q. Zang, "One-dimensional copper bromide based inorganic-organic hybrids as fuels for hypergolic bipropellants with hydrogen peroxide as oxidizer," *Chemical Engineering Journal*, vol. 455, p. 140587, 2023. [Online]. Available: https://doi.org/10.1016/j.cej.2022.140587

[42] A. Cervone, L. Torre, L. D'Agostino, A. J. Musker, G. T. Roberts, C. Bramanti, and G. Saccoccia, "Development of hydrogen peroxide monopropellant rockets," presented at the 42nd AIAA/ASME/SAE/ASEE Joint Propulsion Conference, Sacramento, CA, July 9-12 2006. [Online]. Available: https://doi.org/10.2514/6.2006-4504

[43] S. A. Whitmore, I. W. Armstrong, M. C. Heiner, and C. J. Martinez, "High-performing hydrogen peroxide hybrid rocket with 3-d printed and extruded abs fuel," presented

at the AIAA Propulsion and Energy 2018 Forum, Cincinnati, OH, July 9-11 2018. [Online]. Available: http://doi.org/10.2514/6.2018-4443

[44] R. Amri, D. Gibbon, and T. Rezoug, "The design, development and test of one newton hydrogen peroxide monopropellant thruster," *Aerospace Science and Technology*, vol. 25, no. 1, pp. 266–272, 2013. [Online]. Available: http://doi.org/10.1016/j.ast.2012.02.002

[45] K. Sobczak, P. Surmacz, B. Bartkowiak, A. Okninski, G. Rarata, D. Kublik, and F. V. Bel, "Test Campaign of a Green Liquid Bi-propellant Rocket Engine Using Catalytically Decomposed 98% Hydrogen Peroxide as Oxidizer," presented at the 53rd AIAA/SAE/ASEE Joint Propulsion Conference. Atlanta, GA: American Institute of Aeronautics and Astronautics, July 10-12 2017. [Online]. Available: https://doi.org/10.2514/6.2017-4926

[46] M. Santi, I. Dorgnach, F. Barato, and D. Pavarin, "Design and Testing of a 3D Printed 10 N Hydrogen Peroxide Monopropellant Thruster," presented at the AIAA Propulsion and Energy 2019 Forum, Indianapolis, IN, August 19-22 2019. [Online]. Available: https://doi.org/10.2514/6.2019-4277

[47] B. Ahn, H. Kang, E. Lee, Y. Yun, and S. Kwon, "Design of multiport grain with hydrogen peroxide hybrid rocket," *Journal of Propulsion and Power*, vol. 34, no. 5, pp. 1189–1197, 2018. [Online]. Available: http://doi.org/10.2514/1.B36949

[48] J. Anthoine, J.-Y. Lestrade, J. Messineo, and S. Casu, "Performances of a multi-pulsed hybrid rocket engine operating with highly concentrated hydrogen peroxide," presented at the 53rd AIAA/SAE/ASEE Joint Propulsion Conference, Atlanta, GA, July 10-12 2017.

[49] S. Bonifacio, G. Festa, and A. Russo Sorge, "Novel structured catalysts for hydrogen peroxide decomposition in monopropellant and hybrid rockets," *Journal of Propulsion and Power*, vol. 29, no. 5, pp. 1130–1137, 2013. [Online]. Available: http://doi.org/10.2514/1.B34864

[50] O. Bozic, D. Porrmann, D. Lancelle, and S. May, "Enhanced development of a catalyst chamber for the decomposition of up to 1.0kg/s hydrogen peroxide," *CEAS Space Journal*, vol. 8, no. 2, pp. 77–88, 2016. [Online]. Available: https://doi.org/10.1007/s12567-015-0109-x

[51] V. K. Bhosale, J. Jeong, and S. Kwon, "Ignition of boron-based green hypergolic fuels with hydrogen peroxide," *Fuel*, vol. 255, p. 115729, 2019. [Online]. Available: https://doi.org/10.1016/j.fuel.2019.115729

[52] D. A. Castaneda and B. Natan, "Experimental investigation of the hydrogen peroxide – solid hydrocarbon hypergolic ignition," *Acta Astronautica*, vol. 158, pp. 286–295, 2019. [Online]. Available: https://doi.org/10.1016/j.actaastro.2018.05.058

[53] J. Jeong, V. K. Bhosale, and S. Kwon, "Ultrafast igniting, low toxicity hypergolic hybrid solid fuels and hydrogen peroxide oxidizer," *Fuel*, vol. 286, p. 119307, 2021. [Online]. Available: https://doi.org/10.1016/j.fuel.2020.119307

[54] J. Jeong, K.-S. Kim, V. K. Bhosale, and S. Kwon, "Demonstration of ammonia borane-based hypergolic ignitor for hybrid rocket," *Acta Astronautica*, vol. 196, pp. 85–93, 2022. [Online]. Available: https://doi.org/10.1016/j.actaastro.2022.04.009

[55] J. Jeong, S. Rang, V. M. Pierre Ugolini, and S. Kwon, "Hypergolicity improvement by activated carbon-supported catalysts for hydrogen peroxide oxidizer," *Acta Astronautica*, vol. 198, pp. 720–727, 2022. [Online]. Available: https://doi.org/10.1016/j.actaastro.2022.06.011

[56] S. Rang, J. Jeong, V. Khandu Bhosale, and S. Kwon, "Reactivity of hypergolic hybrid solid fuel with industrial grade hydrogen peroxide," *Fuel*, vol. 330, p. 125543, 2022. [Online]. Available: https://doi.org/10.1016/j.fuel.2022.125543

[57] M. Weismiller, T. Connell, G. Risha, and R. Yetter, "Characterization of Ammonia Borane (NH3BH3) Enhancement to a Paraffin Fueled Hybrid Rocket System," presented at the 46st AIAA/SAE/ASEE Joint Propulsion Conference. Nashville, TN: American Institute of Aeronautics and Astronautics, July 25-28 2010, pp. 1–12. [Online]. Available: https://doi.org/10.2514/6.2010-6639

[58] H. Karakas, O. Kara, I. Ozkol, and A. M. Karabeyoglu, "Performance Enhancing Additives for Hybrid Rockets," presented at the AIAA Propulsion and Energy 2019 Forum. Indianapolis, IN: American Institute of Aeronautics and Astronautics, Aug. 19-22 2019. [Online]. Available: https://doi.org/10.2514/6.2019-3922

[59] P. V. Ramachandran, A. S. Kulkarni, M. A. Pfeil, J. D. Dennis, J. D. Willits, S. D. Heister, S. F. Son, and T. L. Pourpoint, "Amine-Boranes: Green Hypergolic Fuels with Consistently Low Ignition Delays," *Chemistry - A European*

Journal, vol. 20, no. 51, pp. 16 869–16 872, Dec. 2014. [Online]. Available: http://doi.wiley.com/10.1002/chem.201405224

[60] K. J. Stober, "Optical Investigation of Hypergolic Ignition and Combustion in Paraffin-based Hybrid Rockets," PhD dissertation, Stanford University, Stanford, CA, 2017. [Online]. Available: https://www.proquest.com/dissertations-theses/optical-investigation-hypergolic-ignition/docview/2501890352/se-2

[61] M. J. Baier, P. V. Ramachandran, and S. F. Son, "Characterization of the Hypergolic Ignition Delay of Ammonia Borane," *Journal of Propulsion and Power*, vol. 35, no. 1, pp. 182–189, nov 2018. [Online]. Available: https://doi.org/10.2514/1.b37075

[62] K. Clements, M. Baier, P. V. Ramachandran, and S. Son, "An Experimental Study of Factors Affecting Hypergolic Ignition of Ammonia Borane," presented at the AIAA Propulsion and Energy 2019 Forum, Indianapolis, IN, Aug. 19-22 2019. [Online]. Available: https://doi.org/10.2514/6.2019-4101

[63] K. J. Stober, B. J. Cantwell, and R. A. L. Otaibi, "Hypergolic Ignition of Lithium–Aluminum–Hydride-Doped Paraffin Wax and Nitric Acid," *Journal of Propulsion and Power*, vol. 36, no. 3, pp. 435–445, may 2020.

[64] K. A. Clements, M. J. Baier, P. V. Ramachandran, and S. F. Son, "Experimental Study of Factors Affecting Hypergolic Ignition of Ammonia Borane," *Journal of Propulsion and Power*, vol. 37, no. 2, pp. 202–210, mar 2021.

[65] S. Nath, I. Laso, and J. Lefkowitz, "Parametric ignition study of a green hypergolic hybrid rocket fuel," presented at the AIAA SCITECH 2022 Forum. San Diego, CA: American Institute of Aeronautics and Astronautics, Jan. 4-6 2022. [Online]. Available: https:/doi.org/10.2514/6.2022-1484

[66] S. Nath, I. Laso, L. Mallick, Z. Sobe, S. Koffler, B. Blumer-Ganon, E. Borzin, N. Libis, and J. K. Lefkowitz, "Comprehensive ignition characterization of a non-toxic hypergolic hybrid rocket propellant," *Proceedings of the Combustion Institute*, vol. 39, no. 3, pp. 3361–3370, 2023. [Online]. Available: https://doi.org/10.1016/j.proci.2022.07.118

[67] S. de Persis, A. Dollet, and F. Teyssandier, "Pressure Dependence of Gas-Phase Reaction Rates," *Journal of Chemical Education*, vol. 81, no. 6, p. 832, June 2004. [Online]. Available: https://pubs.acs.org/doi/abs/10.1021/ed081p832

[68] A. Benhidjeb-Carayon, J. McCormick, C. Yilmaz, J. R. Gabl, B. E. Whitehead, and T. L. Pourpoint, "Hypergolic Hybrid Rocket Motor Characterization with

MON-25 at Atmospheric and Reduced Pressures," presented at the AIAA Propulsion and Energy 2019 Forum, Indianapolis, IN, Aug. 19-22 2019. [Online]. Available: https://doi.org/10.2514/6.2019-4338

[69] A. Benhidjeb-Carayon, M. P. Drolet, J. R. Gabl, and T. L. Pourpoint, "Reactivity and hypergolicity of solid fuels with mixed oxides of nitrogen," *Journal of Propulsion and Power*, vol. 35, no. 2, pp. 466–474, 2019. [Online]. Available: https://doi.org/10.2514/1.B37297

[70] A. Benhidjeb-Carayon, J. M. McCormick, C. Yilmaz, J. R. Gabl, B. E. Whitehead, and T. L. Pourpoint, "Hypergolic ignition of a paraffin-based hybrid motor with mon-25 at 100,000 ft simulated altitude," presented at the AIAA Propulsion and Energy 2020 Forum. Virtual: American Institute of Aeronautics and Astronautics, Aug. 24-28 2020. [Online]. Available: https://doi.org/10.2514/6.2020-3728

[71] A. Cortopassi and J. E. Boyer, "Hypergolic ignition testing of solid fuel additives with mon-3 oxidizer," presented at the 53rd AIAA/SAE/ASEE Joint Propulsion Conference. Atlanta, GA: American Institute of Aeronautics and Astronautics, July 10-12 2017. [Online]. Available: https://doi.org/10.2514/6.2017-5050

[72] A. Benhidjeb-Carayon, J. Gabl, and T. L. Pourpoint, "Hypergolic Ignition and Relights of a Paraffin-based Hybrid Grain," presented at the AIAA Propulsion and Energy 2018 Forum, Cincinnati, OH, July 9-11 2018. [Online]. Available: https://doi.org/10.2514/6.2018-4661

[73] A. Benhidjeb-Carayon, J. R. Gabl, B. E. Whitehead, and T. L. Pourpoint, "Hypergolic hybrid rocket engine ignition and relights with mixed oxides of nitrogen," *Journal of Propulsion and Power*, vol. 38, no. 1, pp. 111–121, 2022. [Online]. Available: https://doi.org/10.2514/1.B38266

[74] B. Oglesby, A. Prince, G. Story, and A. Kam, "Qualification of a Hybrid Propulsion System for a Mars Ascent Vehicle," presented at the 2019 IEEE Aerospace Conference, Big Sky, MT, Mar. 2-9 2019. [Online]. Available: https://ieeexplore.ieee.org/document/8741599

[75] A. C. Karp, B. Nakazono, G. Story, J. Chaffin, and G. Zilliac, "Hybrid Propulsion Technology Development for a Potential Near- Term Mars Ascent Vehicle," presented at the 2019 IEEE Aerospace Conference, Big Sky, MT, Mar. 2-9 2019. [Online]. Available: https://ieeexplore.ieee.org/document/8741854/

[76] G. T. Story, A. Schnell, D. Yaghoubi, A. C. Karp, B. Nakazono, and G. G. Zilliac, "A Single Stage to Orbit Design for a Hybrid Mars Ascent Vehicle," presented at the AIAA Propulsion and Energy 2019 Forum, Indianapolis, IN, Aug. 19-22 2019. [Online]. Available: https://doi.org/10.2514/6.2019-3840

[77] S. Nath, L. Mallick, and J. Lefkowitz, "Spray ignition studies on a green hypergolic hybrid rocket propellant," presented at the AIAA SCITECH 2023 Forum. National Habor, MD: American Institute of Aeronautics and Astronautics, Jan. 23-27 2023. [Online]. Available: https://doi.org/10.2514/6.2023-1831

[78] G. Marxman, C. Wooldridge, and R. Muzzy, "Fundamentals of Hybrid Boundary Layer Combustion," presented at the Heterogeneous Combustion Conference. Palm Beach, FL: American Institute of Aeronautics and Astronautics, Dec. 11-13 1963. [Online]. Available: https://doi.org/10.2514/6.1963-505

[79] G. A. Marxman, C. E. Wooldridge, and R. J. Muzzy, "Fundamentals of Hybrid Boundary-Layer Combustion," *Progress in Astronautics and Rocketry*, vol. 15, pp. 485–522, Jan. 1964. [Online]. Available: https://doi.org/10.1016/B978-1-4832-2730-6.50025-7

[80] L. D. Strand, R. L. Ray, F. A. Anderson, and N. S. Cohen, "Hybrid rocket fuel combustion and regression rate study," presented at the AIAA/ASME/SAE/ASEE 28th Joint Propulsion Conference and Exhibit, American Institute of Aeronautics and Astronautics, Ed., Nashville, TN, July 6-8 1992. [Online]. Available: https://doi.org/10.2514/6.1992-3302

[81] L. D. Strand and R. L. Ray, "Hybrid rocket combustion study," presented at the AIAA/ASME/SAE/ASEE 29th Joint Propulsion Conference and Exhibit, American Institute of Aeronautics and Astronautics, Ed., Monterey, CA, June 28-30 1993. [Online]. Available: https://doi.org/10.2514/6.1993-2412

[82] M. J. Chiaverini, G. C. Harting, Y.-C. Lu, K. K. Kuo, N. Serin, and D. K. Johnson, "Combustion of Solid Fuel Slabs with Gaseou Oxygen in a Hybrid Motor Analog," National Aeronautics and Space Administration, Tech. Rep., 1995. [Online]. Available: https://ntrs.nasa.gov/search.jsp?R=19960033268

[83] M. J. Chiaverini, N. Serin, D. K. Johnson, Y. C. Lu, K. K. Kuo, and G. A. Risha, "Regression rate behavior of hybrid rocket solid fuels," *Journal of Propulsion and Power*, vol. 16, no. 1, pp. 125–132, 2000.

[84] M. J. Chiaverini, K. K. Kuo, A. Peretz, and G. C. Harting, "Regression-rate and heat-transfer correlations for hybrid rocket combustion," *Journal of Propulsion and Power*, vol. 17, no. 1, pp. 99–110, 2001.

[85] E. T. Jens, "Hybrid Rocket Combustion And Applications To Space Exploration Missions," PhD dissertation, Stanford University, 2015. [Online]. Available: http://purl.stanford.edu/hq136qf4444

[86] J.-Y. Lestrade, "Modélisation de la régression des combustibles liquéfiables dans un moteur hybride," PhD dissertation, Université de Toulouse - ISAE, Toulouse, France, 2012. [Online]. Available: https://www.theses.fr/2012ESAE0039

[87] S. Hikone, S. Maruyama, T. Isiguro, and I. Nakagawa, "Regression Rate Characteristics and Burning Mechanism of Some Hybrid Rocket Fuels," presented at the 46th AIAA/ASME/SAE/ASEE Joint Propulsion Conference & Exhibit, American Institute of Aeronautics and Astronautics, Ed. Nashville, TN: American Institute of Aeronautics and Astronautics, July 25-28 2010, pp. 1–7. [Online]. Available: https://doi.org/10.2514/6.2010-7030

[88] Y. Wada, Y. Kawabata, R. Kato, N. Kato, and K. Hori, "Observation of Combustion Behavior of Lowmelting Temperature Fuel for a Hybrid Rocket Using Double Slab Motor," *International Journal of Energetic Materials and Chemical Propulsion*, vol. 15, no. 5, pp. 351–369, 2016. [Online]. Available: https://doi.org/10.1615/IntJEnergeticMaterialsChemProp.2017011278

[89] H. K. Ciezki, J. Sender, W. Clauß, A. Feinauer, and A. Thumann, "Combustion of solid-fuel slabs containing boron particles in step combustor," *Journal of Propulsion and Power*, vol. 19, no. 6, pp. 1180–1191, 2003. [Online]. Available: https://doi.org/10.2514/2.6938

[90] M. Kobald, H. Ciezki, and S. Schlechtriem, "Optical Investigation of the Combustion Process in Paraffin-based Hybrid Rocket Fuels," presented at the 49th AIAA/ASME/SAE/ASEE Joint Propulsion Conference, American Institute of Aeronautics and Astronautics, Ed. San Jose, CA: American Institute of Aeronautics and Astronautics, July 14-17 2013, pp. 1–16. [Online]. Available: https://doi.org/10.2514/6.2013-3894

[91] M. Kobald, C. Schmierer, H. Ciezki, S. Schlechtriem, E. Toson, and L. T. De Luca, "Evaluation of paraffin-based fuels for hybrid rocket engines," presented at the 50th

AIAA/ASME/SAE/ASEE Joint Propulsion Conference 2014, American Institute of Aeronautics and Astronautics, Ed., Cleveland, OH, July 28-30 2014, pp. 1–16.

[92] M. Kobald, I. Verri, and S. Schlechtriem, "Theoretical and experimental analysis of liquid layer instability in hybrid rocket engines," *CEAS Space Journal*, vol. 7, no. 1, pp. 11–22, Mar. 2015. [Online]. Available: https://doi.org/10.1007/s12567-015-0076-2

[93] M. Kobald, A. Petrarolo, and S. Schlechtriem, "Combustion visualization and characterization of liquefying hybrid rocket fuels," presented at the 51st AIAA/SAE/ASEE Joint Propulsion Conference, American Institute of Aeronautics and Astronautics, Ed. Orlando, FL: American Institute of Aeronautics and Astronautics, July 27-29 2015. [Online]. Available: https://doi.org/10.2514/6.2015-4137

[94] M. Kobald, E. Toson, H. Ciezki, S. Schlechtriem, S. di Betta, M. Coppola, and L. T. De Luca, "Rheological, optical, and ballistic investigations of paraffin-based fuels for hybrid rocket propulsion using a two-dimensional slab-burner," in *Progress in Propulsion Physics*, M. Calabro, L. DeLuca, S. Frolov, L. Galfetti, and O. Haidn, Eds., vol. 8. Les Ulis, France: EDP Sciences, jul 2016, pp. 263–282. [Online]. Available: http://www.eucass-proceedings.eu/10.1051/eucass/201608263

[95] E. Toson, M. Kobald, E. Cavanna, L. T. De Luca, G. Consolati, and H. Ciezki, "FEASIBILITY STUDY OF PARAFFIN-BASED FUELS FOR HYBRID ROCKET ENGINE APPLICATIONS," *International Journal of Energetic Materials and Chemical Propulsion*, vol. 13, no. 6, pp. 559–572, 2014. [Online]. Available: https://doi.org/10.1615/IntJEnergeticMaterialsChemProp.2014011243

[96] A. Petrarolo, M. Kobald, and S. Schlechtriem, "Visualization of Combustion Phenomena in Paraffin-Based Hybrid Rocket Fuels at Super-Critical Pressures," presented at the AIAA Propulsion and Energy 2018 Forum, American Institute of Aeronautics and Astronautics, Ed. Cincinnati, OH: American Institute of Aeronautics and Astronautics, July 9-11 2018, pp. 1–15. [Online]. Available: https://doi.org/10.2514/6.2018-4927

[97] A. Petrarolo, M. Kobald, H. K. Ciezki, and S. Schlechtriem, "Principal and independent component analysis of hybrid combustion flame," *International Journal of Energetic Materials and Chemical Propulsion*, vol. 18, no. 1, pp. 9–29, 2019. [Online]. Available: https://doi.org/10.1615/IntJEnergeticMaterialsChemProp.2019028035

[98] A. Petrarolo, M. Kobald, and S. Schlechtriem, "Optical analysis of the liquid layer combustion of paraffin-based hybrid rocket fuels," *Acta Astronautica*, vol. 158, pp. 313–322, May 2019. [Online]. Available: https://doi.org/10.1016/j.actaastro.2018.05.059

[99] L. Galfetti, L. Merotto, M. Boiocchi, F. Maggi, and L. T. DeLuca, "Experimental investigation of paraffin-based fuels for hybrid rocket propulsion," *Progress in Propulsion Physics*, vol. 4, pp. 59–74, Mar. 2013. [Online]. Available: http://www.eucass-proceedings.eu/10.1051/eucass/201304059

[100] A. Chandler, E. T. Jens, B. J. Cantwell, and S. Hubbard, "Visualization of the Liquid Layer Combustion of Paraffin Fuel for Hybrid Rocket Applications," presented at the 48th AIAA/ASME/SAE/ASEE Joint Propulsion Conference & Exhibit, American Institute of Aeronautics and Astronautics, Ed. Atlanta, GA: American Institute of Aeronautics and Astronautics, July 30- Aug. 1 2012, p. 11.

[101] E. T. Jens, F. S. Mechentel, and B. J. Cantwell, "Combustion Visualization of Paraffin-Based Hybrid Rocket Fuel at Elevated Pressures," presented at the 50th AIAA/ASME/SAE/ASEE Joint Propulsion Conference, American Institute of Aeronautics and Astronautics, Ed. Cleveland, OH: American Institute of Aeronautics and Astronautics, July 28-30 2014, pp. 1–10. [Online]. Available: https://doi.org/10.2514/6.2014-3848

[102] E. T. Jens, V. A. Miller, F. S. Mechentel, B. J. Cantwell, and S. Hubbard, "A Visual Study of the Combustion of High-Regression Rate and Classical Hybrid Rocket Fuels," presented at the 51st AIAA/SAE/ASEE Joint Propulsion Conference, American Institute of Aeronautics and Astronautics, Ed. Orlando, FL: American Institute of Aeronautics and Astronautics, July 27-29 2015. [Online]. Available: https://doi.org/10.2514/6.2015-3830

[103] E. T. Jens, V. A. Miller, and B. J. Cantwell, "Schlieren and OH* chemiluminescence imaging of combustion in a turbulent boundary layer over a solid fuel," *Experiments in Fluids*, vol. 57, no. 3, p. 39, mar 2016. [Online]. Available: https://doi.org/10.1007/s00348-016-2124-x

[104] E. T. Jens, A. C. Karp, V. A. Miller, G. S. Hubbard, and B. J. Cantwell, "Experimental Visualization of Hybrid Combustion: Results at Elevated Pressures," *Journal of Propulsion and Power*, pp. 1–14, oct 2019. [Online]. Available: https://doi.org/10.2514/1.B37416

[105] M. A. Karabeyoglu and B. J. Cantwell, "Combustion of Liquefying Hybrid Propellants Part 2, Stability of Liquid Films," *Journal of Propulsion and Power*, vol. 18, no. 3, pp. 621–630, May 2002. [Online]. Available: https://doi.org/10.2514/2.5976

[106] C. C. McDougall, C. Hill, C. Heinrichs, and C. T. Johansen, "Spectroscopic Techniques for Measuring Regression Rates of Liquefying Hybrid Rocket Fuels," presented at the AIAA Propulsion and Energy 2019 Forum, American Institute of Aeronautics and Astronautics, Ed. Indianapolis, IN: American Institute of Aeronautics and Astronautics, Aug. 19-22 2019. [Online]. Available: https://doi.org/10.2514/6.2019-4098

[107] C. Hill, C. C. McDougall, T. Messinger, and C. T. Johansen, "Modification of Paraffin-based Hybrid Rocket Fuels Using Structural Lattices," presented at the AIAA Propulsion and Energy 2019 Forum, American Institute of Aeronautics and Astronautics, Ed. Indianapolis, IN: American Institute of Aeronautics and Astronautics, Aug. 19-22 2019. [Online]. Available: https://doi.org/10.2514/6.2019-4191

[108] K. Veale, S. Adali, J. Pitot, and M. Brooks, "A review of the performance and structural considerations of paraffin wax hybrid rocket fuels with additives," *Acta Astronautica*, vol. 141, pp. 196–208, Dec. 2017. [Online]. Available: https://doi.org/10.1016/j.actaastro.2017.10.012

[109] R. Theba, K. Veale, and C. Bemont, "Development of a Combustion Visualisation Hybrid Rocket Motor," *Journal of the South African Institution of Mechanical Engineering*, vol. 33, no. 33, pp. 97–104, 2017. [Online]. Available: http://www.scielo.org.za/scielo.php?script=sci_arttext&pid=S2309-89882017000100001

[110] Y. Wang, S. qi Hu, X. li Liu, and L. lin Liu, "Boundary layer combustion of htpb/paraffin fuels for hybrid propulsion applications," *Aerospace Science and Technology*, vol. 129, p. 107850, 2022. [Online]. Available: https://doi.org/10.1016/j.ast.2022.107850

[111] Y. Wang, S. qi Hu, X. li Liu, Y. Zhang, and L. lin Liu, "Droplet entrainment and its role in the combustion of htpb/paraffin fuels," *Acta Astronautica*, vol. 204, pp. 107–115, 2023. [Online]. Available: https://doi.org/10.1016/j.actaastro.2022.12.042

[112] C. Glaser, R. Gelain, A. Bertoldi, Q. Levard, J. Hijlkema, J.-Y. Lestrade, P. Hendrick, and J. Anthoine, "Experimental regression rate profiles of stepped fuel grains in

hybrid rocket engines," *Acta Astronautica*, vol. 204, pp. 186–198, 2023. [Online]. Available: https://doi.org/10.1016/j.actaastro.2022.12.045

[113] N. T. Smith, M. J. Lewis, and R. Chellappa, "Detection, localization, and tracking of shock contour salient points in schlieren sequences," *AIAA Journal*, vol. 52, no. 6, pp. 1249–1264, Apr. 2014. [Online]. Available: https://doi.org/10.2514/1.J052367

[114] G. S. Settles and M. J. Hargather, "A review of recent developments in schlieren and shadowgraph techniques," *Measurement Science and Technology*, vol. 28, no. 4, Apr. 2017. [Online]. Available: https:/doi.org/10.1088/1361-6501/aa5748

[115] B. F. Bathel, C. R. Litzner, S. B. Jones, S. A. Berry, N. T. Smith, and T. J. Garbeff, "High-Speed Schlieren Analysis of Retropropulsion Jet in Mach 10 Flow," *Journal of Spacecraft and Rockets*, pp. 1–16, Aug. 2019. [Online]. Available: https://doi.org/10.2514/1.a34522

[116] V. Nori and J. Seitzman, "Evaluation of chemiluminescence as a combustion diagnostic under varying operating conditions," presented at the 46th AIAA Aerospace Sciences Meeting and Exhibit, Reno, NV, Jan. 7-10 2008, pp. 1–14. [Online]. Available: https://doi.org/10.2514/6.2008-953

[117] C. S. Panoutsos, Y. Hardalupas, and A. M. Taylor, "Numerical evaluation of equivalence ratio measurement using OH* and CH* chemiluminescence in premixed and non-premixed methane-air flames," *Combustion and Flame*, vol. 156, no. 2, pp. 273–291, 2009. [Online]. Available: http://doi.org/10.1016/j.combustflame.2008.11.008

[118] M. Lauer and T. Sattelmayer, "On the adequacy of chemiluminescence as a measure for heat release in turbulent flames with mixture gradients," *Journal of Engineering for Gas Turbines and Power*, vol. 132, no. 6, pp. 1–8, 2010. [Online]. Available: https://doi.org/10.1115/1.4000126

[119] V. N. Nori and J. M. Scitzman, "CH* chemiluminescence modeling for combustion diagnostics," *Proceedings of the Combustion Institute*, vol. 32 I, pp. 895–903, 2009. [Online]. Available: 10.1016/j.proci.2008.05.050

[120] O. Jobin, C. Mottillo, H. M. Titi, J. M. Marrett, M. Arhangelskis, R. D. Rogers, B. Elzein, T. Friščić, and E. Robert, "Metal–organic frameworks as hypergolic additives for hybrid rockets," *Chemical Science*, vol. 13, pp. 3424–3436, 2022. [Online]. Available: https://doi.org/10.1039/D1SC05975K

[121] O. Jobin, B. Dumas, J. Zahlawi, M. Chartray-Pronovost, and Étienne Robert, "Hypergolic ignition of paraffin-based hybrid rocket fuels by sprays of liquid oxidizer," *Proceedings of the Combustion Institute*, vol. 39, no. 4, pp. 5073–5082, 2023. [Online]. Available: https://doi.org/10.1016/j.proci.2022.08.072

[122] R. D. Mehta and P. Bradshaw, "DESIGN RULES FOR SMALL LOW SPEED WIND TUNNELS." *Aeronautical Journal*, vol. 83, no. 827, pp. 443–449, 1979. [Online]. Available: https://www.doi.org/10.1017/S0001924000031985

[123] J. Scheiman and J. D. Brookst, "Comparison of experimental and theoretical turbulence reduction from screens, honeycomb, and honeycomb-screen combinations," *Journal of Aircraft*, vol. 18, no. 8, pp. 638–643, 1981. [Online]. Available: https://doi.org/10.2514/3.57538

[124] R. D. Mehta, "Turbulent boundary layer perturbed by a screen," *AIAA Journal*, vol. 23, no. 9, pp. 1335–1342, 1985. [Online]. Available: https://doi.org/10.2514/3.9089

[125] R. R. Burley and D. E. Harrington, "EXPERIMENTAL EVALUATION OF HONEYCOMB/SCREEN CONFIGURATIONS AND SHORT CONTRACTION SECTION FOR NASA LEWIS RESEARCH CENTER'S ALTITUDE WIND TUNNEL." National Aeronautics and Space Administration, Tech. Rep., 1987. [Online]. Available: https://ntrs.nasa.gov/search.jsp?R=19870014229

[126] C. Glaser, J. Hijlkema, and J. Anthoine, "Evaluation of regression rate enhancing concepts and techniques for hybrid rocket engines," *Aerotecnica Missili & Spazio*, vol. 101, no. 3, pp. 267–292, Sep 2022. [Online]. Available: https://doi.org/10.1007/s42496-022-00119-4

[127] S. S. Aphale, K. Budzinski, G. Surina, and P. E. DesJardin, "Influence of O2/N2 oxidizer blends on soot formation and radiative heat flux in PMMA-air 2D slab burner fo," *Combustion and Flame*, vol. 234, p. 111628, dec 2021. [Online]. Available: https://doi.org/10.1016/j.combustflame.2021.111628https://linkinghub.elsevier.com/retrieve/pii/S0010218021003710

[128] K. McLaren and B. Rigg, "Xii-the sdc recommended colour-difference formula: Change to cielab," *Journal of the Society of Dyers and Colourists*, vol. 92, no. 9, pp. 337–338, 1976. [Online]. Available: https://doi.org/10.1111/j.1478-4408.1976.tb03300.x

[129] S. Gordon and B. J. Mcbride, "Computer Program for Calculation of Complex Chemical Equilibrium Compositions and Applications - I Analysis," *NASA RP-1311*, October 1994.

[130] G. Sutton and O. Biblarz, *Rocket Propulsion Elements*, 8th ed. New York, USA: John Wiley & Sons, 2010.

[131] J. Malm, "Inclusion of Substances of Very High Concern in the Candidate List (Decision of the European Chemicals Agency), Document # ED/31/2011," European Chemicals Agency, Tech. Rep., 2011. [Online]. Available: https://echa.europa.eu/documents/10162/c5b972a9-f57f-4fd5-8177-04b4e46c5e93

[132] R. V. Petrescu, R. Aversa, B. Akash, R. Bucinell, J. Corchado, F. Berto, M. Mirsayar, A. Apicella, F. I. T. Petrescu, B. Akash, R. Bucinell, J. Corchado, A. Apicella, and F. I. T. Petrescu, "Modern Propulsions for Aerospace-A Review," *Journal of Aircraft and Spacecraft Technology*, vol. 1, no. 1, pp. 1–8, jan 2017. [Online]. Available: https://doi.org/10.3844/jastsp.2017.1.8

[133] T. Harrison, A. Hunter, K. Johnson, and T. Roberts, *Implication of Ultra-Low-Cost Access to Space*. New York, USA: Rowman & Littlefield, 2017. [Online]. Available: https://www.csis.org/analysis/implications-ultra-low-cost-access-space

[134] R. W. Conversano, D. M. Goebel, R. R. Hofer, I. G. Mikellides, and R. E. Wirz, "Performance Analysis of a Low-Power Magnetically Shielded Hall Thruster: Experiments," *Journal of Propulsion and Power*, vol. 33, no. 4, pp. 975–983, jul 2017. [Online]. Available: https://doi.org/10.2514/1.B36230

[135] J. M. Bergthorson, Y. Yavor, J. Palecka, W. Georges, M. Soo, J. Vickery, S. Goroshin, D. L. Frost, and A. J. Higgins, "Metal-water combustion for clean propulsion and power generation," *Applied Energy*, vol. 186, pp. 13–27, jan 2017. [Online]. Available: https://doi.org/10.1016/J.APENERGY.2016.10.033

[136] D. Ma, J. Murray, and J. N. Munday, "Controllable Propulsion by Light: Steering a Solar Sail via Tunable Radiation Pressure," *Advanced Optical Materials*, vol. 5, no. 4, p. 1600668, feb 2017. [Online]. Available: https://doi.org/10.1002/adom.201600668

[137] National Aeronautics and Space Administration, *Reference Guide to The International Space Station*, 2015. [Online]. Available: https://www.nasa.gov/sites/default/files/atoms/files/np-2015-05-022-jsc-iss-guide-2015-update-111015-508c.pdf

[138] B. A. Palaszewski, M. L. Meyer, L. Johnson, D. M. Goebel, H. White, and D. J. Coote, "In-Space Chemical Propulsion System Roadmap," in *Chemical Rocket Propulsion*. Springer, 2017, pp. 655–671. [Online]. Available: https://doi.org/10.1007/978-3-319-27748-6_26

[139] M. C. Vilela Salgado, M. C. N. Belderrain, and T. C. Devezas, "Space Propulsion: a Survey Study About Current and Future Technologies," *Journal of Aerospace Technology and Management*, vol. 10, pp. 1–23, feb 2018. [Online]. Available: https://doi.org/10.5028/jatm.v10.829

[140] A. Mazzetti, L. Merotto, and G. Pinarello, "Paraffin-based hybrid rocket engines applications: A review and a market perspective," *Acta Astronautica*, vol. 126, pp. 286–297, sep 2016. [Online]. Available: https://doi.org/10.1016/J.ACTAASTRO.2016.04.036

[141] S. G. Kulkarni, V. S. Bagalkote, S. S. Patil, U. P. Kumar, and V. A. Kumar, "Theoretical Evaluation and Experimental Validation of Performance Parameters of New Hypergolic Liquid Fuel Blends with Red Fuming Nitric Acid as Oxidizer," *Propellants, Explosives, Pyrotechnics*, vol. 34, no. 6, pp. 520–525, dec 2009. [Online]. Available: https://doi.org/10.1002/prep.200800061

[142] L. He, G.-H. Tao, D. A. Parrish, and J. M. Shreeve, "Nitrocyanamide-Based Ionic Liquids and Their Potential Applications as Hypergolic Fuels," *Chemistry - A European Journal*, vol. 16, no. 19, pp. 5736–5743, may 2010. [Online]. Available: https://doi.org/10.1002/chem.200902651

[143] Y. Zhang, H. Gao, Y.-H. Joo, and J. M. Shreeve, "Ionic Liquids as Hypergolic Fuels," *Angewandte Chemie International Edition*, vol. 50, no. 41, pp. 9554–9562, oct 2011. [Online]. Available: https://doi.org/10.1002/anie.201101954

[144] Y. Zhang and J. M. Shreeve, "Dicyanoborate-Based Ionic Liquids as Hypergolic Fluids," *Angewandte Chemie International Edition*, vol. 50, no. 4, pp. 935–937, jan 2011. [Online]. Available: https://doi.org/10.1002/anie.201005748

[145] S. Schneider, T. Hawkins, Y. Ahmed, M. Rosander, L. Hudgens, and J. Mills, "Green Bipropellants: Hydrogen-Rich Ionic Liquids that Are Hypergolic with Hydrogen Peroxide," *Angewandte Chemie International Edition*, vol. 50, no. 26, pp. 5886–5888, jun 2011. [Online]. Available: https://doi.org/10.1002/anie.201101752

[146] P. V. Ramachandran, A. S. Kulkarni, M. A. Pfeil, J. D. Dennis, J. D. Willits, S. D. Heister, S. F. Son, and T. L. Pourpoint, "Amine-Boranes: Green Hypergolic Fuels with Consistently Low Ignition Delays," *Chemistry - A European Journal*, vol. 20, no. 51, pp. 16 869–16 872, dec 2014. [Online]. Available: http://doi.org/10.1002/chem.201405224

[147] G. P. Rachiero, H. M. Titi, and R. D. Rogers, "Versatility and remarkable hypergolicity of exo-6, exo-9 imidazole-substituted nido-decaborane," *Chemical Communications*, vol. 53, no. 55, pp. 7736–7739, 2017. [Online]. Available: http://doi.org/10.1039/C7CC03322B

[148] J. Yu, T. N. Jensen, W. K. Lewis, C. E. Bunker, S. P. Kelley, R. D. Rogers, O. M. Pryor, S. D. Chambreau, G. L. Vaghjiani, and S. L. Anderson, "Combustion Behavior of High Energy Density Borane–Aluminum Nanoparticles in Hypergolic Ionic Liquids," *Energy & Fuels*, vol. 32, no. 7, pp. 7898–7908, jul 2018. [Online]. Available: https://doi.org/10.1021/acs.energyfuels.8b01334

[149] A. K. Chinnam, N. Petrutik, K. Wang, A. Shlomovich, O. Shamis, D. S. Tov, M. Sućeska, Q.-L. Yan, R. Dobrovetsky, and M. Gozin, "Effects of closo -icosahedral periodoborane salts on hypergolic reactions of 70% H 2 O 2 with energetic ionic liquids," *Journal of Materials Chemistry A*, vol. 6, no. 41, pp. 19 989–19 997, 2018. [Online]. Available: http://doi.org/10.1039/C8TA03780A

[150] K. Wang, A. K. Chinnam, N. Petrutik, E. P. Komarala, Q. Zhang, Q.-L. Yan, R. Dobrovetsky, and M. Gozin, "Iodocuprate-containing ionic liquids as promoters for green propulsion," *Journal of Materials Chemistry A*, vol. 6, no. 45, pp. 22 819–22 829, 2018. [Online]. Available: http://doi.org/10.1039/C8TA08042A

[151] H. M. Titi, M. Arhangelskis, G. P. Rachiero, T. Friščić, and R. D. Rogers, "Hypergolic Triggers as Co-crystal Formers: Co-crystallization for Creating New Hypergolic Materials with Tunable Energy Content," *Angewandte Chemie International Edition*, vol. 58, no. 51, pp. 18 399–18 404, dec 2019. [Online]. Available: https://doi.org/10.1002/anie.201908690

[152] K. Wang, T. Liu, Y. Jin, S. Huang, N. Petrutik, D. Shem-Tov, Q.-L. Yan, M. Gozin, and Q. Zhang, ""Tandem-action" ferrocenyl iodocuprates promoting low temperature hypergolic ignitions of "green" EIL–H 2 O 2 bipropellants," *Journal of Materials Chemistry A*, vol. 8, no. 29, pp. 14 661–14 670, 2020. [Online]. Available: http://doi.org/10.1039/D0TA04620E

[153] Q.-Y. Wang, J. Wang, S. Wang, Z.-Y. Wang, M. Cao, C.-L. He, J.-Q. Yang, S.-Q. Zang, and T. C. W. Mak, "o -Carborane-Based and Atomically Precise Metal Clusters as Hypergolic Materials," *Journal of the American Chemical Society*, vol. 142, no. 28, pp. 12 010–12 014, jul 2020. [Online]. Available: https://doi.org/10.1021/jacs.0c04638

[154] L. Liang, Y. Zhong, Y. Xu, G. Lei, J. Chen, H. Huang, Z. Li, J. Zhang, and T. Zhang, "Cyanoborohydride (CBH)-based hypergolic coordination compounds for versatile fuels," *Chemical Engineering Journal*, vol. 426, p. 131866, dec 2021. [Online]. Available: https://doi.org/10.1016/j.cej.2021.131866

[155] R. Masse, M. Allen, R. Spores, and E. A. Driscoll, "Af-m315e propulsion system advances and improvements," presented at the 52nd AIAA/SAE/ASEE Joint Propulsion Conference. Salt Like City, UT: American Institute of Aeronautics and Astronautics, July 25-27 2016, pp. 1–10. [Online]. Available: https://doi.org/10.2514/6.2016-4577

[156] R. Amrousse, T. Katsumi, N. Azuma, and K. Hori, "Hydroxylammonium nitrate (HAN)-based green propellant as alternative energy resource for potential hydrazine substitution: From lab scale to pilot plant scale-up," *Combustion and Flame*, vol. 176, pp. 334–348, feb 2017. [Online]. Available: https://doi.org/10.1016/J.COMBUSTFLAME.2016.11.011

[157] H. M. Titi, M. Arhangelskis, A. D. Katsenis, C. Mottillo, G. Ayoub, J.-L. Do, A. M. Fidelli, R. D. Rogers, and T. Friščić, "Metal–Organic Frameworks as Fuels for Advanced Applications: Evaluating and Modifying the Combustion Energy of Popular MOFs," *Chemistry of Materials*, vol. 31, no. 13, pp. 4882–4888, jul 2019. [Online]. Available: https://doi.org/10.1021/acs.chemmater.9b01488

[158] J. T. Hughes, T. D. Bennett, A. K. Cheetham, and A. Navrotsky, "Thermochemistry of Zeolitic Imidazolate Frameworks of Varying Porosity," *Journal of the American Chemical Society*, vol. 135, no. 2, pp. 598–601, jan 2013. [Online]. Available: https://doi.org/10.1021/ja311237m

[159] F. Baitalow, J. Baumann, G. Wolf, K. Jaenicke-Rößler, and G. Leitner, "Thermal decomposition of b–n–h compounds investigated by using combined thermoanalytical methods," *Thermochimica Acta*, vol. 391, no. 1, pp. 159–168, 2002. [Online]. Available: https://doi.org/10.1016/S0040-6031(02)00173-9

[160] B. Evans, N. Favorito, G. Risha, E. Boyer, R. Wehrman, and K. Kuo, "Characterization of nano-sized energetic particle enhancement of solid-fuel burning rates in an x-ray transparent hybrid rocket engine," presented at the 40th AIAA/ASME/SAE/ASEE Joint Propulsion Conference and Exhibit. Fort Lauderdal, FL: American Institute of Aeronautics and Astronautics, July. 11-14 2012, pp. 1–12. [Online]. Available: https://doi.org/10.2514/6.2004-3821

[161] S. Li, H. Gao, and J. M. Shreeve, "Borohydride ionic liquids and borane/ionic-liquid solutions as hypergolic fuels with superior low ignition-delay times," *Angewandte Chemie International Edition*, vol. 53, no. 11, pp. 2969–2972, 2014. [Online]. Available: https://doi.org/10.1002/anie.201309044

[162] C. Wang, Y.-J. Wang, C.-L. He, Q.-Y. Wang, and S.-Q. Zang, "Assembling silver cluster-based organic frameworks for higher-performance hypergolic properties," *JACS Au*, pp. 1–6, 2021. [Online]. Available: https://doi.org/10.1021/jacsau.1c00334

[163] M. Barrere, A. Jaumotte, B. Fraeijis de Veubeke, and J. Vandenkerckhove, *Rocket Propulsion (Propulsion de la fusée)*. Elsevier, 1960.

[164] S. J. Clark, M. D. Segall, C. J. Pickard, P. J. Hasnip, M. I. J. Probert, K. Refson, and M. C. Payne, "First principles methods using CASTEP," *Zeitschrift für Kristallographie - Crystalline Materials*, vol. 220, no. 5-6, pp. 567–570, 2005. [Online]. Available: https://doi.org/10.1524/zkri.220.5.567.65075

[165] T. Björkman, "CIF2Cell: Generating geometries for electronic structure programs," *Computer Physics Communications*, vol. 182, no. 5, pp. 1183–1186, 2011. [Online]. Available: https://doi.org/10.1016/j.cpc.2011.01.013

[166] K. Burke, J. P. Perdew, and M. Ernzerhof, "Why the generalized gradient approximation works and how to go beyond it," *International Journal of Quantum Chemistry*, vol. 61, no. 2, pp. 287–293, 1997. [Online]. Available: https://doi.org/10.1002/(SICI)1097-461X(1997)61:2<287::AID-QUA11>3.0.CO;2-9

[167] S. Grimme, "Semiempirical GGA-type density functional constructed with a long-range dispersion correction," *Journal of Computational Chemistry*, vol. 27, no. 15, pp. 1787–1799, 2006. [Online]. Available: https://doi.org/10.1002/jcc.20495

[168] M. J. Baier, A. J. McDonald, K. A. Clements, C. S. Goldenstein, and S. F. Son, "High-speed multi-spectral imaging of the hypergolic ignition of ammonia borane," *Proceedings of the Combustion Institute*, vol. 38, no. 3, pp. 4433–4440, 2021. [Online]. Available: https://doi.org/10.1016/j.proci.2020.08.025

[169] M. B. Padwal, D. A. Castaneda, and B. Natan, "Hypergolic combustion of boron based propellants," *Proceedings of the Combustion Institute*, vol. 38, no. 4, pp. 6703–6711, 2020. [Online]. Available: https://doi.org/10.1016/j.proci.2020.06.116

[170] H. Kang, S. Park, Y. Park, and J. Lee, "Ignition-delay measurement for drop test with hypergolic propellants: Reactive fuels and hydrogen peroxide,"

Combustion and Flame, vol. 217, pp. 306–313, jul 2020. [Online]. Available: https://doi.org/10.1016/j.combustflame.2020.04.017

[171] Y. Xia, L. Khezzar, M. Alshehhi, and Y. Hardalupas, "Droplet size and velocity characteristics of water-air impinging jet atomizer," *International Journal of Multiphase Flow*, vol. 94, pp. 31–43, 2017. [Online]. Available: https://doi.org/10.1016/j.ijmultiphaseflow.2017.04.014

[172] H. Hinterbichler, H. Steiner, and G. Brenn, "Self-similar pressure-atomized sprays," *Journal of Fluid Mechanics*, vol. 889, p. A17, apr 2020. [Online]. Available: https://doi.org/10.1017/jfm.2020.97

[173] R. Sijs, S. Kooij, H. J. Holterman, J. van de Zande, and D. Bonn, "Drop size measurement techniques for sprays: Comparison of image analysis, phase Doppler particle analysis, and laser diffraction," *AIP Advances*, vol. 11, no. 1, p. 015315, jan 2021. [Online]. Available: https://doi.org/10.1063/5.0018667

[174] S. Kooij, R. Sijs, M. M. Denn, E. Villermaux, and D. Bonn, "What Determines the Drop Size in Sprays?" *Physical Review X*, vol. 8, no. 3, p. 031019, jul 2018. [Online]. Available: https://doi.org/10.1103/PhysRevX.8.031019

[175] A. H. Lefebvre and V. G. Mcdonell, *Atomization and Sprays*, 2nd ed. Taylor & Francis Group, 2017.

[176] N. Dombrowski and R. P. Fraser, "A photographic investigation into the disintegration of liquid sheets," *Philosophical Transactions of the Royal Society of London. Series A, Mathematical and Physical Sciences*, vol. 247, no. 924, pp. 101–130, sep 1954. [Online]. Available: https://doi.org/10.1098/rsta.1954.0014

[177] K. U. Reddy and D. P. Mishra, "Studies on Spray Behavior of a Pressure Swirl Atomizer in Transition Regime," *Journal of Propulsion and Power*, vol. 24, no. 1, pp. 74–80, jan 2008. [Online]. Available: https://doi.org/10.2514/1.31156

[178] G. A. Vijay, N. S. V. Moorthi, and A. Manivannan, "INTERNAL AND EXTERNAL FLOW CHARACTERISTICS OF SWIRL ATOMIZERS: A REVIEW," *Atomization and Sprays*, vol. 25, no. 2, pp. 153–188, 2015. [Online]. Available: https://doi.org/10.1615/AtomizSpr.2014010219

[179] C. Indiana, M. Bellenoue, and B. Boust, "EXPERIMENTAL INVESTIGATIONS OF DROP SIZE DISTRIBUTIONS WITH IMPINGING LIQUID JETS USING

PHASE DOPPLER ANEMOMETER," *International Journal of Energetic Materials and Chemical Propulsion*, vol. 14, no. 3, pp. 241–264, 2015. [Online]. Available: https://doi.org/10.1615/IntJEnergeticMaterialsChemProp.2015011292

[180] C. Indiana, B. Boust, M. Bellenoue, and N. Azuma, "Effect of Injector Design on the Combustion of Ethanol and Hydrogen-Peroxide Sprays," *Journal of Propulsion and Power*, vol. 35, no. 3, pp. 652–661, may 2019. [Online]. Available: https://doi.org/10.2514/1.B37286

[181] D. Zhang, P. Zhang, Y. Yuan, and T. Zhang, "Hypergolic ignition by head-on collision of N,N,N',N'-tetramethylethylenediamine and white fuming nitric acid droplets," *Combustion and Flame*, vol. 173, pp. 276–287, 2016. [Online]. Available: https://doi.org/10.1016/j.combustflame.2016.08.010

[182] K.-S. Kim, V. K. Bhosale, and S. Kwon, "Synergistic effect of a hybrid additive for hydrogen peroxide-based low toxicity hypergolic propellants," *Combustion and Flame*, vol. 231, p. 111450, 2021. [Online]. Available: https://doi.org/10.1016/j.combustflame.2021.111450

[183] F. H. Stephens, R. T. Baker, M. H. Matus, D. J. Grant, and D. A. Dixon, "Acid initiation of ammonia–borane dehydrogenation for hydrogen storage," *Angewandte Chemie International Edition*, vol. 46, no. 5, pp. 746–749, 2007. [Online]. Available: https://doi.org/10.1002/anie.200603285

[184] M. R. Weismiller, A. C. T. van Duin, J. Lee, and R. A. Yetter, "Reaxff reactive force field development and applications for molecular dynamics simulations of ammonia borane dehydrogenation and combustion," *The Journal of Physical Chemistry A*, vol. 114, no. 17, pp. 5485–5492, 2010. [Online]. Available: https://doi.org/10.1021/jp100136c

APPENDIX A CHECKLIST SLAB BURNER

☐ **Safety**

- ☐ All non-mandatory personnel leave the test room
- ☐ Put on Personal Protective Equipment

☐ **Labview control software**

- ☐ Connect the two (2) USB cables (NI-DAQ and Mass flow meter) to the computer
- ☐ Start the LabView program

☐ **Control panel**

- ☐ Verify that all valves are connected
- ☐ Set the arc igniter switch to OFF
- ☐ Connect the two igniter wires to the arc igniter
- ☐ Connect the two igniter **control** wires from the control panel to the side of the arc igniter
- ☐ Set the arc igniter to "I"
- ☐ Press the green power button to turn on the control panel; it should light green
- ☐ Power up the NI-DAQ and the Coriolis mass flow meter

☐ **Ventilation**

- ☐ Close the ventilation in **A385.4**
- ☐ Confirm thatvrhe ventilation is working in **A385.5**

☐ **N2 line**

- ☐ Connect N2 tank to the N2 line
- ☐ Open N2 tank
- ☐ Set N2 pressure regulator to 450 psi
- ☐ Confirm good pressure reading on the Labview software

☐ **Air line**

- ☐ Connect Air tank to the Air line
- ☐ Set wall air regulator to $>$ 100 psi

- ☐ Set secondary air regulator to 100 psi
- ☐ Open manual valves connected to the main valve
- ☐ Confirm good pressure reading on the Labview software

☐ **Camera**

- ☐ Install Photron camera and connect Ethernet cable to the computer
- ☐ Connect the BNC trigger cable from the control panel to Input 2
- ☐ Set and **note** fps, resolution and exposure
- ☐ Calibrate the camera by clicking the SHADING button
- ☐ Take a picture of the calibration target on the back and front windows
- ☐ Install Nikon camera

☐ **O2 line**

- ☐ Connect O2 tank to the O2 line
- ☐ Open O2 tank
- ☐ Set O2 pressure regulator to desired pressure
- ☐ Confirm good pressure measurement on the Labview software

☐ **Acetone igniter**

- ☐ Use the custom-made acetone dispense to put 3 to 5 droplets of acetone on the front of the slab

☐ **Pre-test procedure completed**

Test procedure

- ☐ **Software checklist - Automatic test**
  - ☐ Make sure pre-test procedure is completed
  - ☐ Start recording from Nikon camera
  - ☐ Input warm-up time
  - ☐ Input test duration time
  - ☐ Input purge duration time
  - ☐ Verify that air pressure is > 100 psi
  - ☐ Verify that N2 pressure is > 450 psi
  - ☐ Verify that O2 pressure is at desired pressure
  - ☐ Verify that the emergency stop button is not pressed
  - ☐ Open valve main O2 valve a few seconds to verify that the flow rate is adequate
  - ☐ Enter record path + file name
  - ☐ Start Record
  - ☐ Check status on Record/Connection Status; must be green
  - ☐ **Visual confirmation that no one is around**. From now on, no one can enter the test room.
  - ☐ Set control mode to automatic
  - ☐ Unlock
  - ☐ Open Air valve
  - ☐ Take emergency button in hands
  - ☐ Set camera on triggering state
- ☐ **Start test**

Shutdown procedure

☐ **Software shutdown AFTER test**

- ☐ Lock valve state in LabView program
- ☐ Verify data files
- ☐ Press STOP PROGRAM button in LabView program
- ☐ Save video(s) from high-speed camera(s)
- ☐ Close LabView program

☐ **Hardware shutdown**

- ☐ Depressurize air line
- ☐ Close O2 tank
- ☐ Press the green button to turn off the control panel; it should NOT be lit
- ☐ Disconnect all electrical power
- ☐ Close N2 cylinder

Emergency procedures

☐ **Fire outside the slab**

- ☐ Purge manually with LabView by opening N2 main valve
- ☐ Use fire extinguisher
- ☐ **If the fire is not controlled**: Exit the lab and call Polytechnique's security and 911

☐ **Fire inside the slab**

- ☐ Purge manually with LabView by opening N2 main valve
- ☐ Use fire extinguisher
- ☐ **If the fire is not controlled**: Exit the lab and call Polytechnique security and 911

☐ **Computer crash in a test**

- ☐ Hit emergency stop
- ☐ All valves should close automatically
- ☐ Monitor the fire if any, proceed to above steps depending on fire location

☐ **Purge valve fails**

- ☐ Monitor the fire if any, proceed to above steps depending on fire location

☐ **Purge doesn't work**

- ☐ Monitor the fire if any, proceed to above steps depending on fire location

☐ **Overpressure**

- ☐ If combustion pressure $>$ 280 psi, pressure relief valve opens
- ☐ If combustion pressure $>$ 300 psi, automatic shutdown mode of LabView program
- ☐ Hit emergency stop
- ☐ Monitor the fire if any, proceed to above steps depending on fire location

APPENDIX B CHECKLIST HYPERGOLIC SLAB BURNER

Pre-test procedures

☐ **Safety**

- ☐ All non-mandatory personnel leaves test room)
- ☐ Put on Personal Protective Equipment
  - ☐ TYCHEM 5000 suit
  - ☐ Acid-resistant boots
  - ☐ Faceshield with organic vapor cartridges
  - ☐ Appropriate gloves (Latex/Neoprene, DO NOT USE NITRILE GLOVES)
  - ☐ Tape gloves to the suit using ChemTape

☐ **LabVIEW control software**

- ☐ Connect the three (3) USB cables (NI-DAQ, NI-USB DAQ and Mass flow meter) to the computer
- ☐ Start the LabVIEW program

☐ **Control panel**

- ☐ Verify that all valves are connected
- ☐ Press the green power button to turn on the control panel; it should glow green
- ☐ Power up the two (2) NI-DAQs and the Coriolis mass flow meter

☐ **Camera**

- ☐ Install Photron camera and connect Ethernet cable to the computer
- ☐ Connect the BNC trigger cable from the control panel to Input 2
- ☐ Set and **note** fps, resolution and exposure
- ☐ Calibrate the camera by clicking SHADING button
- ☐ Take a picture of the calibration target on the back and front windows
- ☐ Install Nikon camera if needed

☐ **Ventilation**

- ☐ Close the ventilation in **A385.4**
- ☐ Confirm that the ventilation is working in **A385.5**

☐ **Water pool**

- ☐ Fill the pool with water
- ☐ Close the water filling valve

☐ **Verification: make sure that all systems are depressurized**

☐ **Water rinse line**

- ☐ Fill the water tank
- ☐ Connect the water tank to the water line
- ☐ Connect the air pressure line to the water tank
- ☐ Turn off the water rinse manual valve on top of the WFNA tank

☐ **N2 line - Carrier gas**

- ☐ Connect the N2 tank to the N2 line
- ☐ Open N2 tank
- ☐ Set N2 pressure regulator to 100 psi
- ☐ Confirm good pressure reading in the LabVIEW software
- ☐ Verify that there is enough of N2 in the tank (at least 400 psi)

☐ **Air line**

- ☐ Connect Air tank to the Air line
- ☐ Set wall air regulator to $>$ 100 psi
- ☐ Set secondary air regulator to 100 psi
- ☐ Open manual valves connected to the main valve
- ☐ Confirm good pressure reading in the LabVIEW software

☐ **O2 line**

- ☐ Connect O2 tank to the O2 line
- ☐ Set O2 regulator to desired pressure
- ☐ Confirm good pressure reding in the LabVIEW software
- ☐ Verify that there is enough O2 in the tank (at least 400 psi)

- ☐ **WFNA fill**
  - ☐ Connect the secondary N2 tank to the N2/WFNA line
  - ☐ Verify that there is no pressure in the WFNA tank
  - ☐ Close all manual valves
  - ☐ Open the flush WFNA valve using the LabVIEW software
  - ☐ Dispense the desired amount of WFNA in the beaker
  - ☐ Open the top manual valve
  - ☐ Use the syringe to dispense the desired amount into the WFNA tank
  - ☐ Close the top manual valve
  - ☐ Close the flush WFNA valve using the LabVIEW software
  - ☐ Rinse the beaker and the syringe with large volume of water
- ☐ **WFNA pressurisation**
  - ☐ Open the N2 tank
  - ☐ Set N2 pressure regulator to 200 psi
  - ☐ Make sure all manual valves are closed
  - ☐ Open N2 manual valve to pressurize the WFNA
  - ☐ Confirm good pressure reading in the LabVIEW software
  - ☐ Verify that there is sufficient N2 in the tank (at least 400 psi)
  - ☐ Exit the room
- ☐ **Pre-test procedure completed**

Test procedures

☐ **Software checklist - Automatic test**

- ☐ Make sure pre-test procedure is completed
- ☐ Verify that there is enough free space on the computer (about12 Gb)
- ☐ Start recording from Nikon camera
- ☐ Input injection AND test AND purge duration time
- ☐ Verify that air pressure > 100 psi
- ☐ Verify that N2 carrier gas pressure = 100 psi
- ☐ Verify that WFNA = 200 psi
- ☐ Verify that O2 pressure is at desired pressure
- ☐ Verify that the emergency button is not pressed
- ☐ Open carrier gas line to purge air and fill the combustion chamber with N2
- ☐ Turn off (red) the camera trigger button
- ☐ Enter record path + file name
- ☐ Start Record
- ☐ Verify status on Record/Connection Status; must be green
- ☐ **Visual confirmation that no one is around**. From now on, no one can enter the test room.
- ☐ Set control mode to automatic
- ☐ Unlock
- ☐ Open Air valve
- ☐ Take emergency button in hands
- ☐ set camera to triggering state
- ☐ Close carrier gas line

☐ **Start test**

After test procedures

☐ **WFNA depressurisation**

- ☐ Close manual valve N2
- ☐ Exit the room
- ☐ Open WFNA bleed valve using LabVIEW program

☐ **Injector rinse**

- ☐ Make sure emergency stop button is not engaged
- ☐ Open main valve
- ☐ Open the water valve using LabVIEW program
- ☐ Rinse for several seconds
- ☐ Close the water valve using LabVIEW program
- ☐ Close main valve
- ☐ Open WFNA bleed valve using LabVIEW program

☐ **Combustion chamber rinse**

- ☐ Remove the top window
- ☐ Flush the chamber manually with water using the squeeze bottle
- ☐ Remove the bottom slab holder
- ☐ Remove the injector plate
- ☐ Remove the carrier gas holding plate
- ☐ Remove the first part of the carrier gas cylinder
- ☐ Use air hose and a shop towel to clean the carrier gas cylinder

List of parts that need to be rinsed with water

- ☐ **WFNA tank/line**
- ☐ **Syringe**
- ☐ **Top valve (!)**
- ☐ **Beakers**
- ☐ **Injector plate**
- ☐ **Slab Holder**
- ☐ **Carrier gas holding plate**
- ☐ **First part of the carrier gas cylinder**
- ☐ **All tools used**
- ☐ **Nuts and bolts**

Shutdown procedures

☐ **Hardware shutdown AFTER test**

- ☐ Depressurize air line
- ☐ **Close N2 tanks**
- ☐ Remove remaining pressure in the lines
- ☐ Press the green power button to turn off the control panel; it must NOT be lit.
- ☐ Disconnect all electrical power

☐ **Software shutdown AFTER test**

- ☐ Lock valve state in LabVIEW program
- ☐ Verify data files
- ☐ Press STOP PROGRAM button in LabVIEW program
- ☐ Save video(s) from high-speed camera(s)
- ☐ Close the LabVIEW program